QUANTITATIVE METHODS FOR INFERRING PROCESS-STRUCTURE-PROPERTY RELATIONS IN MACHINING

A Dissertation
Presented to
The Academic Faculty

By

Patxi Fernandez-Zelaia

In Partial Fulfillment
of the Requirements for the Degree
Doctor of Philosophy in the
School of Mechanical Engineering

Georgia Institute of Technology

December 2018

QUANTITATIVE METHODS FOR INFERRING PROCESS-STRUCTURE-PROPERTY RELATIONS IN MACHINING

Approved by:

Dr. Shreyes N. Melkote, Advisor
School of Mechanical Engineering
Georgia Institute of Technology

Dr. Surya Kalidindi
School of Mechanical Engineering
& School of Materials Science
Georgia Institute of Technology

Dr. Christopher Saldana
School of Mechanical Engineering
Georgia Institute of Technology

Dr. Roshan J. Vengazhiyil
School of Industrial & Systems Engineering
Georgia Institute of Technology

Dr. Troy Marusich
Protolabs

Date Approved: November 2, 2018

ACKNOWLEDGEMENTS

First and foremost I would like to thank my advisor, Dr. Shreyes N. Melkote. His oversight, guidance, and vision were critical for focusing my curiosities and efforts into valuable research objectives. He offered me the flexibility to explore various research avenues without which this work would not be possible. Dr. Roshan V. Joseph has been an encouraging influence and an invaluable technical mentor – I cannot thank him enough for the interactions we have shared. I owe a great deal of gratitude to Dr. Surya Kalidindi, who in my second year, offered for the first time the introductory *Materials Informatics* course. The structure and content of the course, as well as the passion with which he taught, spurred my fascination with the topic. I had the pleasure of working with Dr. Christopher Saldana and Dr. Troy Marusich in a joint DoE GOALI project at the beginning of my Ph.D. and I am grateful for the interactions I've shared with them since.

There are far too many graduate students, colleagues, and friends I would like to thank. This includes high school, college, Atlanta, and D.C. friends. I would like to thank the Montgomery machine shop staff whose help was critical for the experimental portion of this work. Special thanks to the experimentalists in the MINED group who trained me to use their experimental equipment, maintained the equipment, and provided technical advice when needed. Thanks to the many graduate students with whom I prepared with for the qualifier exams. I would like to also thank the many people I interacted with during the job search towards the end of this endeavour. This includes people industry, national labs, and academia who shared their candid insights with me as I decided on which post-graduate path to pursue.

Thanks, of course, to my parents, Mertxe and Humberto, and my sister, Amaia, whose support has enabled me to explore and pursue my interests. Their confidence has encouraged and comforted me throughout my life.

TABLE OF CONTENTS

LIST OF TABLES

LIST OF FIGURES

SUMMARY

Machining is net shape or near net shape subtractive secondary manufacturing process. It usually follows primary processes such as casting and forging. The geometric precision and accuracy offered by machining cannot be obtained using other processes and as such has been a critical enabler of mass production following the industrial revolution. Beginning approximately fifty years ago, researchers began to study the microstructural evolution imposed by machining processes on metallic systems. These works rigorously quantify machined structures using advanced characterization techniques used by materials scientists (diffraction, TEM, etc.). In the 1980s modeling research began to investigate the simulation of machining processes using finite element methods. These models can be utilized to estimate key process responses (forces, temperatures) without the need to run costly physical experiments.

The machined material consist of novel microstructures, which are produced by severe plastic deformation at high rates. This is a unique thermomechanical process that is difficult to emulate using traditional mechanical testing. The goal of studying the machined microstructures is to establish the process-structure-property relationships which govern material evolution. This understanding can enable the design and manufacture of functional materials and surfaces. Despite many advances made in this field, there is still a need to better *quantify* these relationships. An expert scientist can look at an image and describe it - but how can this process be made more efficient? How can the interpretation of the expert and the knowledge derived be distilled into numeric data? What are the most informative and robust numerical descriptors of the resulting microstructure? Quantification is critical as it then enables a wealth of analysis methods for mathematically rigorous identification of the process-structure-property linkages e.g. regression, classification, etc..

Similarly, there are still several unresolved issues pertaining to finite element modeling of machining processes. Substantial effort has been made toward establishing inelastic

constitutive descriptions of materials subject to machining. However, an outstanding issue associated with these works is the difficulty of *calibrating* these models. Physical models are often complex with many unknown parameters. Even simple models, such as the ubiquitous Johnson-Cook model, can be difficult to calibrate for machining applications. The machining literature contains many works, which report different Johnson-Cook calibration parameters for identical material systems. There is an issue of *nonuniqueness* associated with the unknown parameters; different combinations of parameters all appear to "work".

This thesis presents an investigation focused on robust machining process modeling at the macroscopic level (forces, temperatures) and microstructure scale. Macroscopic level machining modeling focuses on constitutive model calibration and uncertainty quantification. We treat the nonuniqueness issue from a probabilistic perspective; there are many permissible combinations of constitutive model parameters and thus we treat them as random variables that come from some unknown distribution. Inference is thus on the *probability densities* of these parameters. The microscale modeling portion of the work focuses on novel material characterization methods and determination of the process-structure-property relationships using data-driven techniques.

Mechanical properties of machined microstructures are usually reported in terms of their hardness. Inference of uniaxial properties is difficult since the machined chips are small in scale ($\sim 1\,mm$) and the deformed subsurface is on the order of $100\,\mu m$ or less. Recently established spherical indentation protocols enable the inference of elastic and post elastic behavior subject to indentation deformations. Mapping to uniaxial equivalent values however is not possible in the post-elastic region. Estimates exist for the mapping but the uncertainty of these estimates does not. Therefore, we establish an efficient Bayesian methodology for estimating this mapping using a surrogate FE model.

Microstructures are quantified using both scanning electron microscopy (SEM) and orientation imaging microscopy (OIM). SEM can identify certain defect structures and scan times are relatively fast. OIM data is richer since it captures crystallographic informa-

tion however scans are slow and therefore expensive. Hence, we utilized both methods to characterize the machined microstructures. Numerical quantification is achieved using statistical techniques popularized in the Materials Informatics community. SEM images are quantified using chord length statistics. OIM data is characterized using a generalized spherical harmonics representation and a novel spatial statistic we derive. Numerically wieldable data is generated in both settings by distilling the raw data using unsupervised dimensionality reduction. Regression is performed using data-driven statistical modeling.

Finally, we we return to the macroscopic level machining challenge associated with model calibration. Direct calibration of the constitutive models embedded in the finite element framework is difficult since the model is computationally expensive. Therefore, we develop a surrogate model to emulate the behavior of the finite element model. The data generated by the finite element model displays complex behavior and therefore a more complex surrogate is required. Calibration is performed by regressing machining forces onto the surrogate model. Validation is performed by comparing the chip geometries produced by the calibrated finite element model to experimentally measured chip geometries.

In summary, this work describes the investigation of machining modeling at *both* the macroscopic process-scale and microstructure-scale. Characterization of the machining process using rigorous quantitative methods enables efficient inverse modeling and design of functional component surfaces.

CHAPTER 1
INTRODUCTION

Machining or cutting is a subtractive manufacturing process which produces net shape or net near shape components by the shearing and removal of material with a cutting tool. Metal cutting operations became scalable during the industrial revolution with the the development of steam power. Material removal operations continue to be of great importance at the present time as it is estimated that their yearly cost is 10% the gross national product [1]. The study of cutting processes have traditionally focused on (1) improvement of cutting operations, (2) improvement of workpiece quality, and (3) improvements of the rates of production [1]. Today, research on improving component surface quality focuses either on geometric characteristics (tolerances, surface topology) or the surface and subsurface material behavior. Experimental approaches study the microstructure and properties of machined materials to better understand the process physics or empirically identify trends. There is considerable effort to realize the aforementioned improvements through modeling and simulation, which in turn relies on description of the constitutive behavior of the material i.e. constitutive model. The current state of the art in both of these approaches is practically limited in a few ways. Constitutive model approaches attempt to capture the relevant physics using mathematical descriptions of the relevant quantities (plastic strain, flow stress, internal state variables, etc.). However, these descriptions often contain many unknown "calibration parameters" which are difficult to estimate and are often nonunique. Furthermore, recent work suggests that identification of the constitute law parameters may be confounded by uncertainties in the tribological model [2]. Experimental microstructure characterization often lacks this mathematical rigor and instead relies on the expertise of domain experts to interpret the meaning of generated data e.g. images. Therefore, there is a need to identify efficient methods for building machining constitutive models and to es-

tablish mathematically rigorous methods for quantifying experimentally obtained material data i.e. properties and microstructure.

1.1 Material modeling

The phenomenological Johnson-Cook model is ubiquitously found in finite element analysis (FEA) across many engineering disciplines [3]. The popularity of this constitutive description is likely associated with its simplicity $\sigma = (A + B\epsilon^n)(1 + c\log\dot{\epsilon})(1 - \theta^m)$. This three term multiplicative description accounts for strain and rate hardening as well as thermal softening (θ the homologous temperature). Many modifications have since been introduced to accommodate additional mechanisms. In the machining community perhaps one of the better known modifications, introduced by Calamaz, Coupard, and Girot, includes additional strain softening mechanisms [4]. More sophisticated physics inspired models have also been established to accommodate for the evolution of internal state variable (ISV) quantities which may include microstructure descriptors [5, 6, 7]. However, identification of the unknown constitutive model constants is a difficult challenge that is seldom explicitly addressed in these works. Furthermore, the literature contains a wide range of published "calibration constants" for identical models and identical material systems which suggests the presence of model nonuniqueness [6]. Calibration is made difficult as FEA simulations, necessary to evaluate the efficacy of a constitutive model, are computationally costly. The first focused study on FE model constitutive model calibration for machining was done by Ozel and his colleagues [8, 9]. The approach iteratively identifies the unknown model parameters via brute force evaluation of the FE model until a cost function is minimized. The solution is therefore costly to obtain and only produces a point estimate with no corresponding measure of solution confidence. The approach of Calamaz, Coupard, and Girot was to simply evaluate the model at a few trial settings and accept the "best" of these trials as the solution [4]. Agmell et al. used a Kalman filter for parameter identification and built an interaction-free polynomial surrogate model which is suppose to

emulate FE model [10, 11]. Although the approach is appealing, it is limited by the inadequacy of the surrogate. Polynomials are inadequate surrogates for deterministic simulations and neglecting interactions between model parameters (A,b,n,c,m) and the flow stress (σ) is an poor assumption. Kloche et al. estimated parameters by linearly interpolating the constitutive parameters from several trial evaluations in order to "match" experimental forces [12]. This strategy is only valid if the interactions are linear which they are clearly not. It is clear that constitutive model calibration in the machining community is still inadequate. Statisticians have understood this issue and have established efficient methods for addressing these difficulties [13, 14, 15]. Computational burden is alleviated by establishing a *Gaussian Process* (GP) surrogate model which interpolates the true complex model and is much more stable than other surrogate choices [13, 14]. Identification of the unknown parameters, and their uncertainties, can then be obtained using the computationally cheap GP surrogate and statistical inference [15].

1.2 Material characterization

Pioneer M. Eugene Merchant contributed a great deal to the study of metal cutting mechanics in the 1940s [16]. Later on Milton Shaw and Ranga Komanduri continued this research and dedicated some of their focus on the study of microstructure evolution during machining [1, 17]. Modern works have adopted advanced characterization methods used in materials science and have identified the mechanisms that drive microstructure evolution in cutting operations. These mechanisms include: dynamic recrystallization, nanotwinning, formation of dislocation cells, crystallographic texture evolution, and phase transformations [18, 19, 20, 21, 22, 23, 24]. Property quantification in machined structures is often limited to nano and micro hardness testing as traditional mechanical testing (uniaxial testing) is difficult to perform on small machined samples such as chips or the workpiece surface [25, 26]. Therefore, modern mechanics-centered machining research strives to identify the process-structure-property (PSP) linkages induced during machining processes. Estab-

lishment of this knowledge enables the design and manufacture of functional workpiece surfaces with improved performance capabilities.

Microstructure quantification in much of the existing machining work requires the careful interpretation of images by experts which is qualitative in nature [25, 19, 20, 26, 27, 28]. Quantitative methods for describing microstructures often require ad hoc descriptors i.e. mean grain size, mean dislocation density, grain aspect ratio, etc.. More recent works include quantitative measures using *distributions* of parameters [18, 29, 30, 31]. However, often these distributions (grain size, misorientation) are generated by OIM post processing software which require a priori assumptions on how to define grains and grain boundaries i.e. misorientations $> 15^{\circ}$ constitute a grain boundary. Furthermore, these distributions are unwieldy - how can distributions, or histograms, be quantitatively compared or used in analysis? Only very recent work in the machining community utilizes more generalized quantitative microstructure descriptors for crystallographic texture which are free from ad hoc assumptions or definitions. Basu et al. employ an information entropy measure which experimentally quantifies the evolution of crystallographic texture using the empirically derived orientation distribution function [32, 33]. Therefore most works rely heavily on laborious qualitative interpretation of results by qualified domain subject experts, some obtain quantitative descriptions by invoking certain a priori assumptions, and only very recent work focuses on robust descriptors.

Material evolution modeling is often established using both process-structure and direct process-property linkages [20, 19]. These mappings are often illustrated using mechanism maps [20, 19] analogous to the ubiquitous Ashby diagrams [34]. Some works utilize regression to model strain-structure relationships [32, 33]. Prediction of microstructure and property evolution is rarely data-driven and instead manufacturers usually rely on numerical simulation [35, 30, 31, 32, 5, 7, 6]. Materials informatics (MI) is an emerging field within the materials community which is the materials analogue to cheminformatics and bioinformatics. MI approaches leverage statistical methods for the rigorous quantification

of microstructures and data-driven building of the full PSP linkages [36, 37].

From this brief overview several limitations in the modeling of machining processes may be identified. Firstly, constitutive model calibration using complex FE simulations is lacking. Most works estimate point estimate parameters using brute force iteration directly using expensive simulations and none address model parameter uncertainty which drives nonuniqueness. A few works utilize surrogate models, however, they are poor emulators of the actual FE code. Furthermore, no works address tribological-constitutive interactions present in the model. Second, property quantification is limited to hardness which is an insufficient descriptor for detailed functional component surface design. Uniaxial modulus, strength, hardening rate, etc. are desirable mechanical behavior descriptors which currently cannot be efficiently inferred. Lastly, the machining literature is lacking in robust quantitative methods for establishing process-structure-property linkages. Often these relationships are hard-coded into physics models and the process response is estimated via simulation. A data-driven strategy, however, is an alternative means to establish these relationships.

1.3 Research objectives

In light of the reviewed state of the art in machining research this thesis is focused on employing statistical methods for alleviating several of the identified limitations. Specifically the objectives of this work are,

1. Identify an efficient methodology for calibration of machining finite element (FE) models. This effort should consider both constitutive model parameters and tribological considerations in a coupled fashion. In addition to obtaining calibration parameters the *uncertainty* in those quantities is also desired.

2. Establish a framework for estimating the uniaxial equivalent constitutive post-elastic behavior of machined microstructures from indentation experiments.

3. Establish the mathematical PSP linkages of machined materials using microscopy

and indentation. Illustrate a viable inverse strategy for identifying the property $\mapsto$ process mapping which may be used for design of functional surfaces.

These objectives may be achieved by first considering a thorough literature review of works related to these objectives and a scientific treatment using both experimental and numerical techniques.

1.4 Research approach

Indentation stress-strain curves from various machined chips are shown in Figure 1.1. The indentation stress strain curves illustrate the different constitutive responses produced by the different structures. However, it is unclear how exactly these curves map to uniaxial equivalent quantities. Furthermore, we also wish to obtain uncertainty estimates associated with the uniaxial equivalent constitutive behavior e.g. we wish to claim "this structure has yield strength $300 \pm 25\ MPa$."

A methodology for doing so using Bayesian methods and surrogate finite element (FE) models is introduced in Chapter 3. First, an inexpensive FE surrogate model is built from a finite number of expensive FE model evaluations. The established surrogate model emulates the FE response and can thus be used to efficiently infer the unknown parameters. A Bayesian strategy is adopted to capture constitutive model parameter uncertainty.

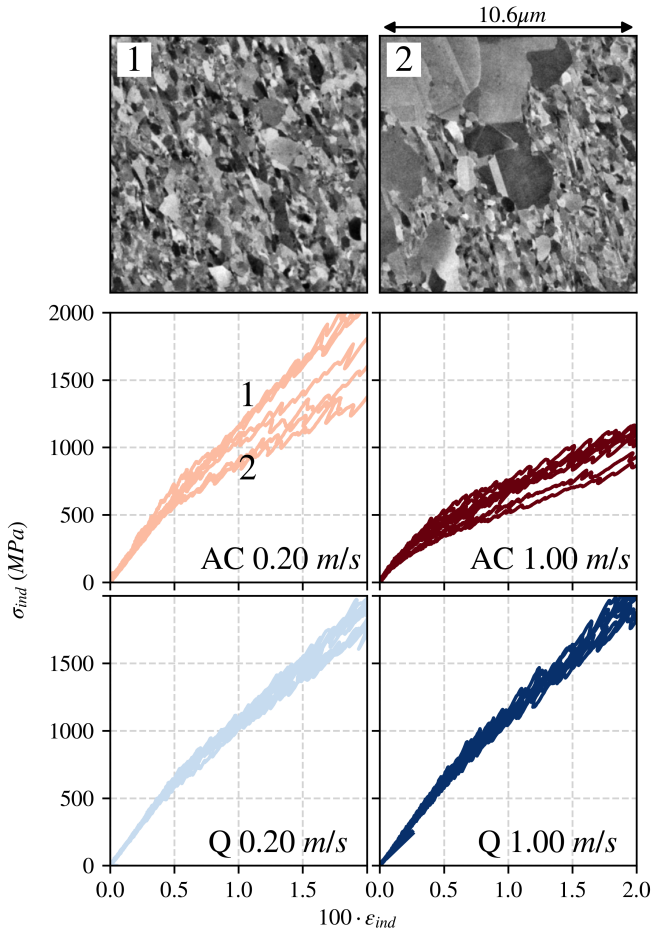

Figure 1.1: Machined chip indentation stress strain curves for various process conditions.

Electron backscatter diffraction (EBSD) inverse pole figure micrographs corresponding to machined copper are shown in Figure 1.2. The grid corresponds to different values of cutting speeds and rake angles. For each rake angle the approximate corresponding shear strain is also shown. Clearly, there is a very pronounced visual trend present in the micrographs. Namely, grain refinement is drastically increased with increasing strains. Furthermore, it is quite clear that local *misorientations* are more pronounced going from $\alpha = 15°$ to $\alpha = 5°$. This agrees well with the dynamic recrystallization theory, which states that microstructure evolution is driven by cell formation and lattice misorientation [19]. Furthermore, there is evidence which suggests that at high cutting speeds and strain

the misorientation appears to be less severe; for example there is greater crystallographic spatial correlation present in the OIM data at $\alpha = 5^\circ \,\&\, V = 1.00\, m \cdot s^{-1}$ than at $\alpha = 5^\circ \,\&\, V < 1.00\, m \cdot s^{-1}$.

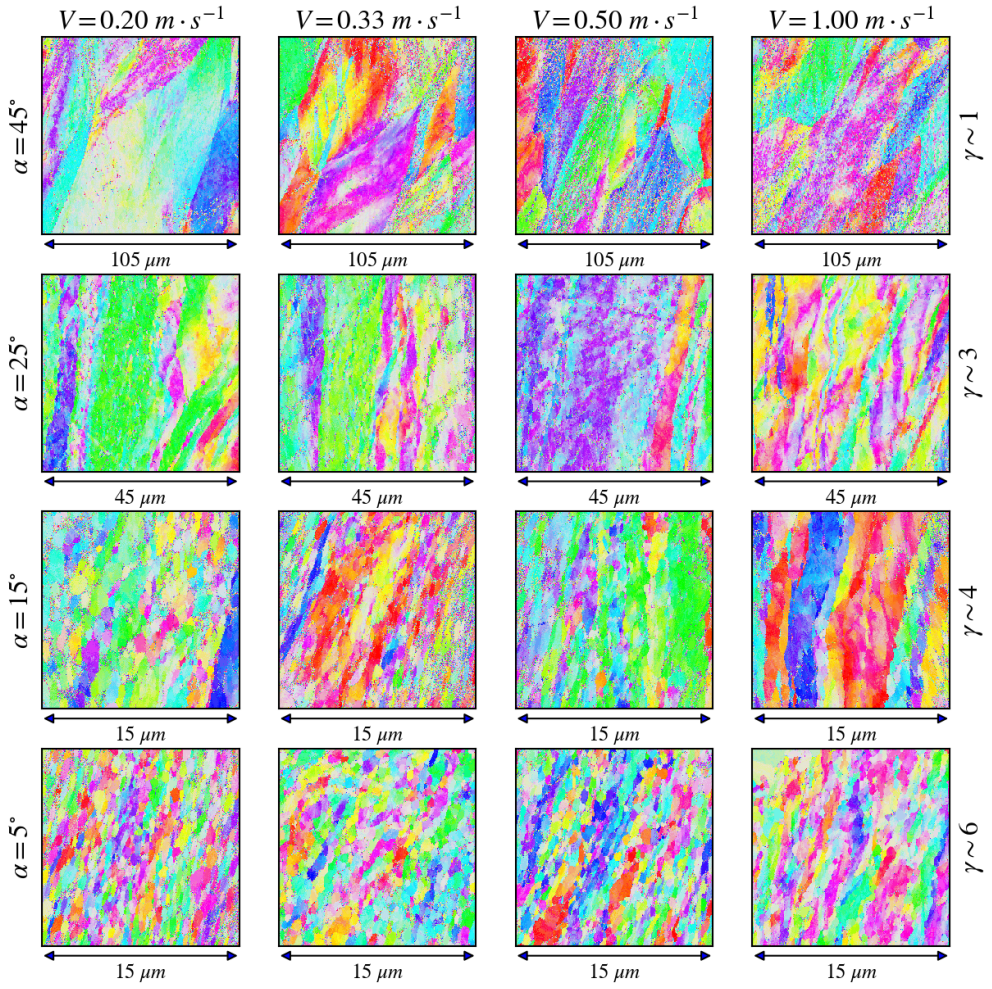

Figure 1.2: EBSD images of the various microstructures produced via machining.

It is these structural features that we exploit when developing a suitable microstructure descriptor in Chapter 4. The derived morphological descriptor may then be utilized to quantify the machining process-structure map. Property measurements will be obtained using a combination of instrumented spherical indentation tests and traditional microhardness measurements. A data-driven multiple output Gaussian Process model will be established, which combines these individual maps into a full process-structure-property knowledge

system.

Next consider the micrographs shown in Figure 1.3. These are machined chips produced at various cutting speeds with the rake angle fixed at 5°. It is clear that the microstructure varies from nearly fully recrystallized to nearly fully annealed. These microstructures were obtained by allowing machined chips to *air cool* following deformation. Identical tests that produced *quenched* chips were also conducted. Again, it is the following qualitative features we wish to quantify: grain size, preferred orientation, and microstructural population morphology (bimodal structure distribution).

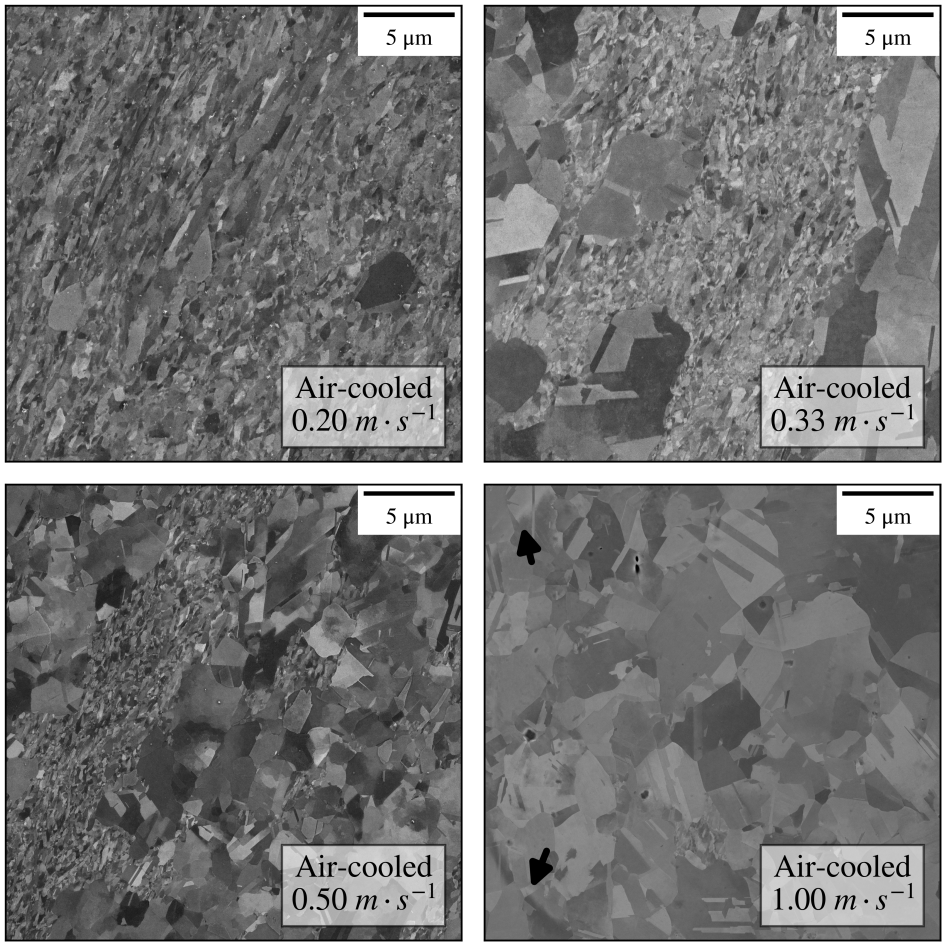

Figure 1.3: Generated air cooled microstructures. Micrograph corresponding to $V = 1.00m \cdot s^{-1}$ was indented and arrows are shown to indicate the contact radius edge.

We present a robust methodology for quantifying the process-structure-property maps

of these generated structures in Chapter 5. A large data set of micrographs are acquired and each micrographs is processed to obtain its angularly resolved chord length statistic. This ensemble of high dimensional chord length statistics are then distilled into lower dimensions using principle component analysis. Uniaxial property measurements are obtained from machined chips using instrumented spherical nanoindentation protocols and the aforementioned Bayesian inverse methods. The full process-structure-property relationships are established using a multiple output Gaussian process model. A Bayesian strategy is proposed to illustrate a methodology for identifying the inverse property-process.

Finally we wish to be able to infer the post-elastic constitutive behavior of materials directly from machining experiments. The output of three finite element simulations using three sets of Johnson-Cook constants is shown in Figure 1.4. Parameters obtained from split-Hopkinson tests and quasi-static compression tests overpredict strain hardening, which results in chips that are too thick (and forces that are too high). Forces and chips obtained using our calibration approach best explain physically measured forces and chips. Therefore, we hypothesize that the "best" machining constitutive models may be obtained by directly using machining data for model calibration. Fundamentally this is because machining conditions correspond to large deformations, high rates, and elevated temperatures, which are conditions that are difficult to emulate in standard mechanical tests. However, unlike traditional mechanical tests, the measurements obtained in machining experiments (forces, chip morphology, temperatures, etc.) cannot be used to directly estimate flow stress curves. Therefore, statistical inference is necessary to indirectly estimate the underlying constitutive behavior.

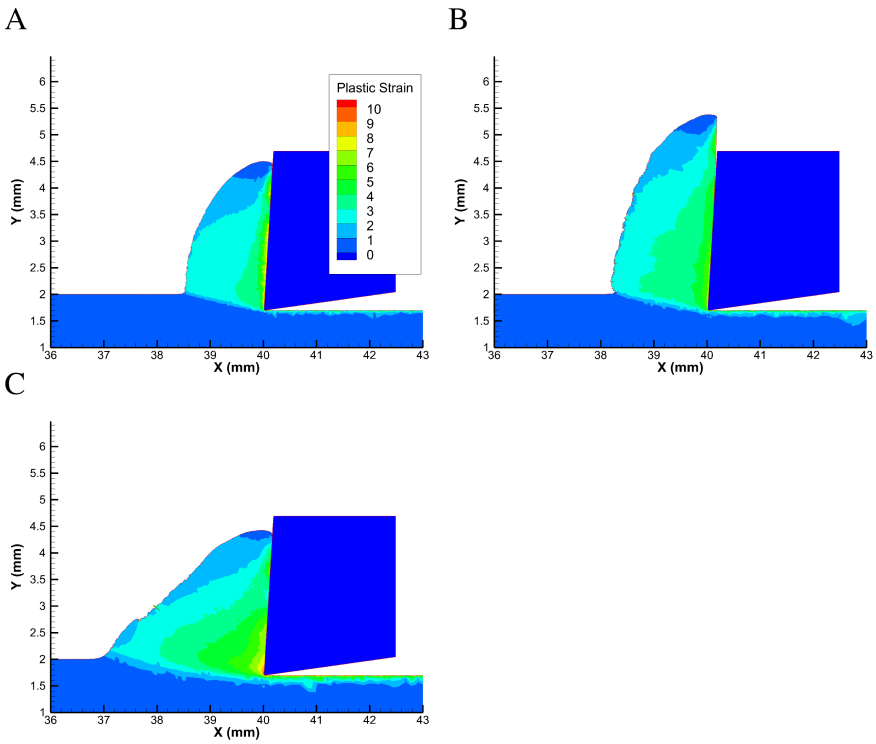

Figure 1.4: Al6061-T6 machining simulations at $\alpha = 5°$ and $V = 12\,m \cdot min^{-1}$. (A) friction and constitutive parameters corresponding to the posterior distribution mean from this work, (B) constitutive parameters from study using JC and Oxley's model cutting model [38] and the experimental apparent friction coefficient, and (C) constitutive parameters obtained via split-Hopkinson bar testing[39] and the experimental apparent friction coefficient

.

We present a methodology for identifying material models directly from machining forces in Chapter 6. First, a computationally cheap surrogate model of the complex FE machining model is established. The inexpensive model is then utilized to regress the material model onto the observed cutting forces.

1.5 Dissertation outline

The outline of this thesis is as follows. First, Chapter 2 contains a critical review of the relevant works pertaining to this research effort. Chapter 3 proposes a Bayesian methodology for estimated constitutive post-elastic properties and their confidence bounds from spheri-

cal indentation experiments. Chapter 4 focuses on the development of a new microstructure descriptor, which captures morphological or misorientation information from OIM data. In addition, a novel PSP framework is introduced using Multiple Output Gaussian Process Regression (MOGPR). Chapter 5 studies novel bimodal machined microstructures which may be quantified using chord length statistics. Chapter 6 introduces an efficient machining constitutive model calibration strategy, which simultaneously considers both the constitutive description as well as tribological uncertainties associated with the tool-chip contact. Finally, Chapter 7 summaries this work with key conclusions and suggests areas of future work.

CHAPTER 2

BACKGROUND

2.1 Machining Mechanics

A schematic of a simplified machining process is shown in Figure 2.1. This two dimensional configuration, represents an orthogonal cutting model where the cutting action occurs within a two-dimension plane [1]. Although production processes deviate from this simplified configuration it is a useful model for fundamental studies of the effects of process parameters. These include the cutting speed V, the uncut chip thickness t_o, and the rake angle α. Shearing occurs in the primary shear zone and the degree of shearing is controlled by both the uncut chip thickness and rake angle. Depending on the process conditions chosen shear strains can vary between 1-10, rates $10^3 - 10^5\ s^{-1}$, and temperatures up to 0.7 θ (homologous temperature).

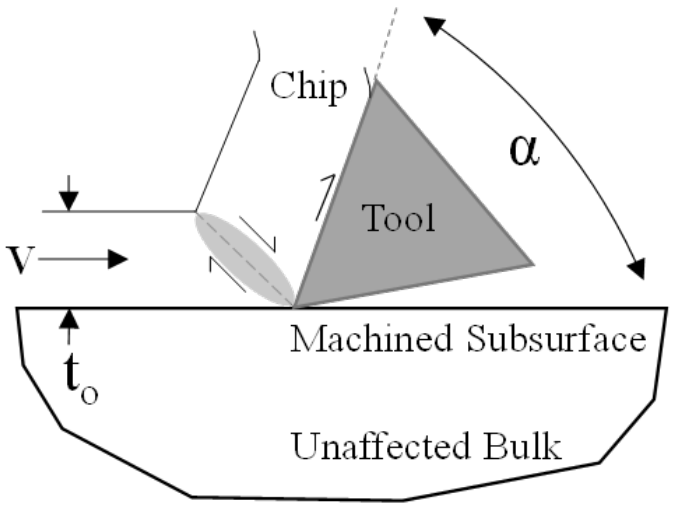

Figure 2.1: Orthogonal cutting schematic.

Relevant deformation quantifies may be obtained from the simplified orthogonal cutting

model shown in Figure 2.1 [1]. The expression for the imposed shear strain is,

$$\begin{aligned} \gamma &= \frac{cos\alpha}{sin\Psi cos\left(\Psi - \alpha\right)} \\ tan\Psi &= \frac{rcos\alpha}{1 - rsin\alpha} \\ r &= \frac{t_o}{t_c}, \end{aligned} \tag{2.1}$$

where α is the rake angle, Ψ the shear angle, and r the uncut-to-cut chip ratio. Note that α is prescribed by the tool geometry but Ψ and r are measured quantities obtained from experiments. The shear strain rate may be estimated from,

$$\dot{\gamma} = \frac{cos\alpha}{cos\left(\Psi - \alpha\right)} \frac{V}{\Delta}, \tag{2.2}$$

where V is the imposed cutting speed and Δ is the shear plane thickness. Note that the shear plane thickness is difficult to acquire experimentally. Estimates may be obtained using particle image velocimetry. In Figure 2.2 the PIV strain field for large strain extrusion machining (LSEM) is shown [19]. LSEM modifies the machining process with additional constraint on the free surface of the chip so that the cut chip thickness can be prescribed a priori. It is clear that the primary shear zone is confined to a narrow region which under these conditions was found to be $100\,\mu m$ for $V < 100\,mm \cdot s^{-1}$ and $50\mu m$ otherwise.

Cutting temperatures may be estimated as follows by considering an energy balance in the shear zone,

$$\begin{aligned} \Delta T &= R_1 \frac{F_s V_s}{c\rho V b t_o} \\ R_1 &= \left[1 + 1.328\left(\frac{K_1 \gamma}{V t_o}\right)\right]^{-1}, \end{aligned} \tag{2.3}$$

where F_s is the force acting on the shear plane, V_s is the shear plane speed, c the heat capacity, ρ the density, and b is the width of cut (into the page in Figure 2.1). R_1 is a correction factor that quantifies the fraction of heat that remains in the chip and K_1 is the thermal diffusivity of the deformed material [1]. Note that cutting forces were measured

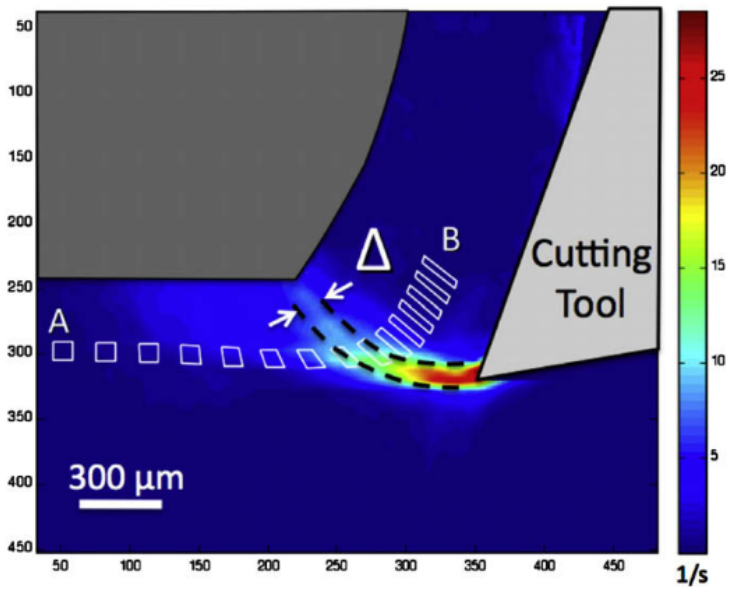

Figure 2.2: Strain rate field for OFHC Cu subject LSEM with cutting conditions $\alpha = 20°$ and $V = 5\,mm \cdot s^{-1}$ [19].

in all experiments and therefore F_s, as well as V_s, may be obtained from force balance and geometry [1].

A lumped heat capacitance model is used to estimate the time required for samples to cool to a specified temperature T',

$$\Delta t = \frac{\rho c}{h}\left(\frac{V}{A}\right)\log\left(\frac{T_o - T}{T_o - T'}\right), \tag{2.4}$$

where h is the convective heat transfer coefficient, V the volume of the produced chip, A the total surface area of the produced chip, T_o is the reference/initial temperature taken to be $20°C$, and T the temperature of the processed chip obtained from Eqn. 2.3.

As a result of the large strains ($\sim 1 - 10$) imposed during machining the material undergoes microstructural evolution. A micrograph of a partially formed chip in Figure 2.3 clearly illustrates that the chip material is different than the parent material [1]. Ti-6Al-4V deformed chips are shown in Figure 2.4 illustrate again that the microstructure undergoes microstructural evolution [17]. Furthermore, in certain classes of materials where shear

banding is promoted the chips may have a heterogeneous distribution of microstructure [17]. Another partially deformed chip and a corresponding TEM micrograph of the chip microstructure is shown in Figure 2.5.

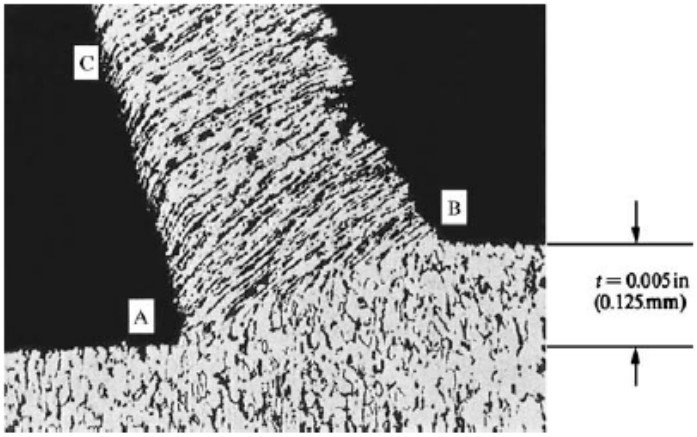

Figure 2.3: Partially deformed AISI 1015 steel cut at $0.13\,m \cdot s^{-1}$ with undeformed chip thickness $125\,\mu m$ [1].

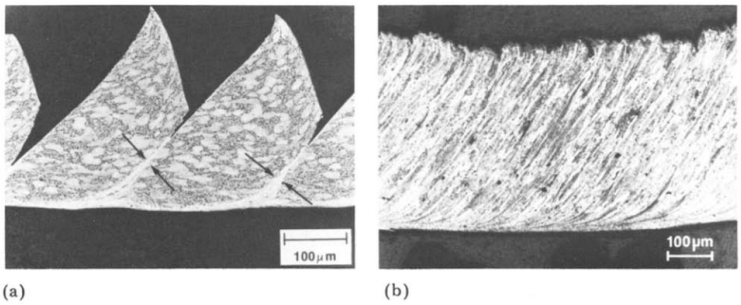

Figure 2.4: Ti-6Al-4V machined chips which illustrate (a) serrated chips due to the presence of shear bands and (b) continuous chips [17].

In their seminal work, Brown et al. [19] studied the PSP relationships in machined copper under varying conditions. TEM micrographs (Figure 2.6) of the produced structures revealed a rich class of different microstructures, which depend on the process conditions imposed during the machining process. Cryogenic conditions suppressed elevated temperatures imposed during machining, which promoted twinning and nanotwinning processes. Large strains imposed in ambient conditions promoted discontinuous and continuous dy-

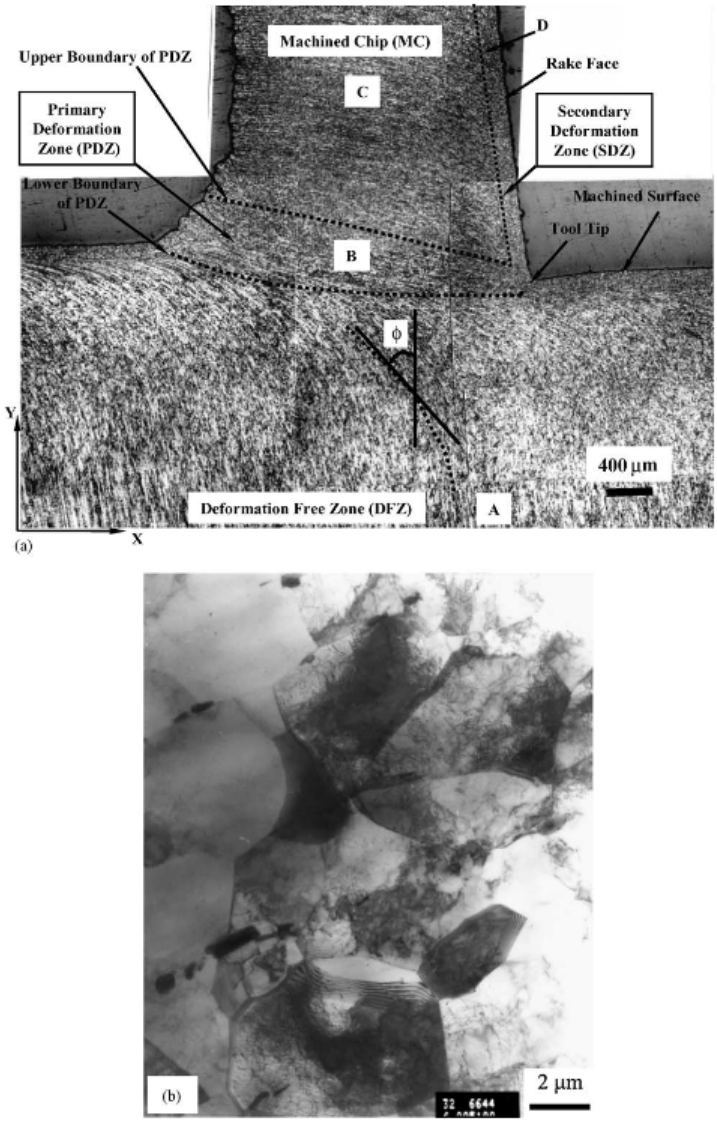

Figure 2.5: Partially deformed 1100 series aluminum and a corresponding TEM micrograph of the refined chip material [25]

.

namic recrystallization (DDRX and CDRX) mechanisms. The process-structure linkages were identified and quantified in a mechanism map shown in Figure 2.7. The X-axis here is the Zener-Holloman parameter $\dot{\epsilon} \exp Q/RT$, which is a metric that captures the effects of strain rate and temperature simultaneously [40]. The expression captures the physics of deformation, which consists of a competition between various rate-controlling thermal processes.

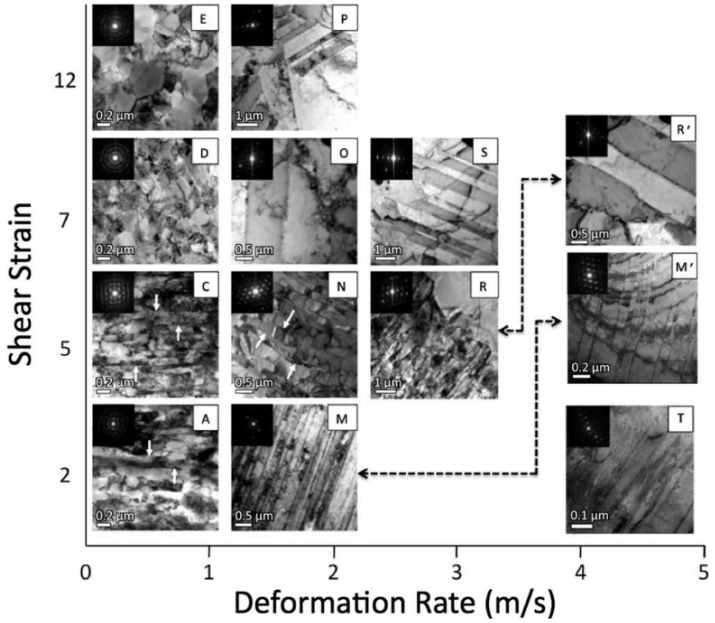

Figure 2.6: TEM micrographs of machined OFCU Cu subject to various process conditions [19]

.

The CDRX process is driven by the following mechanisms: (1) dislocations nucleate and multiply in the crystalline lattice due to the imposed deformations, (2) dislocation cell structures organize into low misorientation cell-like structures to reduce the energy of the system [41], (3) subsequent deformation induces lattice rotations between the low angle boundary (LAB) cells, and (4) after sufficient straining the LABs form into high angle boundaries (HABs). A schematic of the process is shown in Figure 2.8. Another schematic illustrating the formation of LABs from dislocation cells is shown in Figure 2.9.

Experimental results illustrating the evolution of misorientation and grain scale is shown

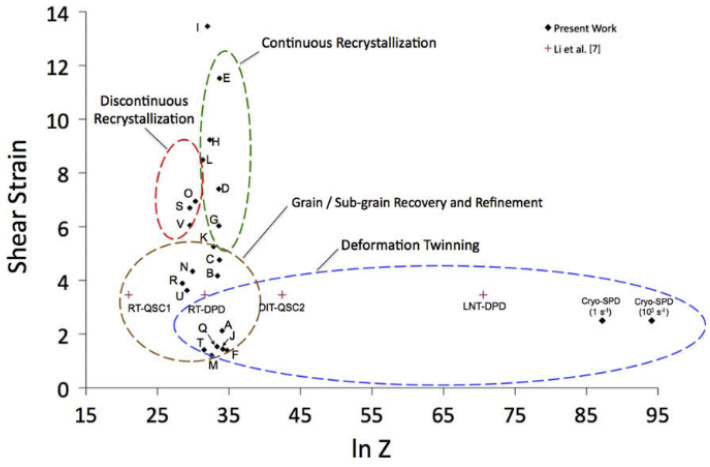

Figure 2.7: Deformation mechanisms map for OFHC Cu subject to machining [19]

.

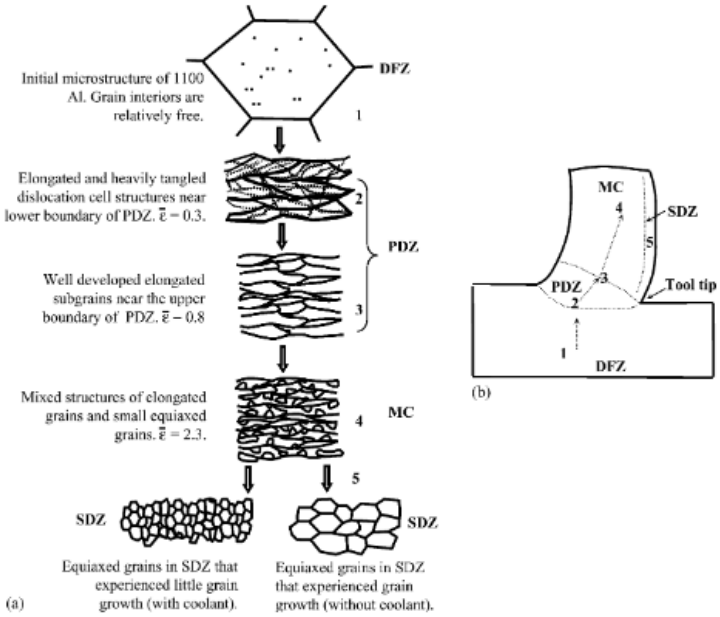

Figure 2.8: Continuous dynamic recrystallization mechanism driven by severe plastic deformation incuded by machining [25].

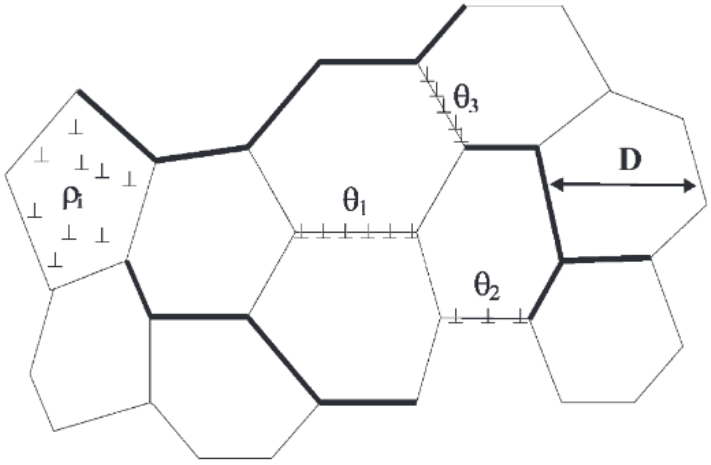

Figure 2.9: Low angle boundary dislocation cell formation in severe plastic deformation processes [42]

.

in the electron backscatter diffraction (EBSD) maps shown in Figure 2.10. In Figure 2.11 the misorientations computed over the EBSD images is shown in a histogram. It is clear that misorientations grow as additional deformation is imposed in the severe plastic deformation (SPD) process. In Figure 2.12 the evidence of subsurface refinement in Al 7075 is illustrated.

The constitutive behavior of machined microstructures is difficult to acquire since the physical scale of the generated samples is small. Chips are on the order of $\sim 1\,mm$ and irregularly shaped. The deformed subsurface is on the order of $20 - 100\,\mu m$ in depth depending on the material system considered and the process conditions. Therefore most studies are limited to reporting the hardness of machined microstructures. Micro/nano hardness measurements from various studies are shown in Figures 2.13-2.15. Note that there is one work in the literature that obtained tensile test results for SPD machined OFHC Cu [18]. They obtained tensile yield stress of 560 and 450 MPa for low and high speed cutting experiments, respectively. However, it is unclear from the manuscript how the authors obtained the results.

A recent publication analyzed the measured EBSD maps of the machined subsurface

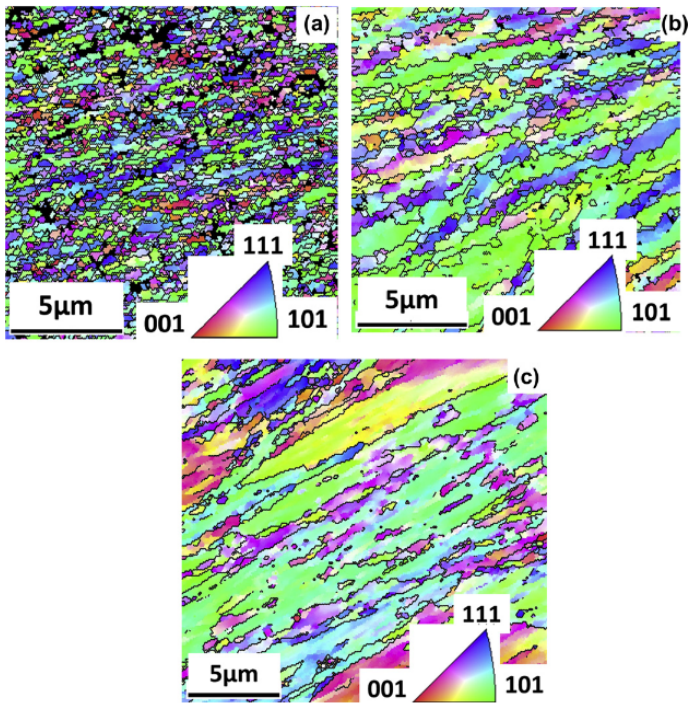

Figure 2.10: EBSD micrographs of machined OFHC Cu subject to (a) $\epsilon = 8.7$ & $\dot{\epsilon} = 60\, s^{-1}$ (b) $\epsilon = 3.9$ & $\dot{\epsilon} = 1290\, s^{-1}$ (c) $\epsilon = 2.3$ & $\dot{\epsilon} = 4030\, s^{-1}$ [43]

.

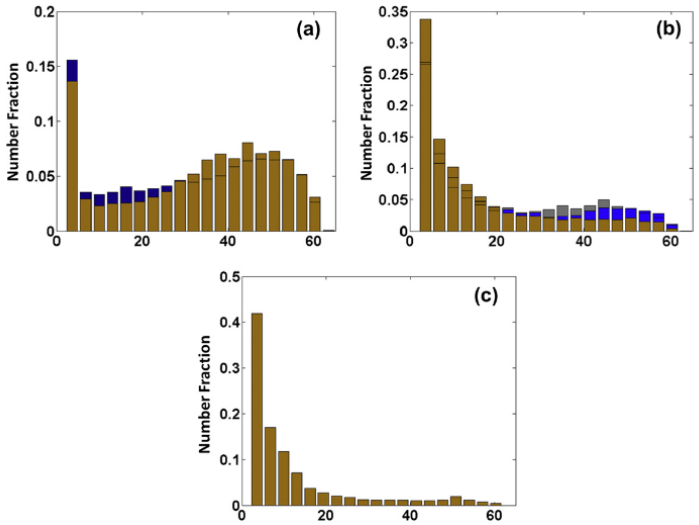

Figure 2.11: Misorientation histograms corresponding to machined OFHC Cu subject to (a) $\epsilon = 8.7$ & $\dot{\epsilon} = 60\, s^{-1}$ (b) $\epsilon = 3.9$ & $\dot{\epsilon} = 1290\, s^{-1}$ (c) $\epsilon = 2.3$ & $\dot{\epsilon} = 4030\, s^{-1}$ [43]

.

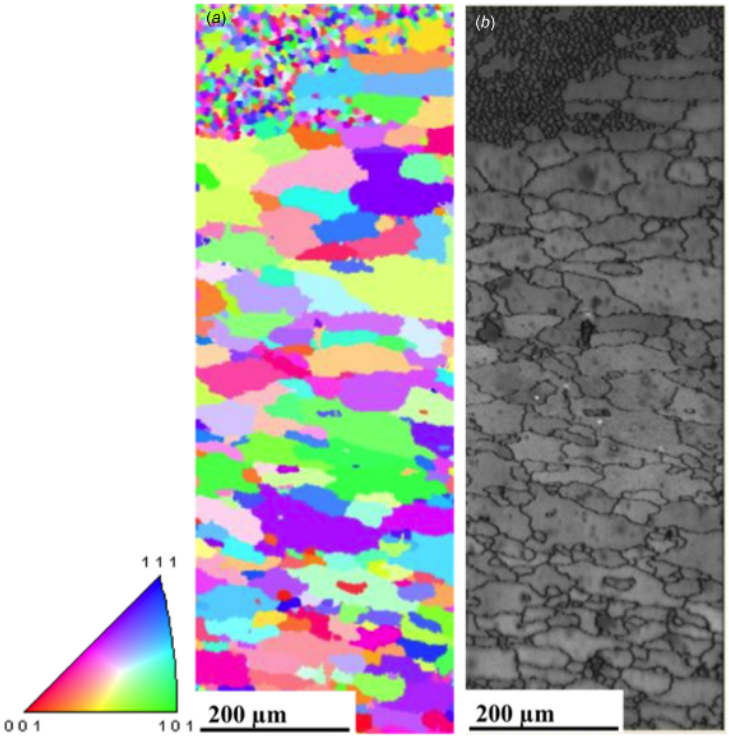

Figure 2.12: Subsurface refinement in hard turned Al 7075 [44]

.

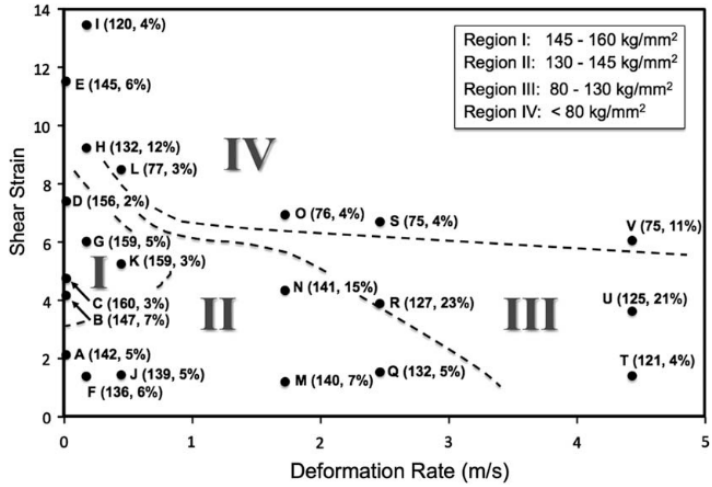

Figure 2.13: Microhardness measurements for OFHC Cu chips [19]

.

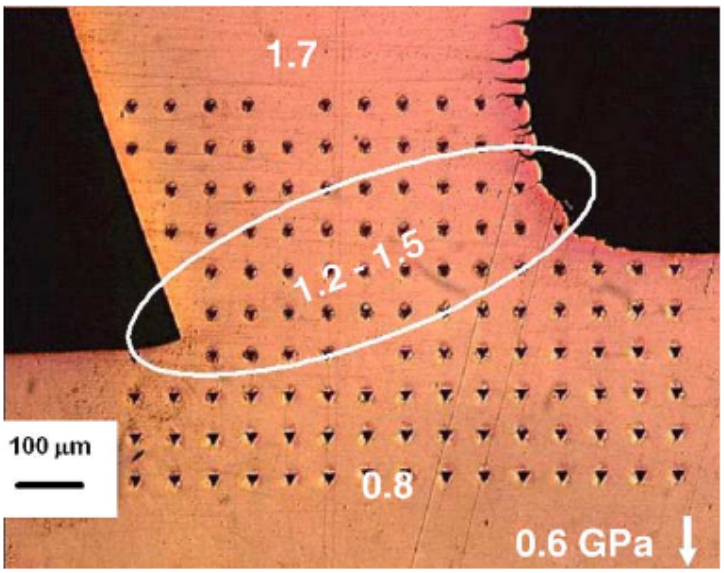

Figure 2.14: Nanohardness measurements in partially deformed OFHC Cu [27]

.

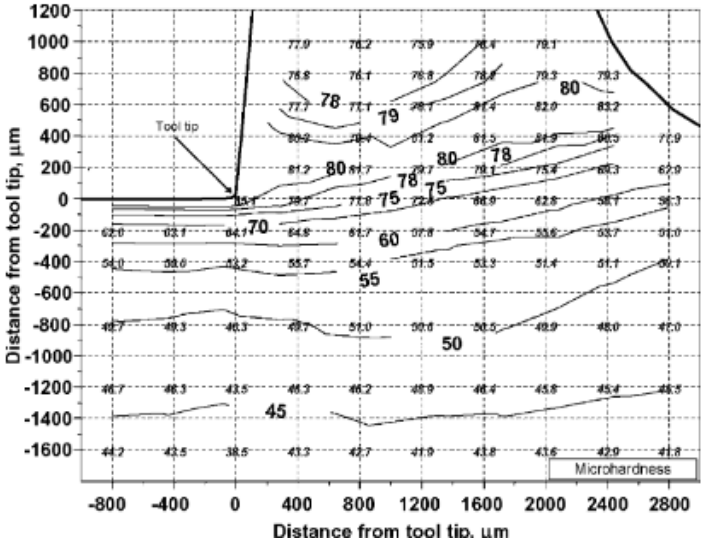

Figure 2.15: Micohardness map in the partially deformed machined Al 1100 chip [25]

.

layer utilizing generalized spherical harmonics (GSH). GSH will be introduced later in Section 2.6 and a novel implementation of GSH and spatial statistics will be introduced in Chapter 4. GSH is a basis representation of the orientation distribution function (ODF) tha compactly describes crystallographic texture. The authors generated several samples subject to various feed rates to search for process-structure trends. Their results suggest that the GSH representation does capture microstructural evolution in the subsurface as shown in Figure 2.16.

2.2 Materials Informatics

The new paradigm in materials research is the popularization of Materials Informatics (MI) [46, 47, 37]. This field employs statistical methods and techniques for building mathematically rigorous PSP models. These models can then be utilized for solving the inverse materials design problem; identifying process conditions which yield desired structure and hence properties.

The structure of materials (at certain scales) is inherently stochastic. Consider the two realizations shown in Figure 2.17. These microstructures were generated using the same procedure with identical constituents and volume fractions. Although by eye we recognize that they are "similar" in some sense clearly the images are different. This is clearly evident in experimental micrographs as well. Images of the same material at different spatial locations will be different but will display similar "randomness". The classic statistical analogue is drawing N samples from some distribution $f(x)$. If the drawing is repeated many times each sample will clearly be different but the *sample statistics* (sample mean, sample variance, etc.) will be similar (if N is sufficiently large).

Since microstructures are inherently random then a statistical framework is requisite for analysis. Here we adopt a framework introduced by Adams, Guo, and Kalidindi [48]. An excellent textbook on the approach was published by Kalidindi [37]. Note that perhaps the earliest, and most well known, materials scientist to adopt a statistical treatment of

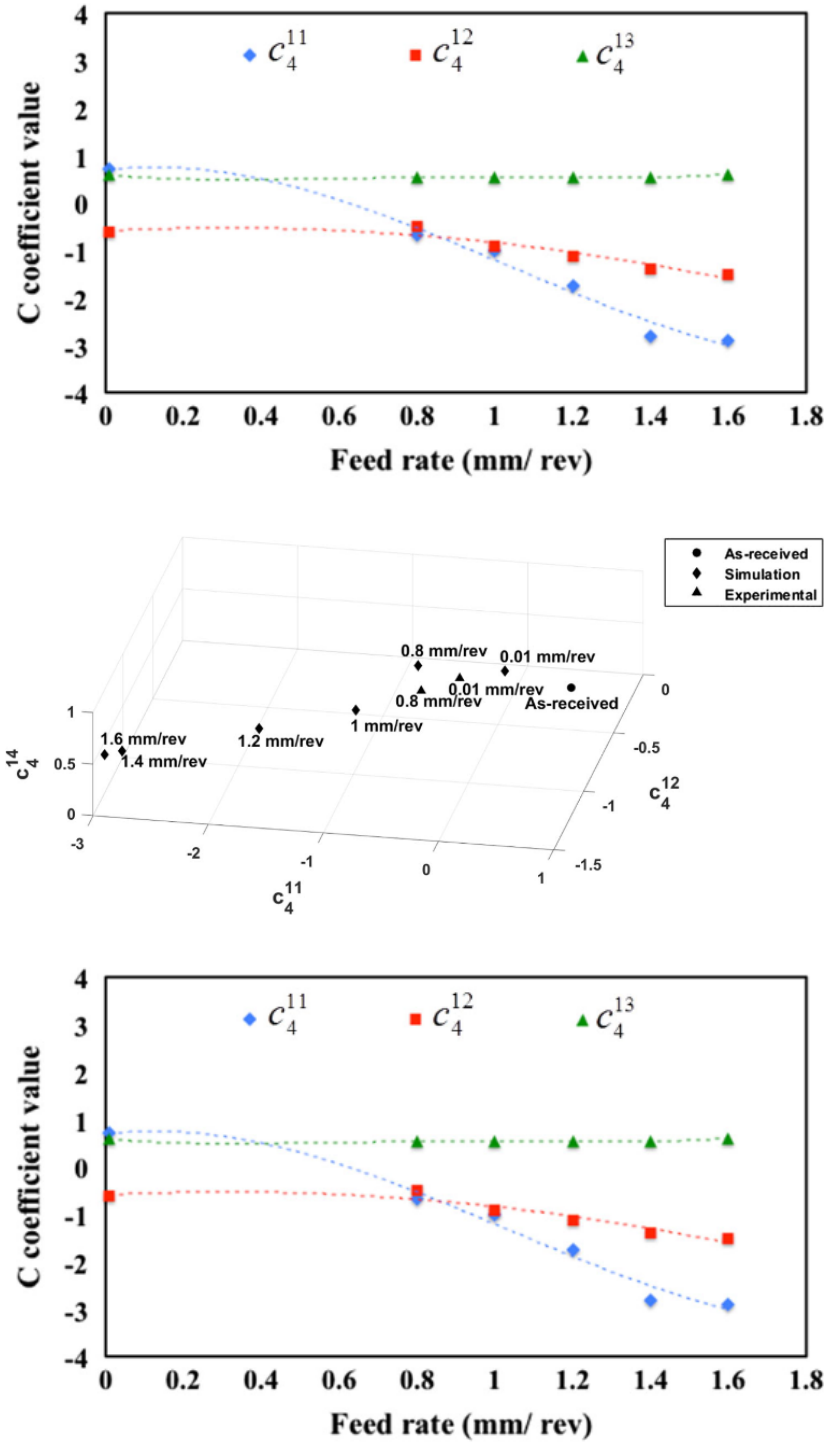

Figure 2.16: GSH coefficient evolution in the machined subsurface subject to different machining feed rate [45].

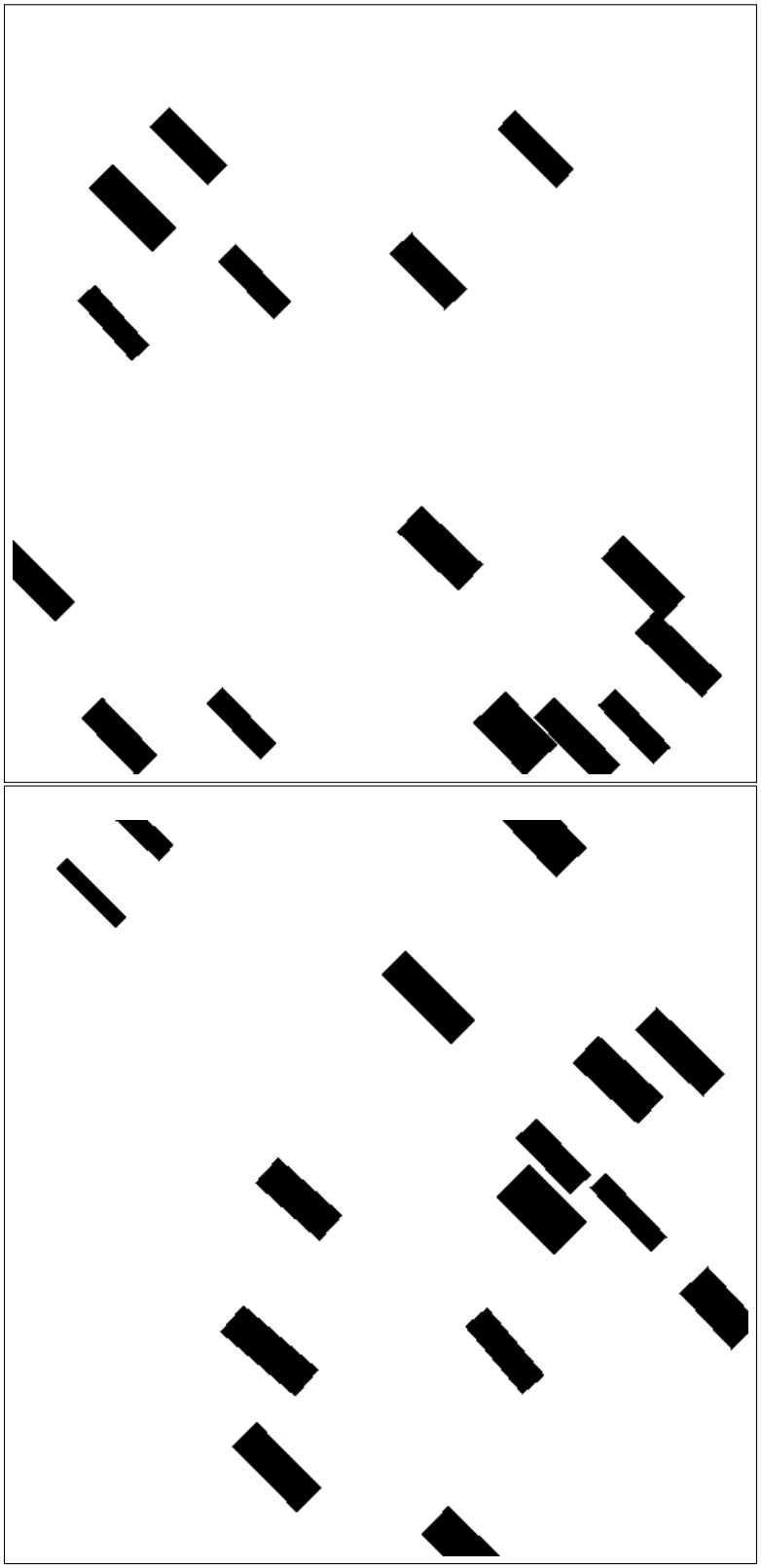

Figure 2.17: Random microstructure realizations.

materials was Torquato and his colleagues [36]. The Adams, Guo, and Kalidindi treatment introduces the statistical microstructure function $m(h, \boldsymbol{x})$ which in deterministic systems describes the probability of finding microstructure state h at spatial location $\boldsymbol{x}$. If h and $\boldsymbol{x}$ are instead continuous then the usual probability rules apply and $m(h, \boldsymbol{x})d\boldsymbol{x}dh$ describes the probability of finding a microstructure state between $[h, h + dh]$ in spatial location $[\boldsymbol{x}, \boldsymbol{x} + d\boldsymbol{x}]$. The discrete treatment is conceptually and notationally simpler and therefore will be used for the remainder of this section. The notation for $m(h, \boldsymbol{x})$ can be simplified by instead writing m_s^h which describes the probability of finding state h in spatial bin s. A spatial bin is purposefully left to be generic but can represent multiple indices. For instance it is a two dimensional index if images are being considered where each pixel describes a spatial bin. For a three-dimensional map (computerized tomography x-ray scan, serial sectioning microscopy, etc.) s represented three spatial indices. For the discrete case $\sum_{h=1}^{H} m_s^h = 1$ and $0 \leq m_s^h \geq 1$ ensures that the microstructure function is an appropriate probability function at each spatial bin. H is the total number of states present in the microstructure. Intuitively these rules state that each spatial bin must consist entirely of the H considered states otherwise the problem is ill-posed.

A commonly used measure of microstructure is *volume fraction* of a particular phase. Volume fraction can actually be described as a *one point spatial statistic*. This language describes that it is a measure that solely depends on one point in the microstructure. This is in contrast to two point, or in general n point, statistics which look for spatial relationships of two or more points. The one point statistic (volume fraction) can be described as,

$$f_s^h = \frac{1}{S} \sum_{s=1}^{S} m_s^h. \tag{2.5}$$

Which is easily identified as a simple average over all bins in the microstructure. In Figure 2.17 the volume fraction of black pixels (h=1) can clearly be obtained by simply averaging over the image if white pixels are 0 and black 1. This result is trivia but the framework introduced can easily be extended to high order statistics.

Now consider that the spatial arrangement of microstructural states is desired for quantifying the random structure. The simplest of these statistics is the two point statistic $f_{rs}^{hh'}$ which describes *conditional* probability of finding h' at spatial bin s given that spatial bin r contains state h. If $h = h'$ then this represents *autocorrelation* and otherwise the quantity represents *cross-correlation*. This quantity can be expressed as a function of the microstructure function,

$$\begin{aligned} f_{rs}^{hh'} &= \frac{1}{J}\sum_{j=1}^{J} {}^{(j)}m_r^{h\,(j)}m_s^{h'} \\ f_{\boldsymbol{t}}^{hh'} &= \frac{1}{S}\sum_{s=1}^{S} m_s^h m_{s+\boldsymbol{t}}^{h'}, \end{aligned} \tag{2.6}$$

where the first sum is over man ensembles of images. ${}^{(j)}m_r^h$ is m_r^h in the j^{th} image of the ensemble. ${}^{(j)}m_s^{h'}$ has similar definition. Consider for instance a 500×500 image. There is only one (7,499) pixel. Therefore to obtain $f_{7,499}^{hh'}$ many images are needed. More generally this is clearly necessary since there is only 1 observation of all (r, s) pairs in a particular image and hence averaging must be performed over many images. This approach is clearly costly - many images are needed simply to produce a single statistic. However the final line assumes that the statistical behavior of the microstructure is *stationary* and hence bins r, s can instead be represented by $s, s + \boldsymbol{t}$ where $\boldsymbol{t}$ is the vector that defines the difference between r and s. There are many $\boldsymbol{t}$ vectors in an image (Figure 2.18) so the statistic can be obtained for each image. Stationarity assumes that within a single realization (an image) the statistics will be the same for any $\boldsymbol{t}$. Intuitively this states that the "randomness" of the microstructure is the same everywhere in the realization. An example where this assumption does not hold is illustrated in Figure 2.18

Note that Eqn. 2.6 is a convolution over all spatial bins (pixels in an image). The computation can be performed extremely efficiently by exploiting the convolution property

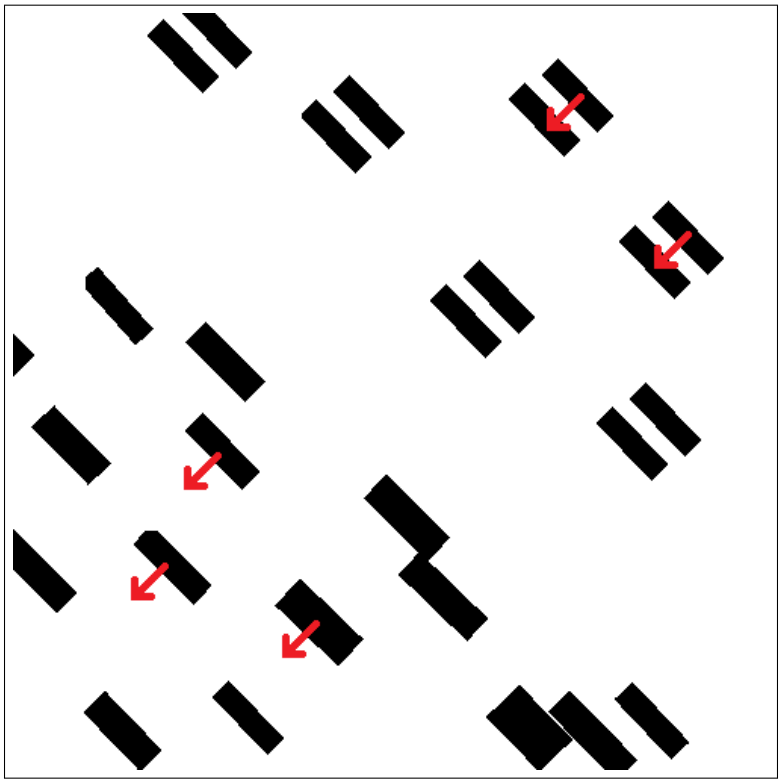

Figure 2.18: Nonstationary microstructure where the two point statistics are different in the upper right and lower left portions of the image. Red arrows are instantiations of the vector $\boldsymbol{t}$.

of discrete Fourier transforms (DFT).

$$\begin{aligned} f_{\boldsymbol{t}}^{hh'} &= \frac{1}{S}\sum_{s=1}^{S} m_s^h m_{s+\boldsymbol{t}}^{h'} \\ \mathscr{F}\left(f_{\boldsymbol{t}}^{hh'}\right) &= \frac{1}{S} M_{\boldsymbol{k}}^{h*} M_{\boldsymbol{k}}^{h'}, \end{aligned} \tag{2.7}$$

where $M_{\boldsymbol{k}}^h$ is the frequency space representation of the microstructure function $m_{\boldsymbol{t}}^h$ and the subscript * indicates the complex conjugate. This key shortcut enables extremely fast computation of the two point statistics. Assuming a matrix/array representation of the microstructure function the procedure for obtaining the two point spatial statistics is: (1) transform the microstructure function to frequency space, (2) element-wise multiply the quantities, finally (3) transform back to spatial coordinates. For additional details and descriptions of the relationships between the various statistics for $H > 2$ refer to [37].

The extension to higher order statistics (three point, four point, etc.) is conceptually trivial however the same tricks employed in establishing two point statistics can no longer be used. Efficient computation of these statistics is difficult and still an active area of research. One recent work inferred important higher order statistics through the used a single layer three dimensional convolutional neural network (CNN) [49]. The inference of these statistics was enabled by the use of a single layer which allows for physical interpretation from the CNN weight matrix. Another work employed a similar strategy but allowed for multiple layers of the CNN (deep learning) which yielded exceptional predictiveness for the structure-property linkage [50]. This approach contrasts with the single-layer CNN in that it is far less interpretable - the inclusion of additional layers confounds the ability to interpret the underlying physical relationships.

In addition there are a number of other statistics used in describing microstructures. This includes but is not limited to: surface correlation functions [51], radial distribution function (also known as two-point Pearson correlation) [36], cluster functions [36], chord length distribution [36], and the lineal path function [36]. A qualitative description of the

information contained in these is illustrated in Figure 2.19.

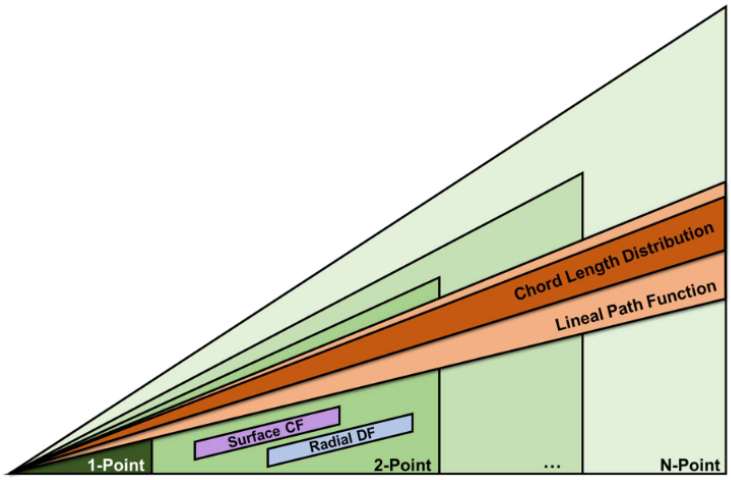

Figure 2.19: Illustration of various microstructure statistics and a qualitative description of the information contained in each [52].

In Chapter 5 we study the microstructure evolution of a machining process where a single phase polycrystalline system undergoes large changes in the scale and morphology of the grain structure. In this setting it is not possible to clearly identify at least two microstructure states ($H \geq 2$). Therefore we employ angularly resolved chord length distribution statistics [53]. This is an extension of the traditional chord length statistics [36] which is a statistical extension of line intercept methods commonly utilized in metallurgy. Chord length statistics (and the closely related lineal path function) have been effectively utilized in several engineering problems [54, 55, 56, 57].

The lineal path function (LPF) is defined as [36]

$$L^{(i)}(z) = \text{Probability that a linear segment of length } z \text{ lies wholly in phase } i \text{ when randomly thrown into the sample..} \tag{2.8}$$

The closely related chord length distribution (CLD) can be defined as [36]

$$p^{(i)}(z)dz = \text{Probability of finding a chord of length between } z \text{ and } z + dz \text{ in phase } i. \tag{2.9}$$

The two quantities are related through the expression [36, 53]

$$p^{(i)}(z)dz = \frac{l_c}{V^{(i)}} \frac{d^2 L^{(i)}(z)}{dz^2}, \tag{2.10}$$

where l_c is the mean chord length along the direction z and $V^{(i)}$ is the volume fraction for phase i. Angularly resolved chord length statistics can be efficiently computed using an algorithm presented by Turner et al. [53]. A schematic of a two phase microstructure and a horizontal intersecting line is show in Figure 2.20.

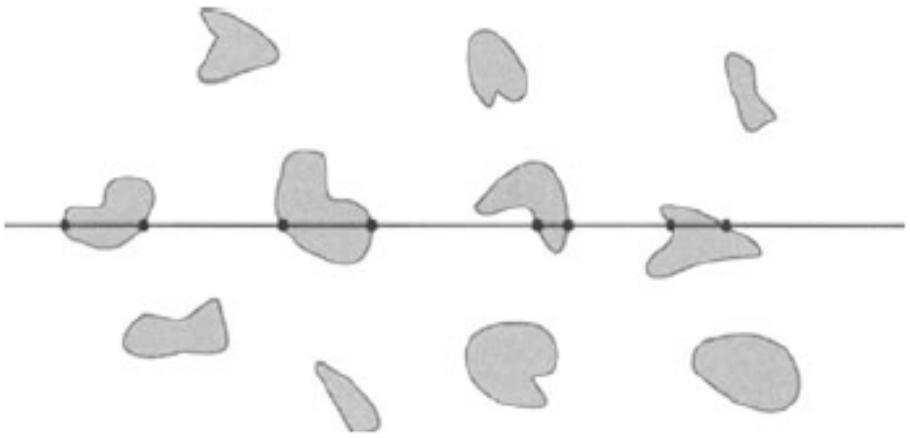

Figure 2.20: Two phase microstructure and intersecting horizontal line [36].

An illustration comparing CLD statistics to two point autocorrelations is shown in Figure 2.21.

These results illustrate key differences between CLD and two point statistics. Firstly, two point statistics are much faster to compute because they exploit the efficiency of DFTs. Sec-

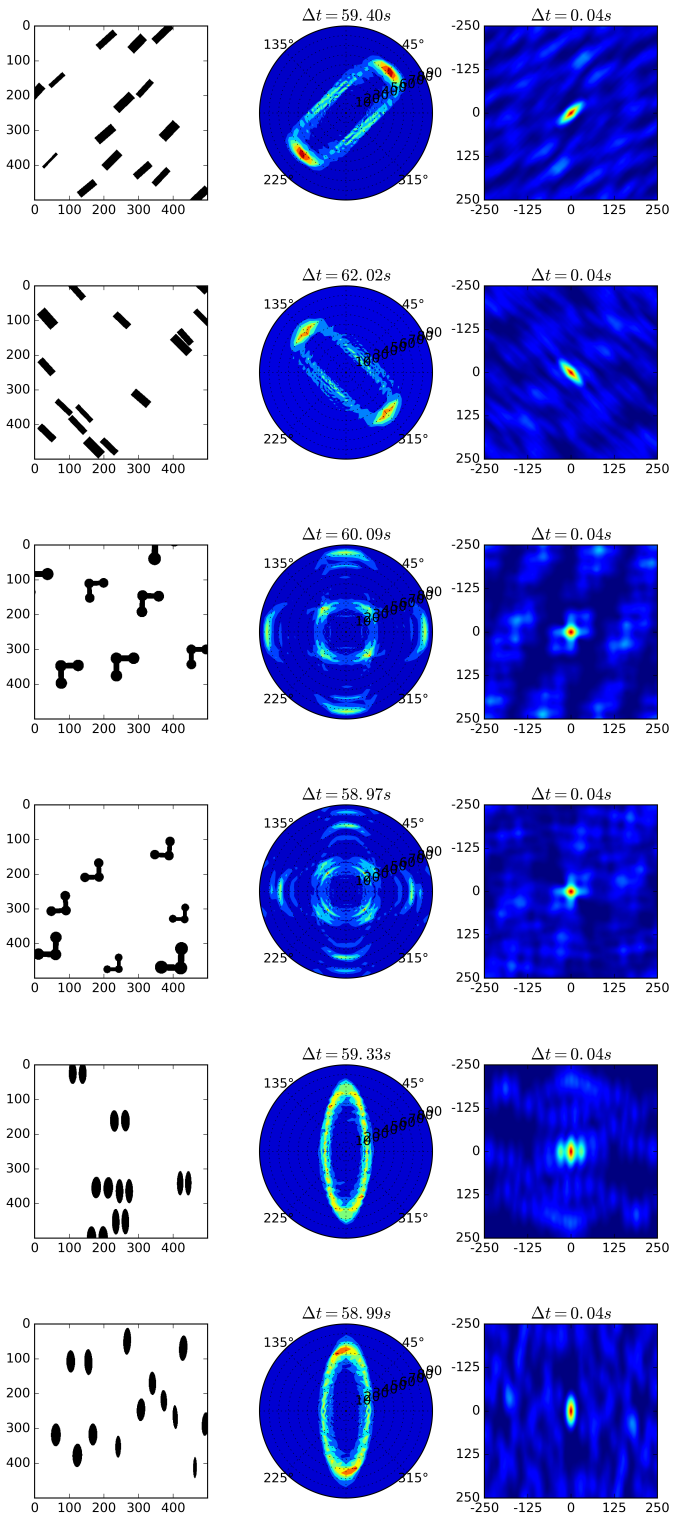

Figure 2.21: CLD and two point autocorrelation statistics for six realizations of six different microstructures. Each microstructure contains the same volume fraction of black pixels.

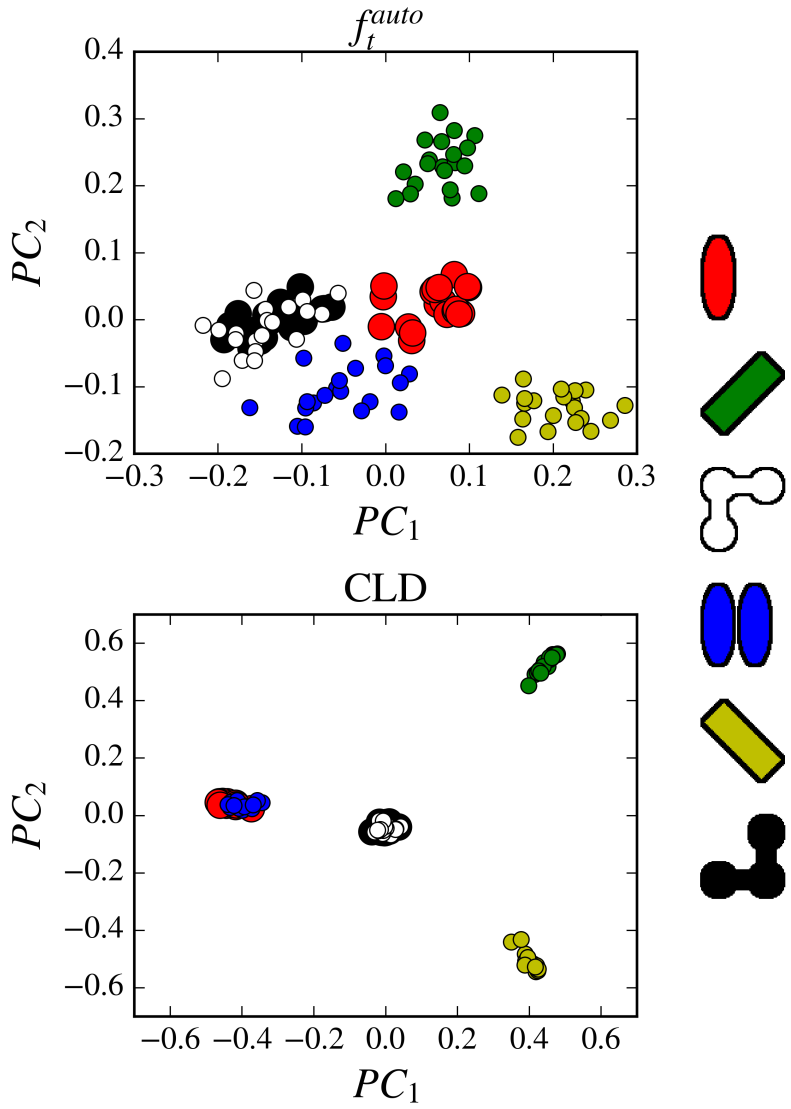

Figure 2.22: Comparison of CLD and autocorrelation two point statistics in two dimensional reduced PC space.

ondly, CLD can only capture the shape or morphology of the microstructural constituents. Any kind of spatial patterns (illustrated in the "paired" ellipse example) cannot be captured by the CLD statistic. Two point statistics however clearly do capture the pattern in the fifth micrograph – ellipses appear together in pairs which is illustrated in the high probability region to the left and right of center in the corresponding autocorrelation map. Finally, however, both CLD and two point statistics fail to capture differences in the second and third micrographs. Clearly these micrographs are different (rotated 180°) but higher order statistics (three point stats) are needed to capture this discrepancy. It is important to understand the limitations and assumptions built into these microstructure descriptors prior to using them so that the derived results may be interpreted appropriately.

CLD statistics have traditionally been used to describe the statistic in a few key directions (e.g. horizontal, vertical, etc.) [36, 54, 56, 57]. A more recent work applied the angularly resolved CLD variant to a synthetic dataset of various polycrystalline microstructures [55]. They were able to clearly distinguish between equiaxed, bimodal, and two elongated microstructures. An illustration from their work is shown in Figure 2.23.

Now consider that for each image that is processed a corresponding high dimensional statistic is produced. Returning to the example in Figure 2.21 the 500×500 pixel images produce corresponding 500×500 autocorrelation maps. The CLD statistics were made using 5° angular bins (180/5 + 1 = 37) and 30 radial bins. Therefore the autocorrelation maps can be described as 500^2-length vectors and the CLD statistics as $37 \times 30 = 1110$-length vectors. 20 realizations of each microstructure were generated for a total of dataset of size $6 \times 20 = 120$. The data is therefore extremely high dimensional yet small which is often referred to as "wide" data. Any analysis is made difficult in this setting (regression, classification, etc.) and therefore some dimensionality reduction is required. The favored approach is to employ principal component analysis (PCA) to reduce the dimensionality of the data [37]. PCA is a method for establishing a statistically optimal basis for describing the data. The basis can be truncated yielding a reduced order description

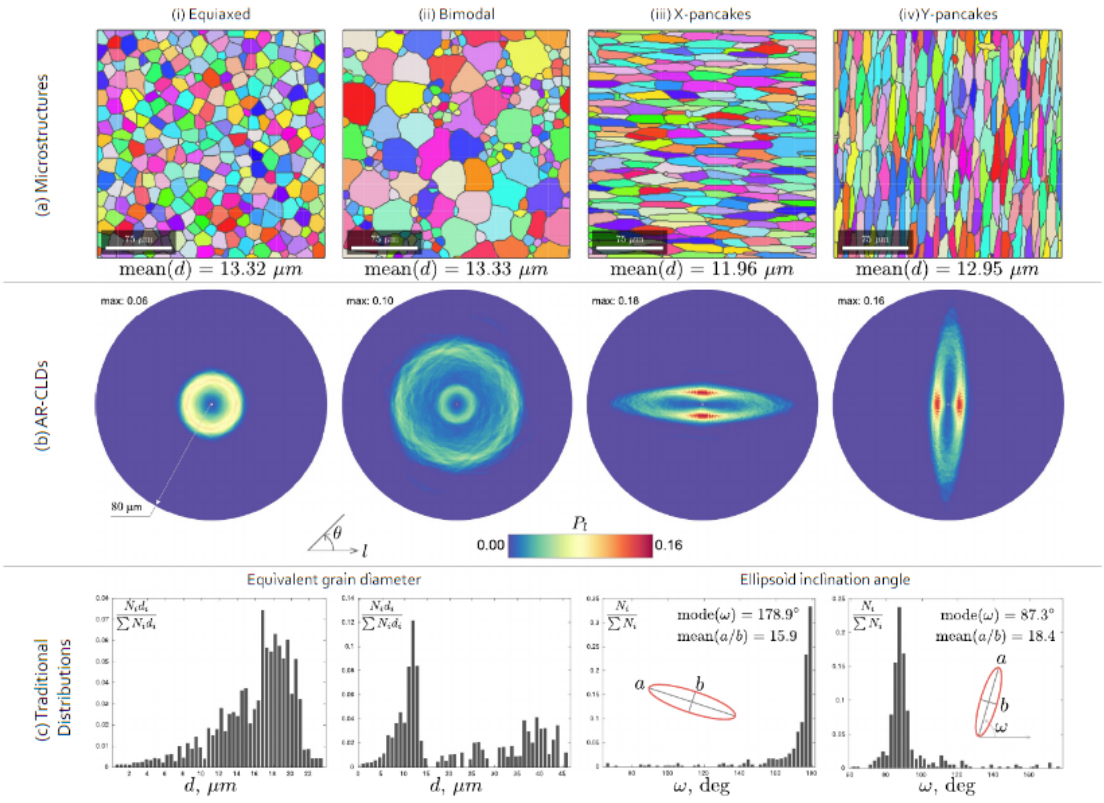

Figure 2.23: Microstructure realizations and the corresponding CLD statistics [55].

of the original dataset. The truncated basis weights are subsequently used to describe the high dimensional microstructure statistic images and for use in subsequent statistical modeling. A intuitive illustration of the PCA procedure on the toy example shown in Figure 2.21 is shown in Figure 2.24. Again neither of the methods can discriminate between the L-shaped structures. Autocorrelation does discriminate between the paired and unpaired ellipses where CLD does not.

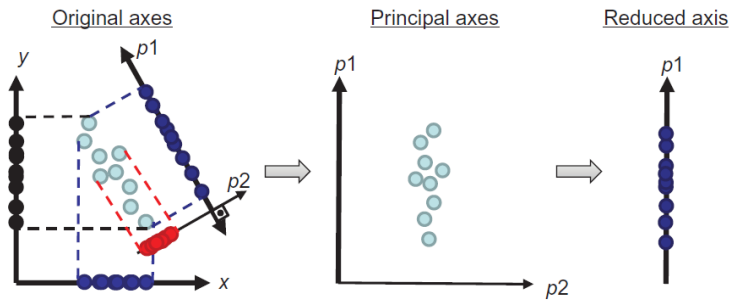

Figure 2.24: Schematic of PCA dimensionality reduction [37].

2.3 Bayesian statistics

Bayes formula can be obtained by manipulation of some basic conditional probability properties,

$$\begin{aligned} p(A,B) &= p\left(A|B\right)p(B) \\ &= p\left(B|A\right)p(A) \\ p(A|B) &= \frac{p(B|A)p(A)}{p(B)}, \end{aligned} \tag{2.11}$$

where A and B are random events (or variables). $p(A)$ and $p(B)$ are the *prior* beliefs and $p\left(B|A\right)$ is the conditional probability of B given A. Consider that this manipulation may be useful in cases where $p\left(B|A\right)$ is easy to obtain however $p\left(A|B\right)$ is not.

Now consider a physical system that is being studied which has input parameters $\boldsymbol{x}$ and some output y. In the absence of noise the output is assumed to be a function of the input

e.g. $y = f(\boldsymbol{x})$. When experiments are performed the output is "corrupted" by noise when taking observations. The corresponding *statistical model* is,

$$\begin{aligned} y_i &= f(\boldsymbol{x}_i) + \epsilon_i \\ \epsilon_i &\sim \mathcal{N}\left(0, \sigma_\epsilon^2\right), \end{aligned} \tag{2.12}$$

where ϵ_i are assumed to be independent and identically distributed(i.i.d.) coming from a zero mean normal process with variance σ_ϵ^2. Now assume that the function $f(\boldsymbol{x})$ can be *parameterized* with as $f(\boldsymbol{x};\boldsymbol{\beta})$ where $\boldsymbol{\beta}$ are the familiar regression coefficients. Note that the regression need not be linear regression; $f(\boldsymbol{x};\boldsymbol{\beta})$ may be nonlinear in $\boldsymbol{\beta}$. In the case where several experiments are performed an observation vector $\boldsymbol{Y}$ is collected as well as a data matrix $\boldsymbol{X}$, where each row corresponds to a single experiment's covariate settings $\boldsymbol{x}_i^T$. The unknown model parameters, ($\boldsymbol{\beta}$,σ_ϵ^2), can be estimated using Bayes' theorem,

$$\begin{aligned} p\left(\boldsymbol{\beta}, \sigma_\epsilon^2 | \boldsymbol{X}, \boldsymbol{Y}\right) &= \frac{p\left(\boldsymbol{Y}|\boldsymbol{X}, \boldsymbol{\beta}, \sigma_\epsilon^2\right) p\left(\boldsymbol{\beta}, \sigma_\epsilon^2 | \boldsymbol{X}\right)}{p\left(\boldsymbol{Y}|\boldsymbol{X}\right)} \\ p\left(\boldsymbol{Y}|\boldsymbol{X}\right) &= \int_{\boldsymbol{\beta}, \sigma_\epsilon^2} p\left(\boldsymbol{Y}|\boldsymbol{X}, \boldsymbol{\beta}, \sigma_\epsilon^2\right) p\left(\boldsymbol{\beta}, \sigma_\epsilon^2 | \boldsymbol{X}\right) d\boldsymbol{\beta} d\sigma_\epsilon^2 \\ p\left(\boldsymbol{\beta}, \sigma_\epsilon^2 | \boldsymbol{X}, \boldsymbol{Y}\right) &\propto p\left(\boldsymbol{Y}|\boldsymbol{X}, \boldsymbol{\beta}, \sigma_\epsilon^2\right) p\left(\boldsymbol{\beta}, \sigma_\epsilon^2 | \boldsymbol{X}\right). \end{aligned} \tag{2.13}$$

The final line states that the posterior density, $p\left(\boldsymbol{\beta}, \sigma_\epsilon^2 | \boldsymbol{X}, \boldsymbol{Y}\right)$, is proportional to the numerator term. This is because the denominator, $p\left(\boldsymbol{Y}|\boldsymbol{X}\right)$, is solely a function of the data ($\boldsymbol{\beta}$ has been "integrated out") and therefore is a constant scalar necessary for normalizing the posterior to give $\int p\left(\boldsymbol{\beta}, \sigma_\epsilon^2 | \boldsymbol{X}, \boldsymbol{Y}\right) d\boldsymbol{\beta} d\sigma_\epsilon^2 = 1$. This is important to acknowledge since the integral is actually difficult to compute in many instances [58]. Exceptions include conditions when the model $f(\boldsymbol{x};\boldsymbol{\beta})$ is linear and appropriate priors are placed on $\boldsymbol{\beta}$ and σ_ϵ^2. In these cases the posterior density can be exactly computed. The quantity $p\left(\boldsymbol{Y}|\boldsymbol{X}, \boldsymbol{\beta}, \sigma_\epsilon\right)^2$ is the *likelihood* function which is a frequentist measure of how plausible the data is conditional on some $(\boldsymbol{\beta}, \sigma_\epsilon^2)$. Point estimates obtained maximizing the likelihood correspond to the maximum likelihood estimate (MLE) which is a common frequentist approach. The

corresponding Bayesian point estimate corresponds to the parameters which maximize the posterior density (or the numerator) and is referred to as the maximum a posteriori (MAP) estimate.

In the case where the normalized posterior density is difficult to compute Markov Chain Monte Carlo (MCMC) methods may be utilized to obtain a *sample* from the posterior distribution [59, 58]. For notational simplicity consider the variable $\boldsymbol{\theta}$ to represent the unknown statistical model parameters. In the regression example this corresponds to $\boldsymbol{\theta} = (\boldsymbol{\beta}, \sigma_\epsilon^2)$ In this approach a chain of length N_{MC} is generated, $\{\boldsymbol{\theta}_1, \ldots, \boldsymbol{\theta}_{N_{MC}}\}$, which represents a sample from the desired posterior density. This sample, if large enough, is equivalent to having the posterior itself. The chain is generated by performing a random walk within the unknown parameter space. In Gibbs sampling the distribution of each "component" of $\boldsymbol{\theta}$ can be analytically determined conditional on the remaining components [58]. This is an extremely efficient sampling method but can be only be exploited in certain well defined problems. An alternative is the Metropolis-Hastings (MH) algorithm where walks are performed by "stepping" in random directions specified by the *proposal distribution* e.g. $\boldsymbol{\theta}_{trial} = \boldsymbol{\theta}_i + \Delta\boldsymbol{\theta}$. $\Delta\boldsymbol{\theta}$ here is drawn from zero mean process specified by the proposal distribution $p(\boldsymbol{\theta}_i)$. The trial is accepted with probability,

$$\alpha = min\left[1, \frac{p\left(\boldsymbol{\theta}_{trial}|\boldsymbol{X}, \boldsymbol{Y}\right) p\left(\boldsymbol{\theta}_{trial}|\boldsymbol{\theta}_i\right)}{p\left(\boldsymbol{\theta}_i|\boldsymbol{X}, \boldsymbol{Y}\right) p\left(\boldsymbol{\theta}_i|\boldsymbol{\theta}_{trial}\right)}\right]. \tag{2.14}$$

The quantity $p\left(\boldsymbol{\theta}_i|\boldsymbol{\theta}_{trial}\right)$ is the density evaluated at $\boldsymbol{\theta}_i$ conditional on the previous step being at $\boldsymbol{\theta}_{trial}$ and $p\left(\boldsymbol{\theta}_{trial}|\boldsymbol{\theta}_i\right)$ is defined similarly. Loosely speaking the ratio of the two quantifies represents relative probability associated with starting at $\boldsymbol{\theta}_i$ and jumping to $\boldsymbol{\theta}_{trial}$ versus starting at $\boldsymbol{\theta}_{trial}$ and jumping to $\boldsymbol{\theta}_i$. In the case that symetric proposal densities are utilized then $p\left(\boldsymbol{\theta}_i|\boldsymbol{\theta}_{trial}\right)/p\left(\boldsymbol{\theta}_{trial}|\boldsymbol{\theta}i\right) = 1$ and the acceptance rule yields the original result proposed by Metropolis et al. [60]. The case where an asymmetric proposals are allowed was introduced later by Hastings [61]. The algorithm therefore bares their names. Asymmetric proposal densities may be obtained when considering more sophisticated sampling

procedures which may consider dynamic quantities (momentum) or derivative information about the posterior density [59, 62, 63, 64]. Development of these algorithms is currently an active area of research. An illustration of the MH MCMC sampling algorithm on the ubiquitous banana density is shown in 2.25. A simple isotropic normal proposal density was utilized. Notice that this is a difficult to sample density - isotropic proposals on the long and narrow tails may be inefficient. Furthermore, this introduces correlation into the data. The sampler "gets stuck" in a tail and requires a long time to "escape" and explore the other tail. Such an effect is undesirable because what is truly desires is an *independent* sample from the posterior. To alleviate this issue practitioners may use more sophisticated samplers or generate a larger sample but then only keep every n^{th} sample (practice called thinning).

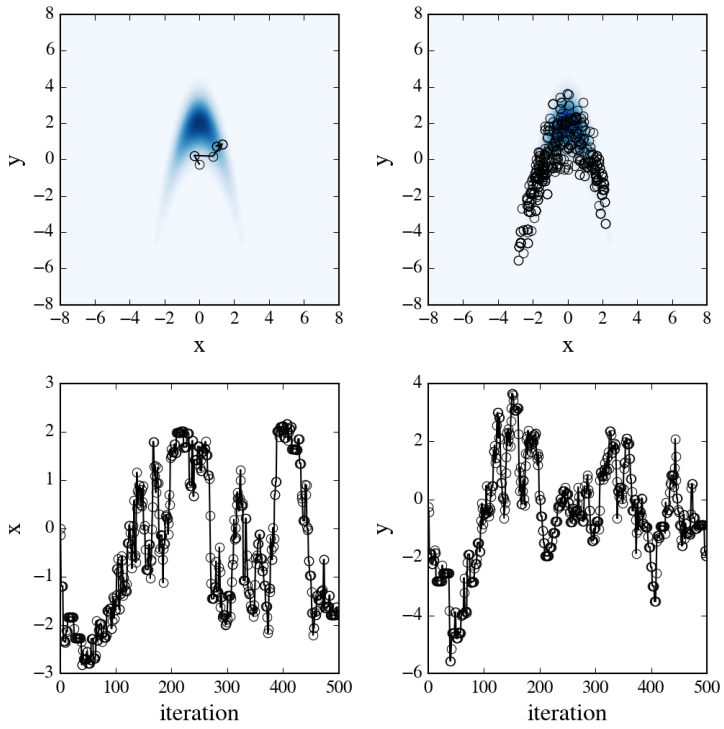

Figure 2.25: MH MCMC illustration on banana density. (top left) first ten steps in MH chain, (top right) additional 500 steps, (bottom left) sample chain for x, (bottom right) sample chain for y.

Another potential concern associated with posterior sampling is associated with pos-

terior multimodal densities. Since MH MCMC samplers propose new points close to the current point then there exists the possibility of becoming *stuck* in a single mode of a multimodal density. Hamiltonian Monte Carlo (HMC) partially mitigates this issue by introducing momentum into the sampling strategy. Momentum propels the chain out of local minima in the posterior which mitigates against becoming stuck. Another strategy is to utilize simulated annealing methods [65].

Transitional is a MCMC sampling procedure which exploits simulated annealing to obtain the posterior sample [65]. Simulated annealing methods are popular in optimization and have recently been employed for constrained optimization in cheminformatics [66]. Consider the following transformation on the posterior density,

$$\begin{aligned} p^{n_j}\left(\boldsymbol{\theta}|\boldsymbol{X},\boldsymbol{Y}\right) &\propto p^{n_j}\left(\boldsymbol{Y}|\boldsymbol{X},\boldsymbol{\theta}\right) p^{n_j}\left(\boldsymbol{\theta}|\boldsymbol{X}\right) \\ 0 = n_o < n_1 \leq \ldots < n_j &= 1. \end{aligned} \tag{2.15}$$

where n_j is the exponential constant which "tempers" the posterior density. At $n_j = 0$ the posterior becomes flat density (uniform), $n_j = 1$ the desired density is achieved, and intermediate densities are therefore in between. The procedure therefore begins at the flat density which can easily be sampled, and progressively approaches the desired density. At each step the sample is resampled according to the probability that a point will "survive" the transition to the next intermediate density. Following this step a short (10-100 steps) MCMC random walk is performed for each point to promote mixing. The process is repeated until $n_j = 1$. Resampling is performed with each point weighed by the following probability,

$$\begin{aligned} \hat{W}_i^{(j)} &= \frac{p^{n_j}\left(\boldsymbol{\theta}_i|\boldsymbol{X},\boldsymbol{Y}\right)}{p^{n_{j-1}}\left(\boldsymbol{\theta}_i|\boldsymbol{X},\boldsymbol{Y}\right)} \\ W_i^{(j)} &= \frac{\hat{W}_i^{(j)}}{\sum_{j=1}^{N_{MC}} \hat{W}_i^{(j)}}, \end{aligned} \tag{2.16}$$

where $W_i^{(j)}$ is the probability of sampling point i at the j^{th} annealing step and $\boldsymbol{\theta}_i$ the i^{th}

point in the sample. Note that this algorithm is well suited for parallelization since each point performs the MCMC walk independent of all others.

Of critical concern is how to increment n_j. If increments are too small then the annealing schedule will be slow. If increments are too large then only a few unique points may survive in step (2) which is deleterious for efficient exploration over the entire space. Consider that a fraction of unique points, ν', is desired to remain at each resampling step; $\nu' = 1/2$ is a common choice [67, 68]. The following estimate yields the fraction of points remaining from a sample size of N_{MC} [69, 67, 68],

$$\nu\left(n_j\right) = \frac{1}{N_{MC}} \frac{\left(\sum_{j=1}^{N_{MC}} W_i^{(j)}\right)^2}{\sum_{j=1}^{N_{MC}} \left(W_i^{(j)}\right)^2}. \tag{2.17}$$

This is a function of solely one variable, n_j, and therefore $\nu\left(n_j\right) = \nu'$ is usually solved with fewer than ~ 10 iterations using simple root finding techniques such as the bisection method. The same banana density is sampled and snap shots at various n_j are shown in Figure 2.26.

Note that constraints may be incorporated into the problem via the prior beliefs $p\left(\boldsymbol{\theta}|\boldsymbol{X}\right)$. For instance perhaps in the banana problem only $x > 0$ is desired. The prior would therefore place probability of 0 on the $x < 0$ space. However posteriors with discontinuities introduced via hard constraints are difficult to sample from. This may be alleviated incorporating additional flexibility in the simulated annealing approach where hard constraints are numerically made "soft" [67, 68]. Soft constraints are introduced employing functions which map from the real number line to $[0, 1]$,

$$I\left[\boldsymbol{g}\left(\boldsymbol{\theta}\right)\right] = \prod_{i=1}^{N_c} \Phi\left(-\omega_j \cdot \max\left[0, g_i\left(\boldsymbol{\theta}\right)\right]\right), \tag{2.18}$$

where $\boldsymbol{g}$ is a vector of constraint functions, ω_j is related to the tempering exponent n_j, and Φ is the standard normal cumulative density function. In this formulation $g_i < 0$ constitutes the constraints being met. Consider that if all the constraints are met ($g_i < 0$ all i) then

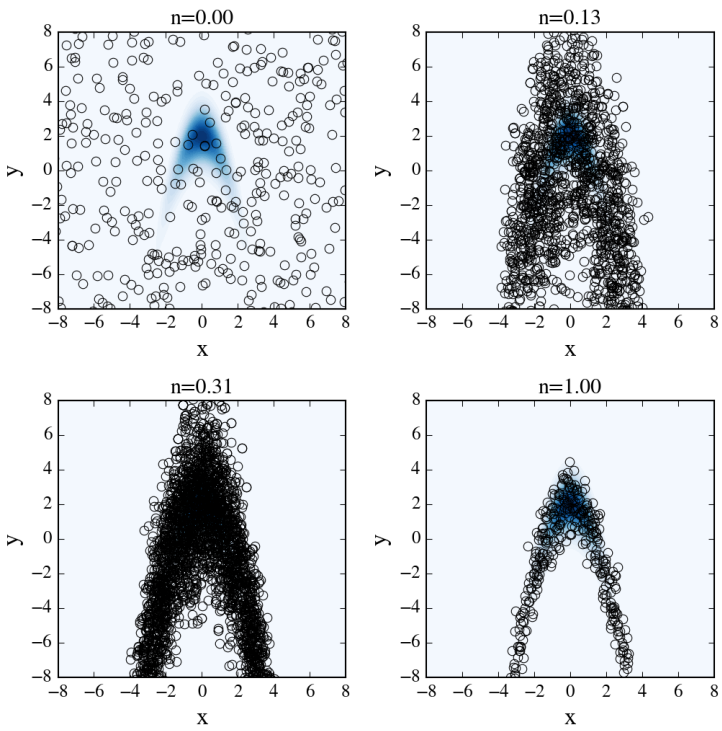

Figure 2.26: TMCMC snap shots at various n during the annealing schedule.

$I = \Phi(0)^{N_c} = 2^{-N_c}$. It is unimportant that $I \neq 1$ since the MCMC sampler is insensitive to scaling by constants (hence proportionality in Eqn. 2.13) [58, 59]. In the case where one constraint violates the constraints then I is scaled by $\Phi\left(-\omega_j g_i\left(\boldsymbol{x}'\right)\right)$. Therefore ω_j controls the *penalty* imposed on the posterior density. This of course extends to an arbitrary number of constraints being violated.

In the simulated annealing procedure ω_j takes on values beginning at a suitably small value, $\omega_o = 10^{-6}$, which numerically yields a lack of constraint. This of course depends on the scales of $g_i\left(\boldsymbol{\theta}\right)$ and so practitioners should exercise caution. The annealing scale is gradually increased to large values, $\omega_f = 10^6$, which numerically imposes the desired hard constraints. The exponential quantity can be obtained by using $n_j = (\omega_j - \omega_o)/(\omega_f - \omega_o)$ or an analogous ratio computed using logarithmic values. The same banana density is sampled, subject to the constraint $x > 0$, and snap shots at various n_j are shown in Figure 2.27.

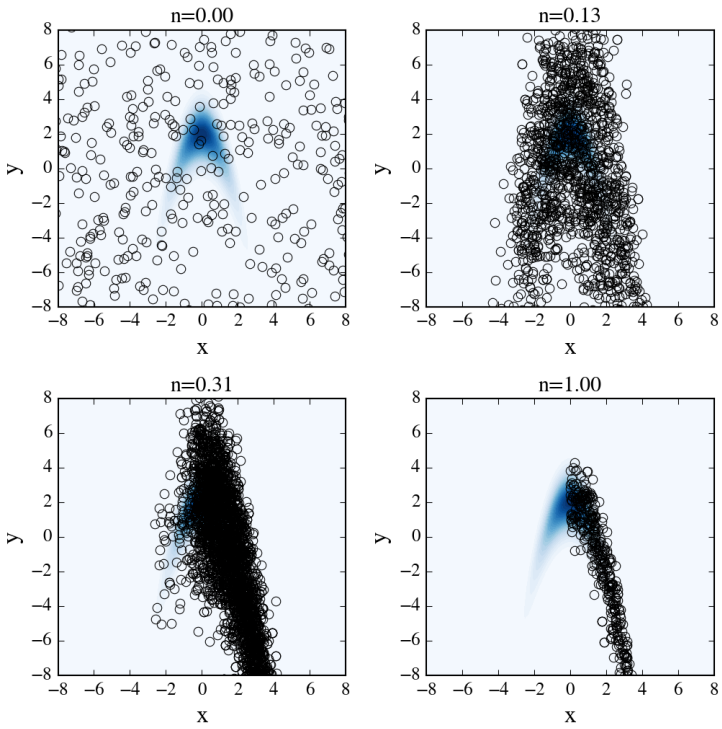

Figure 2.27: Constrained TMCMC snap shots at various n during the annealing schedule.

2.4 Gaussian process models

2.4.1 Single output stationary

$$Y \sim \mathcal{N}\left(\mu(\boldsymbol{x}), \sigma_y^2 R\left(\cdot,\cdot\right)\right) + \epsilon, \tag{2.19}$$

where ϵ is observation error e.g. white noise $\mathcal{N}(0, \sigma_\epsilon^2)$, $\mu(\boldsymbol{x})$ is a mean function, σ_y^2 is the variance of the process, and $R\left(\cdot,\cdot\right)$ is the correlation function. Note that $\mu(\boldsymbol{x})$ can be any model. A constant value is ordinary Kriging [14]. A linear regression model is universal Kriging [14]. Solutions to PDEs have been utilized as mean functions [70]. Even other GPs can be utilized as the mean function [71]; global behavior is captured with the mean function and local systematic variations with the composite GP. The correlation function describes how different observations are $\boldsymbol{x}_i$ and $\boldsymbol{x}_j$ are *spatially* correlation. If two points are close their responses (y_i and y_j) are expected to be close and therefore the two points

are said to be strongly spatially correlated.

Now consider that N observations are made. The data can be interpreted as coming from a N-dimensional multivariate normal process,

$$\begin{aligned} \boldsymbol{Y} &\sim \mathcal{N}\left(\boldsymbol{\mu}, \sigma_y^2 \boldsymbol{R} + \sigma_\epsilon^2 \boldsymbol{I}\right) \\ \mathrm{Cov}\left[y_i, y_j\right] &= \sigma_y^2 R\left(\boldsymbol{x}_i, \boldsymbol{x}_j\right) + \sigma_\epsilon^2 \delta_{ij}, \end{aligned} \tag{2.20}$$

There are a wide range of correlation function classes but here we use a Gaussian correlation function [14],

$$R(\boldsymbol{x}_i, \boldsymbol{x}_j) = \exp\left(-\sum_{k=1}^{d} \phi_k (x_{ik} - x_{jk})^2 - \sum_{k=1}^{q} \gamma_k I\left(x_{ik} \neq x_{jk}\right)\right), \tag{2.21}$$

where d is the number of quantitative variables in $\boldsymbol{x}$, q the number of qualitative variables, ϕ_k are correlation length scales, γ_k a penalty term if $x_{ik} \neq x_{jk}$, and I is the indicator function. Note that if $\boldsymbol{x}_i$ and $\boldsymbol{x}_j$ are the same with the exception of one qualitative variables then $R(\boldsymbol{x}_i, \boldsymbol{x}_j) = exp\left(-\gamma_k\right)$. It is clear from this explanation that the γ_k control penalty in correlation associated with qualitative factors. The ϕ_k have analogous effects associated with the distance measure for each quantitative dimension of $\boldsymbol{x}$.

Estimates of the hyperparameters can be obtained from the posterior density of the hyperparameters $p\left(\boldsymbol{\beta}, \boldsymbol{\phi}, \sigma_y^2, \sigma_\epsilon^2, \boldsymbol{\gamma} | \boldsymbol{X}, \boldsymbol{Y}\right)$. Here $\boldsymbol{\beta}$ are any unknown parameters in the mean function. A fully Bayesian approach attempts to obtain a sample from the posterior density. In practice this is extremely challenging at the model is highly nonlinear with

respect to the unknown parameters. Often a simple point estimate is used,

$$\begin{aligned}\hat{\boldsymbol{\Psi}} &= \arg\min_{\boldsymbol{\Psi}} p\left(\boldsymbol{\Psi}|\boldsymbol{X},\boldsymbol{Y}\right) \\ &= \arg\min_{\boldsymbol{\Psi}} \left[p\left(\boldsymbol{Y}|\boldsymbol{X},\boldsymbol{\Psi}\right)p\left(\boldsymbol{\Psi}|\boldsymbol{X}\right)\right] \\ \log p\left(\boldsymbol{Y}|\boldsymbol{X},\boldsymbol{\Psi}\right) &= -\frac{1}{2}\log 2\pi - \frac{1}{2}\log\left|\sigma_y^2\boldsymbol{R}+\sigma_\epsilon^2\boldsymbol{I}\right| - \\ &\quad \frac{1}{2}\left(\boldsymbol{\mu}-\boldsymbol{Y}\right)^T\left(\sigma_y^2\boldsymbol{R}+\sigma_\epsilon^2\boldsymbol{I}\right)^{-1}\left(\boldsymbol{\mu}-\boldsymbol{Y}\right),\end{aligned} \tag{2.22}$$

where $\boldsymbol{\Psi} = \left\{\boldsymbol{\beta}, \boldsymbol{\phi}, \sigma_y^2, \sigma_\epsilon^2, \boldsymbol{\gamma}\right\}$ is introduced for compactness. Note that if there are no priors then the point estimate is equivalent to the a maximum likelihood estimate (MLE). A point estimate including priors corresponds to the maximum a posteriori (MAP) estimate.

Now consider that a noise-free prediction $y(\boldsymbol{x})$ is desired. Since the assumption is that all observations come from a common process then $y(\boldsymbol{x})$ is jointly distributed with all prior observations $\boldsymbol{Y}$,

$$\begin{aligned}\begin{pmatrix}\boldsymbol{Y}\\ y(\boldsymbol{x})\end{pmatrix} &\sim \mathcal{N}\left(\begin{bmatrix}\boldsymbol{\mu}\\ \mu(\boldsymbol{x})\end{bmatrix}, \begin{bmatrix}\sigma_y^2\boldsymbol{R}+\sigma_\epsilon^2\boldsymbol{I} & \sigma_y^2\boldsymbol{r}\\ \sigma_y^2\boldsymbol{r}^T & \sigma_y^2\end{bmatrix}\right) \\ y(\boldsymbol{x}) &= \mu(\boldsymbol{x}) - \sigma_y^2\boldsymbol{r}^T\left(\sigma_y^2\boldsymbol{R}+\sigma_\epsilon^2\boldsymbol{I}\right)^{-1}\left(\boldsymbol{\mu}-\boldsymbol{Y}\right) \\ \hat{y}(\boldsymbol{x}) &= \mu(\boldsymbol{x}) - \boldsymbol{r}^T\left(\boldsymbol{R}+\frac{\sigma_\epsilon^2}{\sigma_y^2}\boldsymbol{I}\right)^{-1}\left(\boldsymbol{\mu}-\boldsymbol{Y}\right),\end{aligned} \tag{2.23}$$

where $r_i = R\left(\boldsymbol{x}, \boldsymbol{x}_i\right)$ measures the correlation of the new point, $\boldsymbol{x}$, with all other observed points. The final two lines are direct applications of the conditional normal formula. The final line is an algebraic manipulation which yields the variable $\frac{\sigma_\epsilon^2}{\sigma_y^2}$ which is the intuitive *signal to noise ratio*. Larger signal to noise ratios will contribute more to the diagonal of the correlation matrix. The effect is that points will only be correlated with themselves! The implication is therefore that the correlation across points is weak and therefore there are few "patterns" available from which future estimates can be made. This agrees well

with intuition. An estimate of the variance associated with a prediction $\hat{y}(\boldsymbol{x})$ is,

$$\operatorname{Var} \hat{y}(\boldsymbol{x}) = \sigma_y^2 \left[1 - \boldsymbol{r}^T \left(\boldsymbol{R} + \frac{\sigma_\epsilon^2}{\sigma_y^2} \boldsymbol{I} \right)^{-1} \boldsymbol{r} \right], \tag{2.24}$$

2.4.2 Single output nonstationary

The GP introduced in Section 2.4.1 is a *stationary* model. Stationarity requires that the random process "behaves" identically for all $\boldsymbol{x}$. An example of a nonstationary function is shown in Figure 2.28. Consider that at large x the function has lower mean, larger variation, and weaker spatial correlation than the function at small x. Therefore the function exhibits nonstationary behavior. The nonstationary in the mean can be accommodated for using a better mean function that captures the step response. However the nonstationary behavior associated with correlation and variance are more difficult to capture.

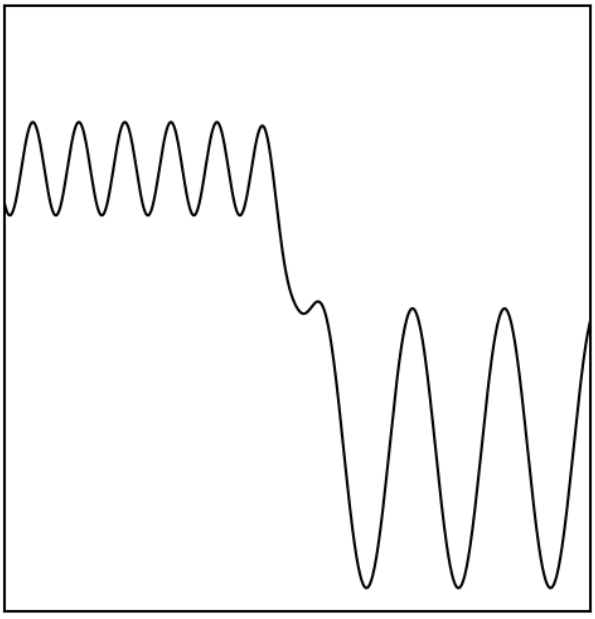

Figure 2.28: Nonstationary function illustrating nonstationary in (1) mean, (2) variance, (3) spatial correlation.

Building nonstationary GP models is a current area of research in the statistics community. There are many approaches some of which include: using nonstationary convolution kernels [72], treed GPs [73], local GPs [74], limit Kriging [75], composite GPs [71], and high-frequency Kriging [76]. High-frequency Kriging is a very natural extension of the already introduced GP models which considers that the actual observed process, $V(\boldsymbol{x})$, is generated from a weighted sum of independent GPs,

$$V(\boldsymbol{x}) = \sum_{k=1}^{K} w_k(\boldsymbol{x}) Z_k(\boldsymbol{x}), \tag{2.25}$$

where $w_k(\boldsymbol{x})$ are the weight functions (which sum to 1) and $Z_k(\boldsymbol{x})$ the GPs that contribute to $V(\boldsymbol{x})$. Note that all the $Z_k(\boldsymbol{x})$ are independent from one another e.g. $\mathrm{Cov}\left(Z_i(\boldsymbol{x}_l), Z_j(\boldsymbol{x}_k)\right) = \sigma_i^2 R\left(\boldsymbol{x}_l, \boldsymbol{x}_k\right) \delta_{ij}$. Therefore,

$$\mathrm{Cov}\left[V(\boldsymbol{x}_i), V(\boldsymbol{x}_j)\right] = \sum_{k=1}^{K} w_k^2(\boldsymbol{x}) \mathrm{Cov}\left[Z_k(\boldsymbol{x}_i), Z_k(\boldsymbol{x}_j)\right], \tag{2.26}$$

The flexibility enabled by this method allows for different processes to "kick in" in different regions of $\boldsymbol{x}$. However the more complex model comes at a price. $w_k(\boldsymbol{x})$ will certainly have additional hyperparameters and there are K such functions. In addition there are K sets of hyperparameters corresponding to each process Z_k. Therefore either the nonstationary trends must be extremely pronounced or there must be sufficiently large dataset. The concepts of over fitting in regression also applies in the GP modeling setting. Practitioners may alleviate this issue by employing appropriate assumptions about the nature of the nonstationarity. For instance the nonstationary may only be associated with the process variance in which case the same correlation parameters ($\boldsymbol{\gamma}$, $\boldsymbol{\phi}$) may be used for all K processes.

2.4.3 Multiple output stationary

Consider a process who's input are $\boldsymbol{x}$ and that has multiple outputs $[Y_1, Y_2, \ldots, Y_K]$ which are observed with some measurement error $\boldsymbol{\epsilon}$. This process can be modeled using a multivariate GP model,

$$\begin{pmatrix} Y_1(\boldsymbol{x}) \\ Y_2(\boldsymbol{x}) \\ \vdots \\ Y_M(\boldsymbol{x}) \end{pmatrix} \sim \mathcal{N}(\boldsymbol{\mu}(\boldsymbol{x}), \boldsymbol{S} + \mathrm{Cov}\boldsymbol{\epsilon}) \tag{2.27}$$

$$S_{ij} = \mathrm{Cov}(Y_i, Y_j),$$

where the mean behavior of the outputs varies according to a mean function $\boldsymbol{\mu}(\boldsymbol{x})$, *cross-correlations* between outputs are captured through $\boldsymbol{S}$, and the observation errors are in general allowed to be correlated and perhaps have different scales for each outputs e.g. $\mathrm{Cov}\boldsymbol{\epsilon}$ is purposefully generic. The mean function may be described using a parametric regression strategy e.g. $\boldsymbol{\mu}(\boldsymbol{x}) = \boldsymbol{f}(\boldsymbol{x})\boldsymbol{\beta}$ where $\boldsymbol{\beta}$ are regression coefficients and $\boldsymbol{f}(\boldsymbol{x})$ a vector of regressors. At first cross-correlations will be treated as spatially invariant and therefore stationary.

Now consider that observations of each output Y_i are made at $\boldsymbol{x}_{ij}$ where $j = 1, \ldots, N_i$. This notation is flexible enough to allow each Y_i output to have N_i unique observations $\boldsymbol{x}_{ij}$ with a total number of $N = \sum_{i=1}^{K} N_i$. Again this is valuable if the Y_i have different experimental costs associated with obtaining them (optical vs TEM). The accumulated dataset

therefore can be expressed as another multivariate normal,

$$\begin{pmatrix} Y_1(\boldsymbol{x}_{11}) \\ \vdots \\ Y_1(\boldsymbol{x}_{1N_1}) \\ Y_2(\boldsymbol{x}_{21}) \\ \vdots \\ Y_2(\boldsymbol{x}_{2N_2}) \\ \vdots \\ Y_M(\boldsymbol{x}_{M_1}) \\ \vdots \\ Y_M(\boldsymbol{x}_{MN_M}) \end{pmatrix} \sim \mathcal{N}(\boldsymbol{\mu}, \boldsymbol{C} + \boldsymbol{\Sigma}) \tag{2.28}$$

$$\mathrm{Cov}\left[Y_i(\boldsymbol{x}_{ik}), Y_j(\boldsymbol{x}_{jl})\right] = S_{ij}R(\boldsymbol{x}_{ik} - \boldsymbol{x}_{jl}) + \sigma_{ij}\delta_{ij}\delta_{kl} + \sigma_{ij}\delta_{kl},$$

where $\boldsymbol{\Sigma}$ is the total error covariance matrix. Note that $\boldsymbol{\Sigma}$ is comprised of σ_{ij} and contains some flexibility for different kinds of experiments. Observations have some measurement variance σ_{ij} when outputs are identical ($i = j$) and are observed at the same $\boldsymbol{x}$ ($k = l$) however if there are *paired* observations (Y_i, Y_j) at each observation ($k = l$) then there may also be correlations in the errors. One example where this may be relevant is when considering the PC-weights as microstructure descriptors which will generate pairs (or tuples in higher dimensions) of data for each micrograph. If observations are not measured in pairs then they should be independent and share no correlation. Note that if all experiments are performed at the same $\boldsymbol{x}$ then the above covariance structure has a Kronecker structure which can be exploited for computational efficiency [77]. The covariance structure imposes that there is a distance-based criteria for quantifying correlations (R), that there are cross-correlations across outputs ($\boldsymbol{\Sigma}$), and that there is a random component associated with measurement uncertainty ($\boldsymbol{\Sigma}$).

The *prior* placed on the data is that observations can be explained by interpreting them

as coming from some multivariate normal generating process. Unknown hyperparameters $\boldsymbol{\Phi} = [\boldsymbol{\beta}, \phi, \boldsymbol{S}, \boldsymbol{\Sigma}]$ can be obtained from,

$$\hat{\boldsymbol{\Phi}} = \arg\min_{\boldsymbol{\Phi}} \left(|\boldsymbol{C} + \boldsymbol{\Sigma}| + (\boldsymbol{Y} - \boldsymbol{\mu})^T (\boldsymbol{C} + \boldsymbol{\Sigma})^{-1} (\boldsymbol{Y} - \boldsymbol{\mu}) \right). \tag{2.29}$$

Note that in the inference there are two matrix quantities that need to be estimated. To improve efficiency of the estimation and maintain that these matrices remain positive definite inverse-Wishart priors are placed on the matrix quantities and the inference is reparameterized. A review of this strategy can be found in [58].

Another class of multiple output GPs considers multiple output data where the outputs correspond to observations made on a regular grid or interval. A simulation or experiment that produces time series data is an example. A visualization of such data is shown in Figure 2.29.

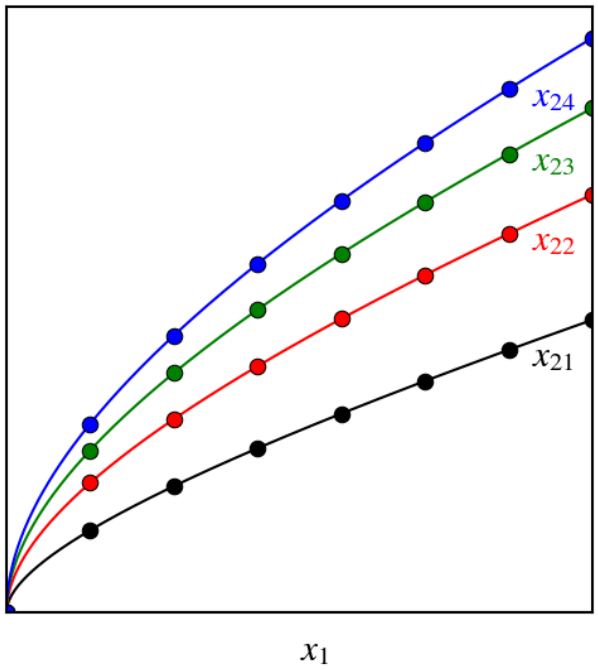

Figure 2.29: Data structure amenable towards Kronecker product.

In this example imagine that there are four experiments or simulations performed each of which produces a time history where observation times are always identical. The experiments correspond to different values of x_2 (x_{21} to x_{24}). In this example there are $M = 8$ interval values and $N = 4$ different experiments so a total of $N \cdot M = 32$ data points. The cost associated with inverting the correlation matrix is $\mathcal{O}\left(N^3 M^3\right)$. Clearly as N and M grow this becomes prohibitively expensive. However if the data is ordered appropriately the interval structure in the data can be exploited for efficiency.

$$\begin{pmatrix} \boldsymbol{Y}\left(x_{21}; \boldsymbol{x}_1\right) \\ \boldsymbol{Y}\left(x_{22}; \boldsymbol{x}_1\right) \\ \boldsymbol{Y}\left(x_{23}; \boldsymbol{x}_1\right) \\ \boldsymbol{Y}\left(x_{24}; \boldsymbol{x}_1\right) \end{pmatrix} \sim \mathcal{N}\left(\boldsymbol{\mu}, \sigma_y^2 \boldsymbol{R}_{x_1} \otimes \boldsymbol{R}_{x_2}\right), \tag{2.30}$$

where $\otimes$ is the Kronecker product. Note that intuitively the correlation component associated with x_1 is identical in each experiment since x_1 is on a regular grid. The benefit of this strategy is that $|\boldsymbol{R}_{x_1} \otimes \boldsymbol{R}_{x_2}| = |\boldsymbol{R}_{x_2}|^M |\boldsymbol{R}_{x_1}|^N$ and $\left(\boldsymbol{R}_{x_1} \otimes \boldsymbol{R}_{x_2}\right)^{-1} = \boldsymbol{R}_{x_2}^{-1} \otimes \boldsymbol{R}_{x_2}^{-1}$ [78]. Therefore the computational cost is reduced to $\mathcal{O}\left(N^3 + M^3\right)$. The idea can be extended to higher dimensional grids which yield a similar $\boldsymbol{R}_1 \otimes \cdots \otimes \boldsymbol{R}_d$ structure where d is the grid dimension.

Note that the expression in Eqn. 2.28 can also be expressed with the Kronecker structure if every observation produces every one of the M outputs. However if any observation is missing then the Kronecker structure is destroyed.

2.4.4 Multiple output nonstationary

A natural nonstationary extension to the case where there there are a finite number of experiment/simulation outputs, which do not correspond observations such as time or some

other quantitative variable, can be expressed as

$$\begin{aligned} \boldsymbol{y} &\sim \mathcal{N}\left(\boldsymbol{\mu}, \boldsymbol{C}\right) \\ \boldsymbol{C} &= \sum_{k}^{K} \boldsymbol{S}_k \otimes \left(\boldsymbol{w}_k^T \boldsymbol{w}_k \circ \boldsymbol{R}_k\right). \end{aligned} \tag{2.31}$$

2.4.5 Cross validation

Consider that cross-validation is a powerful tool for assessing the predictiveness of a trained model. The cross validation error associated with removing a subset of data of size N_i, represented by multi-index i, can be expressed as

$$\boldsymbol{cv}_i = \boldsymbol{y}_i - \hat{\boldsymbol{f}}_{(i)}(\boldsymbol{x}_i), \tag{2.32}$$

where $\boldsymbol{y}_i$ are the responses corresponding to i and $\hat{\boldsymbol{f}}_{(i)}(\boldsymbol{x}_i)$ is the corresponding estimate for a model which is trained by withholding data belonging to i. $\boldsymbol{cv}_i$ is a vector with multiple observations of a potentially multivariate output. The model estimate is given by

$$\hat{\boldsymbol{f}}_{(i)}(\boldsymbol{x}_i) = \boldsymbol{\mu}(\boldsymbol{x}_i) + \boldsymbol{r}_{(i)}^T \boldsymbol{C}_{(i)}^{-1} \left(\boldsymbol{y}_{(i)} - \boldsymbol{\mu}_{(i)}\right) \tag{2.33}$$

where quantities containing subscript (i) represent quantities computed with data from i missing.

Now consider the complete covariance matrix where the ordering of the data is rearranged such that the block corresponding to i is shifted to the final rows/columns,

$$\boldsymbol{C} = \begin{bmatrix} \boldsymbol{C}_{(i)} & \boldsymbol{r}_{(i)} \\ \boldsymbol{r}_{(i)}^T & \widetilde{\boldsymbol{\Sigma}}_i \end{bmatrix}, \tag{2.34}$$

To compute $\boldsymbol{C}^{-1}$ the Sherman-Morrison-Woodbury formula can be applied,

$$\boldsymbol{C}^{-1} = \begin{bmatrix} \boldsymbol{C}_{(i)}^{-1} + \boldsymbol{B}\boldsymbol{r}_{(i)}^T\boldsymbol{C}_{(i)}^{-1} & -\boldsymbol{B} \\ -\boldsymbol{B}^T & \left(\widetilde{\boldsymbol{\Sigma}}_i - \boldsymbol{r}_{(i)}^T\boldsymbol{C}_{(i)}^{-1}\boldsymbol{r}_{(i)}\right)^{-1} \end{bmatrix}, \quad (2.35)$$

where $\boldsymbol{B} = \boldsymbol{C}_{(i)}^{-1}\boldsymbol{r}_{(i)}\left(\widetilde{\boldsymbol{\Sigma}}_i - \boldsymbol{r}_{(i)}^T\boldsymbol{C}_{(i)}^{-1}\boldsymbol{r}_{(i)}\right)^{-1}$. This manipulation enables the interpretation of quantity
$\left(\widetilde{\boldsymbol{\Sigma}}_i - \boldsymbol{r}_{(i)}^T\boldsymbol{C}_{(i)}^{-1}\boldsymbol{r}_{(i)}\right)^{-1}$ as the i^{th} "block-diagonal" entry of $\boldsymbol{C}^{-1}$. This refers to the $N_i \times N_i$ entry corresponding to indices i which will be noted as $\boldsymbol{C}_{ii}^{-1}$. Similarly
$-\left(\widetilde{\boldsymbol{\Sigma}}_i - \boldsymbol{r}_{(i)}^T\boldsymbol{C}_{(i)}^{-1}\boldsymbol{r}_{(i)}\right)^{-1}\boldsymbol{r}_{(i)}^T\boldsymbol{C}_{(i)}^{-1}$ is the i^{th} "block-row" of $\boldsymbol{C}^{-1}$. Note this is really a $N_i \times (N_{tot} - N_i)$ matrix, where N_{tot} is the total number of data points, but it will be referred to it as a "block-row" because of its association with the i^{th} rows of the correlation matrix. This quantity will be noted $\boldsymbol{C}_{i,(i)}^{-1}$ e.g. the i^{th} block-row of $\boldsymbol{C}^{-1}$ not including the i^{th} block-diagonal portion. Therefore

$$\begin{aligned} \boldsymbol{C}_{i,(i)}^{-1} &= -\left(\widetilde{\boldsymbol{\Sigma}_i} - \boldsymbol{r}_{(i)}^T\boldsymbol{C}_{(i)}^{-1}\boldsymbol{r}_{(i)}\right)^{-1}\boldsymbol{r}_{(i)}^T\boldsymbol{C}_{(i)}^{-1} \\ &= -\boldsymbol{C}_{ii}^{-1}\boldsymbol{r}_{(i)}^T\boldsymbol{C}_{(i)}^{-1} \\ \boldsymbol{r}_{(i)}^T\boldsymbol{C}_{(i)}^{-1} &= -\left(\boldsymbol{C}_{ii}^{-1}\right)^{-1}\boldsymbol{C}_{i,(i)}^{-1}. \end{aligned} \quad (2.36)$$

The advantage of these manipulations will become clear when returning to equations

2.32 and 2.33

$$
\begin{aligned}
\boldsymbol{cv}_i &= \boldsymbol{y}_i - \boldsymbol{\mu}(\boldsymbol{x}_i) - \boldsymbol{r}_{(i)}^T \boldsymbol{C}_{(i)}^{-1} \left(\boldsymbol{y}_{(i)} - \boldsymbol{\mu}_{(i)}\right) \\
&= \boldsymbol{y}_i - \boldsymbol{\mu}(\boldsymbol{x}_i) + \left(\boldsymbol{C}_{ii}^{-1}\right)^{-1} \boldsymbol{C}_{i,(i)}^{-1} \left(\boldsymbol{y}_{(i)} - \boldsymbol{\mu}_{(i)}\right) \\
&= \boldsymbol{y}_i - \boldsymbol{\mu}(\boldsymbol{x}_i) + \\
&\quad \left(\boldsymbol{C}_{ii}^{-1}\right)^{-1} \begin{bmatrix} \boldsymbol{C}_{i,(i)}^{-1} & \boldsymbol{C}_{ii}^{-1} \end{bmatrix} \left(\begin{bmatrix} \boldsymbol{y}_{(i)} \\ \boldsymbol{y}_i \end{bmatrix} - \begin{bmatrix} \boldsymbol{\mu}_{(i)} \\ \boldsymbol{\mu}_i \end{bmatrix} \right) \\
&\quad - \left(\boldsymbol{C}_{ii}^{-1}\right)^{-1} \boldsymbol{C}_{ii}^{-1} \boldsymbol{y}_i + \left(\boldsymbol{C}_{ii}^{-1}\right)^{-1} \boldsymbol{C}_{ii}^{-1} \boldsymbol{\mu}_i \\
\boldsymbol{cv}_i &= \left(\boldsymbol{C}_{ii}^{-1}\right)^{-1} \boldsymbol{C}_i^{-1} \left(\boldsymbol{y} - \boldsymbol{\mu}\right) \\
\boldsymbol{cv} &= blockdiag \left(\boldsymbol{C}^{-1}\right)^{-1} \boldsymbol{C}^{-1} \left(\boldsymbol{y} - \boldsymbol{\mu}\right).
\end{aligned}
\tag{2.37}
$$

In the above manipulations $\boldsymbol{\mu}(\boldsymbol{x}_i) = \boldsymbol{\mu}_i$, $\begin{bmatrix} \boldsymbol{C}_{i,(i)}^{-1} & \boldsymbol{C}_{ii}^{-1} \end{bmatrix} = \boldsymbol{C}_i^{-1}$ e.g. the i^{th} block-row, and $\left(\boldsymbol{C}_{ii}^{-1}\right)^{-1} \boldsymbol{C}_{ii}^{-1} = \boldsymbol{I}$ where $\boldsymbol{I}$ is the identity matrix. These manipulations enable the direct computation of the leave-i-out cross validation. Computationally this is a much more favorable estimate over the alternative which would require retraining many times for however many i there are. This methodology can easily be applied towards *k-folds* cross-validation where the previously introduced i would correspond indices in the matrix belonging to each of the k-folds.

An expression for the leave-one-out prediction variance can be obtained using the same matrix manipulations. For i^{th} hold out case the prediction covariance for $\hat{\boldsymbol{f}}_{(i)}(\boldsymbol{x}_i)$ can be obtained from,

$$
\boldsymbol{S}_i = \left(\boldsymbol{C}_{ii}^{-1}\right)^{-1} \boldsymbol{C}_i^{-1} \boldsymbol{C}_i^T, \tag{2.38}
$$

the diagonal of which contains the prediction variance estimates.

2.5 Crystallography

The behavior of polycrystalline materials depends on the individual response of each crystal constituent as well as their spatial arrangement and relative orientations. Two schematics of polycrystalline rolled sheets are shown in Figures 2.30 & 2.31. In Figure 2.30 there is regular order in how the crystals are oriented relative to the sheet which produces a cube *texture*. To fully describe this arrangement both the orientation of the crystals and the orientation of the sample are necessary. This is illustrated in Figure 2.31 where each is appropriately labeled according to some a priori criteria. Components with strong crystallographic textures may inherit anisotropic properties from the crystallographic anisotropic response [79, 80, 81, 82, 83, 84]. This is not only limited to mechanical properties - Sn based solder for instance displays anisotropic electron carrying behavior [85, 86].

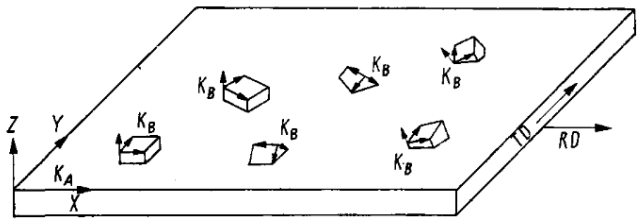

Figure 2.30: Polycrystalline sheet [79].

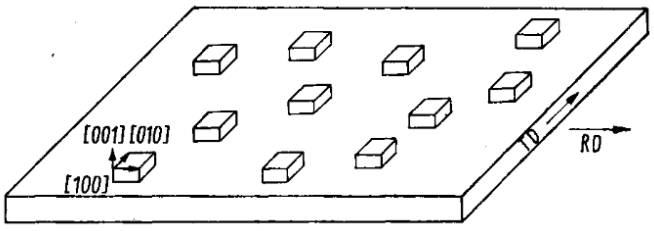

Figure 2.31: Polycrystalline sheet with strong cube texture [79].

Crystallographic orientation can be quantified using the Bunge-Euler angles $\boldsymbol{g} = (\phi_1, \Phi, \phi_2)$ which are of course continuously defined over the fundamental zone (FZ) [79]. An illus-

tration is shown in Figure 2.32. For cubic crystals crystallographic symmetries constrain the FZ to be defined over $0 \leq \phi_1 \leq 2\pi$, $\cos^{-1}\left(\frac{cos\phi_2}{1+cos^2\phi_2}\right) \leq \Phi \leq \pi/2$, and $0 \leq \phi_2 \leq \pi/3$. Therefore in this setting the microstructure function may be re-introduced as $f_s\left(\boldsymbol{g}\right)$ where the microstructure state is described by the continuous variables $\boldsymbol{g}$ [87, 83].

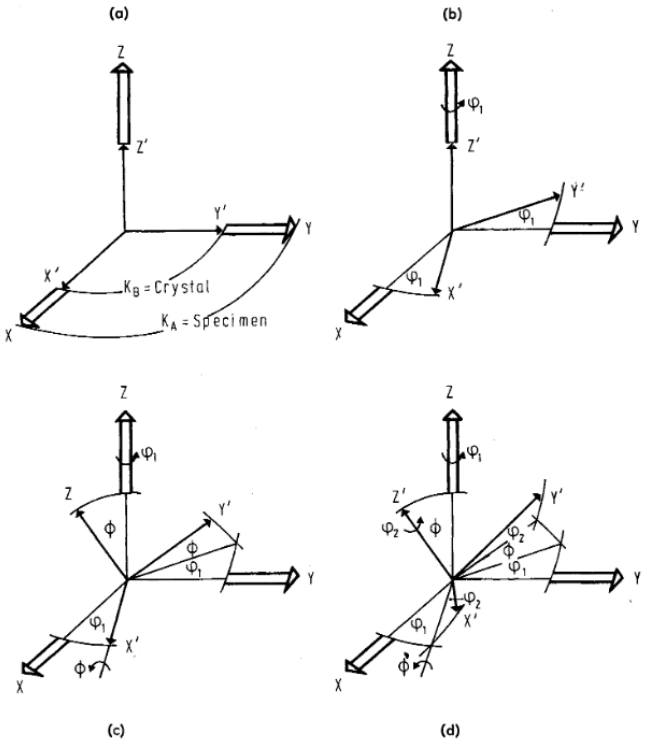

Figure 2.32: Bunge-Euler convention for quantifying crystal orientation [79].

Consider that experiments are performed to obtain the spatial distribution of crystal orientations. For a polycrystalline aggregate the a crystallographic *distribution function* may be generated which describes the preferred orientations observed in the sample. There are many ways to describe and communicate the results but perhaps most popular are the pole figure (PF) and inverse pole figure (IPF) [79]. Recall that to properly describe the results both crystal orientations and sample orientations must be specified. PF and IPF are shown in Figures 2.33 & 2.34. The results describe which crystal orientations are preferred with respect to sample coordinates and visa versa.

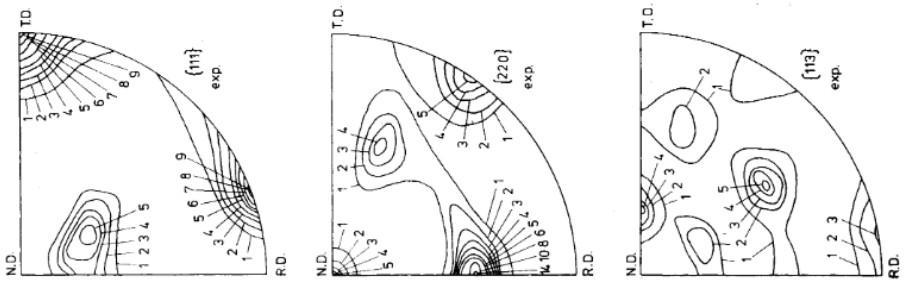

Figure 2.33: Pole figure for rolled FCC material [79].

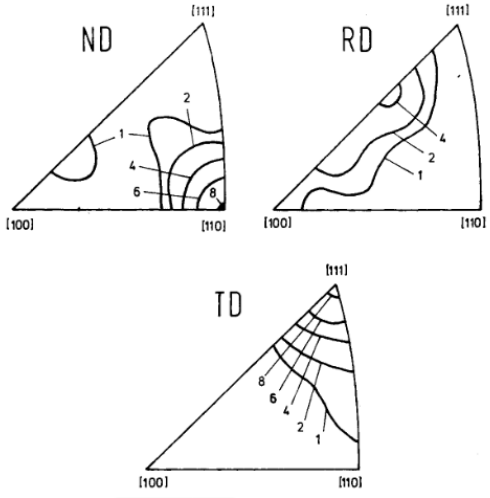

Figure 2.34: Inverse pole figure for rolled FCC material [79].

2.6 Generalized Spherical Harmonics

Now consider that a mathematical representation of the distribution function is desired. A critical requirement is that the description preserve crystallographic *symmetries* associated with the crystal system. For instance in FCC systems [001] and [100] are identical directions due to symmetry. Generalized spherical harmonics (GSH) have served as an efficient basis function for describing crystal orientation [79]. There have been several works that have adopted the use of generalized spherical harmonics (GSH) for describing the microstructure function in polycrystalline systems $\boldsymbol{g}$ [87, 83, 84]. Using the GSH basis the microstructure function can be rewritten,

$$f_{\boldsymbol{x}}(\boldsymbol{g}) = \sum_{\mu,n,l} F_{l\boldsymbol{x}}^{\mu n} \dot{\dot{T}}_l^{\mu n}(\boldsymbol{g}), \tag{2.39}$$

where μ, n, l represent multiple indices for multiple sums, $F_{l\boldsymbol{x}}^{\mu n}$ is the complex-valued coefficient at $\boldsymbol{x}$ which corresponds to the complex valued GSH basis $\dot{\dot{T}}_l^{\mu n}$. Note that the $\dot{\dot{T}}_l^{\mu n}$ preserve crystal symmetries and are orthogonal to their complex conjugate $\dot{\dot{T}}_l^{\mu n*}$ e.g. $\int_{FZ} \dot{\dot{T}}_l^{\mu n} \dot{\dot{T}}_{l'}^{\mu' n'*} d\boldsymbol{g} = (2l+1)^{-1}$ if all the indices "match" else 0. The coefficients $F_{l\boldsymbol{x}}^{\mu n}$ can be obtained in the analogous way to how Fourier coefficients are determined (exploiting orthogonality),

$$F_{l\boldsymbol{x}}^{\mu n} = (2l+1) \int_{FZ} f_{\boldsymbol{x}}(\boldsymbol{g}) \, \dot{\dot{T}}_l^{\mu n}(\boldsymbol{g}) \, d\boldsymbol{g}. \tag{2.40}$$

Note that if the spatial bin occupying $\boldsymbol{x}$ (a pixel in an indexed EBSD scan) contains only one crystal orientation $\boldsymbol{g}_o$ then Eqn. 2.40 is simplified to $F_{l\boldsymbol{x}}^{\mu n} = (2l+1)\dot{\dot{T}}_l^{\mu n}(\boldsymbol{g}_o)$.

The GSH microstructure representation was combined with spatial statistics in two recent publications [83, 84]. In these works the authors established a new methodology for quantifying spatial statistics of the GSH basis which encode information about the crystallographic texture as well as spatial morphological features. Consider that the expression in Eqn. 2.39 may be truncated to a total of N terms. A natural extension of two point statis-

tics (Eqn. 2.6) is to therefore consider the auto and cross correlations between the different basis weights,

$$F_{\boldsymbol{t}}^{LK} = \frac{1}{S}\sum_{s=1}^{S} M_s^L M_{s+\boldsymbol{t}}^K \tag{2.41}$$

where $F_{\boldsymbol{t}}^{LK}$ is the correlation between truncated basis weights L and K, $L, K = 1, \ldots, N$. A naive estimate of the total number of possible $L - K$ pairs, if the truncation is done at $N = 6$, is 6-choose-2=15. However there are many redundancies in the correlations so the total number is actually $2L - 1 = 5$ [83]. The appendix of that work contains a discussion on the sensitivity of the analysis to selection of these pairs [83]. In addition there is a discussion on the physics contained in the pair correlations e.g. contains only texture information, only morphological information, a mix, etc.. Several microstructural realizations and their reduced order PC representations are shown in Figure 2.35. The prediction validation for effective modulus and yield strength is shown in Figure 2.36.

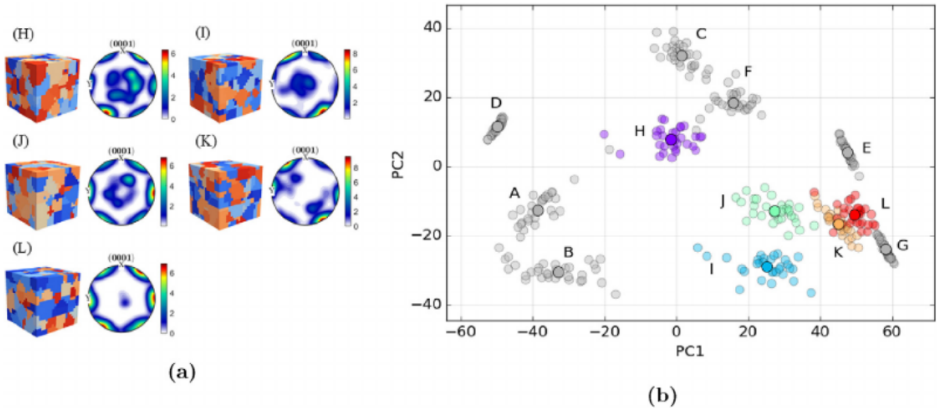

Figure 2.35: Polycrystalline microstructure realizations and their reduced order representations [83].

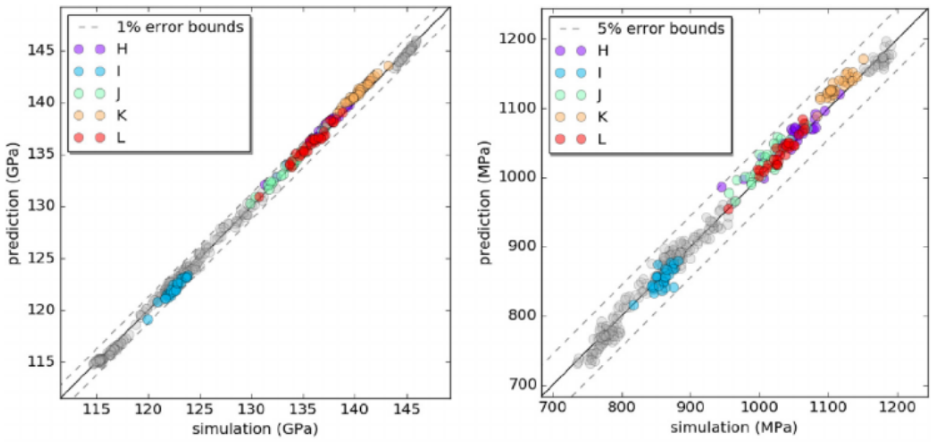

Figure 2.36: Data-driven reduced order PC weight model validation against FE simulation results for effective modulus (left) and yield strength (right) [83].

2.7 Bootstrapping

Consider that a dataset is acquired which is experimentally difficult to obtain. From that dataset several statistics may be computed (sample mean, sample variance, max, min, max-min range, etc.). In addition the experimenter wishes to obtain a measure of the variance of the estimate e.g. standard error. Consider a dataset of real values $\boldsymbol{X} = [X_1, X_2, \ldots, X_N]$ where it is assumed that the observations are independent and identically distributed. The mean is

$$\mathrm{E}\left[X\right] = \frac{1}{N}\sum_{i=1}^{N} X_i. \tag{2.42}$$

The variance of the mean is

$$\begin{aligned} \mathrm{Var}\left[\mathrm{E}\left[X\right]\right] &= \mathrm{Var}\left[\frac{1}{N}\sum_{i=1}^{N} X_i\right] \\ &= \frac{1}{N^2}\sum_{i=1}^{N} \mathrm{Var}\left[X_i\right] \\ &= \frac{1}{N}\mathrm{Var}\left[X_i\right] \end{aligned} \tag{2.43}$$

which for normally distributed random variables yields the familiar form for the standard error of the mean, $\sigma/\sqrt{N}$. Now consider however that want a standard error for a difficult to function of the entire dataset $s(\boldsymbol{X})$... The derivation of a standard error for this quantity $\hat{se}_s$ is not clear.

In these settings the standard error may be estimated using *simulation* methods in statistics. One of the most popular of which is the familiar bootstrapping technique [88]. The procedure is to resample the dataset N times with replacement to yield $\boldsymbol{X}^*$ which has a corresponding statistic S^*. Repeat this many times and the distribution of S^* can be derived which easily yields the standard error estimate. A schematic of this procedure is shown in Figures 2.37-2.38.

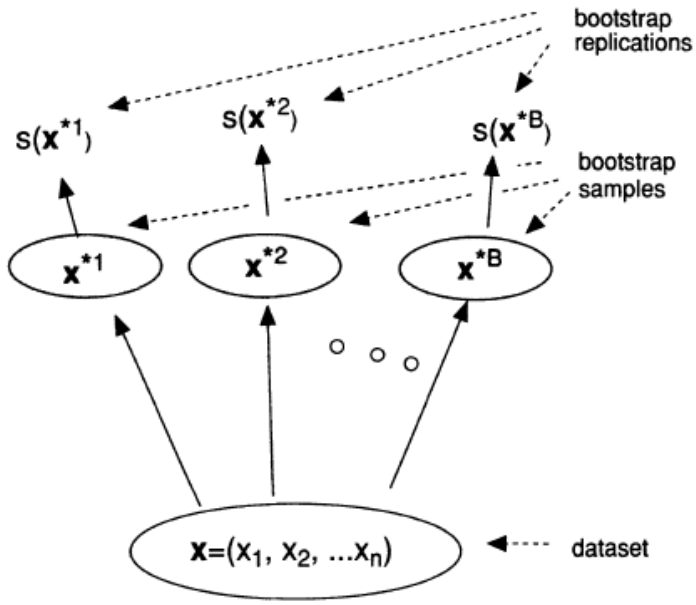

Figure 2.37: Bootstrapping strategy using resampling for obtaining standard error measurements of mean statistics from a single dataset [88].

This procedure works because conditional on the observed data $\boldsymbol{X}$ the *best* estimate for X's distribution function, $F(x)$, is the empirical distribution function $\hat{F}(x) = Pr(X < x) = \sum_{i=1}^{N} I(X_i < x)$. Therefore the best estimate for a future drawing of N samples from the same experiment is simply a drawing N samples from $\hat{F}(x)$. This is equivalent to

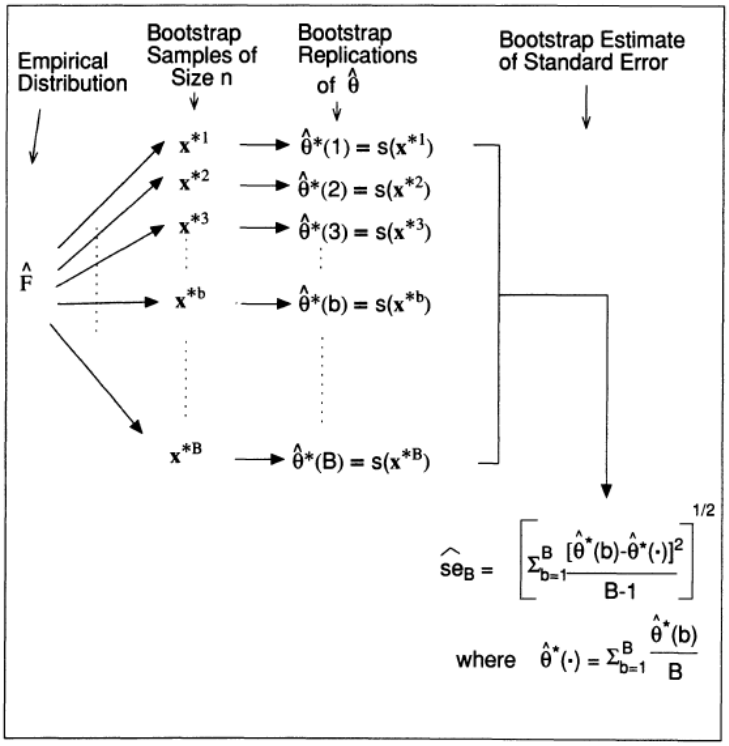

Figure 2.38: Bootstrapping strategy using the empirical distribution function for obtaining standard error measurements of mean statistics from a single dataset [88].

resampling with replacement. Figure 2.38 illustrates this information by also including the empirical distribution in the diagram.

Bootstrapping can also be extended towards correlated data. Direct application of the above algorithm however would destroy the inherent correlations present in the data. Therefore resampling must be done intelligently to not destroy the correlation structure. The solution is to perform "block" resampling where the size of the block is a representative "unit" associated with the correlation scale. This idea is illustrated in Figure 2.39 on a time series example.

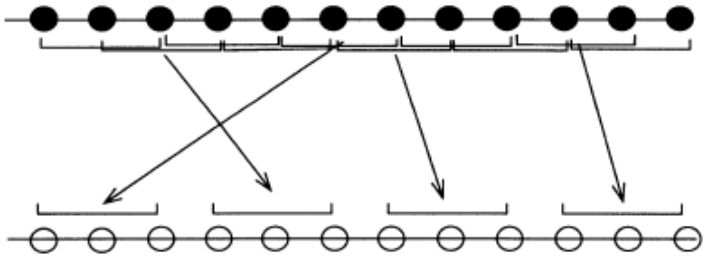

Figure 2.39: Time series "block" resampling strategy for bootstrapping of correlated data [88].

2.8 Spherical Indentation

Recent advances in indentation testing have yielded experimental methods that reliably generate indentation stress-strain curves characterizing both elastic and post-elastic behavior [89, 90]. These methods are enabled by superimposing periodic unloading segments on the overall loading segment. In systems equipped with continuous stiffness measurement (CSM), this is accomplished in an automated manner by superimposing a harmonic signal (amplitude 2 nm at 45 Hz) on the prescribed monotonic displacement history. For systems without the CSM capability, the periodic loading-unloading may be directly prescribed [91, 92, 93]. During unloading, the material is assumed to deform elastically. These elastic unloading segments may be analyzed using Hertzian mechanics to estimate the indentation stress and the indentation strain.The Hertzian solution for frictionless contact between an

indenter and a sample exhibiting quadratic surfaces and isotropic elastic constitutive response is expressed as,

$$\begin{aligned} P &= \frac{4}{3} E_{eff} R_{eff}^{1/2} h_e^{3/2} \\ a &= \sqrt{R_{eff} h_e} \\ \frac{1}{E_{eff}} &= \frac{1-\nu_s^2}{E_s} + \frac{1-\nu_i^2}{E_i} \\ \frac{1}{R_{eff}} &= \frac{1}{R_s} + \frac{1}{R_i} \end{aligned} \tag{2.44}$$

,

where a is the contact radius, P the indentation load, h_e the elastic indentation depth, R_{eff} the effective radius, E_{eff} the effective modulus, E modulus, ν Poisson's ratio, and subscripts i and s refer to the indenter and sample, respectively. For a rigid indenter the indenter modulus is infinite, and for an initially at sample R_s is initially innite. An analytical form for the measured stiffness, S, may be determined from Eqn. 2.44 and further manipulated to enable inference of the contact radius during unloading segments,

$$S = \frac{dP}{dh_e} = 2E_{eff} R_{eff}^{1/2} h_e^{1/2} = 2E_{eff} a. \tag{2.45}$$

Classically, the effective modulus has been determined from the unloading portion of the load-displacement curve at the end of the indentation test. However this calculation is not trivial as the radius of the plastically deformed sample at the end of the test is unknown [94]. Therefore, an alternative approach to compute the sample modulus is to utilize the load-displacement history during the initial contact of the indenter with the sample. This alternate approach is made possible by improvements in accurately quantifying the point of initial contact,with and without CSM; these have been recently established [89, 90]. Once the effective modulus is determined from the initial elastic loading and Eqn. 2.44, the in-situ contact radius can be estimated using Eqn. 2.45. Using these protocols, it is possible to recover an indentation stress-strain curve from the measured indentation load-displacement

data using the following denitions [89, 90],

$$\sigma_{ind} = \frac{P}{\pi a^2}$$
$$\epsilon_{ind} = \frac{4}{3\pi}\frac{h_t}{a}, \tag{2.46}$$

where h_t is the total indentation displacement. Note that for purely elastic deformation the Hertzian expressions from Eqn. 2.44 can be substituted into 2.46 to yield $\sigma_{ind} = E_{eff}\epsilon_{ind}$.

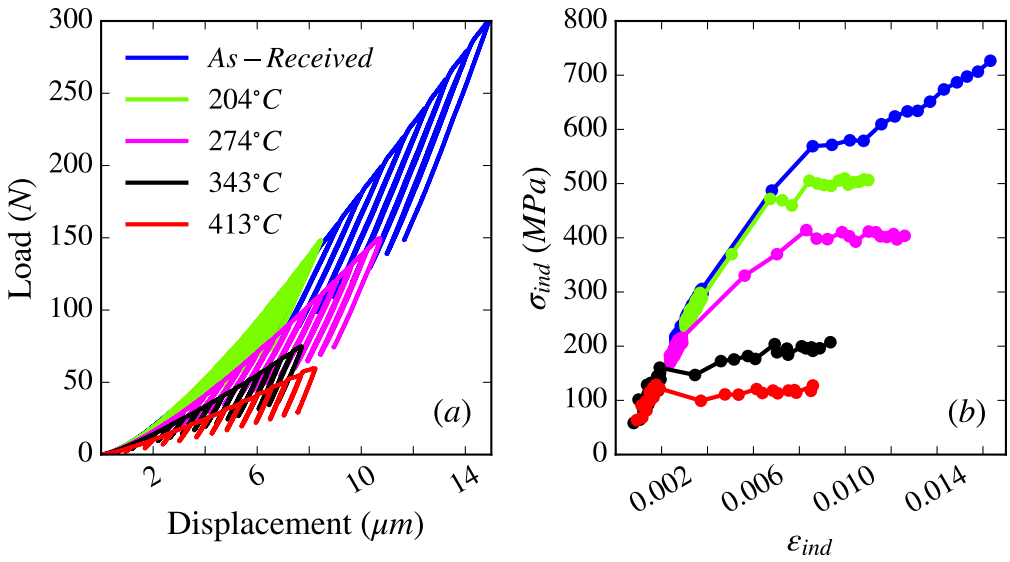

Figure 2.40: Indentation load-displacement curves and indentation stress strain curves for various heat treatments of Al-6061 [92].

CHAPTER 3

BAYESIAN ESTIMATION OF UNIAXIAL CONSTITUTIVE PROPERTIES

The first work on hardness testing was published by Mohs in 1822 as a means to quantify the relative hardness of minerals via scratch testing [95]. Subsequent advances in what is now considered traditional indentation testing were made by Hertz [96], Brinell [97], and Tabor [98]. In these tests, a relatively stiff indenter, originally made of hardened steel and subsequently with cemented tungsten carbide and synthetic diamond, is pressed into the softer material. Hardness is then determined using the peak force attained normalized by an area, generally taken as the projected area of the contact. Modern indentation techniques (nanoindentation, instrumented indentation, depth sensing indentation, etc.) have improved on traditional methods using equipment which automatically measure continuously the time histories of the load-displacement-stiffness in any complex loading-unloading imposed on the sample [99, 100].

Engineers and scientists employ indentation tests to infer a description of the indented materials underlying mechanical constitutive behavior. Hardness, however, is not an intrinsic material property but rather is an aggregate measure of resistance to deformation which includes both elastic and inelastic behavior. Nevertheless, hardness provides a practical and cost effective means to compare quickly the relative resistance to deformation of different materials, especially as a means of implementing quality control. Direct extraction of the elastic-plastic constitutive parameters (such as Youngs modulus, yield strength) is made difficult due to the multiaxial, heterogeneous, deformation beneath the indenter tip. In 1992, Oliver and Pharr proposed robust protocols for inferring the elastic modulus from the unloading slope of the load-displacement curve [94]. Since then many studies have focused on extracting post-elastic properties from instrumented indentation tests using analytical methods often supplemented with finite element analysis (FEA) [101, 102,

103, 82, 104]. Novel protocols for spherical nanoindentation have established physically consistent definitions of indentation stress and strain that provide meaningful descriptions of both elastic and post-elastic material behavior [89, 90]. Although these protocols have demonstrated remarkable reproducibility, the indentation stress-strain curves produced by these protocols do not yet connect directly with the uniaxial stress-strain curves for a broad range of materials.

Finite element analysis has been utilized extensively to simulate the indentation process [102, 103, 105, 106]. These simulations model the forward problem: given the material constitutive properties, the simulation predicts the indentation response (load-displacement curve) for a selected indenter geometry and prescribed loading. The FEA forward model is useful for identifying trends, explaining observations, and establishing appropriate protocols [105, 103]. The more practically useful inverse problem can be defined as follows: given the indentation response, infer the indented materials unknown intrinsic mechanical properties or constitutive response. A nonintrusive approach to solving the inverse problem generally seeks to utilize directly the well-established forward FEA models. This direct approach however is intractable as the inverse methodology is iterative and FEA model evaluations are computationally very expensive. Early approaches to solving the elastic-plastic inverse problem therefore focused on developing strictly analytical, computationally cheap, forward indentation models [8]. More recent work is aimed at synthesizing the information obtained from FEA results to build more robust, physically based, analytical forward mappings that were subsequently employed in an efficient inverse solution strategy [102].

For a material exhibiting isotropic plastic response, the established spherical indentation protocols can directly infer the uniaxial elastic modulus however a generalized mapping for establishing the post-elastic behavior does not exist in closed form [89, 90]. In the case of the anisotropic indentation response of a single grain, even the mapping between elastic properties and the elastic indentation response is difficult to establish. In light of the limitations associated with use of expensive forward models to obtain inverse solutions,

recent efforts have followed a two-step approach [11, 17]: (i) develop a computationally inexpensive surrogate model to emulate the forward problem, and (ii) utilize the surrogate to estimate the unknown mechanical constitutive properties from experimental data. The first work to employ this strategy together with modern spherical indentation protocols was published by Patel et al. [81]. In this work, the authors first create an elastic FEA model of single crystal indentation. The model inputs are the corresponding cubic crystal elastic stiffness constants (C_{11}, C_{12}, C_{44}) and the crystal orientation relative to the indenter; the model output is the effective indentation modulus Eeff. A reduced order model employing surface spherical harmonics as a basis was built to emulate the expensive FEA forward solution. Physical experiments were carried out using electron backscatter diffraction (EBSD) to obtain crystallographic orientation maps in a polycrystalline sample and individual grains were subsequently indented to measure the elastic indentation modulus E_{eff} in each grain. Inverse solution point estimates of the crystal stiffness constants (C_{11}, C_{12}, C_{44}) were subsequently obtained via error-minimization. Recent work has expanded this methodology to include post-elastic behavior of single crystals [82]. Note however that this methodology can be particularly sensitive to experimental noise and solution non-uniqueness. The resulting optimization problem can therefore become ill-posed with many local minima. Furthermore, establishing point estimate confidence bounds in this setting is difficult. In another work, a similar strategy employed polynomial regression to build a reduced order model, and utilized a Bayesian framework and Markov Chain Monte Carlo (MCMC) sampling to derive the crystal stiffness *densities* [107].

In this work, we propose a new methodology for solving the inverse problem of estimating the intrinsic material properties from the spherical indentation stress-strain measurements. More specifically, given the experimental indentation stress-strain data, we wish to infer the underlying intrinsic post-elastic material constitutive behavior. For simplicity, we assume a homogeneous isotropic material model and two of the commonly used parametric forms for the post-elastic constitutive behavior: perfectly plastic and power law hardening.

This idealization allows us to identify the underlying deformation behavior through the calibration of the unknown constitutive model parameters. A FEA model is used to describe the forward problem and a stationary Gaussian Process is used to build a computationally efficient surrogate model, i.e. kriging [14]. Identification of the unknown model parameters and their corresponding probability densities are established using a Bayesian inference framework and a MCMC sampling strategy.

3.1 Statistical Model

The inverse solution strategy we propose seeks to extract the tested materials unknown post-elastic constitutive behavior via a parametric calibration methodology. The intrinsic stress-strain behavior is assumed to follow a parametric form with unknown (to be determined) values of the parameters. Although recent work has addressed nonparametric identification of unknown functions, it requires greater sophistication and a complex framework [108]. Therefore, for the present application, we proceed with a parametric description of the constitutive material behavior. The indentation process is modeled using FEA, and serves as a surrogate for the indentation experiments, especially in generating the forward surrogate model. Our choice of notation follows the seminal Bayesian calibration work of Kennedy and OHagan [15]. Consider a computer experiment where, for a given input vector of material constitutive parameters, $\boldsymbol{x}$, and a prescribed indentation strain, ϵ_{ind}, the underlying FEA indentation stress-strain response, η, produces a realization of the indentation stress,

$$\sigma_{ind} = \eta\left(\boldsymbol{x}, \epsilon_{ind} | M_c\right). \tag{3.1}$$

More specifically $\boldsymbol{x}$ consists of the unknown constitutive model parameters. The underlying constitutive mode, M_c, must be prescribed as an input to the FEA model. Elastic behavior is assumed to be isotropic and follows generalized Hookes law. Post-elastic deformation is assumed to follow a simple isotropic plasticity model based on the J_2 flow

theory. Strain hardening can be expressed as

$$\bar{\sigma}_y = g\left(\boldsymbol{x}, \hat{\epsilon}_p; M_c\right). \tag{3.2}$$

where $\bar{\sigma}_y$ is the flow stress which evolves with the accumulated plastic strain $\hat{\epsilon}_p$. The inverse problem seeks to infer the unknown parameters $\boldsymbol{x}$, which in general may contain elastic and post-elastic parameters, from physical experiments.

Each individual physical experiment yields m observations of the indentation stress, $\boldsymbol{z} = \left[z_1, \ldots, z_m\right]^T$, at m values of indentation strain. Physical observations are assumed to follow model behavior but are corrupted with observation error, e_i,

$$z_i = \eta\left(\boldsymbol{x}, \epsilon_{ind,i} | M_c\right) + e_i. \tag{3.3}$$

This error is treated as an independent and identically distributed (i.i.d.) random variable that can be modeled as a Gaussian random variable with zero mean and standard deviation τ. For data with Gaussian i.i.d. errors, the log-likelihood is defined as

$$\log f\left(\boldsymbol{z}|\boldsymbol{x}, M_c\right) - m\log\tau - \frac{m}{2}\log 2\pi - \frac{1}{2\tau^2}\sum_{i=1}^{m}\left[\eta\left(\boldsymbol{x}, \epsilon_{ind,i}|M_c\right) - z_i\right]^2. \tag{3.4}$$

where $f\left(\boldsymbol{z}|\boldsymbol{x}, M_c\right)$ is the likelihood function conditional on the assumed model parameters $\boldsymbol{x}$ and model M_c. The likelihood function establishes the basis for inference as it provides a quantitative means for comparing candidate solutions of $\boldsymbol{x}$. The remainder of the inference is performed the methods introduced in Section 2.3.

3.2 Finite Element Model

A model of the elastic-plastic indentation process is needed from which we can make inferences. As inputs, the model should accept experimental parameters (friction coefficient,

indenter radius, indentation depth), constitutive material properties, and the indentation strain; the model output must produce the corresponding indentation stress. As Hertzian mechanics is limited to elastically deforming materials, a numerical approach must be utilized to account for plastic deformation in the sample. A finite element model was constructed to simulate the indentation response obtained using an indenter of radius 6.35mm. Simulations were carried out using axisymmetric models built in ABAQUS [109]. The indenter was modeled using an analytical rigid indenter. The interface was assumed to be frictionless to be consistent with Hertzian theory and because the indenter and sample surfaces in the experiment are prepared to be extremely smooth. The material was modeled as $3\,mm \times 3\,mm$ finite domain, which is sufficiently large to avoid boundary effects. The discretized mesh and corresponding applied boundary conditions are shown in Figure 3.1. Linear quadrilateral CAX4 elements were used in regions of the model where a uniform grid mesh structure was desired. Transitions in mesh density were achieved using unstructured regions with a mixture of CAX3 and CAX4 elements. A total of 35,123 elements were used in the model. Regions far from the indentation zone are coarser. A conservatively sized $400\,\mu m \times 400\,\mu m$ zone beneath the indenter, where deformations are expected to be significant, was meshed with $1\,\mu m \times 2\,\mu m$ rectangular elements towards the top transitioning to $2\,\mu m \times 2\,\mu m$ near the bottom. Near the sample surface in the contact zone, four layers of $500\,nm$ elements were used to improve the contact solution stability. Periodic partial unloading of the indenter was prescribed in the simulations to extract values of indentation stress and indentation strain using the protocols described in Section 2.8. At the beginning of the simulation, the indenter tip (not shown) was coincident with the sample surface.

3.3 Constitute Law Description

Two parametric constitutive laws were considered in this work; elastic perfectly-plastic and power-law hardening. In each case Poissons ratio was assumed to be 0.3. The strain

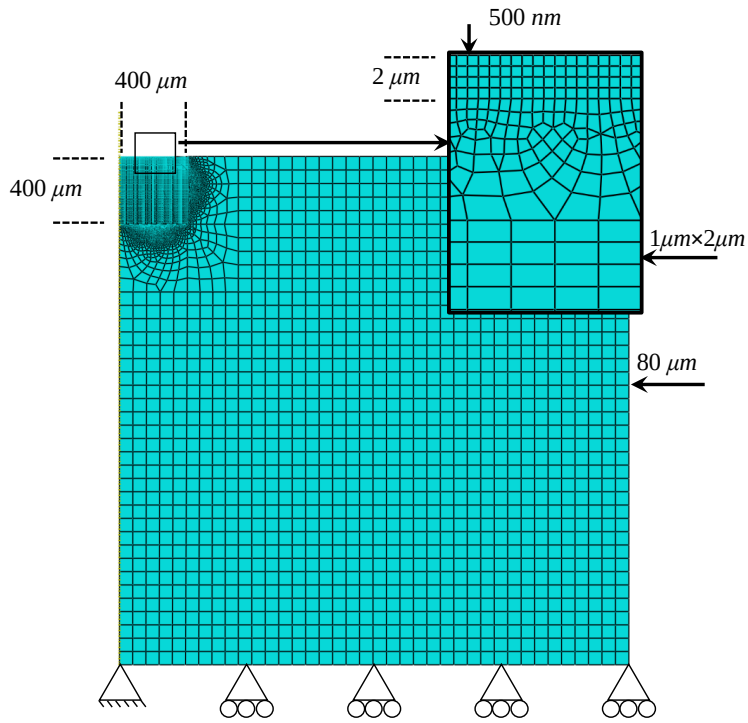

Figure 3.1: Finite element model.

hardening laws in the plastic regime are specified as,

$$\begin{aligned} \bar{\sigma} &= \sigma_o \\ \bar{\sigma} &= \sigma_o + K\bar{\epsilon}_p^n \end{aligned} \tag{3.5}$$

.

where σ_o is the initial yield stress, K is the hardening slope, and n is the hardening exponent. Note that for $n = 0$ we recover the perfectly plastic model with an yield strength of $\sigma_o + K$. Therefore, the power-law model can be considered to include the perfectly plastic condition.

3.4 Surrogate Model

The proposed sampling methodology for inferring the posterior distribution of the unknown experimental constitutive model parameters requires many model evaluations. The FEA

model used to emulate the physical indentation process is computationally expensive to evaluate; each power-law microindentation simulation conducted in this study required 25-50 hrs on 4 2.2 GHz compute nodes. Therefore a posterior sampling, which may require 10,000-100,000 or more samples, becomes computationally intractable if the forward model evaluation is performed using the FEA model. This practical limitation therefore requires employment of a computationally efficient surrogate model, which seeks to emulate the FEA model.

A surrogate model was built using a multiple output GP model introduced in Section 2.4.3. Note that in each simulation a history of indentation strains are produced, Figure 3.2. Each point corresponds to a unload during the load-displacement history. Although these periodic unloadings occur at the same displacement value the corresponding indentation strain values are *not identical* across many simulations. This is because the indentation strain is itself also sensitive to the constitutive behavior! The indentation strain is inversely proportional to the contact radius. Therefore hard to deform materials will produce smaller contact radius and higher strains for the same displacement. Hence it is clear that the Kronecker structure introduced in Section 2.4.3 cannot be directly applied. However since the values are extremely close, and FE simulations produce visually smooth curves, we interpolate all strain values onto a regular grid. This enables the use of the Kronecker structure which greatly improves computational efficiency of training the surrogate model. Validation of the model was performed on a few unused points shown in Figure 3.3.

3.5 Numerical Examples

Two numerical examples are first considered to illustrate the efficacy of the proposed approach for extracting material constitutive properties from indentation stress-strain curves. In each example simulated experiments are generated by evaluating the FEA model at a point in the parameter space which is not included in the design. Gaussian noise with 0 mean and variance 102 MPa^2, e.g. $\mathcal{N}(0, 102)$, is then added to the simulated indentation

stress history. This signal is then treated as the experimental data and the posterior distribution is inferred via TMCMC sampling. The two constitutive models previously discussed, perfectly plastic and power law hardening, are used in the examples.

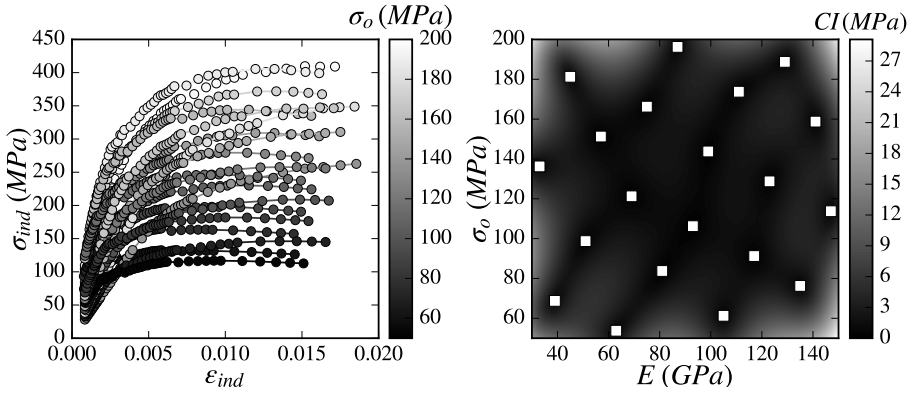

Figure 3.2: (left) Perfectly plastic finite element indentation stress-strain outputs for N=20 design. Markers filled according to yield values. (right) Corresponding maximum projection design and the universal kriging predicted 95% confidence bounds span

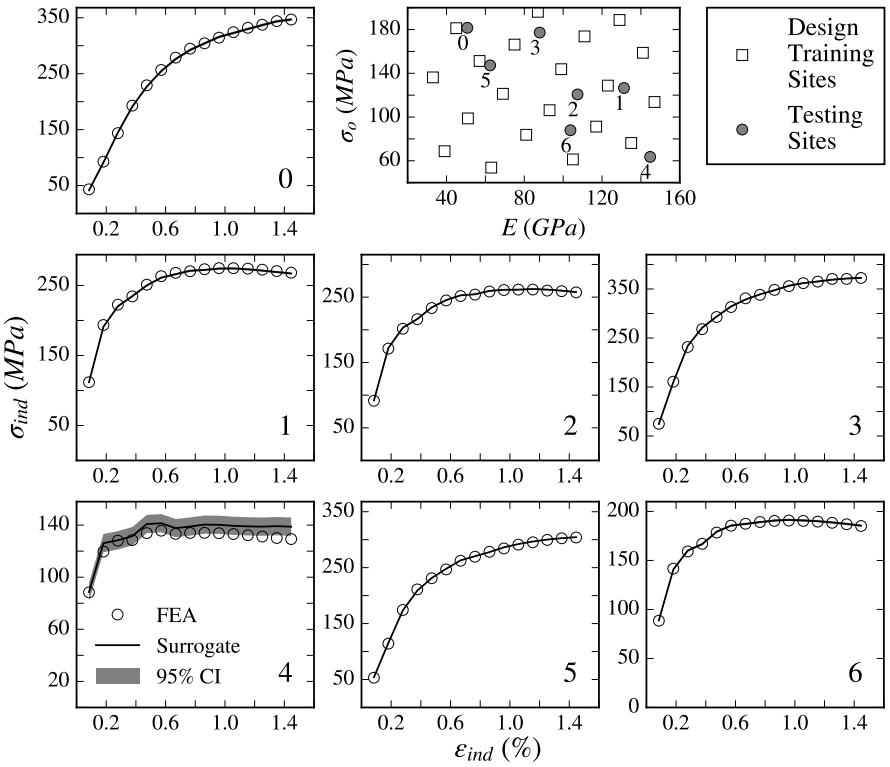

Figure 3.3: Indentation stress-strain model predictions at seven test points.

3.5.1 Perfectly Plastic

The perfectly plastic model constitutive parameter values used to generate the simulated data set correspond to $E = 107.4\,GPa$ and $\sigma_o = 120.7\,MPa$. A 20-run MaxPro design, shown in Figure 3.2, was used to build the surrogate model. In this example a uninformative prior, $f\left(E, \sigma_o | M_c\right) \sim 1$, is used over the rectangular domain $E = [30, 150]$ and $\sigma_o = [50, 200]$. The posterior kernel density, marginal histograms, and indentation stress-strain fit are shown in Figure 3.4. Also shown in the posterior density are the mean and MAP point estimates. The MAP, which identifies the location of the posterior mode, is equivalent to the nonlinear regression or nonlinear least squares (NLLS) solution in the case where uninformative priors are used. When priors are used the MAP can be interpreted as a Bayesian NLLS. The posterior 95% indentation stress-strain curve confidence interval is computed using approximations of the posterior expected value and variance e.g. $\mathrm{E}\left[\sigma_{ind}\right] = \frac{1}{N}\sum_{i=1}^{N} \eta\left(\boldsymbol{x}_i, \epsilon_{ind} | M_c\right)$ where $\boldsymbol{x}_i$ is drawn from the posterior sample.

In this example we know that the range of the 95% confidence interval associated with prediction near the MAP and mean estimates, see Figure 3.2, is $\sim 3\,MPa$ and therefore the surrogate is expected to be accurate. Despite the high expected accuracy of the surrogate the MAP and mean vary slightly from the true solution. This is expected however as convergence on the true solution is achieved only with very large experimental datasets. As there is a limited sample of experimental stress-strain pairs, about 30 points in the plastic regime, it is expected that the point estimates and true solution may not coincide exactly.

3.5.2 Power Law Hardening

Simulated data for the power law hardening case was generated from evaluation the FEA model at ($E = 175.8\,GPa$, $\sigma_o = 288.4\,MPa$, $K = 440.0\,MPa$, $n = 0.49$). A 40-run MaxPro design was used to build the surrogate model. Again uninformative priors were used in the Bayesian methodology. The posterior marginal distributions and indentation stress-strain data and corresponding sample paths are shown in Figure 3.5.

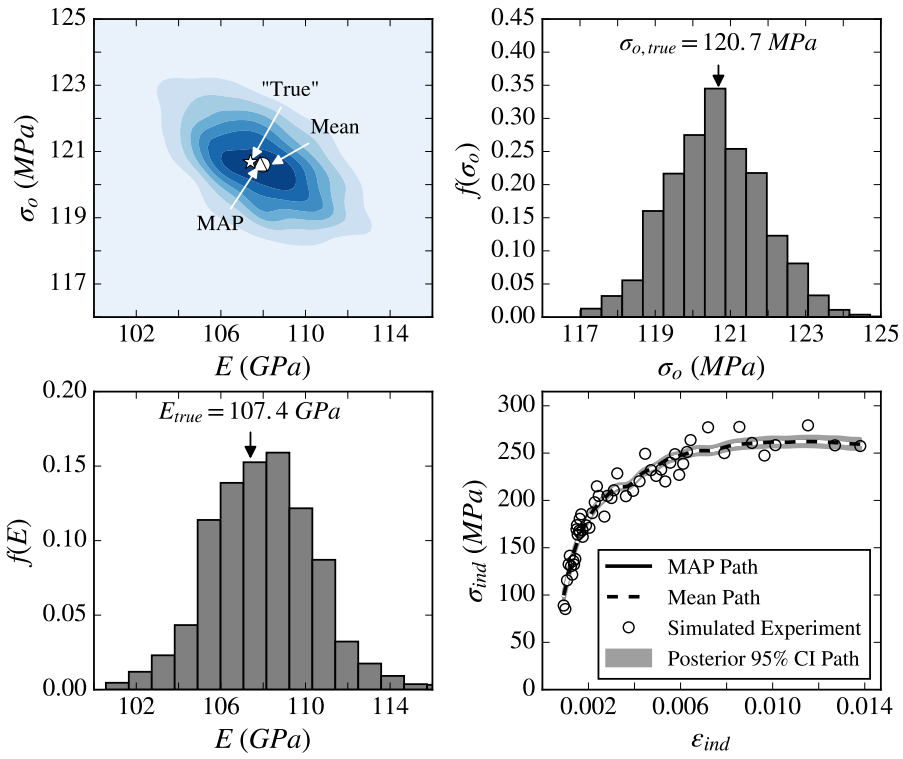

Figure 3.4: Perfectly plastic case study: posterior distribution, marginal distributions, and the model fit.

The inverse method again produces a MAP estimate that deviates from the true solution but is contained in the posterior credible region. The mean in this case however is much closer to the true solution. Note that the MAP solution can be obtained via nonlinear least squares (NLLS) type techniques commonly used in engineering but the mean can only be obtained through fully Bayesian derivation of the posterior densities. In this example, the MAP deviation may be due to a combination of two effects (1) a larger parameter space is considered in the higher dimensional power law model, and (2) the previously discussed uncertainty associated with insufficient experimental sampling. The former point may be alleviated by using a larger design and the later may be tempered by utilizing additional data. However note that the distributions for K and n are relatively more diffuse. This suggests that indentation strains imposed may not be large enough to adequately discriminate between different solutions of K and n. Therefore, it is important to acknowledge that all results are sensitive to the quality and quantity of the experimental data available and that practitioners should exercise caution in interpreting results.

3.6 Physical Microindentation Examples

A caveat associated with the numerical examples presented in Section 3.5.2 is that the underlying constitutive material model is known a-priori. In assuming a particular form of the constitutive law, M_c, we are conditioning the data on that model form. Therefore, it is expected that the inverse solutions of the numerical examples are fairly accurate given that the assumed constitutive models were used to generate the data. However in practice, the constitutive law of a tested material is not known ahead of time nor does it necessarily follow a convenient parametric form. Nevertheless, an experimental example is considered here to showcase the viability and versatility of the proposed methods in inferring post-elastic properties and quantifying the associated uncertainties. Since our FEA model, and consequently our surrogate model, assume homogeneous isotropic material behavior, we consider microindentation data generated using a $6.35\,mm$ indenter tip. The large indenter

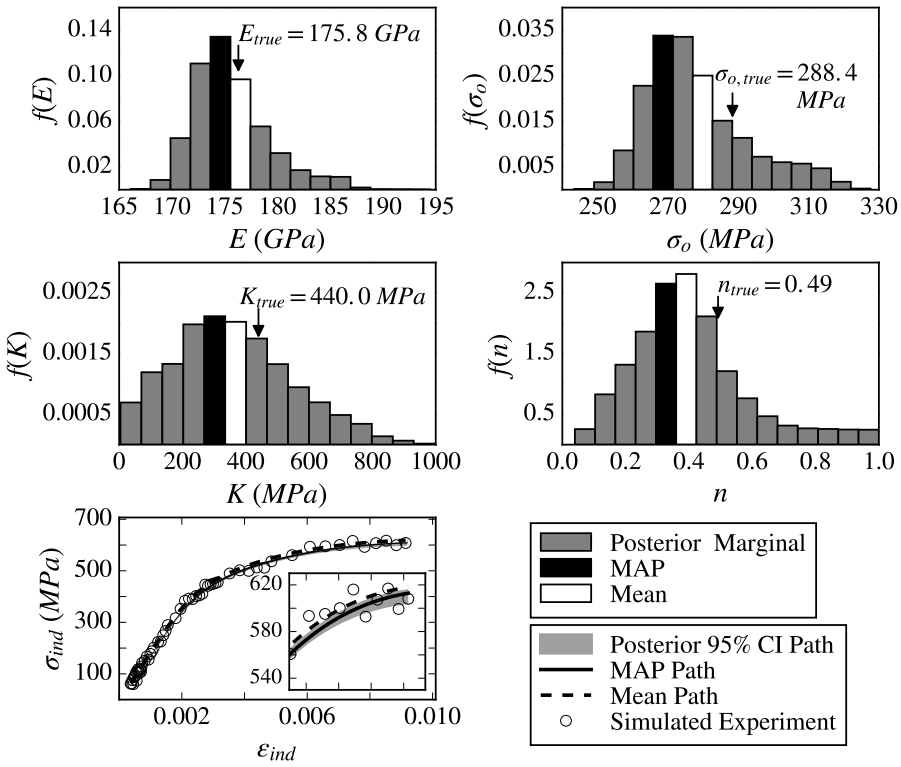

Figure 3.5: Power law hardening case study: posterior marginal distributions and indentation stress-strain fit.

tip deforms a larger volume of material which gives greater confidence that the isotropic and axisymmetric assumptions hold. Experimental data was taken from a previously published study on Al-6061 [92]; some of those experiments are shown in Figure 2.40. This dataset also contains uniaxial tension experimental data which will be used to test and validate the proposed inverse methods.

We assume the experimental noise to have a variance, τ^2, of $25^2 MPa^2$ which is a conservative estimate of what is inferred from the data. The experimental noise could be inferred from the Bayesian framework but we chose to use a frequentist point estimate for simplicity. In addition it is observed that there is larger measurement error in the post-elastic indentation stress values (i.e., heteroscedasticity), but we neglect this detail for simplicity. In each example 50,000 TMCMC samples are generated and the sampling process is tuned to achieve an optimal 30-40% acceptance rate [110] in the MCMC sampling of each annealing stage. The experimental design of the surrogate model consists of 40 points. It was found that a logarithmic transformation of indentation strains and the hardening exponent, n, improved surrogate model accuracy. A single regressor function was used to describe the mean of the kriging GP surrogate model. We found that using a scaled modified power-law model, with as the plastic component of the regressor, produced optimal surrogates. A separate 100-run MaxPro design was generated to validate the efficacy of the surrogate predictor and the corresponding root mean squared predicted error (RMSPE) associated with this validation design is $8.5\, MPa$.

Experimental data for Al-6061 comes from a study on high throughput characterization of Al-6061 subject to an aging heat treatment[92]. A microindentation experiment on a sample aged at $274°C$ for 2 hours is first considered. This treatment is fairly severe as the volume fraction of Mg_2Si strengthening precipitates decreases with increasing aging temperature. A moderately restrictive normal prior $\mathcal{N}(70GPa, 152GPa^2)$ was placed on the modulus and a much more diffuse prior $\mathcal{N}(250MPa, 1002MPa^2)$ was placed on the initial yield stress. The indentation stress-strain power law hardening solution is shown in

Figure 3.6. In order to provide a local validation of the surrogate, that is test the efficacy near the posterior solution, the FEA model was reevaluated at the MAP and mean solutions as well as at 20 posterior support points [111]. Support points correspond to a fixed number of points, selected from the posterior sample, which optimally represent the posterior density [111]. The corresponding validation sample paths and RMSPE, calculated from the 20 support points, are included Figure 3.6. In this setting the support points were used to test the accuracy of the surrogate model and inverse solution method over the span of the posterior density with a minimal number of expensive FEA model evaluations.

The reevaluated FE simulations in the high density posterior region reveal that the surrogate predictions contain some error corresponding to a RMSPE of $16.2\,MPa$. Never the less, the posterior re-evaluated FEA curves reasonably emulate the experimental trend and corresponding variance. Relevant one dimensional marginal distributions are shown in Figure 3.7 and two dimensional marginal distributions are shown in Figure 3.8. The 0.2% offset tensile yield stress is computed by evaluating the power-law expression at a plastic strain of 0.2Note that uncertainty in the inferred constitutive quantities is not influenced by the size of the experimental design (N). This is because uncertainty in the surrogate model is not considered in the Bayesian derivation of the posterior densities; uncertainty in the constitutive parameters is inherited from the experimental data and constitutive model choice. Inclusion of more physical data, or perhaps data which include measurements at larger values of indentation strain, would reduce posterior dispersion. In this case the model appears to fit the data well but in a more general setting it may be appropriate to consider a calibration formulation which also considers the possibility of model-discrepancy [15].

The Al-6061 study [92] also contains a number of uniaxial tension test results. This dataset enables a one-to-one validation against the inferred quantities of interest; uniaxial constitutive properties. Inverse results for microindentation samples treated at $274°C$ and $205°C$ were considered. Tensile test uniaxial stress-strain curve prediction intervals, inferred from the proposed methods, and results from physical tensile tests are shown in

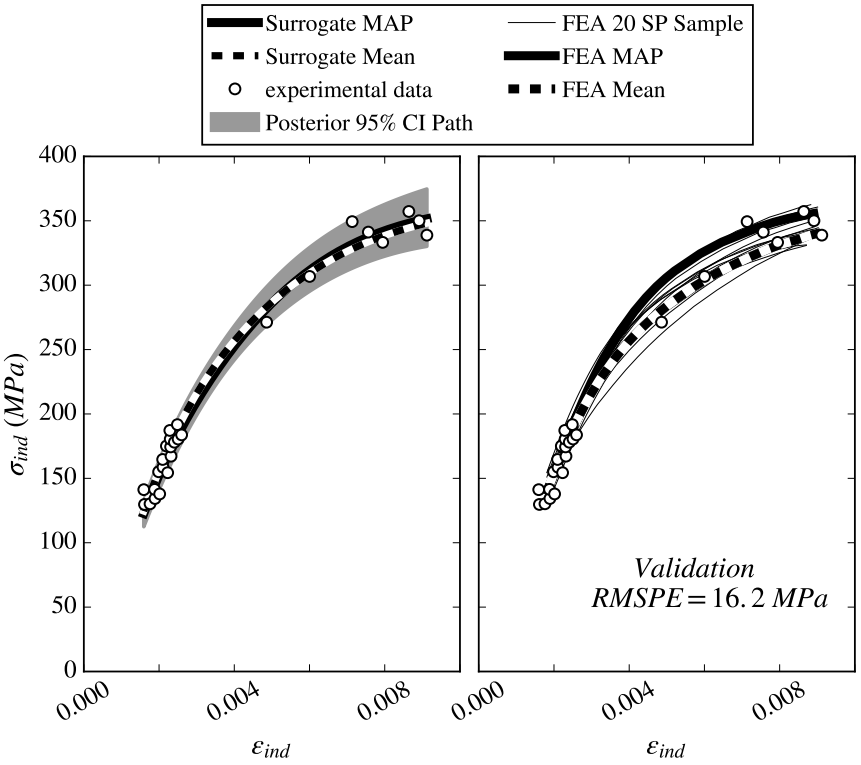

Figure 3.6: Al-6061 power law case study: (left) Solution fit using trained surrogate model (right) FEA solution evaluated at the posterior support points, posterior MAP, and posterior mean.

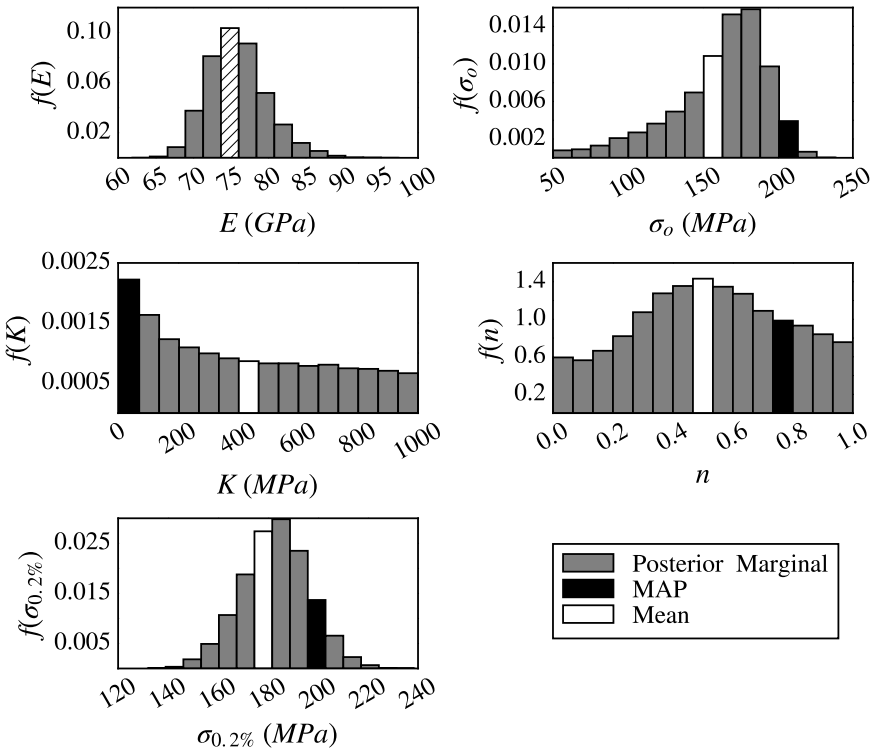

Figure 3.7: Al-6061 power law case study: posterior distributions and predicted 0.2%-offset yield stress density.

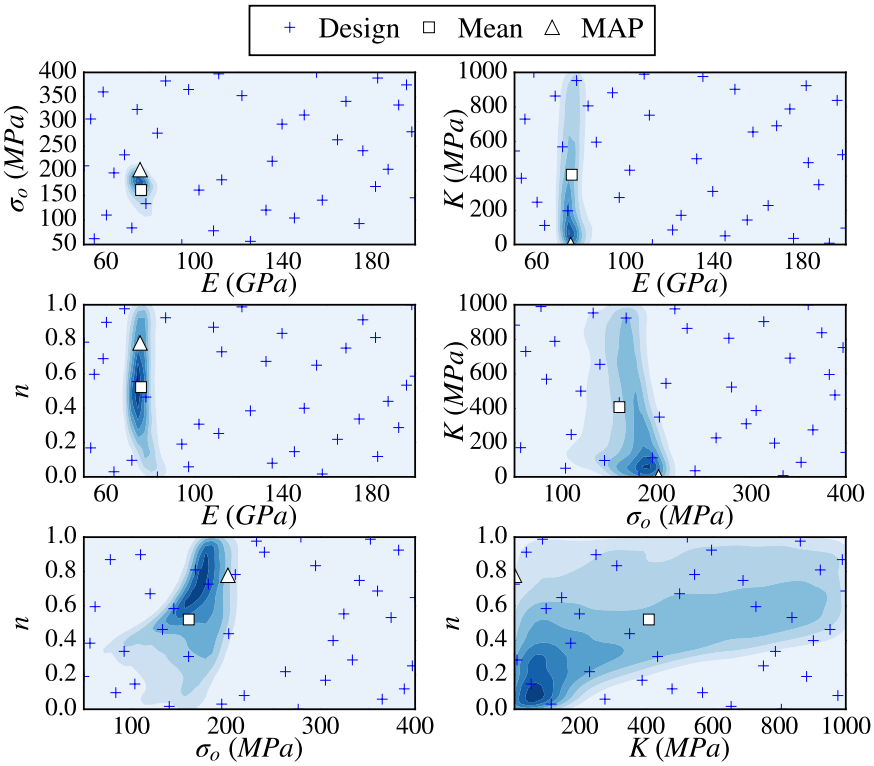

Figure 3.8: Al-6061 power law case study: 2-dimensional marginal kernel density, MAP, mean, and surrogate MaxPro design (training points).

Figure 3.9.

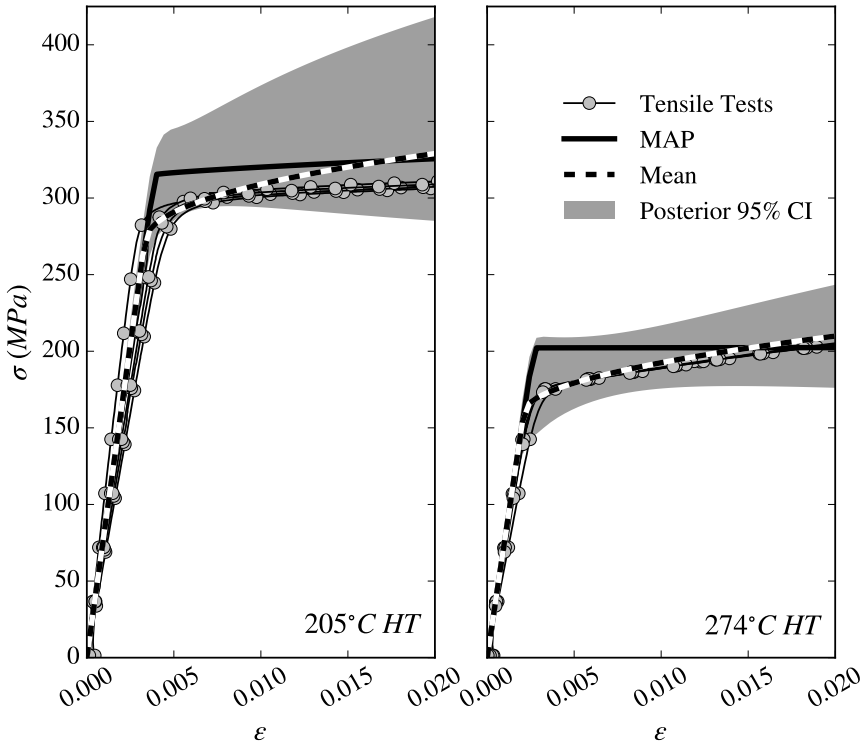

Figure 3.9: Al-6061 power law case study: tensile stress-strain curve estimates. Predictions from indentation inverse analysis and experiments from uniaxial tensile tests from [92].

3.7 Discussion

The proposed Bayesian inverse solution method is effective in identifying the power law hardening parameters, which describe the experimentally observed indentation stress-strain curves. This is evident from the posterior predictive indentation stress-strain curves shown in Figure 6 and Figure 7. Furthermore, the kriging GP model is an effective surrogate for making computationally efficient inferences from the experimental data. Validation of the surrogates for Al-6061 in the posterior high probability region was performed by running 22 additional FEA simulations; simulations at the MAP and mean estimates as well as 20 representative support point samples from the posterior distribution. The corresponding RMSPE in the high probability posterior region is 16.2 MPa which is quite good. The sur-

rogate model could possibly be made more accurate without changing the design by using more sophisticated GP models [112, 113, 114]. Alternatively, larger exhaustive designs may be used however these produce large and potentially unstable correlation matrices, $\boldsymbol{R}$, and therefore would require efficient approximate GP methods [115, 116].

Indentation stress-strain curve realizations generated from the posterior support points match the experimental curves well and produce reasonably tight bounds around the mean behavior. Although the MAP and mean estimates visually appear to produce excellent fits, it is imperative to acknowledge that many constitutive model parameter candidate sets may reasonably describe the experimental indentation observations. This is the benefit of employing a Bayesian approach; the uncertainty emanating from the experimental measurement error and uncertainties associated with model non-uniqueness may be captured in the complex posterior density.

As elastic constants (modulus) can be inferred directly from experiments, it is the post-elastic properties which necessitate statistical inference. For the Al-6061 example considered, the inverse method predicts fairly tight confidence bounds around the initial yield estimates. The results agree with previous findings suggesting that the saturated yield stress is $\sim 2\sigma_o$ [103]. The proposed inverse method builds on this earlier work by also generating the corresponding initial yield confidence bounds. Note that for Al-6061, Figure 3.7, there are values of the initial yield as low as 50 MPa with non-zero density. Although this seems physically unrealistic, note that as the effective initial yield is and not . Therefore, marginal distributions are subject to careful interpretation. With respect to the initial yield it is more appropriate to consider the posterior density of the 0.2% yield. Tensile test validation, shown in Figure 3.9, illustrates that the inverse solution is able to predict the tensile response with reasonable confidence.

The hardening behavior however appears to be more difficult to infer. Marginal distributions illustrate that K and n can take on a large range of values, all of which adequately explain the experimental observations. A physical explanation for this observation may

be found by considering the magnitude of the plastic strains generated beneath the indenter tip. Our simulations, as well as previous works [103, 105], suggest that equivalent accumulated plastic strains beneath the indenter are small ($\sim 10^{-3}$). Therefore, the uncertainty in K and n may be a result of not sufficiently sampling the plastic response of the underlying material. In the examples considered in this paper, it may have been sufficient to simply consider a single perfectly plastic material model class. The difficulty in inferring hardening behavior however may be sensitive to material system and indentation scale. Indentation stress-strain curves produced by probing Ti-6Al-4V using a $16.5\,\mu m$ indenter displayed extremely linear post-elastic hardening curves [93]. In other studies it has been shown that indentation FEA predictions using linear hardening models [103, 105] produce linear hardening indentation stress-strain curves. Therefore, although deformation mechanisms at the grain scale cannot be modeled using macroscale continuum models, it is plausible that certain scales and material systems may be more amenable towards inference of post-elastic hardening characteristics. Nevertheless, from the perspective of a designer, estimates of the posterior distribution of intrinsic constitutive parameters, despite being diffuse, are of great value. These distributions can be utilized to assess the performance of materials subject to specific applications and to quantify uncertainty propagation to various performance metrics.

It is important to note that the posterior densities correspond to inferences made using the surrogate model and not the true finite element simulations. Therefore density estimation is sensitive to surrogate model accuracy. Although convergence to the true densities is desired, doing so efficiently is difficult. One strategy to improve confidence in the predicted posterior densities is to implement a sequential design strategy where the initial design is augmented with new points in the posterior density region and the FEA model is reevaluated as these points. In this manner the surrogate fidelity is efficiently improved by only reevaluating the FEA model in likely parameter regions. For a limited number of experiments this may be acceptable, but in a setting where instrumented indentation is used for

high-throughput testing, this approach would be undesirable. In the power-law examples considered, a fairly lean 40-point design is utilized but perhaps a larger design (80-100 points) would be more appropriate. It is difficult to a priori identify the necessary design size as this quantity is dependent on the complexity of the underlying function, which is initially unknown in the field of computer experiments utilizing 10d design points is a common practice. Larger designs improve the predictive accuracy but, as discussed in the preceding discussion, the GP surrogate may become numerically unwieldy if the design grows too dense. Furthermore, it is important to recognize that even if a perfect surrogate was obtained the derived posterior densities would be still be subject to implicit assumptions inherited from the FEA model and the experimental indentation protocols. This includes assumptions and errors inherited from the constitutive material model form, yield theory, contact behavior, Hertzian assumptions, experimental identification of initial contact, etc.. Therefore, as a practical consideration, strict convergence may not be necessary to obtain informative inferences from experiments.

3.8 Conclusions

A novel method for inferring the intrinsic post-elastic material constitutive properties from instrumented spherical indentation tests was proposed in this paper. Finite element simulations of the indentation process were used to inform and train a Gaussian Process, or kriging, surrogate model. The surrogate model was used within a Bayesian inverse problem framework to efficiently sample from the posterior density of the unknown intrinsic constitutive model parameters. Experimental data were generated from instrumented spherical indentation experiments and modern post-processing protocols. Results for perfectly plastic and power law hardening parametric constitutive models were presented and both numerical and physical examples are considered. Results from the physical experiments indicate that the proposed method produces initial yield estimates that agree with uniaxial test results as well as with prior FEA studies. However, it was observed that discrimi-

nating between the hardening parameters was difficult and this was attributed to difficulty in producing sufficiently large strains during indentation. Nevertheless, quantification of the posterior material constitutive parameter densities is of great value to engineers and designers who wish to evaluate the performance of engineering components and quantify uncertainty propagation.

CHAPTER 4

PROCESS-STRUCTURE-PROPERTY MODELING USING ORIENTATION IMAGING MICROSCOPY AND DATA-DRIVEN TECHNIQUES

4.1 Introduction

Machining is a high rate severe plastic deformation (SPD) manufacturing process. The process can be described using the idealized model shown in Figure 4.1. The imposed thermomechanical loading is fairly extreme with imposed strains as large as $\gamma \sim 10$, deformation rates up to $10^5\, s^{-1}$, and cutting temperatures as high as $0.6\,\theta$ (homologous temperature) [1]. These imposed deformation conditions result in microstructure refinement in both the deformed chip and the component surface [117, 19, 23, 31, 28, 28, 20, 21]. The corresponding mechanical properties of both the chip and the workpiece surface are naturally sensitive to the produced structures [25, 19, 27, 21]. Therefore, identifying the process-structure-property relationships that characterize machining is critical for establishing a synergistic framework where designers, materials scientists, and manufacturers can cooperate to engineer functional surfaces. Furthermore, the SPD structures produced in machining bear a resemblance to structures produced in other SPD processes such as equal channel angular extrusion [118], high pressure torsion [119], and dynamic processes where shear banding may occur [120, 121, 122]. Therefore, the merit in studying machining as a high rate SPD process translates to other fields as well.

The predominant microstructure evolution mechanism in machining under ambient conditions is either continuous or discontinuous dynamic recrystallization (CDRX or DDRX) [19, 25]. CDRX is driven by the formation of dislocation cells that transform to low angle boundary (LAB) sub-grain structures, and finally relative sub-grain rotations generate high angle boundary (HAB) refined grains [25, 123]. DDRX is more closely related to classic

recrystallization where new grains nucleate and grow, often near existing grain boundaries [124]. Since the mechanism driving CDRX is driven by lattice rotations, the structure evolution can be quantified by considering measures of crystallographic misorientation [125, 43, 21, 29]. Mechanical constitutive property measurements are usually limited to hardness since the produced samples are small in scale (machined chips and workpiece surface) [25, 19, 20, 21, 27].

Materials Informatics (MI) is an emerging field within the materials community which, like cheminformatics and bioinformatics, seeks to employ statistics for addressing important domain science problems [46, 47, 37]. Materials research is conducted utilizing statistical approaches for establishing data-driven models, quantifying uncertainty, and the design and planning of experiments. MI addresses the fundamental challenge in materials research, identifying process-structure-property (PSP) relationships, by building mathematically rigorous PSP models. The models, which may be data-driven or mixed data/physics models, may then be exploited for the design of functional materials. Recent works have established reduced-order structure-property (SP) models for single phase polycrystalline systems [83, 84]. These authors utilized generalized spherical harmonics (GSH) to quantify bulk textures and used spatial statistics to quantify the spatial structure describing various simulated microstructure realizations. Another recent work utilized a deep adversarial learning model coupled with a Gaussian process (GP) Bayesian design criteria for computational materials design [126].

In this work we study the evolution of pure copper subject to a high rate SPD machining process. Microstructure is quantified using orientation imagining microscopy (OIM). A microstructure statistic which quantifies the local crystal spatial misorientation is derived. This is done by utilizing a GSH basis to describe the crystallographic orientation and a unique spatial autocorrelation function, which exploits the orthogonality of the GSH basis. Constitutive mechanical properties are quantified using spherical nanoindentation tests. Finally, a Multiple Output Gaussian Process Regression (MOGPR) model is devel-

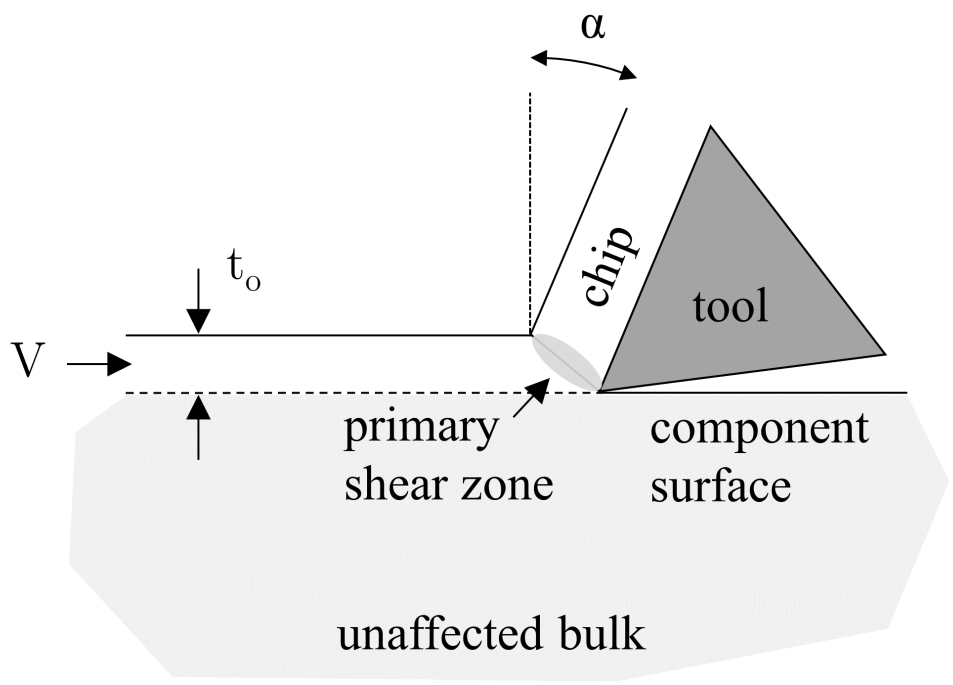

Figure 4.1: Machining process schematic. Controllable parameters include cutting speed (V), the uncut chip thickness (t_o), and rake angle (α).

oped, which captures the full PSP relationships as well as their associated uncertainties. The model is flexible and is well suited for handling multiple *kinds* of data e.g. multi-fidelity modeling.

4.2 Experimental Methods

Oxygen-free high conductivity copper (OFHC Cu) bars were obtained from a supplier (McMaster Carr). The material was subjected to SPD via a machining process. Tube turning experiments were carried out to emulate the idealized two-dimensional orthogonal cutting experiment shown in Figure 4.1. High speed steel cutting tools with nominal rake angles $\alpha = 5^\circ, 15^\circ, 25^\circ, 45^\circ$ were used for all experiments. A constant feed (or undeformed chip

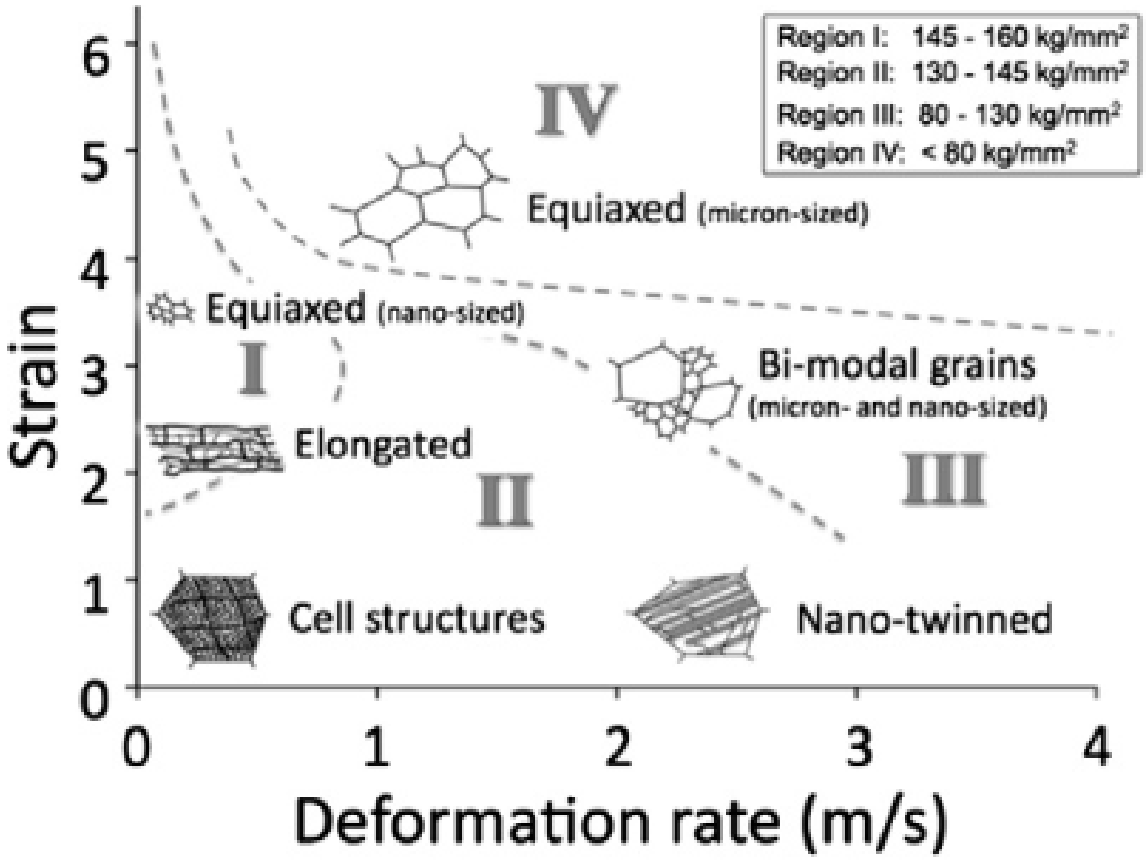

Figure 4.2: Machining process-structure-property map [20].

thickness) (t_o) of $300\ \mu m$ was prescribed for all tests. The prescribed geometry was chosen to impose large shear strains in the primary shear zone, which the machining theory predicts to be $\gamma \sim 1 - 8$ [1]. Four cutting speeds V = $0.20,\ 0.33,\ 0.50,\ 1.00\, m \cdot s^{-1}$were studied, which generate strain rates $\sim 10^3 - 10^4\ s^{-1}$. Higher cutting speeds correspondingly yield increases in chip temperatures as there is less time available for diffusion of heat away from the chip. From the measured cutting forces, the chip temperatures were estimated to reach $\sim 165°C$ for the fastest cutting speeds utilized [1]. Generated chips fell into a quench tank filled with water to freeze the as-machined microstructure.

Collected chips were mounted in epoxy and mechanically ground and polished with up to $1\,\mu m$ diamond suspension polish. Final surface preparation was performed via vibratory polishing in a Buehler VibroMet 2. A Tescan Mira XMH field emission scanning electron microscope (FE-SEM) was utilized to image the generated microstructures. A backscatter emissions (BSE) detector was utilized for all imaging as it was found to yield images with extremely good contrast (see Figure 4.3). A EDAX Hikari EBSD detector with TSL OIM analysis was utilized for orientation imaging.

Nanoindentation experiments were performed on a Agilent G200 nanoindenter with an XP head and continuous stiffness monitoring (CMS). A $100\,\mu m$ diamond indenter was used for all experiments. Spherical indentation stress-strain protocols were utilized to further process experimental data [89, 127]. The derived indentation stress-strain curves capture the mechanical response of the material deformed beneath the indenter. The corresponding contact radius for these experiments varied between $10 - 20\,\mu m$. The microstructures considered vary greatly in their refinement. Under some conditions, very fine structures ($d < 1\,\mu m$) were generated suggesting that the obtained indentation responses are likely well homogenized. Coarser structures however suggest that the local material heterogeneity may introduce additional response variation. In our analysis we will account for this when attempting to establish *mean* property quantities.

Microhardness measurements were performed using a Buehler series 1600 microhard-

ness tester. A diamond tip Vickers indenter loaded to $500g$ was used for all tests.

4.3 Methods

4.3.1 Microstructure quantification

BSE and EBSD micrographs for two different process conditions are shown in Figure 4.3. Images at larger values of the rake angle α (or smaller values of strain since $\gamma \propto \alpha^{-1}$) produced correspondingly coarser microstructures and therefore larger fields of view were required at these settings. The field of view at each setting is illustrated in Figure 4.4. The total number of raster steps in each image was maintained at 300×300 to avoid unnecessarily long scans.

In Figure 4.3, it is clear from both the BSE and EBSD scans that the microstructures are morphologically different. In the $\alpha = 25^\circ$ BSE image however it is difficult to discern which features are grain boundaries; the BSE image is sensitive to defect structures besides grain boundaries. An even clearer pattern is visible in Figure 4.4 particularly at low rake angles of 5° and 15°; with increasing cutting speed it appears as if the structure becomes *smeared*. Statistically, it can be stated that crystal orientations are more *spatially correlated* at higher cutting speeds than at lower cutting speeds. Furthermore, this pattern is also present with increasing rake angle. Consider an experiment where a point is chosen randomly in the micrograph for $(5^\circ,\, 1.00m \cdot s^{-1})$ and we note the crystal orientation at the chosen pixel and at a location 5 μm to its right. Subsequently, the same experiment is performed on the micrograph for $(5^\circ,\, 0.20m \cdot s^{-1})$. On average, over many repetitions, the two pixels from $(5^\circ,\, 1.00m \cdot s^{-1})$ would yield more "similar" orientations than in the micrograph for $(5^\circ,\, 0.20m \cdot s^{-1})$. It is this feature that we wish to quantify and exploit for assessing microstructural anisotropy.

Recent advances in the field of Materials Informatics (MI) have established statistically rigorous methods for quantifying stochastic material systems [37]. For a system with a discrete number of phases or states (e.g. ferrite/martensite, matrix/precipitate, α/β, etc.) the

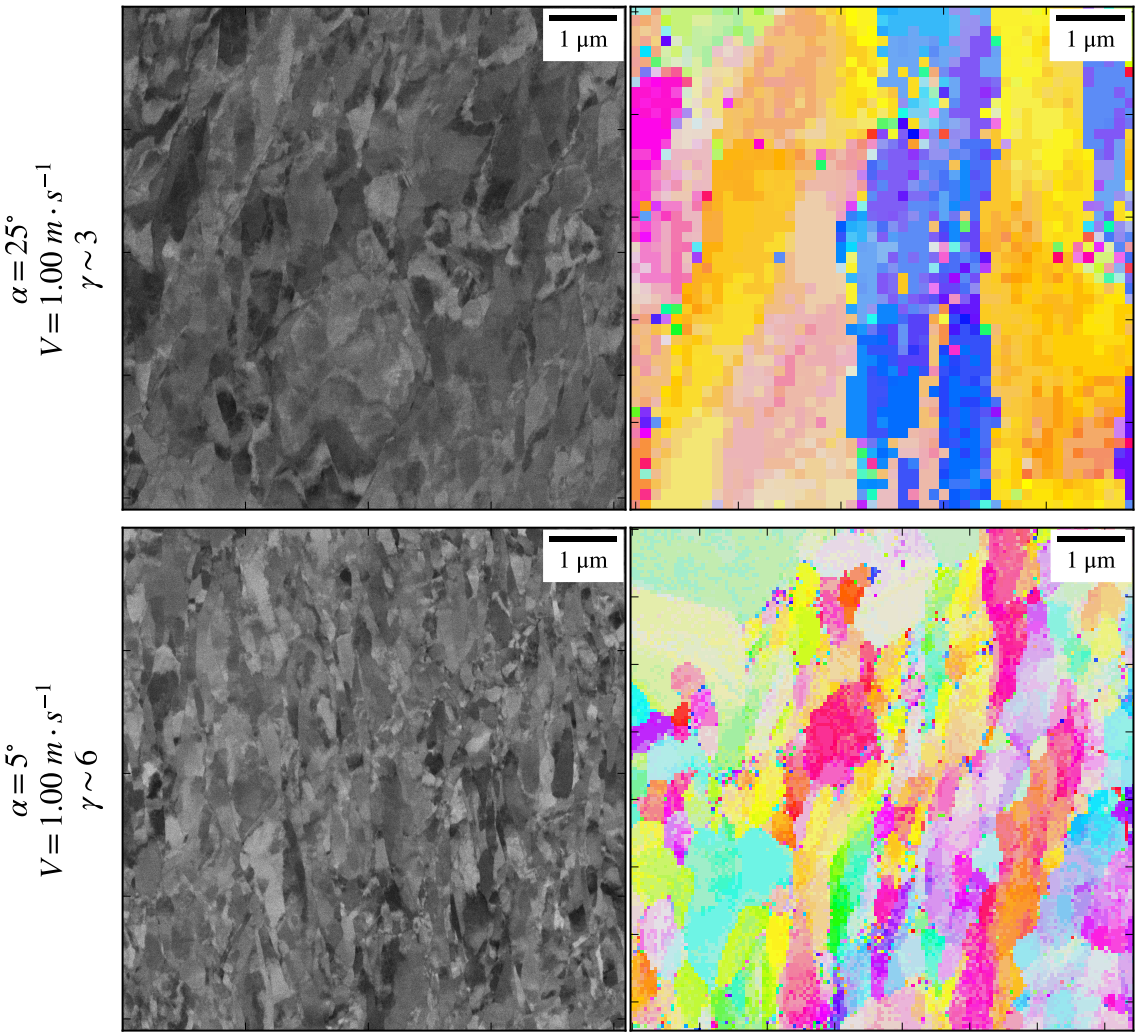

Figure 4.3: BSE-SEM and EBSD images of the generated microstructures. Top images correspond to process conditions that impose less strain relative to the bottom images. BSE and EBSD images are not coincident.

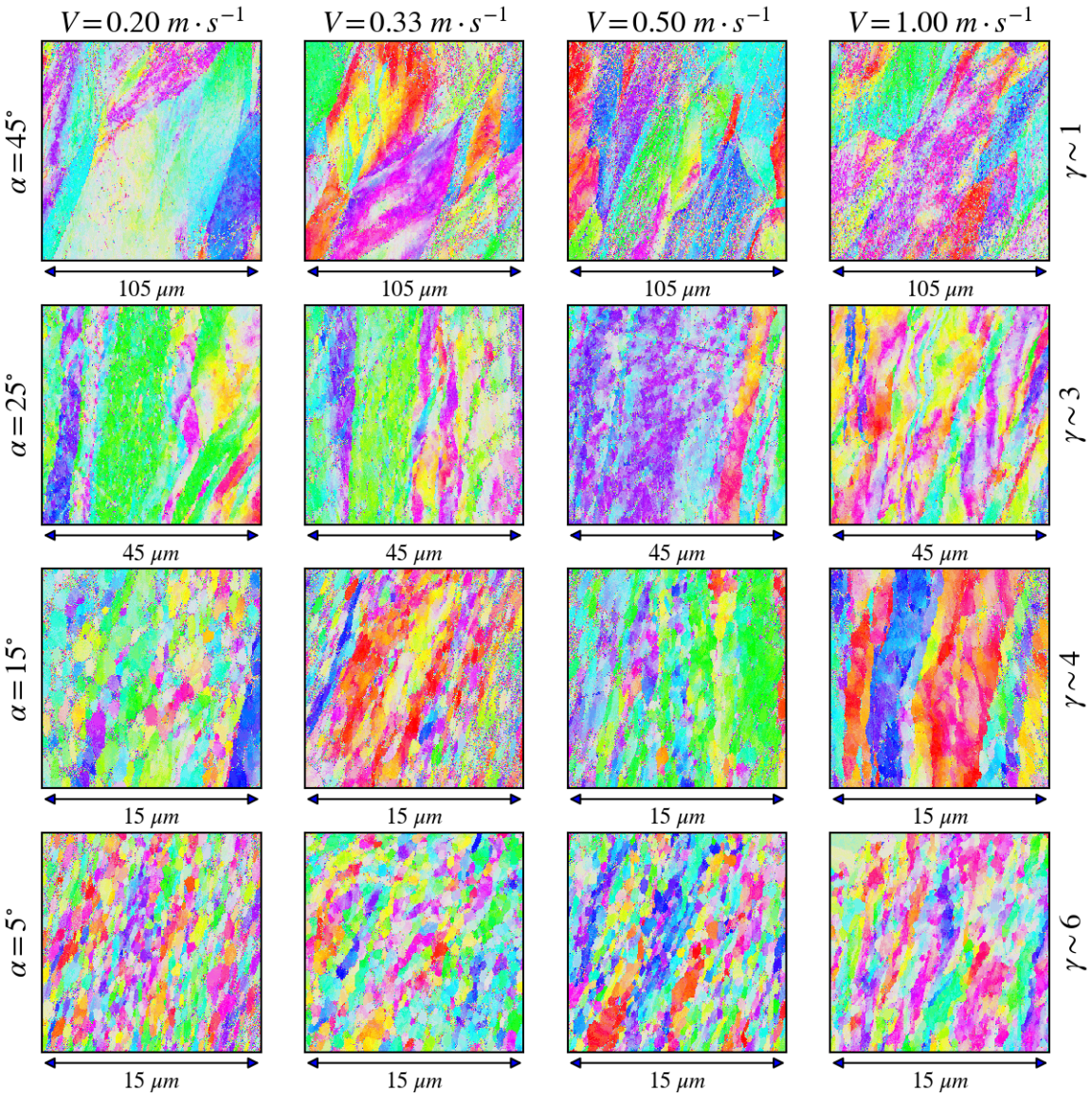

Figure 4.4: EBSD images of the various microstructures produced via machining.

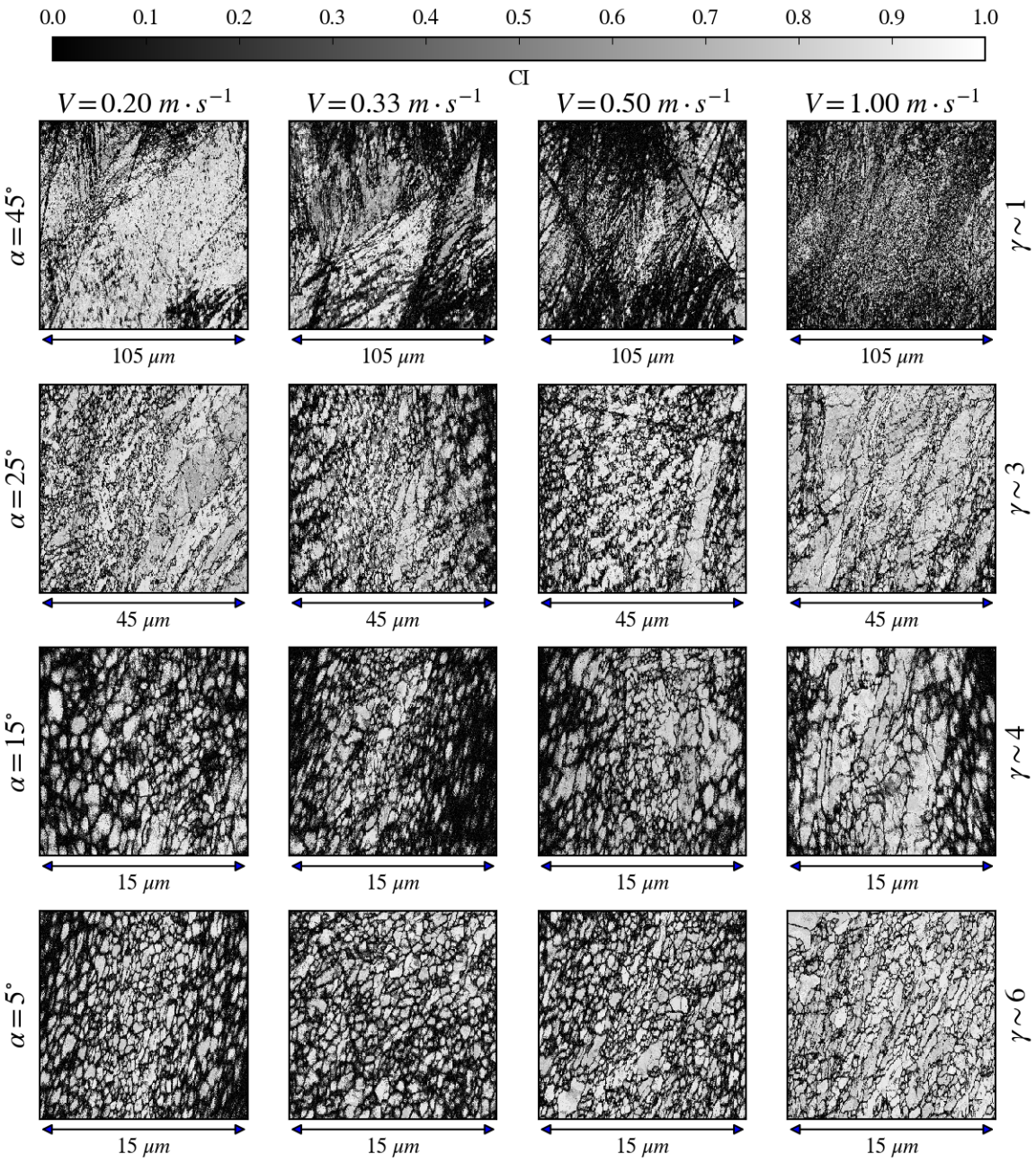

Figure 4.5: Confidence index maps corresponding to each EBSD scan.

local state h (where $h = 1, \ldots, H$) at spatial bin s can be described using the microstructure function m_s^h. This function quantifies the probability of finding state h at spatial location s. Note that s may be multidimensional e.g. pixel, voxel, etc.. Crystallographic orientation can be quantified using the Bunge-Euler angles $\boldsymbol{g} = (\phi_1, \Phi, \phi_2)$, which are continuously defined over the fundamental zone (FZ) [79]. For cubic crystals, crystallographic symmetries constrain the FZ to be defined over $0 \leq \phi_1 \leq 2\pi$, $\cos^{-1}\left(\frac{cos\phi_2}{1+cos^2\phi_2}\right) \leq \Phi \leq \pi/2$, and $0 \leq \phi_2 \leq \pi/3$. Therefore, in this setting, the microstructure function may be re-introduced as $f_s(\boldsymbol{g})$ where the microstructure state is described by the continuous variable $\boldsymbol{g}$ [87, 83].

Spatial correlations between microstructure states can be quantified through the use of spatial statistics [36, 37]. The simplest of these spatial statistics are two-point statistics. These quantities capture spatial correlations by considering the vector distance between two points. The example posed earlier in this section used two-point statistics to qualitatively describe the "spread" of crystals. Formally, the two-point statistics can be described by a conditional probability,

$$p(\boldsymbol{g}, \boldsymbol{g}'|\boldsymbol{t}) = \frac{1}{|\mathcal{X}|} \int_{\mathcal{X}} f_{\boldsymbol{x}}(\boldsymbol{g})\, f_{\boldsymbol{x}+\boldsymbol{t}}(\boldsymbol{g}')\, d\mathcal{X}, \tag{4.1}$$

where $\boldsymbol{t}$ is the vector that separates two points in the microstructure, $\boldsymbol{g}$ is the microstructure state at the tail of the vector, and $\boldsymbol{g}'$ is the microstructure state at the head of the vector. Note that if $\boldsymbol{g}' = \boldsymbol{g}$ then this quantity describes *autocorrelation*. Also note that this quantity is solely a function of the *difference* in spatial location between two points ($\boldsymbol{t}$) and therefore this definition assumes *stationarity* of the microstructure.

Consider now that we wish to obtain a compact representation of the microstructure function. There have been several works that have adopted the use of generalized spherical harmonics (GSH) for describing the microstructure function in polycrystalline systems $\boldsymbol{g}$

[87, 83, 84]. Using the GSH basis, the microstructure function can be rewritten as,

$$f_{\boldsymbol{x}}(\boldsymbol{g}) = \sum_{\mu,n,l} F_{l\boldsymbol{x}}^{\mu n} \dot{T}_l^{\mu n}(\boldsymbol{g}), \tag{4.2}$$

where μ, n, l represent multiple indices for multiple sums, $F_{l\boldsymbol{x}}^{\mu n}$ is the complex-valued coefficient at $\boldsymbol{x}$ which corresponds to the complex valued GSH basis $\dot{T}_l^{\mu n}$. Note that the $\dot{T}_l^{\mu n}$ preserve crystal symmetries and are orthogonal to their complex conjugate $\dot{T}_l^{\mu n*}$. The coefficients $F_{l\boldsymbol{x}}^{\mu n}$ can be obtained in the analogous way to how Fourier coefficients are determined (i.e. by exploiting orthogonality),

$$F_{l\boldsymbol{x}}^{\mu n} = (2l+1) \int_{FZ} f_{\boldsymbol{x}}(\boldsymbol{g}) \dot{T}_l^{\mu n}(\boldsymbol{g}) \, d\boldsymbol{g}. \tag{4.3}$$

Note that if the spatial bin occupying $\boldsymbol{x}$ (a pixel in an indexed EBSD scan) contains only one crystal orientation $\boldsymbol{g}_o$ then Eqn. 4.3 is simplified to $F_{l\boldsymbol{x}}^{\mu n} = (2l+1)\dot{T}_l^{\mu n}(\boldsymbol{g}_o)$.

Naturally, the next step is to redefine the two-point statistics using the GSH basis representation. One practical consideration is that there are an infinite number of $\boldsymbol{g}$ to chose from since it is a continuous function. In recent works, this problem is overcome by computing spatial statistics over the complex valued GSH coefficients themselves [83, 84]. The interpretation is that the different microstructure states are described by the different GSH coefficients indexed over μ, n, l. However, in this work we will introduce one additional definition which produces a different interpretation of the spatial statistics. Here we define an averaged quantity for the spatial autocorrelation, which averages over all $\boldsymbol{g}$. In doing so, information about texture is lost, but this new definition is well suited for capturing the local *misorientation* or local *morphological* spatial behavior. Therefore, we define,

$$\bar{p}_{\boldsymbol{t}} = \frac{1}{V_{FZ}} \int_{FZ} p(\boldsymbol{g}, \boldsymbol{g}|\boldsymbol{t}) \, d\boldsymbol{g}, \tag{4.4}$$

where V_{FZ} is the fundamental zone volume. Again, this quantity describes the spatial autocorrelation of crystallographic orientation *averaged* over all possible crystal orientations.

Some information (texture) is lost but the structural morphological information is retained. The advantage of adopting this strategy is that often very large scans are needed to capture texture, which is inherently a volume-averaged quantity. Therefore, texture requires a large representative volume element (RVE) to be statistically representative of the material as a whole. Conversely, local morphological features may be representative at much smaller RVE length scales.

Combining the GSH representation of Eqn. 4.2, definition in Eqn. 4.4, and two point statistics in Eqn. 4.1 the following expressions may be derived:

$$\begin{aligned}
\bar{p}_{\boldsymbol{t}} &= \frac{1}{|\mathcal{X}|}\frac{1}{V_{FZ}}\int_{\mathcal{X}}\int_{FZ} f_{\boldsymbol{x}}\left(\boldsymbol{g}\right) f^{*}_{\boldsymbol{x}+\boldsymbol{t}}\left(\boldsymbol{g}\right) d\boldsymbol{g}d\mathcal{X} \\
&= \frac{1}{|\mathcal{X}|}\frac{1}{V_{FZ}}\int_{\mathcal{X}}\int_{FZ} \sum_{\mu,n,l} F^{\mu n}_{l\boldsymbol{x}}\dot{T}^{\mu n}_{l}\left(\boldsymbol{g}\right) \sum_{\mu,n,l} F^{\mu n*}_{l\boldsymbol{x}+\boldsymbol{t}}\dot{T}^{\mu n*}_{l}\left(\boldsymbol{g}\right) d\boldsymbol{g}d\mathcal{X} \\
&= \frac{1}{|\mathcal{X}|}\frac{1}{V_{FZ}}\frac{1}{2l+1}\int_{\mathcal{X}} \sum_{\mu,n,l} F^{\mu n}_{l\boldsymbol{x}} F^{\mu n*}_{l\boldsymbol{x}+\boldsymbol{t}} d\mathcal{X} \\
&= \frac{1}{|\boldsymbol{S}|}\frac{1}{V_{FZ}}\frac{1}{2l+1}\sum_{\boldsymbol{s}=1}^{\boldsymbol{S}}\sum_{\mu,n,l} F^{\mu n}_{l\boldsymbol{s}} F^{\mu n*}_{l\boldsymbol{s}+\boldsymbol{t}}
\end{aligned} \tag{4.5}$$

where $f^{*}_{\boldsymbol{x}+\boldsymbol{t}}\left(\boldsymbol{g}\right)$ is the complex conjugate of f. Since f is a real valued function then $f = f^{*}$. This trick enables significant simplification when computing the product of the two large sums since we are using an orthogonal basis; $\int_{FZ}\dot{T}^{\mu n}_{l}\dot{T}^{\mu' n'*}_{l'}d\boldsymbol{g} = \left(2l+1\right)^{-1}$ if all the indices "match" else 0. A similar manipulation was found in [87] but in their case it was for computing localization relationships and not spatial autocorrelations. In fact, the definition introduced in Eqn. 4.4 was purposefully introduced to exploit the orthogonality found in the GSH basis similar to what was done in [87]. The final expression obtained is a function of the autocorrelation statistics (mean) derived in [83, 84]. However, our derivation can be justified with some novel physical interpretation (mean autocorrelation over all $\boldsymbol{g}$).

The final line of Eqn. 4.5 discretizes the domain over $\mathcal{X}$ into a two-dimensional binned domain over $\mathcal{S}$, which corresponds to the EBSD scan pixels. The final expression is a convolution over $\boldsymbol{S}$, which can be efficiently computed using discrete Fourier transforms (DFTs) [37]. The quantity $|\boldsymbol{S}|$ is the total number of spatial bins considered e.g. total number of pixels in a image. In this work we utilized $l = (0, 2, 4)$, which, for cubic crystals, corresponds to 10 total terms in the (μ, n, l) sum. This degree of truncation was found to be suitable in [87].

4.3.2 Feature selection and bootstrapping

The previous section describes a rigorous method for quantifying the microstructure. The mean two point statistics, $\bar{p}_{\boldsymbol{t}}$, derived however is of the same dimensionality as $\boldsymbol{t}$. Correspondingly, $\boldsymbol{t}$ is a vector that can be placed into the microstructure and hence in this case it is bounded by the size of the EBSD scans/images. Therefore, $\bar{p}_{\boldsymbol{t}} \in \mathcal{R}^{N \times M}$ where N and M are the height and width of the images measured in pixels. All EBSD scans in this work are square hence the dimensionality of each statistic derived from the images is N^2. Therefore, it is clear that for interpretability of the results some dimensionality reduction will be necessary. In this work we utilize Principal Component Analysis (PCA), which computes a statistically optimal basis for describing the full feature space. PCA has been employed successfully in many MI works for compact representation of microstructure statistics [128, 37, 129, 130, 84, 83, 91]. Dimensionality reduction is achieved by suitably truncating the basis expansion and using the basis weights (PC weights) to describe the data. This is analogous to Fourier representation of a one dimensional signal where the Fourier coefficients can compactly describe the signal.

Another consideration when constructing the microstructure feature space is the need to ensure rotational invariance of the images. Consider that small deviations in how the samples are mounted in the microscope may result in angular rotation of the images, which therefore affects the microstructure statistics. Looking ahead at Figure 4.9, careful inspec-

tion reveals that the statistics are slightly rotationally misoriented relative to one another. Failure to capture this experimental artifact could result in falsely discriminating two otherwise statistically identical microstructures. Rotational invariance is introduced by utilizing the methods found in [128]. Full details of this method are found in the referenced work and are not reproduced here.

Finally, a strategy is needed to obtain measurements of the *dispersion* of the PC weights. A naive and experimentally costly strategy would require that multiple EBSD scans be taken. From the dispersion (variance, covariance) measures, hypothesis testing could be performed or data-driven models could be built. This approach would be extremely expensive as each single scan is costly to obtain. An alternative strategy is to use the single observations and obtain dispersion estimates from *bootstrapping* of the images [88]. A similar strategy was utilized in [54] for generating statistical volume elements (SVEs).

Bootstrapping seeks to establish dispersion estimates for mean quantities by a resampling of the data [88]. It is appealing because no distributional assumptions are needed (e.g. normality). Furthermore, it can be used to obtain dispersion estimates for complicated functions of the observed data. Consider that we make N observations of a normally distributed quantity X but we want the mean and mean-variance of some complicated function $f(X)$.

In our setting, the data are the EBSD scans and the transformation is the pipeline that transforms the EBSD scans to $\bar{p}_{\boldsymbol{t}}$ and then to the truncated PC weights. Special care is also needed to preserve the spatial correlation structure present in our data. Therefore, we used aa strategy, which is analogous to bootstrapping time-series data [88]: $7.5\mu m \times 7.5\mu m$ images were sub-sampled four times and used to reconstruct a tiled $15\mu m \times 15\mu m$ image. The $7.5\mu m \times 7.5\mu m$ tiles were obtained by randomly selecting pixels from the image and then obtaining $3.75\mu m$ worth of pixels left, right, above, and below the selected point. In the case where the randomly selected pixel was within $3.75\mu m$ of a boundary the sub-sampled image was obtained by "wrapping" around the original image. For comput-

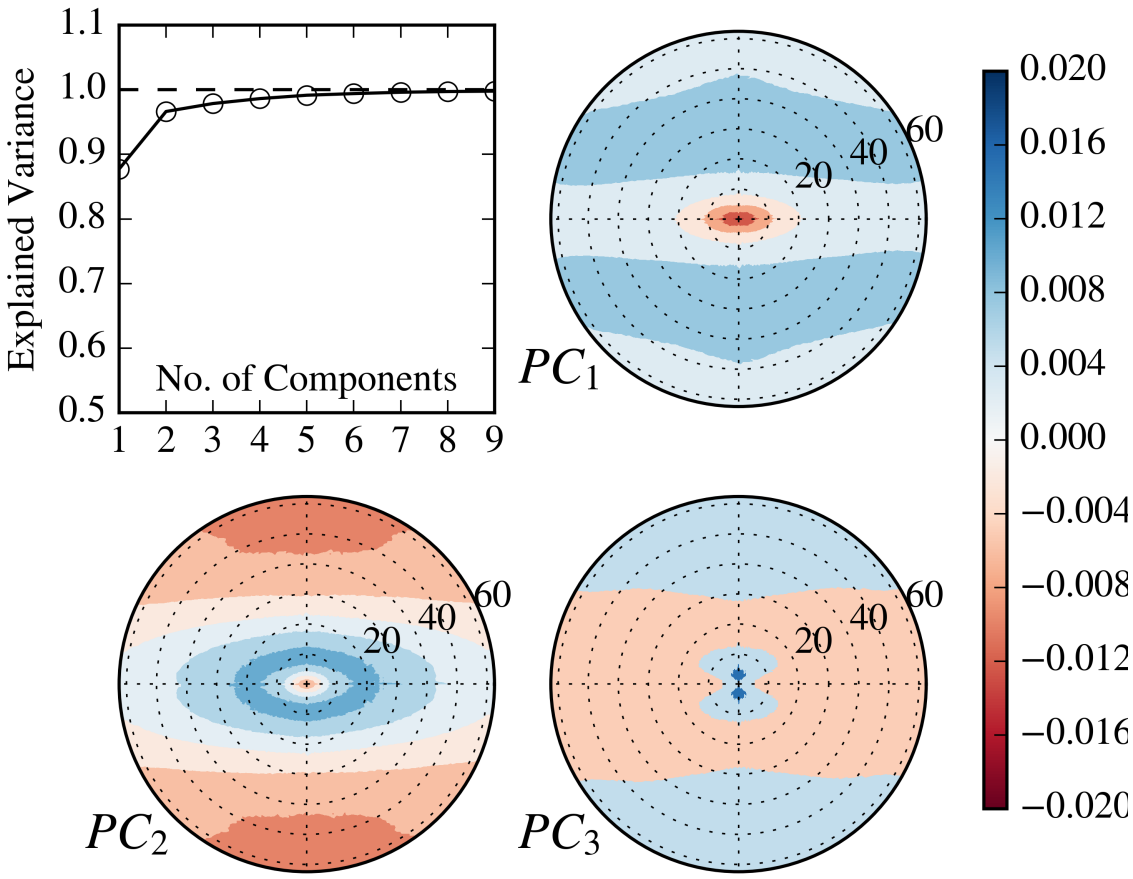

Figure 4.6: Rotationally invariant mean spatial crystallographic autocorrelation basis and accumulated variance explained statistics.

ing spatial statistics this is acceptable since the convolution in Eqn. 4.5 assumes periodic boundary conditions, which is equivalent to assuming that the image "wraps" around itself. This is shown schematically in 4.7. Each resampled $15\mu m \times 15\mu m$ image corresponds to a single bootstrapped sample. For each setting, 500 bootstrapped samples were generated. The entire ensemble was then utilized to establish a PC basis and the corresponding PC weights for each bootstrapped sample were determined. The mean and variance of these bootstrapped PC weights were utilized to establish the mean and mean-dispersion at each unique process setting.

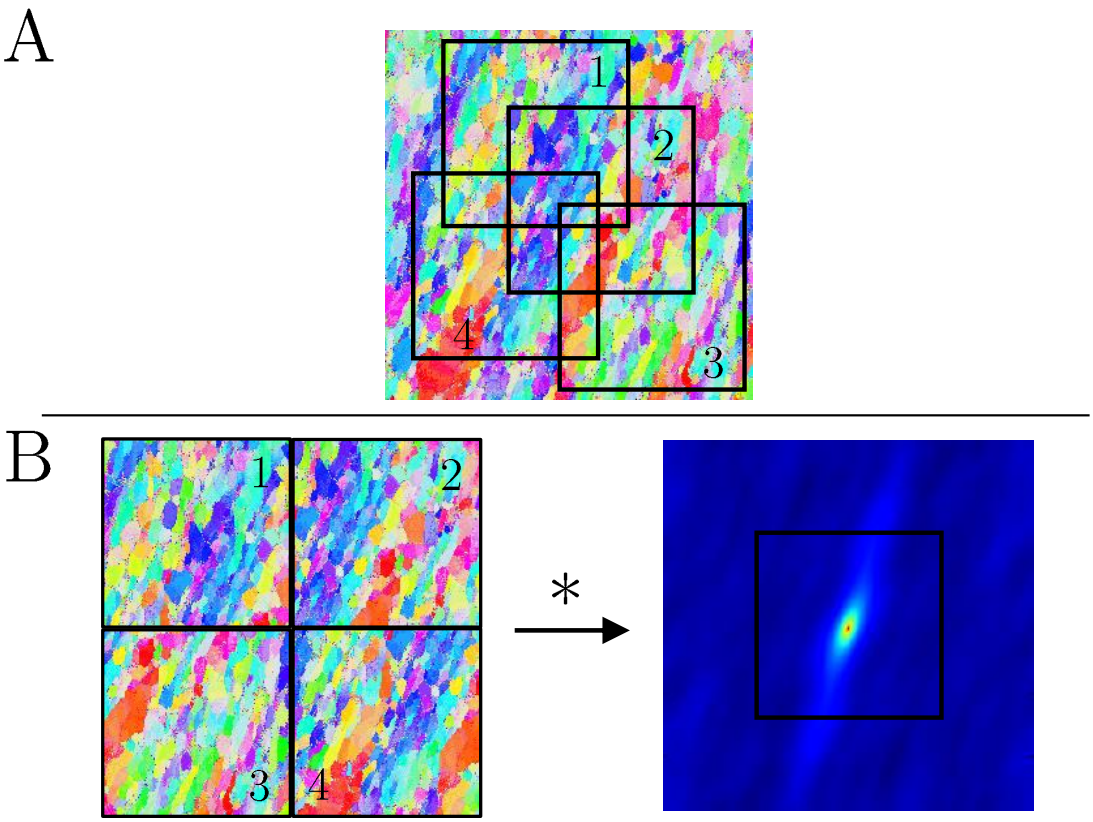

Figure 4.7: Bootstrapping schematic for estimating confidence bounds on mean feature statistics. (A) original EBSD scan and corresponding random samples (B) reconstruction from random sampling and associated bootstrapped mean spatial crystallographic autocorrelation $\bar{p}_t$ sample.

4.3.3 Multiple output Gaussian process regression

A data-driven model is needed to efficiently map the controllable process parameters to the material properties of interest. In this setting, the structure behaves as an intermediate variable, which fundamentally controls the physics and is responsible for the exhibited properties. A statistical interpretation is that the structure variable is a *latent* variable; it is critically important but is either not possible to observe or perhaps can only be observed with great effort. This is an important consideration when identifying the relevant length scales and corresponding salient microstructural features. For instance, consider that TEM micrographs are rich with information at the lowest length scales but are costly to obtain. Conversely, optical micrographs are relatively easy to obtain but may have limited utility for certain problems, which are dependent on the lower length scale physics. Process-property models can sometimes capture the underlying relationships [131], however, inclusion of structure into the modeling pipeline is preferred [37]. The justification is that structure physically governs the underlying behavior and inclusion of such information may alleviate potential ambiguities associated with non-unique process-property mappings.

Modeling of PSP relationships traditionally follows a sequential strategy where the process-structure (P-S) and structure-property (S-P) relationships are established independently of one another and combined in sequence [91]. This is illustrated in the top of Figure 4.8. A difficultly associated with such a framework is that it is not straightforward to quantify uncertainty propagation between P-S and S-P models. The P-S model accepts process parameters as inputs, which are considered to be deterministic. The output microstructure estimates are naturally stochastic since the microstructure observations are stochastic. Computing confidence bounds for the output microstructure estimates is trivial in most statistical frameworks. Additional care however is needed in the subsequent S-P modeling step when transferring forward stochastic structure estimates. As was just argued, the P-S outputs are stochastic and hence the S-P inputs are stochastic. However, most data driven models assume the model inputs are deterministic.

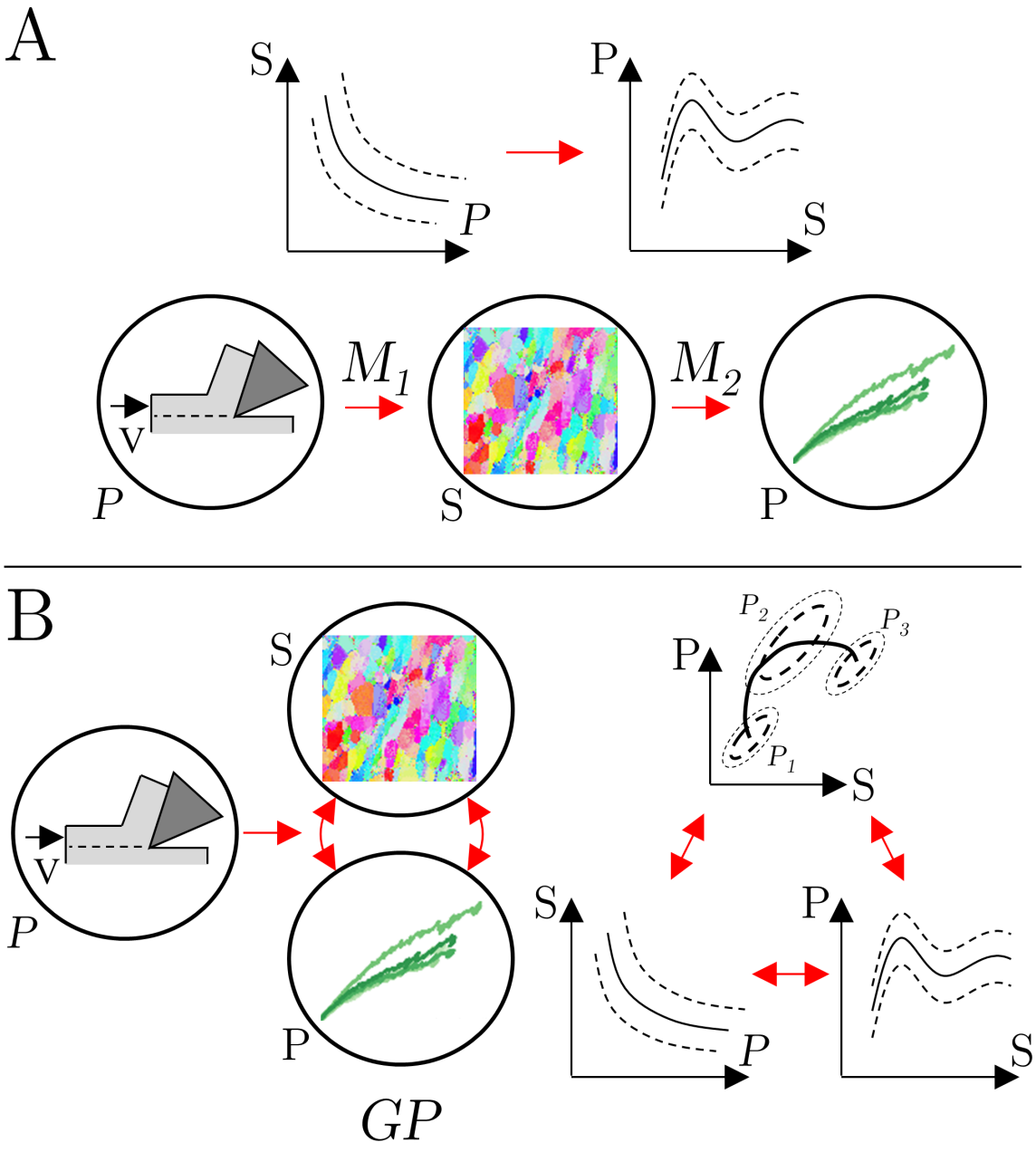

Figure 4.8: Schematic of two modeling strategies for establishing PSP-linkages. Note that italicized *P* refers to the process and normal font P represents properties. (A) A sequential strategy where process-structure and structure-property models are built independently and predictions flow sequentially, (B) jointly developed model using multiple output GP structure, which captures possible cross-correlations in the structure-property structure.

Another limitation of the sequential PSP modeling strategy is that information is not *shared* across the P-S and S-P models. Consider that the model of interest is actually the full PSP model. This model is of course built using the two P-S and S-P sub-models, which are established independently. A better PSP model could perhaps be established if the P-S and S-P models were built concurrently or perhaps with iteration; the best P-S and S-P models established independently may not produce the best PSP model.

Gaussian process regression (GPR) is a non-parametric curve fitting technique [132, 14]. Unlike traditional linear and nonlinear regression, non-parametric methods do not require a priori knowledge of the trends' functional form. Instead, the data is assumed to come from a Gaussian data generating process where observations, y_i and y_j, may be correlated based on their proximity to each other, $\boldsymbol{x}_i - \boldsymbol{x}_j$. Future predictions, $y(\boldsymbol{x})$, can be shown to be a weighted average of all the $[y_1, \ldots, y_N]$ where the weights depend on the proximity of $\boldsymbol{x}$ relative to all observations in the dataset $[\boldsymbol{x}_1, \ldots, \boldsymbol{x}_N]$. The final form of the GPR statistical model is closely related to kernel regression and smoothing methods [133, 132].

In regression, the statistical inference or learning is performed by optimally estimating the unknown regression coefficients. In the GPR setting the inference is performed by estimating the unknown *hyperparameters*. These quantities define the *correlation structure*, which is embedded in the collected observations. For instance, correlation length scales are used to precisely quantify the relative measures of "proximity" mentioned above. In some problems $x_i - x_j = 1$ may be an insignificant difference yet in other instances this may be large.

In this work we attempt to address both these considerations by utilizing a multiple output Gaussian process regression (MOGPR) model for simultaneously identifying the full PSP model (Figure 4.8B). Multiple output implies that y need not be a scalar. This model choice offers several promising features not available using a sequential strategy. Firstly, structure and properties are modeled together as a function of process inputs us-

ing a multivariate normal structure to quantify structure-property correlations. In this way process-property is possible however the model will also infer possible structure-property correlations when present. The structure-property cross-correlation jointly considers the full PSP linkage rather than independent sub-models. Secondly, quantifying the S-P variables simultaneously in a multiple output setting allows for easy uncertainty quantification of all relevant quantities including their cross-correlation structure. Finally, the MOGPR framework is flexible in its treatment of data and enables the inclusion of partial datasets with missing data. For instance consider a study where there are two microstructure descriptors. One is obtained using efficient experiments such as optical microscopy. The other descriptor is obtained using TEM and is therefore costly to acquire. The dataset may therefore contain many times more optical images than TEM images. However, in establishing the S-P linkages standard regression models require *both* covariates for each individual property measurement. Clearly, such a framework cannot pair the two descriptors since one is much more numerous! The state of the art in this setting is to implement a *transfer learning* model which enables sharing of information between the two *kinds* of data [134]. The MOGPR model can automatically accommodate this.

4.3.4 Multi-fidelity property modeling

In this work, structural descriptors come from the PC-weights of the mean crystallographic autocorrelation function ($\hat{p}_{\boldsymbol{t}}$). Property measurements are obtained using spherical nanoindentation. The indentation stress-strain yield strength is used to quantify material strength [89]. The fraction explained variance (Figure 4.6) illustrates that two PC components capture 97% of the variance. Therefore, in this study $M = 3$ where $M = 1, 2$ are the first two PC-weights and $M = 3$ is the indentation yield e.g. the MOGPR model represents the vector (PC_1, PC_2, Y_{ind}). Y_{ind} has some physically meaningful interpretation but is a somewhat noisy observation (see Figure 4.17). This variation is inherited from various sources including microstructure and surface characteristics. In Figures 4.3 and 4.4 it is clear that

the indenter could possibly engage different crystallographic orientations from test to test. Furthermore, there is also morphological heterogeneity across microstructures as seen in Figure 4.5. Although the final contact radius using a $100\mu m$ indenter is on the order of 10-15 μm, the contact radius is at the yield point roughly 1-2μm. Even using a larger $500\mu m$ indenter would not produce RVEs of crystallographic orientation and larger indenters (the next available indenter is 1500 μm) are not feasible due to the load-limits of the machine and the size of our samples (the smallest is 500 μm in thickness). A brute-force strategy would require EBSD imaging of every SVE indentation site, which is experimentally costly. Finally, the response is sensitive to nano-scale asperities, which introduces variation in the form of noise.

Therefore, in this work our strategy is to simply homogenize over these effects and therefore we have conducted many repeated indentation experiments for each unique process setting. However, a complimentary strategy is available that allows the combination of nanoindentation data with cheaper lower-fidelity property data. In the statistics community this is refered to as *multi-fidelity* modeling [135, 136, 15]. For this work we consider the Vickers microhardness (HV) as a cheap property measure. The justification is that the spherical indentation stress-strain protocols enable granular interpretation of both elastic and post-elastic behavior of the indented material whereas hardness does not. Nevertheless, microhardness is easy to obtain and therefore may aid in bolstering confidence in our inferences. Additionally, the hardness data is less noisy because it is less sensitive to the previously described heterogeneities since the volume of material probed is much larger; diagonals produced during indentation at 500g load were on the order of 80-100 μm. A key assumption here is that Y_{ind} and HV follow the same trends. We will introduce some flexibility, however, in case they do not follow the same trends or if they do not follow the same trends under certain process settings. The necessary statistical framework for incorporation of multi-fidelity property data may be found in A.

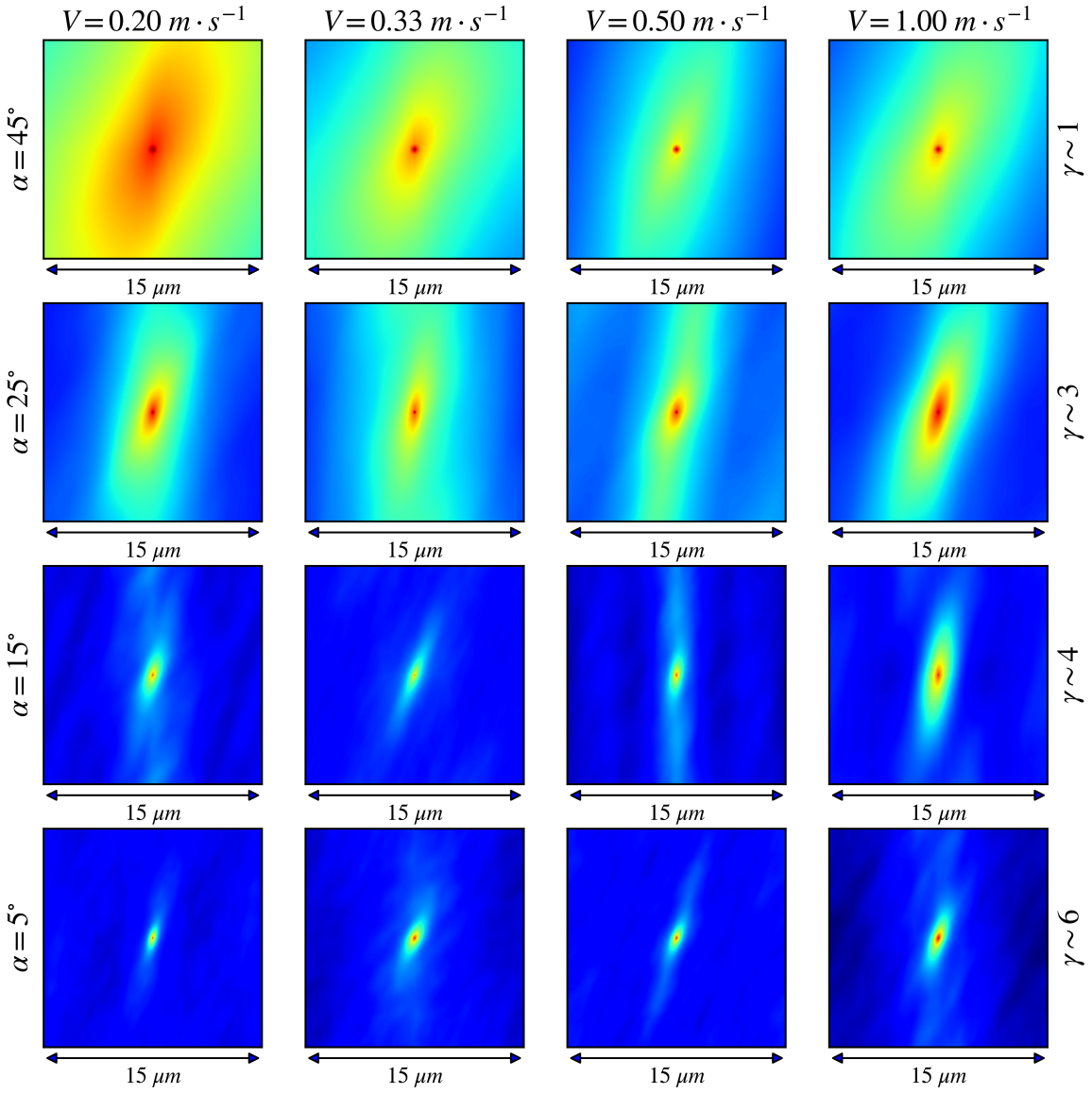

Figure 4.9: Mean spatial crystallographic autocorrelation $\bar{p}_t$ for each process setting. Note that for direct comparison of these statistics must be over the same length scale therefore larger image statistics cropped down to 15 μm.

4.4 Results

The mean crystallographic autocorrelation for each micrograph is shown in Figure 4.9. Note that these autocorrelation statistics are *empirical* quantities as they are computed directly from the data using Eqn. 4.5, which is free from any parametric assumptions. It is important to acknowledge this as subsequent modeling is performed by directly comparing these statistics and therefore the same field of view (FOV) must always be used. All the statistics shown in Figure 4.9 have a field of view of 15 μm. Therefore, images obtained at $\alpha = 25°, 45°$, which have FOV of 45 and 105 μm, were sub-sampled. The analysis therefore does not consider autocorrelation information available at larger correlation lengths in these images. However, this "clipping" is necessary to maintain identical scales across all the empirically computed autocorrelations.

Bootstrapped samples of the rotationally invariant mean crystallographic autocorrelation are shown in Figure 4.10. Recall that 97% of the variance can be captured with a truncated PCA expansion using only two principal components, see Figure 4.6. Also shown in Figure 4.10 is the predicted MOGPR path in PC-space. The bootstrapped samples visually appear to generate scatter close to a bivariate normal distribution. Both the degree of scatter and the correlation in the scatter varies for each unique process setting. Therefore, the components of the observation error covariance matrix, $\boldsymbol{\Sigma}$, which correspond to these structural variables were prescribed using frequentist estimates for each unique process setting. This simplification is justified since the scope of our work is to quantify and model *mean* quantities. Additionally, bootstrapping is an effective method for estimating the dispersion of statistics and therefore the hyperparameter inference in Eqn. 2.29 can be simplified. Furthermore, since the repetitions themselves only capture dispersion information of the data, and the observation error is specified, it is only necessary to utilize the mean value structure variables, $\boldsymbol{P}\bar{\boldsymbol{C}}_i$, when building the MOGPR model. This final point saves a great deal of computational burden associated with inverting $\boldsymbol{C} + \boldsymbol{\Sigma}$. This simplification requires only

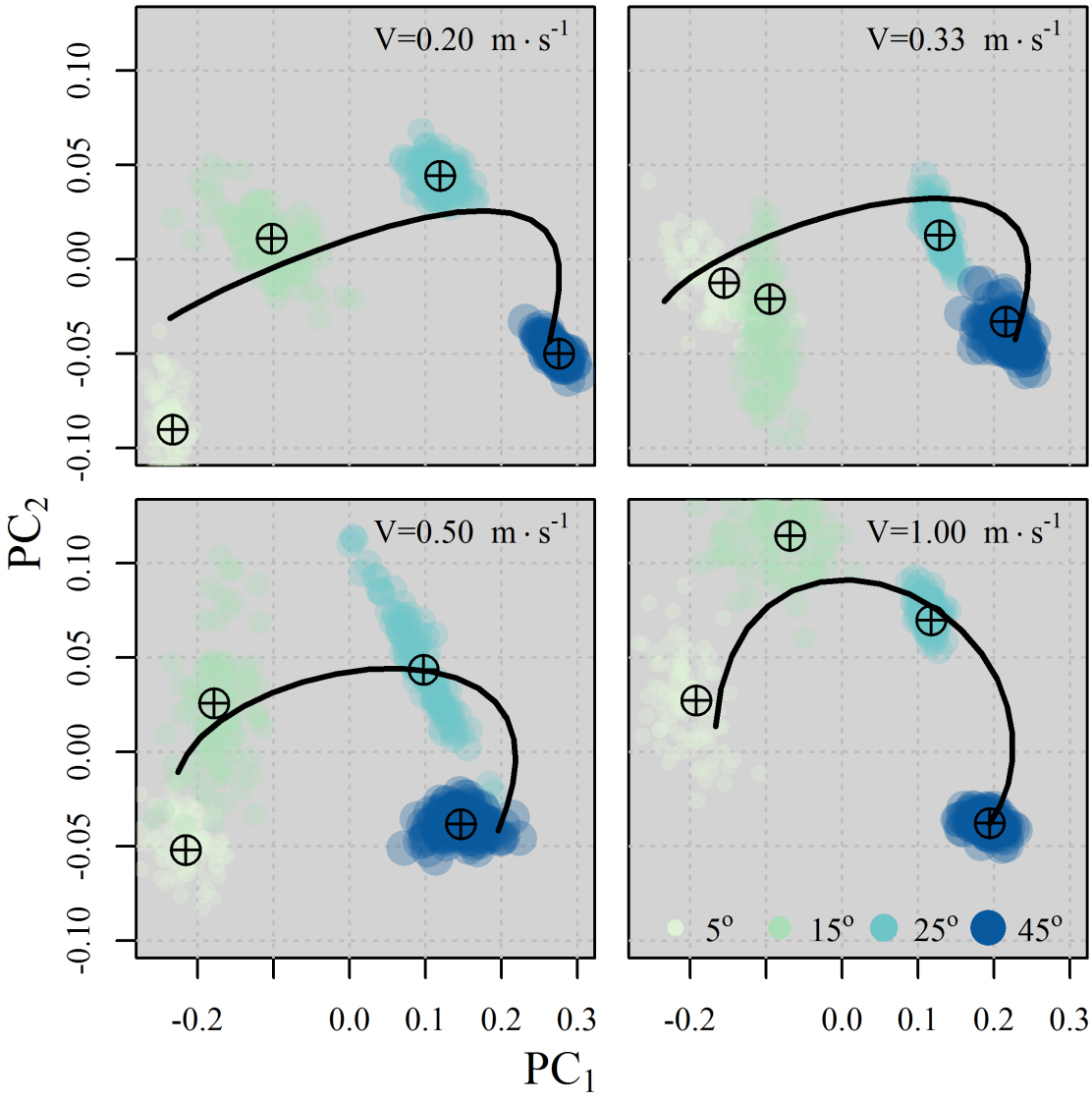

Figure 4.10: Mean PC_1 and PC_2 evolution over process settings and GP model path prediction. Shown data are the 100 bootstrap samples at each process setting and each corresponding mean ($\oplus$).

16 two-dimensional mean values rather than the full data set.

In Figures 4.11 and 4.12 the structure-property relations are shown. Note that structure-property data are not paired; there is not a "corresponding" property measure for each micrograph. Visualization however requires pairing and therefore the mean values and the associated confidence intervals are shown for experimental data. The mean MOGPR path and the confidence *region* are also shown. Note that there is a clear distinction between the confidence region of the mean and confidence region of future observations. Future observations will also contain some observation errors and would therefore have a correspondingly larger confidence region. At $V = 1.00\ m \cdot s^{-1}$ the trends appear to change despite the behavior being fairly consistent across cutting speeds $V < 1.00\ m \cdot s^{-1}$. This experimental setting corresponds to the largest imposed temperatures since $\Delta t \sim 1/V$ and hence there is less time available for conduction of heat away from the generated chips [1].

Process-structure relationships are shown in Figures 4.13-4.16. It is clear that the rake angle, α, has the greatest influence on the generated structures. This agrees with intuition as α controls the geometric configuration of the experiment and therefore has the greatest impact on the imposed shear strains γ. Deformation conversely drives structural refinement and evolution via the DRX mechanism [19].

Finally, the process-property maps are shown in Figure 4.17. Note that process-property *implicitly* considers structural relationships via the MOGPR model. The Vickers hardness data generally follows trends similar to the indentation yield. At the highest cutting speed, $V = 1.00\ m \cdot s^{-1}$, there is a significant decrease in hardness/strength going from $\alpha = 15^{\circ}$ to $\alpha = 5^{\circ}$. This is only observed at the highest speed, which suggests that physically this anomalous behavior is driven by thermal effects.

4.5 Discussion

The proposed mean crystallographic autocorrelation spatial statistic is an effective measure of microstructural morphology. The power of this metric is that it quantifies morphology

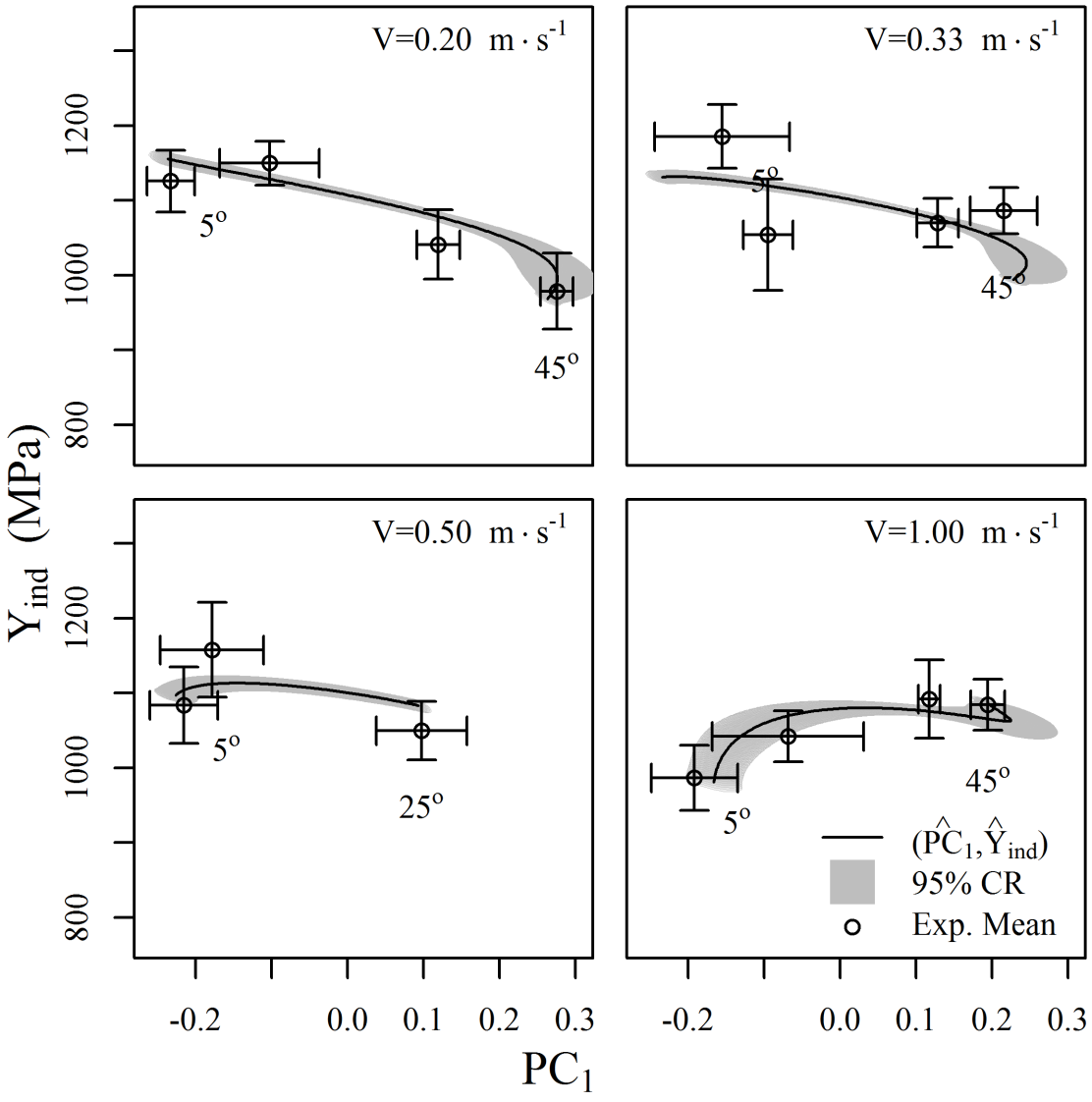

Figure 4.11: Mean PC_1 and Y_{ind} evolution over process settings and GP model path prediction and 95% confidence region. Error bars correspond to mean variation for Y_{ind} and the bootstrapped variation for PC_1.

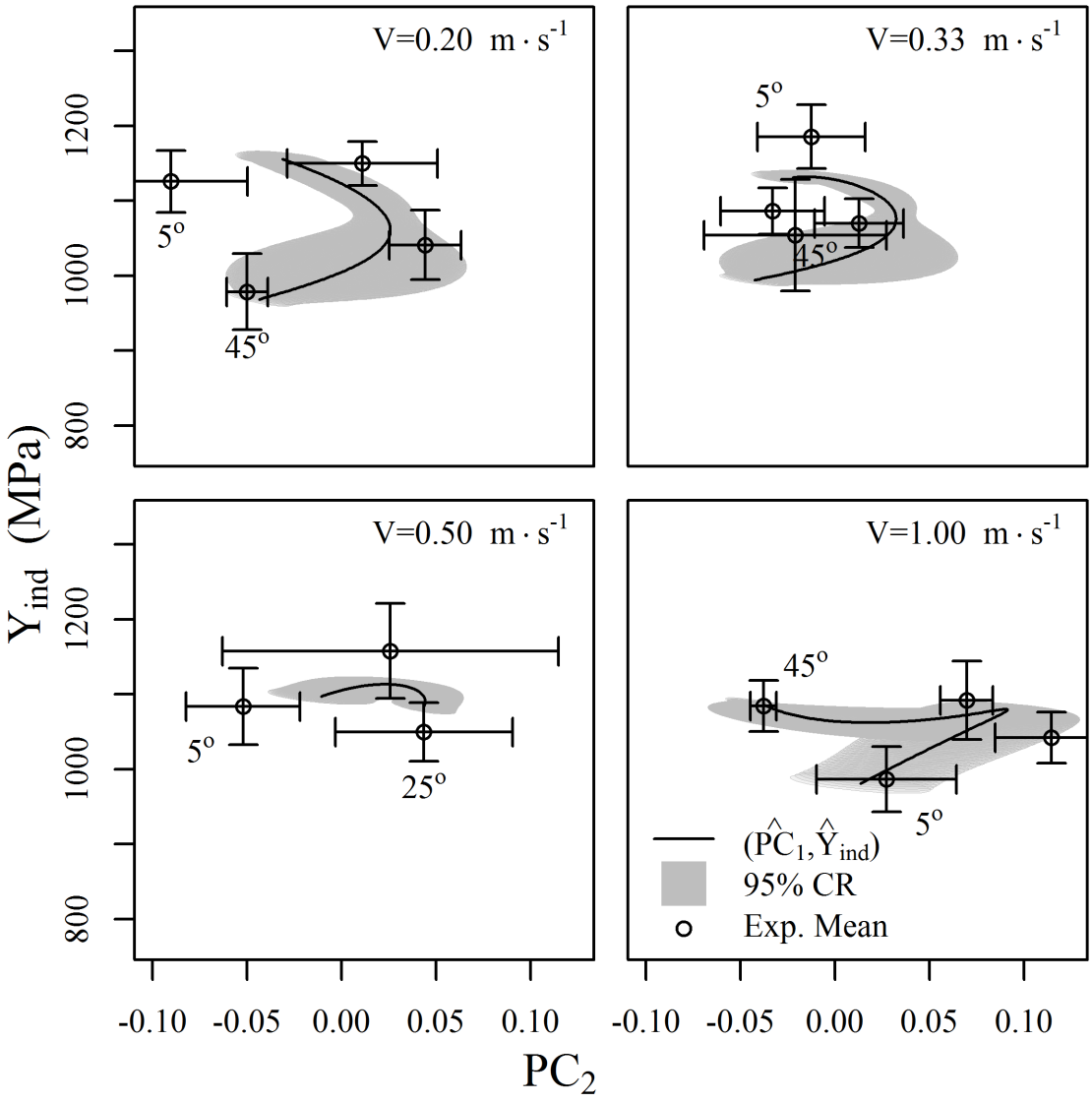

Figure 4.12: Mean PC_2 and Y_{ind} evolution over process settings and GP model path prediction and 95% confidence region. Error bars correspond to mean variation for Y_{ind} and the bootstrapped variation for PC_2.

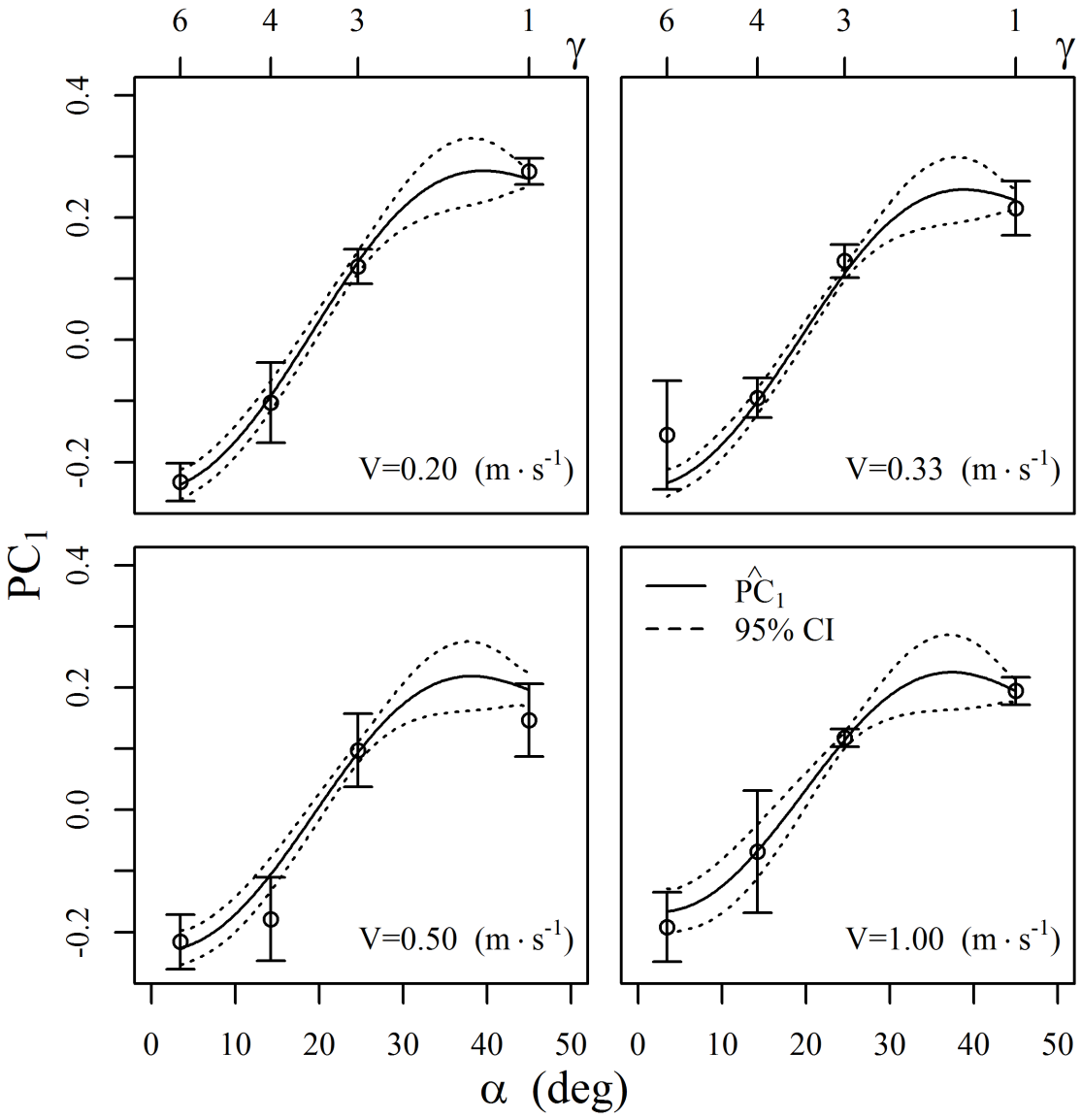

Figure 4.13: Mean PC_1 evolution versus α and the corresponding GP model prediction and 95% confidence bounds. Error bars correspond to the bootstrapped variation for PC_1.

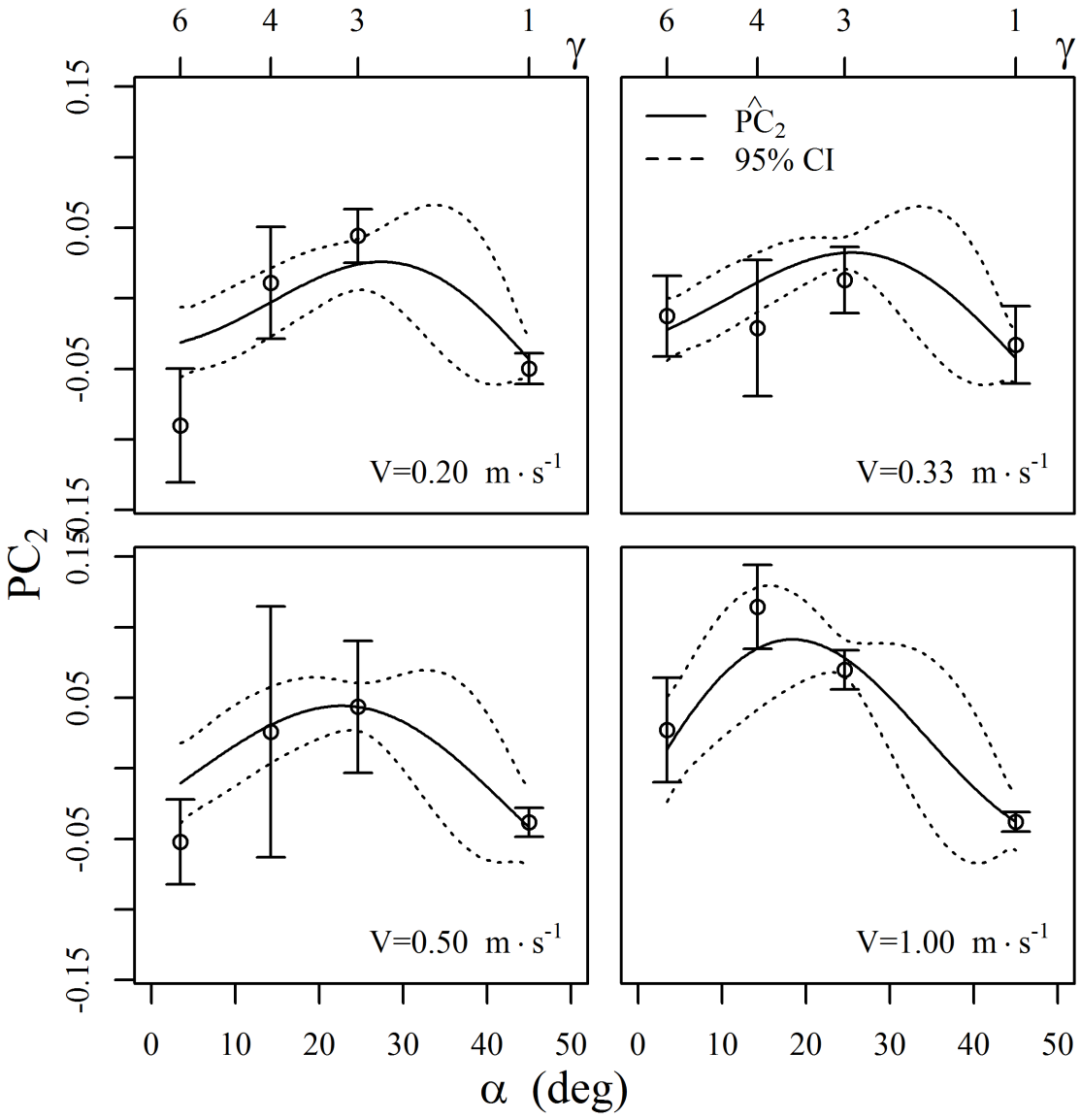

Figure 4.14: Mean PC_2 evolution versus α and the corresponding GP model prediction and 95% confidence bounds. Error bars correspond to the bootstrapped variation for PC_2.

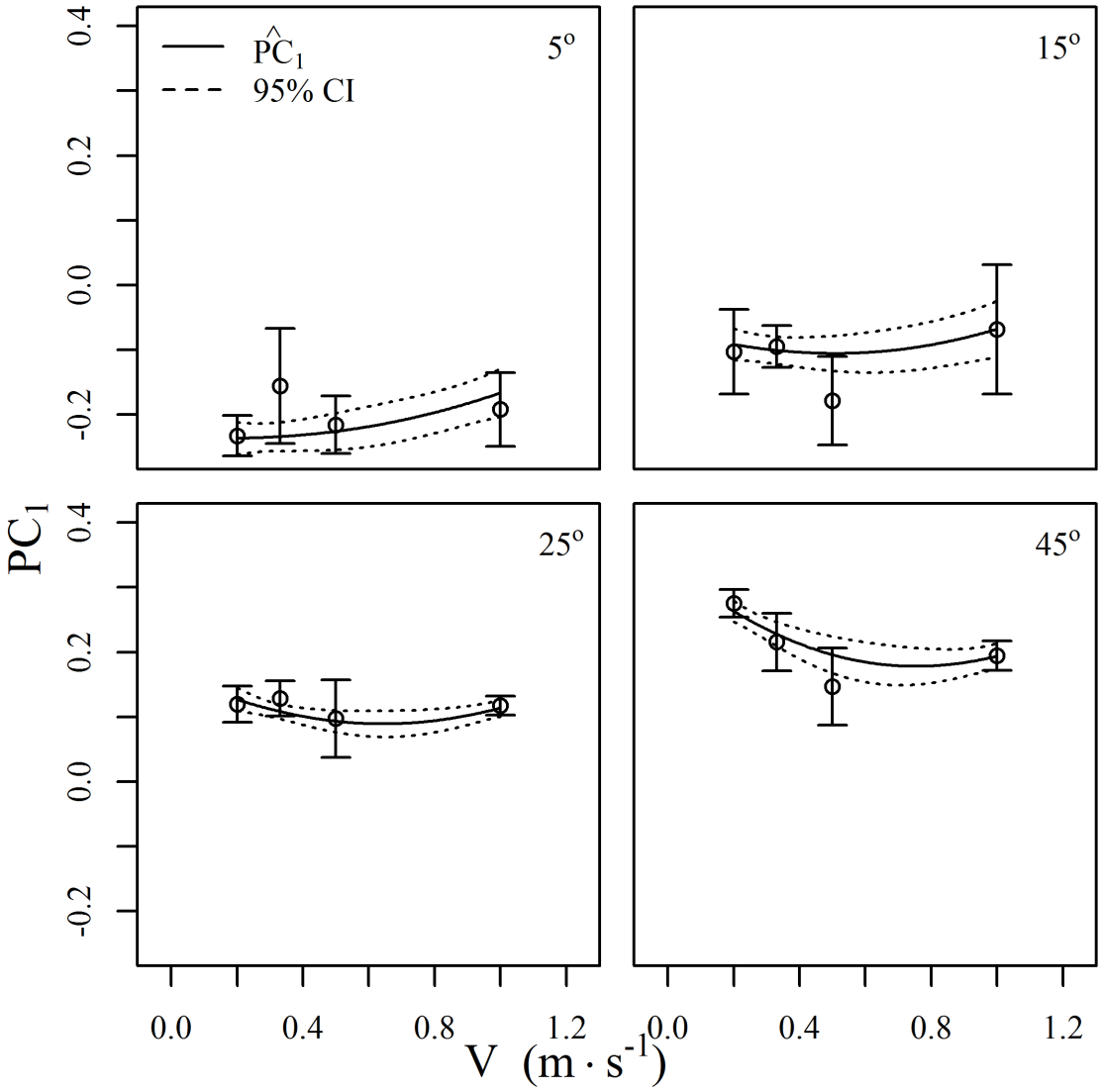

Figure 4.15: Mean PC_1 evolution versus V and the corresponding GP model prediction and 95% confidence bounds. Error bars correspond to the bootstrapped variation for PC_1.

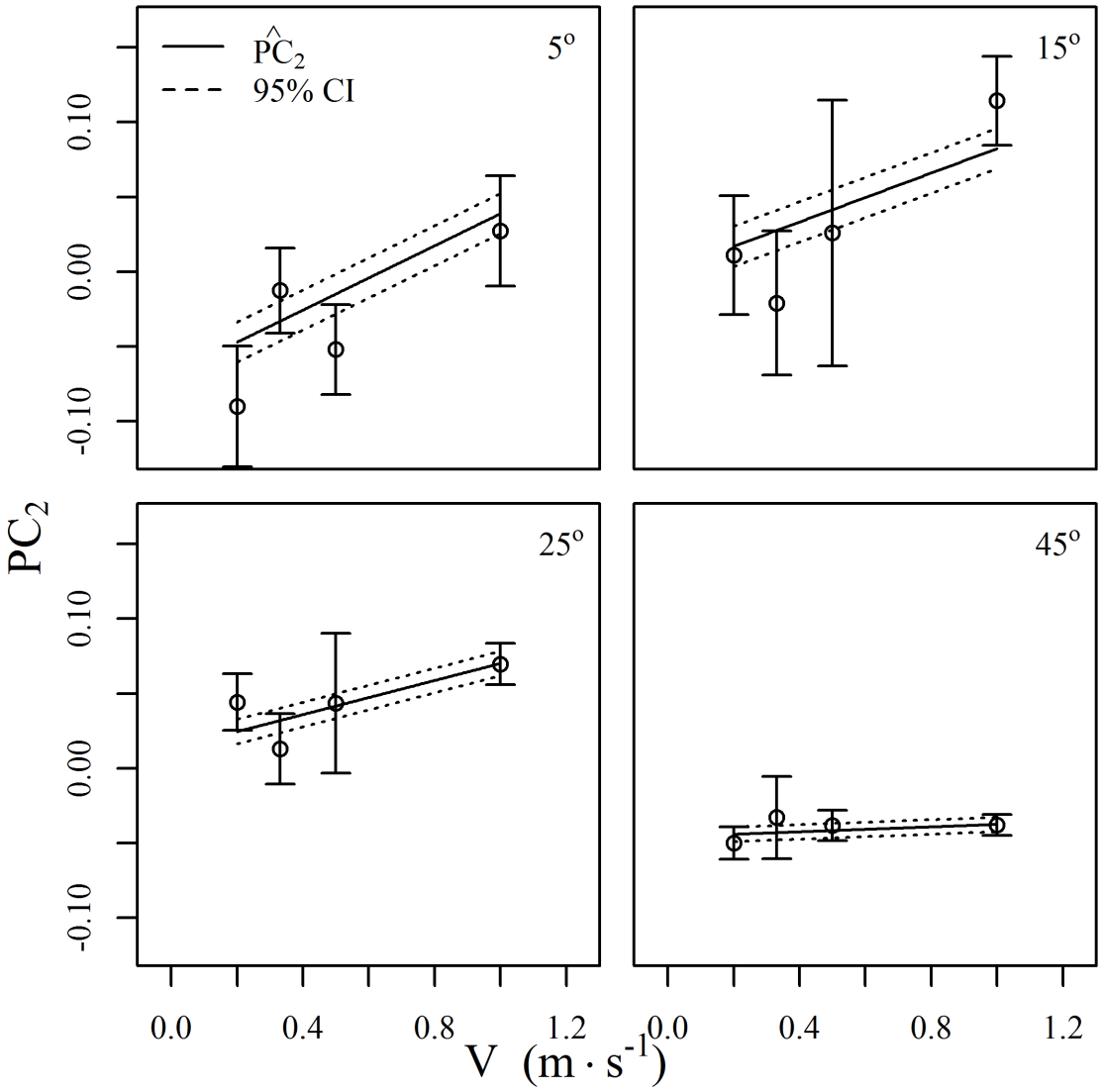

Figure 4.16: Mean PC_2 evolution versus V and the corresponding GP model prediction and 95% confidence bounds. Error bars correspond to the bootstrapped variation for PC_2.

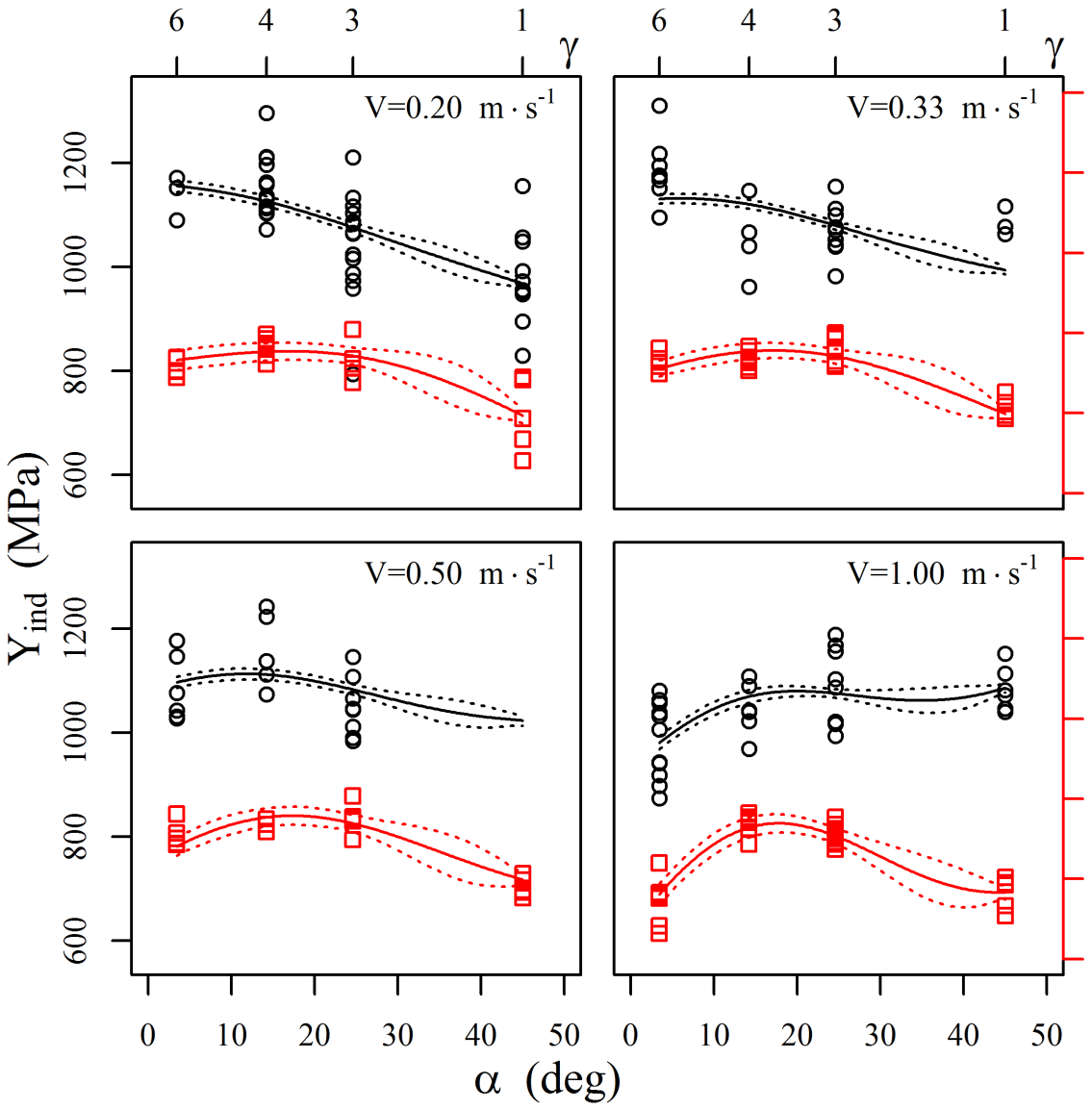

Figure 4.17: Mean Y_{ind} and HV evolution versus α and the corresponding GP model prediction and 95% confidence bounds.

without the need to explicitly define microstructural features. A common assumption when analyzing EBSD data is to define a threshold misorientation value for defining high angle boundaries. At other times, the misorientation distribution itself is utilized as a metric but this necessitates identification of grain boundaries, which is again based on assumed threshold values [31]. Since our statistic only captures morphological features it may be well suited in settings where the scan size is smaller than what is required for accurately quantifying texture. Crystallographic texture is a homogenized quantity and therefore larger scans are typically necessary to accurately capture the representative crystallographic texture. The $15\,\mu m \times 15\,\mu m$ images in Figure 4.4 are certainly not sufficient for identifying texture but can still be used for quantifying morphological features.

Physical interpretation of the obtained microstructure evolution results is possible by considering the PCA bases shown in Figure 4.6. Recall that $\bar{p}_{\boldsymbol{t}}$ measures the degree of spatial crystallographic autocorrelation (similarity). The first principal basis corresponding to PC_1 is highly localized with large negative values towards the center of the basis, some positive asymmetric values away from $\theta = 0°$, and slightly positive in the remainder of the region. The peaked negative region corresponds to a length of about 10 pixels which is $500\,nm$ $(50\,nm/pixel)$. Note that this corresponds to the refined crystallite size observed at the largest strains. Conversely, PC_2 has an even sharper faint negative peak in the center, positive values in the $0.5 - 2\,\mu m$ range, and negative values at large distances. Therefore, one contribution of the PC_1 basis is to control a high autocorrelation region concentrated within a $500\,nm$ region. PC_2 captures competing autocorrelation trends in the $0.5 - 2\,\mu m$ and $> 3\,\mu m$ range. Therefore, it is reasonable that PC_1 is observed to displays the greatest sensitivity to the applied rake angle (Figures 4.13 & 4.14). As the rake angle is decreased, strains are increased, DRX drives refinement, and therefore pixels only retain autocorrelation with very close neighbor points (roughly within a crystal). However, PC_1 does not appear to significantly change with cutting speed (Figure 4.15). This is because cutting speed does not influence spatial similarity at these small scales. PC_2 however does appear

to be sensitive to cutting speed (Figure 4.16) and this sensitivity decreases with increasing rake angle (decreasing strain). This implies that at large imposed strains, as the cutting speed is increased, similarity of crystal orientation extends to include larger neighborhoods in the $0.5 - 2\,\mu m$ region. This observation agrees with the process physics where it is known that cutting temperatures increase with both increasing speeds and strains. Additional straining drives heat generation via plastic dissipation and increased cutting speeds limit the efficacy of conduction to remove heat away from the process zone. At higher temperatures DRX is less impactful [19] and thus there is less misorientation and hence crystal similarity extends over larger spatial distances (less misorientation). Therefore, PC_2 is sensitive to thermal effects, which are implicitly tied to the cutting speeds. With respect to the rake angle, PC_2 has a significant quadratic interaction and this complex behavior may be explained as follows. At high rake angles (low strains) the similarity extends over large distances ($> 3\,\mu m$) and PC_2 is negative, which yields large positive autocorrelation values at large distances. With increasing strain (decreasing rake angle), there is less autocorrelation at large length scales but correlations in the intermediate values ($0.5 - 2\,\mu m$) persist and hence PC_2 increases. However, this trend reverses at the lowest rake angles (highest strains) when the autocorrelation becomes extremely localized ($< 500\,nm$) and thus less similarity is observed in the $0.5 - 2\,\mu m$ range. These interactions are complex because each basis captures several *coupled* physical features (e.g. PC_2 captures negative long range and positive medium range autocorrelation). Furthermore, the bases must interact and balance their respective contributions in order to describe the changing physics at different machining process settings.

Figure 4.17 illustrates that the Vickers hardness and indentation yield produce similar trends with respect to the rake angle. For reference the mean virgin material hardness is $HV = 87.5 \pm 5.0$ (95% confidence interval). At large rake angles (low strains) the generated chips have higher hardness than the virgin material but produce lower range properties relative to measurements at small rake angles (larger strains). This observation is in accor-

dance with deformation induced strain hardening. For cutting speeds $V = 0.20,\ 0.33,\ 0.50\, m \cdot s^{-1}$, the hardness appears to saturate with decreasing rake angle, which indicates that additional straining does not drive an increase in hardness. At the lowest cutting speed, however, indentation yield produces a fairly linear trend which decreased with increasing speed. Therefore, hardness and yield do not always share a one-to-one correspondence but nevertheless the inclusion of hardness is informative (more on this in Section 4.5). At the highest speed and lowest rake angle (highest strain) there is a significant decrease in both hardness and strength. This is likely driven by recovery processes, which occur due to the higher cutting temperatures experienced under these conditions.

In this study we only consider structural morphology and therefore neglect crystallographic effects. This is one potential source of the scatter observed in Figure 4.17. The local crystallographic orientation of the indented site will likely influence the indentation response. However, for simplicity we adopt a strategy where this was neglected and instead homogenized over many observations. When crystallographic information is desirable, the stand alone GSH representation may be augmented as additional features to $\bar{p}_{\boldsymbol{t}}$. Another possibility is to use the strategy established in [83, 84] and use the paired two point statistics between each of the GSH coefficients. Recall that the GSH representation is a sum over multiple indices (μ, n, l) and in this work we truncate to 10 terms. Each of these 10 terms can be used as a measure of microstructural state. Therefore, these state descriptors may be used to compute two point spatial correlations [83]. Including constraints and symmetry considerations, it may be shown that there are $2 \cdot 10 - 1 = 19$ unique correlation pairs [83]. The derived expression in Eqn. 4.5 happens to be the mean over all auto-correlation pairs considered in [83]. The derivation in this work is fairly compact and proves that this mean quantity has a physical interpretation and is a descriptor of morphological spatial crystallographic "spread", which includes misorientation.

Bootstrapping methodology appears to be an effective method for quantifying the dispersion of microstructure in reduced order PC space, as shown in Figure 4.10. To the best

of the author's knowledge, there is only one other work which employs a sub-sampling procedure for quantifying the dispersion of microstructural attributes [137]. In that work, sub-sampling is used to avoid computations on the entire volume ensemble, which would be prohibitively costly. Instead, computations are made more efficient by considering a random sample of smaller volumes. In our regression model bootstrapping is useful as it eliminates the need to estimate the measurement error variances when training the MOGPR model – instead they can be estimated directly from bootstrapping. Note however that bootstrapping of correlated data requires that the original sample be sufficiently large such that it "contains" the relevant correlation length scales. In our setting, the correlation length scales, particularly at large rake angles (low strain), are larger than the image field of view. Nevertheless, the bootstrapped variance estimates will reflect this artifact; inadequately large samples will yield more variance. Additionally, the disparity in microstructures at the lower length scales is sufficiently significant that trends are still clear despite "missing" information at very large length scales.

The MOGPR model is effective at quantifying PSP relationships and provides estimates for coupled structure-property uncertainties. A natural concern however is that perhaps the obtained hyperparameters, $\hat{\mathbf{\Phi}}$ in Eqn. 2.29, neglect structure-property relationships. In Eqn. 2.27 the structure-property linkage is captured through the cross-correlation matrix $\boldsymbol{S}$, which must be inferred from the observed data. This matrix quantifies the covariance (or correlation) between all the outputs considered ($PC_1, PC2, Y_{ind}$). The case where structure-property linkages are neglected the covariance matrix would take a block form,

$$\boldsymbol{C} = \begin{bmatrix} \boldsymbol{C}_{11} + \boldsymbol{\Sigma}_{11} & \boldsymbol{C}_{21} + \boldsymbol{\Sigma}_{21} & \cdots & \mathbf{0} \\ \boldsymbol{C}_{12} + \boldsymbol{\Sigma}_{12} & \boldsymbol{C}_{22} + \boldsymbol{\Sigma}_{22} & \cdots & \mathbf{0} \\ \vdots & \vdots & \ddots & \vdots \\ \mathbf{0} & \cdots & \mathbf{0} & \boldsymbol{C}_M + \boldsymbol{\Sigma}_M \end{bmatrix}, \tag{4.6}$$

which suggests no correlation between the PC's and Y_{ind}. This degenerate case corre-

sponds to two *independent* Gaussian process models; one for the process-structure and another for process-properties. Yet another degenerate case corresponds to a diagonal covariance structure where no correlation exists between any of the considered variables and thus the result is M independent GP models. However, consider that this process is data-driven and therefore it is *possible* that perhaps a process-property relationship does exist. In fact, there is some recent evidence in the literature that suggests that these mappings are plausible in some settings [138]. The inclusion of structural information is physically motivated and is expected to yield better performance as the data is much *richer* if structure information is included. The merit of the MOGPR model is that all possibilities may be considered at once; if a direct process-property linkage exists then the model will identify it. Note that it may seem inappropriate to assume structure-structure cross-correlations between the PC weights as PCA theory generates PC weights which are independent e.g. $\mathrm{Cov}\left(PC_1, PC_2\right) = 0$. However, this is only true in the unsupervised setting; PC weights are independent when nothing is known about the process settings. The PC basis and weights are computed from the unlabeled $p_{\boldsymbol{t}}$ ensemble of observations. In the MOGPR model correlation between PC_1 and PC_2 is possible because the correlation is *conditional* on also knowing the process settings. Two uncorrelated random variables may become correlated when conditioned on a third random variable related to the first two. Clearly, in the second case the two otherwise independent experiments become correlated due to the extra information.

Cross validation results using a leave-one-unique-process-setting-out strategy are displayed in Figure 4.18. The cross validation results may be exactly computed from the fully trained model by employing a short-cut formula from Eqn. 2.37. Four different results are shown to illustrate a few key points: (a) cross validation using Y_{ind} property data not including output cross correlations (the case of M independent GP models), (b) cross validation using Y_{ind} property data with structure-property cross correlations, (c) cross validation using Y_{ind} and HV as coupled properties with no structure-property cross correlations

allowed, and finally (d) cross validation considering all available property data (Y_{ind} and HV) and including output cross-correlations. Notice that strategy (d), which considers all property data and all correlations, yields the best cross validation error (25% improvement from model (a)). Therefore inclusion of the hardness data did improve the overall model performance. Furthermore, each increase in model complexity provides slight improvements over the previous model. In general, however, this may not always be the case. GPR models are also prone to over-fitting when there is an imbalance between model complexity and data. For this reason some researchers prefer to use cross validation strategies for model training [139].

4.6 Conclusions

In this work we studied a severe plastic deformation machining process which drives microstructure evolution via continuous dynamic recrystallization. Various stages of microstructure evolution were captured by considering a wide range of rake angles, which induce a wide range of shear strains. Rate and temperature effects were considered by varying the cutting speed. Large strain conditions produced sub-micron crystal structures whereas low strain experiments yielded highly deformed structures, which still resembled the coarse parent material. At the largest strains a dependence on the cutting speed was observed with higher cutting speeds producing structures with lower crystallographic misorientations. Generalized spherical harmonics were used to efficiently quantify the local orientation state and a novel autocorrelation spatial statistic was derived that captures orientation "spread" or misorientation. The novel descriptor is physically intuitive and targets morphological information present in the orientation imaging data. A data driven multiple output Gaussian process regression model was established for quantifying process-structure-property linkages. The model is flexible, enables inclusion of various kinds of structure and property data, does not necessitate fully paired input data, captures the full process-structure-property pipeline, and produces coupled uncertainty estimates associated

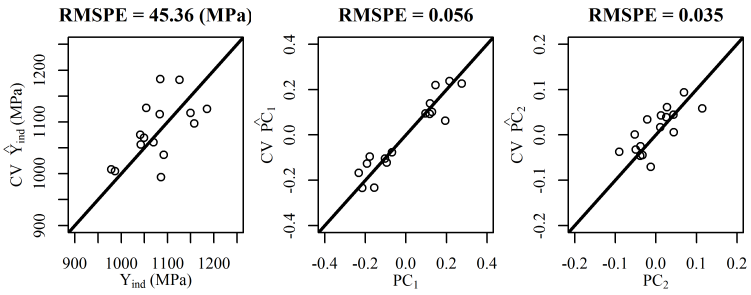

(a) Model only considering Y_{ind} as a property measure with no cross correlations (e.g. direct process-property and process-structure models)

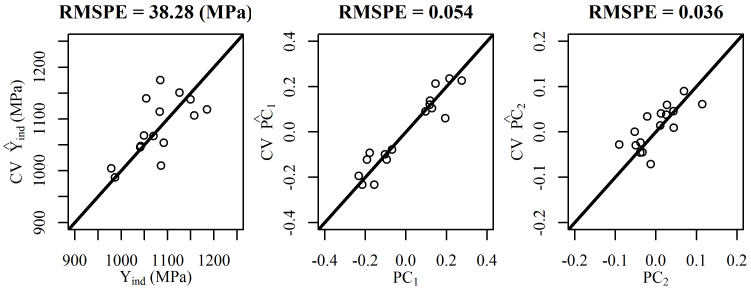

(b) Model only considering Y_{ind} as a property measure with cross correlations

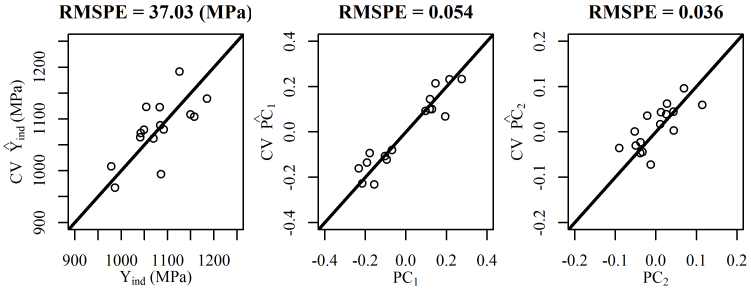

(c) Multi-fidelity model including Y_{ind} and HV with no cross correlations (e.g. direct process-property and process-structure models)

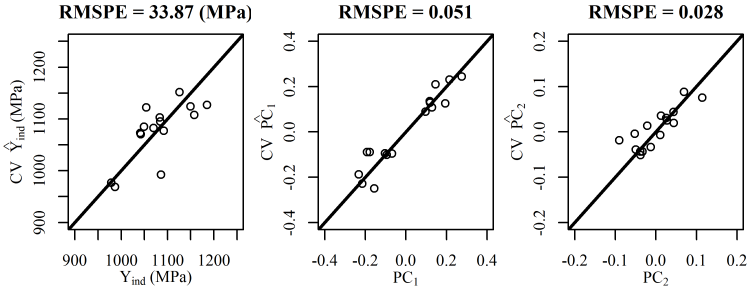

(d) Multi-fidelity model including Y_{ind} and HV as well as structure-property cross correlations

Figure 4.18: Cross validation results removing one unique process setting at a time.

with future predictions.

CHAPTER 5
DATA DRIVEN PROCESS-STRUCTURE-PROPERTY LINKAGES FOR NOVEL BIMODAL MICROSTRUCTURES

5.1 Introduction

Ultra fine grained (UFG) metallic systems exhibit superior strength relative to their coarse grain counterparts [140]. The increase in strength however is usually accompanied by a decrease in ductility. Researchers have discovered that bimodal microstructures consisting of UFG and coarser grain constituents offer excellent strength and ductility [141]. Strength is achieved by the UFG fraction while the coarse grains accommodate strain hardening, which improves the ductility. Several studies on these kinds structures have since been reported [142, 143, 144, 145].

Prior work has considered the production of these bimodal structures via a high rate severe plastic deformation (SPD) process such as machining [18, 20]. The thermomechanical process history imposed on the material by machining drives microstructure evolution, which includes dynamic recrystallization (DRX), nano-twinning, and texture evolution [18, 19, 20, 21, 22, 23]. During the machining operation, the deformed material is removed and exits the processing zone as a machined chip (Figure 5.1) and in doing so the component subsurface is also affected [20, 22, 21]. The generated structures in pure metals can be thermally unstable which promotes recovery, nucleation, and growth processes [146, 147]. At high cutting speeds temperatures are elevated due to plastic dissipation and therefore bimodal microstructures may be generated in situ during machining [18, 20]. Identifying the process-structure-property (PSP) relationships during SPD is therefore important for design of these novel microstructures.

A schematic of a simplified machining process is shown in Figure 5.1. This two dimen-

sional configuration represents a plane strain cutting model where the cutting action occurs within a two-dimensional plane [1]. Although real production processes deviate from this simplified configuration, it is a useful model for fundamental studies of the effects of process parameters, which include the cutting speed V, the uncut chip thickness t_o, and the rake angle α. Intense shearing occurs in the primary shear zone where the degree of shearing is controlled by both the uncut chip thickness and the rake angle. Depending on the process conditions chosen, shear strains up to $\gamma \sim 10$, strain rates between $10^3 - 10^5\, s^{-1}$, and temperatures up to 0.7 T_H (homologous temperature) may be achieved.

Research efforts to quantify the process-structure (PS) relationships in machining have to date focused on a combination of qualitative and quantitative methods. In their seminal work, Brown et al. utilized transmission electron microscopy (TEM) to resolve the structures at small length scales and summarized the findings in the form of a mechanisms map [19]. Other works have utilized scalar quantities such as the recrystallized area fraction and mean grain size [148]. Yet others have utilized probabilistic metrics such as the *distribution* of grain misorientations [43]. For establishing mathematically rigorous PS linkages however, each of these approaches has its limitations. Mechanism maps cannot be used in any analysis setting (regression, classification) as the data is inherently qualitative; an expert must visually inspect the data (images) and make assessments. Point estimates like volume fraction, mean grain size, etc. may be troublesome because they only contain limited information about the microstructure. Two microstructures may have identical recrystallized volume fractions but their morphologies may differ. Probabilistic measures such as grain size distribution, misorientation distribution, etc. are inherently richer as they also contain information about the *randomness* of the material, which is a very natural feature to consider since material structures are inherently stochastic. But it is difficult to directly use a histogram of binned measurements in subsequent analysis. It is clear that a robust *feature engineering* strategy is required for effective establishment of the PS relationships.

Property quantification in machined structures is often limited to nano and micro hard-

ness testing [25, 26, 19, 20, 146, 147]. The generated chips and deformed surface layer of the workpiece are too small for standard mechanical testing and therefore indentation is necessary. Only one work could be identified which provides uniaxial tensile tests for machined chips, however, these experiments are extremely costly to perform [18]. Hardness is not an intrinsic material property but is instead an easy-to-acquire aggregate measure of the resistance to elastic and plastic deformation. To the best of our knowledge, there are no works in the machining literature that have tried to quantify the post-elastic deformation response of these generated structures.

The new paradigm in materials research is the popularization of Materials Informatics (MI) [46, 47, 37]. This field employs statistical methods and techniques for building mathematically rigorous PSP models. In this work, we utilize a MI approach for studying the PSP evolution of copper subjected to machining. The microstructures generated vary from fully UFG, to a bimodal structure, to a fully annealed $\sim 5\mu m$ structure. Uniaxial constitutive behavior is extracted from the machined structures using our previously published Bayesian methodology [77]. Gaussian process regression is utilized to quantify the forward PSP mapping [132]. Finally, we introduce a Bayesian methodology for solving the inverse property $\mapsto$ process mapping. Bayesian methods are well suited for solving inverse problems in science and engineering [15, 108, 59, 58]. Process constraints and many-to-one inverse mappings are captured by utilizing a simulated annealing approach [65, 67, 68, 66, 149]. To the best of the authors knowledge, this work is the first to employ a MI approach studying SPD microstructures.

5.2 Experimental Methods

Oxygen-free high conductivity copper (OFHC Cu) bars were obtained from a supplier (McMaster Carr). The material was subjected to SPD via a plane strain machining process. Tube turning experiments were carried out to emulate the idealized two-dimensional orthogonal cutting configuration shown in Figure 5.1. A custom-built high speed steel cut-

ting tool with a nominal rake angle $\alpha = 5^{\circ}$ and depth of cut (t_o) of $300\ \mu m$ were used for all experiments. The prescribed tool geometry was chosen to impose large shear strains in the primary shear zone, which the machining theory predicts to be $\gamma \sim 5 - 8$ [1]. Four cutting speeds (V) were studied $0.20,\ 0.33,\ 0.50,\ 1.00\, m \cdot s^{-1}$, which generate strain rates of $\sim 10^3 - 10^4\ s^{-1}$. Higher cutting speeds correspondingly yield increases in the chip temperatures as there is less time available for conduction of heat away from the chip. Utilizing the cutting forces measured via a three-component piezoelectric dynamometer (Kistler 9257B), the chip temperatures were estimated to be in the range $100 - 150^{\circ}C$ (Eqn. (5.3)) for the cutting speeds considered [1]. To further study the influence of temperature on the machined microstructures, a quenching experimental factor was included in the study. Cutting experiments were performed twice; once with an empty catch tank to collect the chips, and another with a catch tank filled with water. Quenched chips are assumed to represent the frozen as-machined microstructure while the chips collected in the empty catch tank are subject to air cooling for a short duration subsequent to exiting the deformation zone. Assuming the air cooled chips can be modeled using lumped capacitance and are subject to natural convection with $h \sim 1\ W/m^2/C$, the machined chips are at elevated temperatures ($> 130^{\circ}C$) for less than two minutes. Here, $130^{\circ}C$ is a relevant quantity as a previous study investigating the thermal stability of machined OFHC Cu chips found this to be the critical recrystallization temperature for chips generated under similar processing histories [146]. Practically, the additional quenched and air cooled microstructures considered here could represent microstructures generated with and without the use of a coolant (cutting fluid), respectively.

The collected chips were mounted in epoxy and mechanically ground and polished with up to $1\ \mu m$ diamond suspension polish. Final surface preparation was performed via electropolishing using a Struer's LectroPol-5 machine. Previous work suggests that electropolished surfaces are optimal for spherical nanoindentation [127]. An electrolyte consisting of (by volume) 25% phosphoric acid (85%-wt), 25% ethanol, 50% distilled water was used.

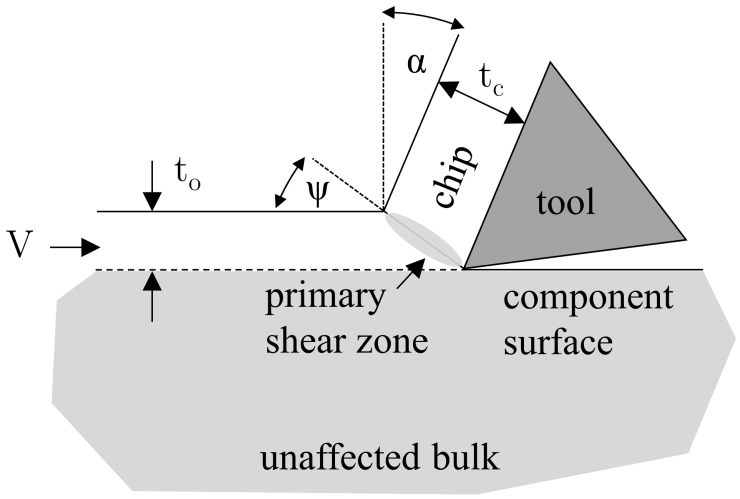

Figure 5.1: Orthogonal cutting schematic.

Optimal electropolishing settings were found to be between $10 - 25\,V$ for $10\,s$. We report a voltage range as it was observed that each sample's response to the applied voltage varied somewhat across different microstructures. A Tescan Mira XMH field emission scanning electron microscope (FE-SEM) was utilized to image the machined chip microstructures. A backscatter emissions (BSE) detector was utilized for all imaging as it was found to yield images with extremely good contrast (see Figures 5.2). A EDAX Hikari EBSD detector with TSL OIM analysis was utilized for orientation imaging.

Nanoindentation experiments were performed on a Agilent G200 nanoindenter with an XP head and continuous stiffness monitoring (CMS). A $500\,\mu m$ diamond indenter was used for all air cooled chip samples and both $500\,\mu m$ and $100\,\mu m$ indenters for quenched samples. A larger indenter was used for the air cooled samples because the corresponding microstructures are coarser and therefore a large indenter was desirable for obtaining better homogenized results. A recent work has shown that the yield behavior is fairly invariant to indenter size, which justifies our experimental procedure [91]. Spherical indentation stress-strain analysis protocols were utilized to further process the measurements [89, 127]. The derived indentation stress-strain curves capture the mechanical response of the material deformed beneath the indenter. Each indent was then imaged to quantify the microstructure.

Table 5.1: Structure/property sampling summary

V (m/s)	HT	No. micrographs	No. indents	No. paired
0.20	air cooled	15	14	8
0.33	air cooled	23	9	8
0.50	air cooled	17	10	7
1.00	air cooled	36	12	8
0.20	quenched	15	29	13
0.33	quenched	31	18	2
0.50	quenched	16	14	0
1.00	quenched	42	32	15
	Total:	195	138	61

This strategy provides *paired* data, which may be more informative if there is significant structure/property variation within a specific experimental setting. The corresponding indentation contact radius for these experiments varied between $50 - 75\,\mu m$. Material with low resistance to deformation (low strength) produced larger contact areas and therefore the variation in contact radius is inherited from variation in properties. The quenched chip microstructures investigated have very fine structure ($d < 1\,\mu m$) while the air cooled structures can contain coarser constituents ($d < 10\,\mu m$).

A summary of the experimental conditions used, images taken, and indentation experiments performed is shown in Table 5.1.

5.3 Methods

The machining process produces UFG microstructures through a continuous DRX mechanism as shown in Figure 5.2 [19]. During this process, dislocation cells first form due to the large imposed strains [41]. Subsequent straining rotates the cells generating low angle grain boundaries and, after sufficient additional deformation, UFG high misorientation structures are generated [19]. Evidence of this mechanism can be found in the EBSD maps shown in Figure 5.3. Much of the refined microstructure consists of high angle grain boundaries although there exist areas where the grain boundaries have low misorientation.

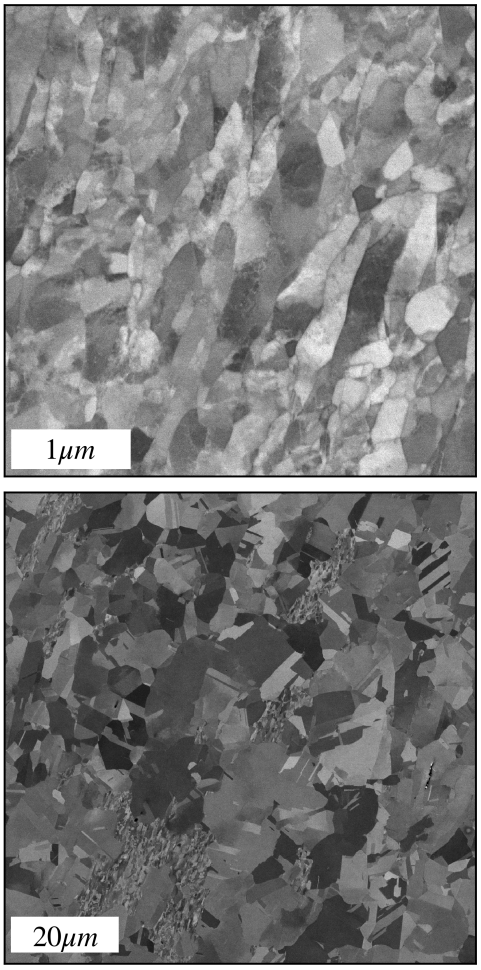

Figure 5.2: Machined OFHC Cu BSE micrographs. (top) Quenched 0.33 $m \cdot s^{-1}$, (bottom) Air cooled 1.00 $m \cdot s^{-1}$.

Similar evidence is also found in the partially annealed structure.

Features indicative of annealing and grain growth can be observed in the air cooled microstructures. A certain fraction of UFG however remains and this appears to be dependent on the cutting speed (and therefore temperature).

The objectives of this work are to (1) establish rigorous methods for quantifying the described microstructures as well as identifying their corresponding mechanical properties, (2) build a data-driven model for estimating the forward PSP mapping and (3) proposing an inverse strategy for estimating the inverse property $\mapsto$ process mapping which can guide in the design and manufacture of functional surfaces. The remaining sections will address

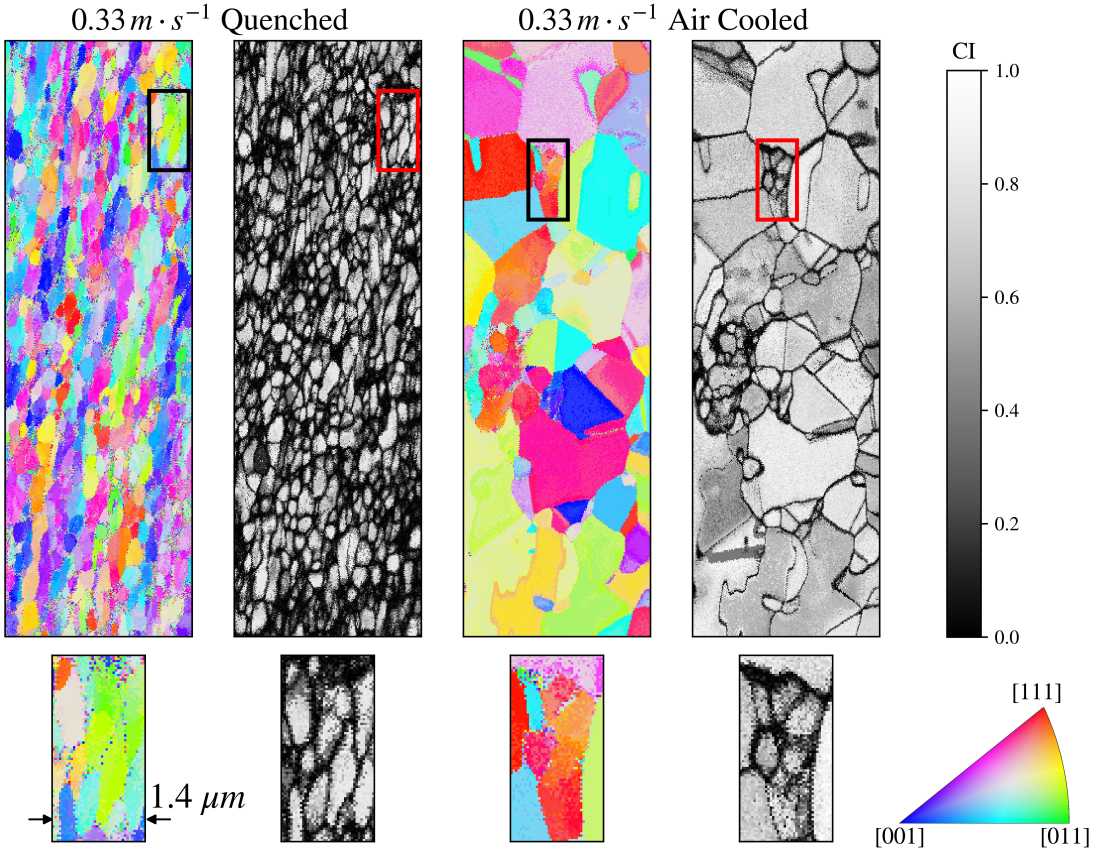

Figure 5.3: EBSD micrographs of quenched and air cooled microstructures. Both inverse pole figures and confidence index maps are shown.

these aspects.

5.3.1 Deformation Mechanics

Relevant deformation quantifies may be obtained from the simplified orthogonal cutting model shown in Figure 5.1 [1]. The expression for the imposed shear strain is,

$$\begin{aligned} \gamma &= \frac{cos\alpha}{sin\Psi cos\left(\Psi - \alpha\right)} \\ tan\Psi &= \frac{rcos\alpha}{1 - rsin\alpha} \\ r &= t_o/t_c, \end{aligned} \tag{5.1}$$

where α is the rake angle, Ψ the shear angle, and r the uncut-to-cut chip ratio. Note that α is prescribed by the tool geometry but Ψ and r are measured quantities obtained from experiments. The shear strain rate may be estimated from,

$$\dot{\gamma} = \frac{cos\alpha}{cos\left(\Psi - \alpha\right)} \frac{V}{\Delta}, \tag{5.2}$$

where V is the cutting speed and Δ is the shear plane thickness. Note that the shear plane thickness is difficult to acquire experimentally. In this work we use $\Delta = 50\mu m$, which was a quantity derived from particle image velocimetry measurements during cutting of OFHC Cu for speeds $V > 0.1\ m \cdot s^{-1}$ [19].

Cutting temperatures may be estimated by considering an energy balance in the shear zone [1],

$$\begin{aligned} \Delta T &= R_1 \frac{F_s V_s}{c\rho V b t_o} \\ R_1 &= \left[1 + 1.328\left(\frac{K_1\gamma}{V t_o}\right)\right]^{-1}, \end{aligned} \tag{5.3}$$

where F_s is the force acting on the shear plane, V_s is the shear plane speed, c the heat capacity, ρ the density, and b is the width of the sample (into the page in Figure 5.1). R_1 is a correction factor that quantifies the fraction of heat that remains in the chip and K_1 is the

thermal diffusivity of the deformed material [1]. Note that cutting forces were measured in all experiments and therefore F_s, as well as V_s, may be obtained from orthogonal cutting analysis [1]. A lumped capacitance model is used to estimate the time required for the chip samples to cool to a specified temperature T' [150],

$$\Delta t = \frac{\rho c}{h}\left(\frac{V}{A}\right)\log\left(\frac{T_o - T}{T_o - T'}\right), \tag{5.4}$$

where h is the convective heat transfer coefficient, V is the volume of the chip, A is the total surface area of the chip, T_o is the reference/initial temperature taken to be $20°C$, and T is the temperature of the deformed chip obtained from Eqn. (5.3). For these computations, values of $h = 1\ W/m^2/°C$ and $h = 100\ W/m^2/°C$ were used for the air cooled and quenched conditions.

5.3.2 Microstructure quantification

Microstructures can be quantified using the probabilistic *microstructure function*, $m(\boldsymbol{x}, h)$, which in the discrete case describes the probability of finding state h at spatial location $\boldsymbol{x}$ [48, 151]. In many engineering materials the microstructure can be quantified considering only discrete states e.g. phases [91, 129, 37]. This definition is naturally well suited for subsequent computation of spatial statistics, which capture the spatial distribution of different phases in multi-phase materials. Recent works have extended this framework using generalized spherical harmonics (GSH) to study single phase polycrystalline systems [83, 84]. This GSH approach however uses crystallographic orientation as the microstructure descriptor and therefore experimentally costly orientation imaging microscopy (OIM) is required.

The material system being considered in this work is a single phase polycrystalline material. The machining process conditions utilized generate microstructures with large variations in grain size as shown in Figure 5.2. Although crystallographic texture strongly influences the bulk properties, we hypothesize that the salient microstructure feature is the

crystallite *scale*. Furthermore, EBSD is experimentally more costly than SEM, particularly when considering that our intention is to image each indent. Therefore, we employ *angularly resolved chord length statistics* to digitize the imaged microstructures and argue that this is sufficient for discriminating between the microstructures shown in this work and to identify the corresponding PSP relationships. A study using this framework for discriminating between different synthetically generated microstructures has been recently published [55].

The chord length distribution (CLD) can be computed from segmented images using the algorithm presented in [53]. A chord is defined as a line segment whose first and last pixel lie on a edge and all pixels in between consist of grain interior pixels. These statistics are generated by first processing the SEM micrographs using morphological transformation to identify the grain boundaries as shown in Figure 5.4. Next, the image is "scanned" with angled lines spanning the length of the image (red in Figure 5.4). Intersections are identified and chord frequencies are binned in two dimensions with respect to the chord angle and length. Furthermore, each observed chord is weighted with respect to its length. This is a critical detail which corrects for a sampling bias of small chords. Consider a bimodal microstructure such as that shown in the bottom of Figure 5.2 - although there is a large volume fraction of annealed grains there is a higher frequency of small chords. The consequence of neglecting this detail would be that small chords would numerically dominate the chord length statistics. In addition, since chord lengths can span 2-3 orders of magnitude across different process conditions ($\sim 100\,nm$ to $\sim 10\,\mu m$), the logarithm of the chord length is used.

5.3.3 Dimensionality reduction

Each image generates a corresponding CLD which consists of two dimensional binned data. In this work we utilized 37 angular bins ($180°/5° + 1$) and 70 bins for the chord length. Note that the CLD is symmetric about $180°$. This corresponds to each image being repre-

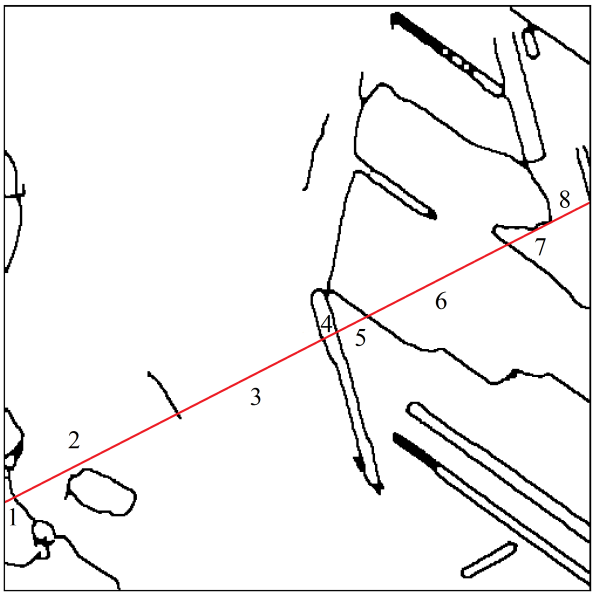

Figure 5.4: Segmented micrograph and chord sampling procedure.

sented by a $37 \times 70 = 2590$ dimensional vector. Any subsequent regression or classification becomes computationally burdensome with such high dimensional data and hence a reduction in the feature space is desirable. Furthermore, directly utilizing a 2590 feature vector in all subsequent analysis may yield difficult-to-interpret results. Prior work has successfully employed principal component analysis (PCA) to reduce the dimensionality of two-point statistics [129, 91, 37] and therefore we adopt the same strategy. Dimensionality reduction is achieved by first identifying a new orthogonal bases which optimally describe the directions of greatest variation present in the data. A reduction in dimensionality is achieved by then truncating the bases. The bases often represent intuitive physical quantities (e.g. short-range features, long-range features, directional features, etc.). Mathematically the basis representation can be written as,

$$f(r,\theta) = \sum_{i}^{N} \alpha_i \phi_i (r,\theta) , \tag{5.5}$$

where $f(r,\theta)$ is the angularly resolved CLD, N is the total number of basis functions needed to perfectly construct the original data, α_i are the basis weights (PC weights), and

$\phi_i(r,\theta)$ are the bases. Now to reduce the dimensionality of the problem, the sum may be truncated at some appropriate value of k terms,

$$\hat{f}(r,\theta) \approx \sum_{i}^{k} \alpha_i \phi_i(r,\theta). \tag{5.6}$$

Using this truncated basis representation, any image can be quantified with the CLD PC-weight vector $\boldsymbol{\alpha} \in \mathbb{R}^k$. The efficacy of this truncation may be quantified by considering the *proportion of variance explained*.

The PCA dimensionality reduction is obtained via a linear projection of the original high dimensional data onto a lower dimensional plane. This is a linear operation that is numerically efficient and enables physical interpretation of the basis vectors $\boldsymbol{\phi}$. However, in some cases the data may instead lie on a nonlinear *manifold*. As will be shown, this is in fact the case for our data. Nonlinear dimensionality reduction was performed using local linear embedding (LLE) [152] which, as the name suggests, performs a local linear mapping in a neighborhood of points. This was implemented in the Python package *Scikit-learn* [153]. Nonlinear mappings however become more difficult to physically interpret since there are no longer global basis vectors, which may contain physical information, but instead only locally varying bases.

It is important to note that prior to employing the dimensionality reduction method described above, images should be made *rotationally invariant*. The presence and degree of anisotropy should be quantified. But in this work the importance of the microstructure directionality relative to the sample geometry is assumed to be unimportant since the indentation is perpendicular to the shown images. Furthermore, small image-to-image rotation variations, and artifacts of how the sample is imaged should not falsely discriminate otherwise similar microstructures. Rotation invariance in this work is accomplished in two steps (1) the length parameter r is integrated out of $f(r,\theta)$ to yield the marginal distribution $f(\theta)$ and (2) images are rotated such that they have identical $f(\theta)$ marginal distributions (if significant). This comparison of distributions can be achieved in a completely non-parametric

way by utilizing a two-sample Kolmogorov-Smirnov test tested at $\alpha = 5\%$ [154]. Note that alternative methods exist for obtaining rotation invariance, which are also easily extended to two-point statistics [128].

5.3.4 Indentation inverse modeling

The indentation stress-strain curves obtained from each indentation experiment represent the mechanical constitutive response subject to indentation loading. The theory utilized to develop these curves is based on Hertzian mechanics of a spherical indenter, which requires several assumptions including isotropic linear elasticity. The elastic modulus corresponding to these curves is proportional to the uniaxial equivalent modulus because all the Hertzian assumptions hold during elastic deformation. However, the plastic portion of the indentation stress-strain curves do not have a direct mapping to the uniaxial stress-strain curves since the elastic assumption no longer holds. Recent work has found that the indentation yield strength is approximately twice the uniaxial yield strength ($\sigma_{ind,o}v \sim 2\sigma_o$) but this can vary slightly and most importantly uncertainty estimates are difficult to obtain using this metric [103]. Therefore, identification of the uniaxial equivalent constitutive behavior, and the corresponding uncertainty, is a statistical inference problem; the data we observe is sensitive to the underlying intrinsic mechanical behavior but these properties cannot be directly measured.

In recent work we overcame this challenge by employing a Bayesian calibration methodology to estimate both the mean uniaxial equivalent behavior and the corresponding confidence bounds [77]. In that work an efficient surrogate Gaussian Process (GP) model is trained to emulate the output of a finite element indentation model. The computationally inexpensive surrogate is then used to infer the underlying uniaxial equivalent constitute parameters through Bayesian regression. A Bayesian strategy is desirable since there are strong prior beliefs about the underlying material behavior. For instance, uniaxial modulus is estimated directly from the indentation stress-strain curves and the uniaxial initial yield

can be approximately estimated as $\sim 1/2\sigma_{ind,o}$.

In this work we assume an isotropic linear-hardening plasticity model to describe the finite element model's constitutive behavior. The inference is therefore over the elastic modulus (E), the initial yield strength (σ_o), and the hardening slope (K). A 30-run Maximum Projection (MaxPro) design was utilized to optimally identify the simulation settings (E, σ_o, K) over which the FE model was evaluated and the surrogate model was built [116]. The experimental design was constrained such that $E > K$ using a greedy algorithm [155, 156]. The surrogate model was validated against a different 50-run MaxPro design and the validation root mean squared predicted error (RMSPE) was $14.7\ MPa$. The GP model and inference problem were programmed in *Stan* [64], a probabilistic programming language, and evaluated in *RStan* [157], the R-language Stan interface. All codes can be found at [158].

5.3.5 Multiple output Gaussian process regression

Gaussian process regression (GPR) is a non-parametric method for performing regression e.g. estimating functions from observed data [132, 14]. Mathematically the formulation is nearly identical to kernel regression and smoothing methods however GPR employs an attractive statistical interpretation of the data [133, 132]. Parametric methods regress functions of assumed functional forms onto data by estimation of the regression coefficients [159]. This is a compact method for establishing data-driven models since once the regression is performed, the original data need no longer be retained. However the constraint imposed in parametric regression is that the functional behavior (the model form) is known a priori. Non-parametric methods conversely make no assumptions on the underlying functional forms instead predictions utilize the entire data ensemble for estimation.

The GPR framework fundamentally assumes that all observations (y_i) come from some common data generating process. Furthermore, the observed data ($\boldsymbol{Y} = [y_1, \ldots y_N]^T$) may be correlated depending on the values of their covariates ($\boldsymbol{X} = \left[\boldsymbol{x}_1^T, \ldots \boldsymbol{x}_N^T\right]^T$). For in-

stance, y_i and y_j are said to be correlated (and therefore close in value) if $\boldsymbol{x}_i$ and $\boldsymbol{x}_j$ are sufficiently "close". In the same way a new prediction, $y(\boldsymbol{x})$, may be estimating by comparing $\boldsymbol{x}$ against all the collected $\boldsymbol{x}_i$. Therefore, in the GPR setting the technical challenge for establishing a regression model is the inference of the underlying *correlation structure*. The question is then how to define a quantitative metric for the closeness between $\boldsymbol{x}_i$ and $\boldsymbol{x}_j$. In GPR the solution is to parameterize the correlation structure and the model is subsequently built by inferring these *hyperparameters*. In a sense this is analogous to regression where the functional forms themselves are parameterized via regression coefficients however GPR is one level less explicit.

We employ a multiple output Gaussian process regression (MOGPR) model for simultaneously modeling both structure-property as a function of the input process. This strategy allows for development of the full PSP linkage, including uncertainty estimates, within a single model. Note that in the model development we distinguish between paired and unpaired structure-property data. A paired observation consists of a micrograph taken at the location of an indent. Unpaired observations lack this correspondence and are only related through the shared process. We hypothesize that paired data should enable better statistical inference since local variations in microstructure should correspond to proportional variations in local properties as shown in Figure 5.5. This schematic illustrates that the mean behavior, μ, linking structure with property follows a linear correlation ρ. In the paired data case deviations from the process mean also follow ρ since the structure variation is assumed to be associated with local heterogeneities. For unpaired measurements variations from the mean for structure and property are independent. The real error correlation, ρ_e, is expected to be less than ρ as the error is also influenced by other sources of error.

5.3.6 Inverse Property-Process mapping

The MOGPR model quantified the forward linkages which provide an estimate for the uniaxial equivalent yield stress as a function of the machining process conditions, $\hat{\sigma}_o(\boldsymbol{x})$.

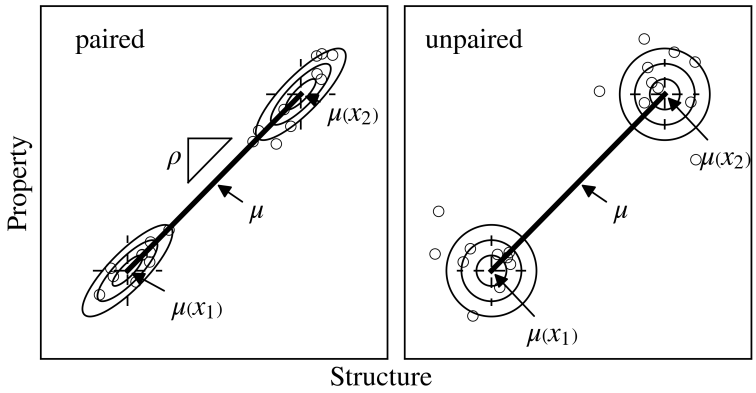

Figure 5.5: Illustration of error structure inherited from material heterogeneity.

Conditional on a particular target yield stress range, which is described as being normally distributed $\mathcal{N}(\sigma_o', s')$, the inverse mapping seeks to find the corresponding process parameters values, $\boldsymbol{x}'$, which best achieves the desired properties. This problem can be therefore cast into a Bayesian problem where the solution to $\boldsymbol{x}'$ can be identified through a posterior density,

$$\begin{aligned} p(\boldsymbol{x}'|\sigma_o', s') &\propto p(\sigma_o'|\boldsymbol{x}', s')\, p(x'|s') \\ &\propto \frac{p(x')}{\sqrt{2\pi}s'} \exp\left(-\frac{1}{2}\frac{(\hat{\sigma}_o(\boldsymbol{x}) - \sigma_o')^2}{s'^2}\right). \end{aligned} \tag{5.7}$$

A schematic of this strategy is illustrated in Figure 5.6 using a GPR model trained on noisy data. Intuitively, this strategy seeks to identify the machining process settings that generate mechanical properties that are "contained" in the target range. Consider that constraints may be imposed on the process parameter space $\boldsymbol{x}$ through the prior. Many constraints may be simultaneously considered using the constraint functions $g_i(\boldsymbol{x}) \leq 0$ for $i = 1, \ldots, N_c$. As an example consider that in a production setting higher speeds correspond to higher production rates and therefore the manufacturer may wish to impose the constraint $V > 0.5\,m \cdot s^{-1}$ which is derived from economic considerations. These constraints impose 0 probability in impermissible regions through an indicator function

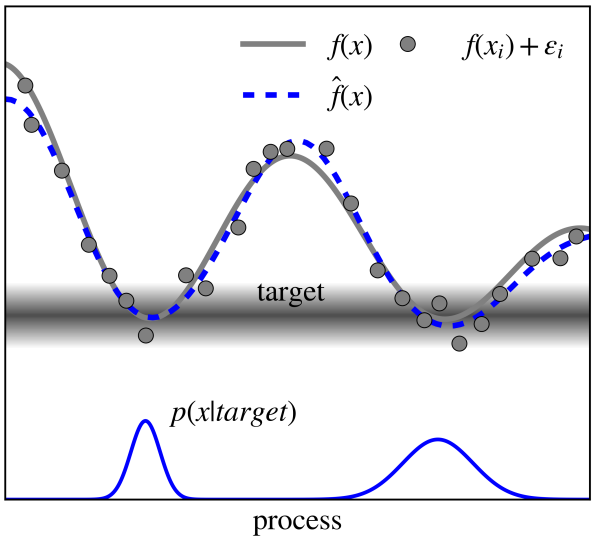

Figure 5.6: Schematic of the Bayesian inverse mapping strategy.

which is 0 if any of the constraints are violated,

$$p\left(\boldsymbol{x}'|\sigma_o'\right) \propto \frac{I\left[\boldsymbol{g}\left(\boldsymbol{x}'\right)\right]}{\sqrt{2\pi}s'} \exp\left(-\frac{1}{2}\frac{\left(\hat{\sigma}_o\left(\boldsymbol{x}\right)-\sigma_o'\right)^2}{s'^2}\right), \tag{5.8}$$

where $\boldsymbol{g}$ is the vector of constraint functions. The posterior may be estimated by obtaining a suitable sample using Markov Chain Monte Carlo (MCMC) methods [59]. Note that sampling from a posterior with discontinuities introduced via hard constraints is numerically challenging. This difficulty may be alleviated by utilizing a simulated annealing approach where hard constraints are numerically made "soft" [67, 68]. A combined simulated annealing MCMC strategy would enable the use of constraints as well as the ability to draw samples from a multimodal posterior as shown in Figure 5.6 [65]. Practically, this may be necessary if there exist many-to-one property $\mapsto$ process mappings. This may occurs in machining where different combinations of process settings can generate the same properties [19, 20]. Simulated annealing methods have been previously employed for constrained optimization in cheminformatics [66]. The output of the analysis is a sample from the posterior in Eqn. (5.8). Simple constraints imposed on cutting speed were utilized to maintain solutions to the experimental range studied $0.20\,m/s \leq V \leq 1.00\,m/s$.

Table 5.2: Thermomechanical Conditions

V (m/s)	γ	$\dot{\gamma}$ (s^{-1})	T $(^{\circ}C)$	$log\,(Z)$ $\log\,(s^{-1})$	$t^{ac}_{130^{\circ}}$ (s)	$t^{q}_{130^{\circ}}$ (s)
0.20	6.81	$4.3 \cdot 10^3$	125	30.3	*NA*	*NA*
0.33	5.98	$7.1 \cdot 10^3$	135	30.2	20.0	0.2
0.50	5.50	$1.1 \cdot 10^4$	142	30.3	44.6	0.4
1.00	4.76	$2.2 \cdot 10^4$	163	30.0	114.5	1.1

5.4 Results

Experimental summary quantities are shown in Table 5.2. Two time variables, one for air cooled (*ac*) and the other quenched (q), estimate the total time the corresponding chip samples are subjected to temperatures above $T' = 130^{\circ}C$. Note that at the lowest cutting speed the generated microstructures do not exceed the critical temperature and hence *NA* is reported in the table. $Z = \dot{\epsilon} \exp\left(Q/RT\right)$ is the Zener-Holloman parameter [40]. The activation energy for grain boundary diffusion in Cu, $Q = 72.5\, kJ/mol$, was used [19].

PCA dimensionality reduction results are shown in Figure 5.7. The first PC basis captures 71.8% of the explained variance, the first two capture 87.3%, and the first three capture 93.1%. As expected, the PC bases assign a physical interpretation to the basis weights. The first basis captures small grains, the second large grains, and the third captures anistropic features. Anistropy is present in the dynamically recrystallized structures (Figure 5.2) due to intense shearing imposed in the primary shear zone during machining.

A two dimensional projection of the reduced order structure data is shown in Figure 5.9. Four micrographs are shown to illustrate the various structures generated at the lowest and highest speeds for both quenched and air cooled processes. Included for reference is the virgin microstructure which consists of 100-300 μm diameter equiaxed grains. Schematic paths are illustrated to show the physical mechanisms that drive microstructure evolution under these settings. Visually it appears as if the cutting speed has significant influence on both air cooled and quenched microstructures, with an increase in cutting speed driving an increase in the structural scale. Air cooled samples at low and medium cutting speeds have

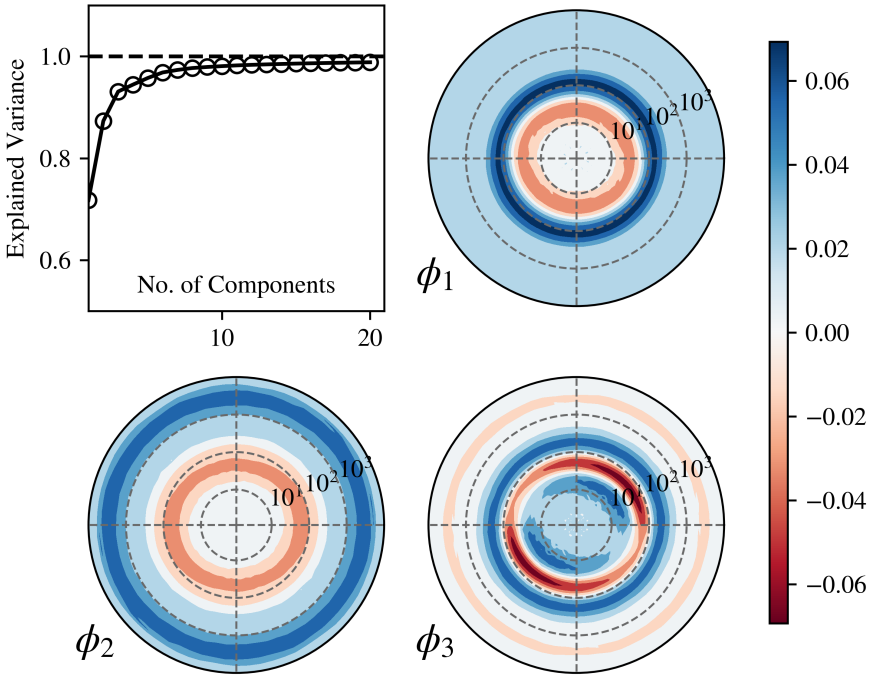

Figure 5.7: Cumulative explained variance and the first three CLD PC basis. The first two basis represent large and small length scale features, respectively. The third basis captures structural anisotropy.

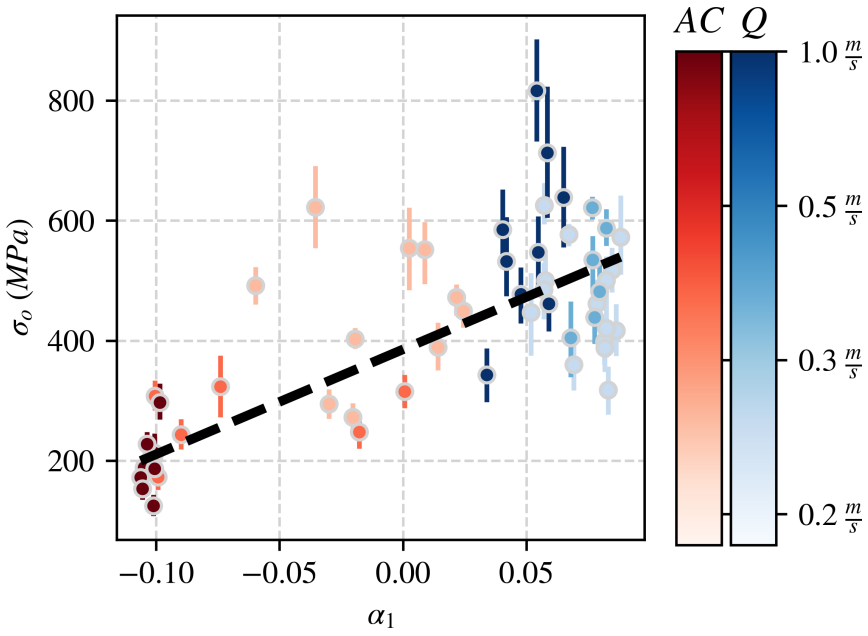

Figure 5.8: LLE reduced order PC-weight representation of the structure-property relationship. Mean values and the 95% posterior interval for each observation is shown. Pearson correlation coefficient of 0.61 with $p = 1.87 \cdot 10^{-7}$.

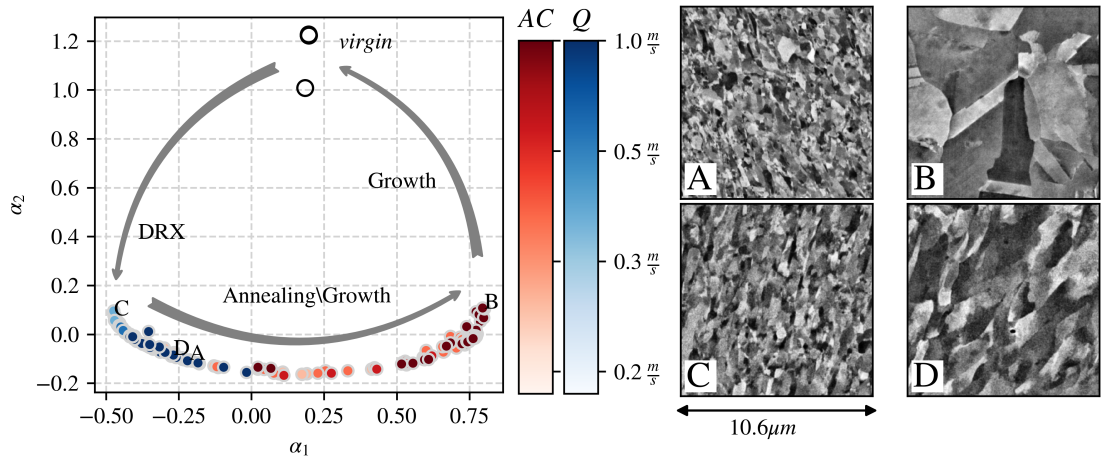

Figure 5.9: Reduced order PC-weight representation of the process-structure relationship. Select micrographs shown for comparison. (A) air cooled $V = 0.20\ m \cdot s^{-1}$, (B) air cooled $V = 1.00\ m \cdot s^{-1}$, (C) quenched $V = 0.20\ m \cdot s^{-1}$, and (D) quenched $V = 1.00\ m \cdot s^{-1}$

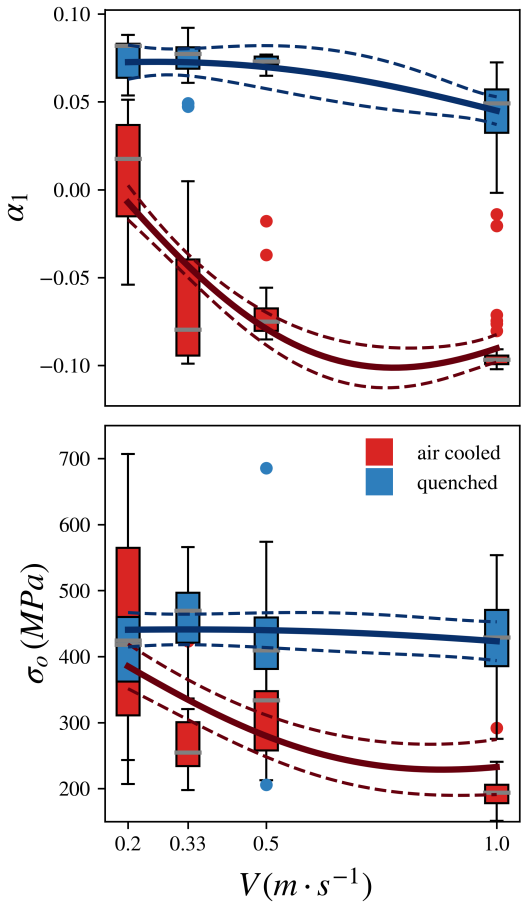

Figure 5.10: Data-driven MOGPR model fit and corresponding 95% confidence region.

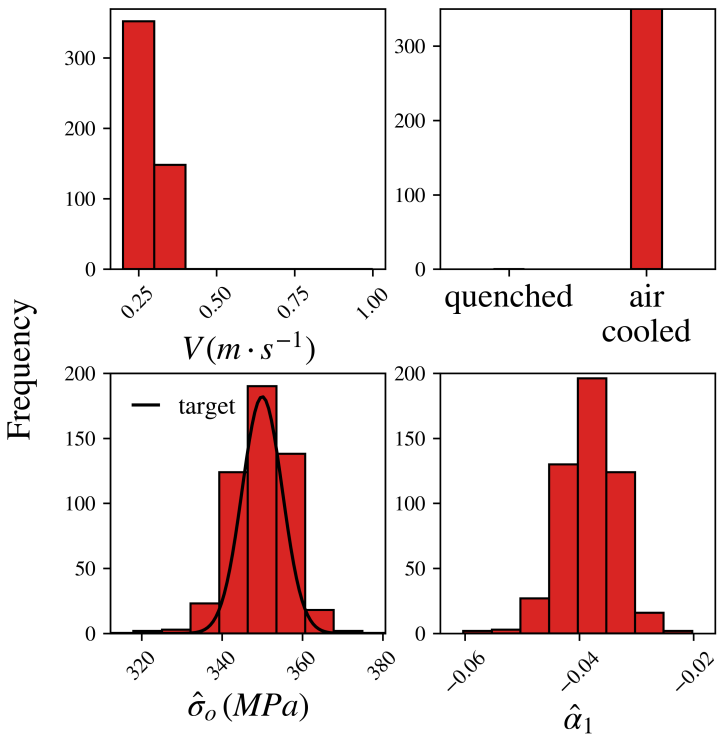

Figure 5.11: Inverse posterior density for cutting speed (V) given a desired mean of $\sigma'_o = 350\,MPa$ and tight bounds of $s' = 5\,MPa$

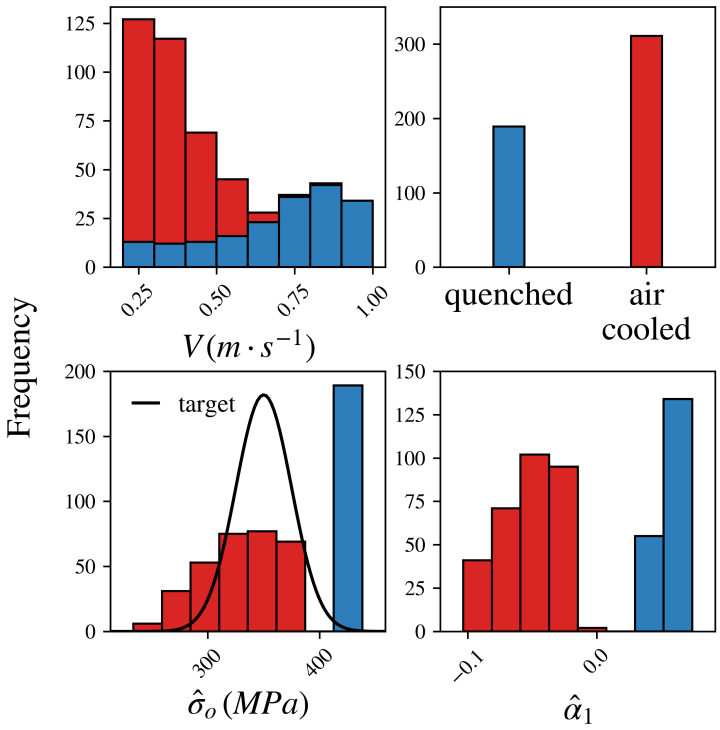

Figure 5.12: Inverse posterior density for cutting speed (V) given a desired mean of $\sigma'_o = 350\,MPa$ and looser bounds of $s' = 25\,MPa$

significant scatter with data occasionally overlapping with high speed quenched samples (D and A). Note that the data could potentially be quantified by considering the *length* along a nonlinear path spanned by the data (C to D to A to B). In Figure 5.8 the LLE projection onto a single structure variable is shown against the cutting speed. At low cutting speed for air cooled samples and at high cutting speeds for the quenched samples there is overlap between the structure measure. The quenched microstructure is less sensitive to cutting speed at lower speeds whereas there is a rapid decay in the structure variable under air cooled conditions.

The structure-property relation is shown in Figure 5.8. Here the structure is quantified using the one-dimensional LLE projection. Property is quantified using the uniaxial tensile yield strength estimate and 95% confidence bounds obtained from the inverse indentation solution. There is a clear linear trend in the data. In another work the authors found that copper subject to equal channel angular pressing (ECAP), another SPD process, obtained a saturated yield stress of $450\,MPa$ which is in agreement with our findings [145]. Shekhar et al. found machined OFHC Cu microstructures to have yield strengths between $\sim 450 - 550\,MPa$ [18]. Our results are therefore in agreement with similar SPD studies. Note that in this dataset some structure-property measurements are paired which is when an indent is subsequently imaged. This is important as otherwise only comparisons of summary statistics (mean structure, mean property) could be made across unique process parameters of which there are only eight. The pairing of data has more statistical *power* and enables greater confidence in the inference of the structure-property relationships.

The MOGPR model fit is shown in Figure 5.10. Inverse results for two considered conditions are shown in Figures 5.11 & 5.12. A single mean was considered ($350\,MPa$) and two target variances ($5^2\,MPa^2$,$25^2\,MPa^2$). These two conditions were chosen to illustrate the effect of using "tight" and "loose" bounds on the desired target properties.

5.5 Discussion

The influence of cutting speed is most apparent for the air cooled chips. The disparity between the quenched and air cooled samples shows that post deformation annealing and growth mechanisms are clearly responsible for the microstructure evolution in the air cooled samples. However, it is less clear if the effect of speed influences the DRX mechanism during deformation of the quenched chips, or if the kinetics are so fast that some growth is possible in the few seconds following deformation when the chip falls towards the quench tank and then remains heated for a short time during quenching. The Zener-Holloman parameter has often been found to correlate with the refinement imposed by DRX [19]. For larger values of Z the microstructure is expected to become more refined. However, in this study the values of Z are nearly constant for the tested conditions (Table 5.2). Hence, the intensity of the DRX mechanism is likely to be similar during all quenched experiments. Therefore, observed grain evolution for the quenched test at $V = 1.00\, m \cdot s^{-1}$ must occur after machining in the few seconds available prior to full quenching.

At the lowest cutting speed there is a great deal of scatter in the air cooled sample microstructure and properties, see Figures 5.9 & 5.10. This suggests that at the lowest cutting speed there exists significant heterogeneity in the air cooled microstructures; some images contained large fractions of refined grains yet others contained some annealed grains. The air cooled structure metric quickly decays with increasing speed. This coincides with the fraction of annealed grains, which is confirmed in Figure 5.13. Notice that at the highest cutting speed both structure and properties of the air cooled sampled shown in Figures 5.9 & 5.10 have relatively less dispersion than at any other condition. This is because at the highest speed the microstructure is nearly $\sim 100\%$ annealed grains and therefore exhibits greater structural homogeneity.

Pairing of indentation-imaging experiments was helpful for mitigating the effects of heterogeneity. Shown in Figure 5.14 are the indentation stress-strain curves corresponding

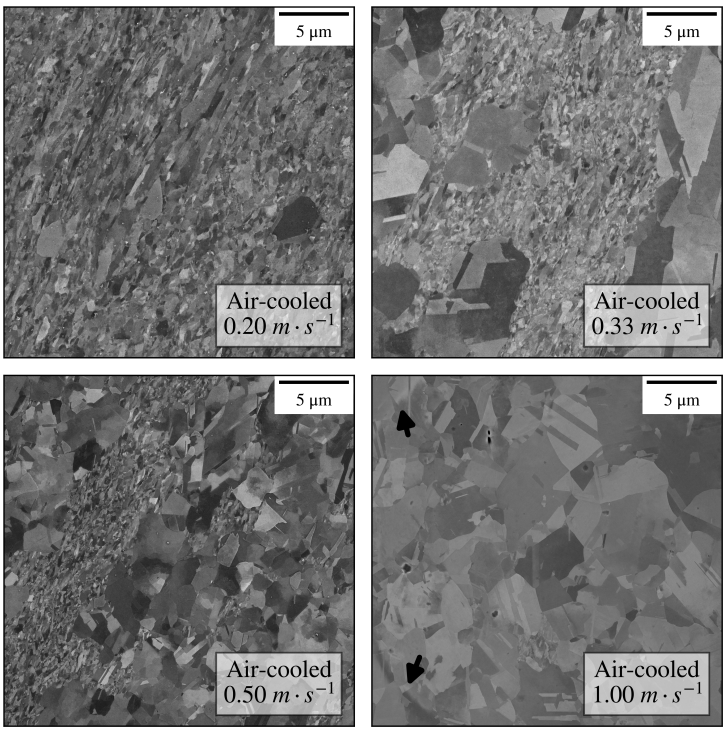

Figure 5.13: Generated air cooled microstructures. Micrograph corresponding to $V = 1.00\ m \cdot s^{-1}$ was indented and arrows are shown to indicate the contact radius edge.

to the lowest and highest cutting speeds for the quenched and air cooled samples. Visually it is clear that there is little difference between the quenched properties. The strength of the air cooled chip corresponding to the highest cutting speed is significantly lower as the microstructure has effectively been annealed. The slowest cutting speed under air cooled conditions however displays a great deal of scatter. Two images corresponding to the lowest and highest strength curves at this setting are also included. Curve 1 exhibits the highest strength and is comparable with behavior observed under the quenched conditions. The corresponding micrograph taken at the location corresponding to Curve 1 exhibits a highly refined structure. Curve 2 however exhibits much lower strength (yet higher than AC $V = 1.00\, m \cdot s^{-1}$) and the corresponding micrograph reveals that there happen to be several annealed grains at the indentation location. Therefore, the observed scatter has physical meaning as some of the source of the scatter is heterogeneity associated with indenting different statistical volume elements (SVEs). The quenched and high speed air cooled samples conversely exhibit relatively less dispersion, which is an indicator that the volume indented in these settings corresponds to representative volume elements (RVEs). Interestingly, it appears that both the fully refined and fully annealed microstructures produce RVE results, yet a mixture does not. This suggests that there are some longer range structural effects and interactions present in the bimodal material. Although the paired image-indentation strategy enables the explanation of *some* of the property dispersion, there is still non-negligible dispersion in property measurements for a given structure. Since the microstructure explained some of the property dispersion, a likely explanation is that the remaining unexplained variation is also derived from the microstructure. Of course, it is difficult to know what is *beneath* the indented surface. Furthermore, it is likely that there is also some structural information which is "unexplained" by the CLD statistics. Crystallographic heterogeneity for instance may be present even when microstructure morphology appears homogeneous (fully refined microstructures).

A linear relationship was found to exist between the yield strength and the LLE mi-

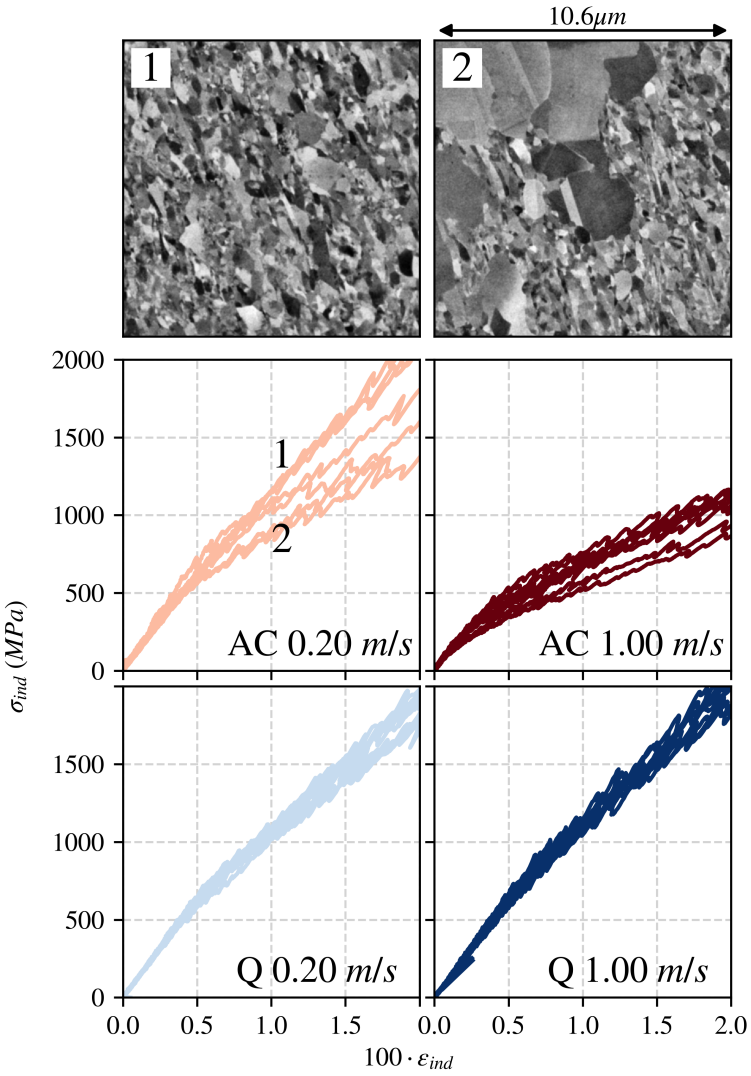

Figure 5.14: Indentation stress strain curves and corresponding micrographs. Scatter at AC 0.20 $m \cdot s^{-1}$ is driven by microstructural heterogeneity in the partially annealed structure.

crostructure descriptor, see Figure 5.8. Correspondingly the MOGPR hyperparameter, $\rho_{\alpha,\sigma}$, which controls the mean behavior of the structure-property correlation, was found to be 0.82 from the posterior estimate (Eqn. (2.29)). An empirical frequentist computation yields 0.61 with a p-value of $1.87 \cdot 10^{-7}$. The data confirms that paired data provides moderate statistical insight as $\rho_e = 0.35$. The empirical computation yields 0.27 with a p-value of 0.037. This suggests that the errors associated with structure-property variation are somewhat correlated and the correlation is significant at the 5% level. Notably the error correlation (ρ_e) is less pronounced than the mean behavior of the structure-property correlation ($\rho_{\alpha,\sigma}$). This is because the observed errors contain other sources of uncertainty not directly associated with heterogeneity. Again, one possibility is that uncertainty is introduced because it is unknown what lies *beneath* the surface during indentation and another may be associated with neglecting the crystallography of the indented region. Finally, there is always experimental error associated with traditional considerations such surface preparation, measurement errors, etc..

The inference confirms that structure-property variables are strongly linearly correlated. The linear relationship, however, is somewhat surprising considering that polycrystalline strength scales according to the well known Hall-Petch relationship which has dependence $\sim d^{-1/2}$. However, the LLE structure metric was estimated not using raw chord length measurements, which may be interpreted as a measure of grain size, but instead using *logarithmic* values. This a-priori transformation is responsible for the simple relationship discovered in the data-driven procedure.

The LLE projection suggests that some of the air cooled microstructures are "close" in morphology to the original virgin microstructure (Figure 5.8). Clearly, this is physically not the case as the virgin microstructure consists of much larger 100-300 μm grains. Recall that LLE works by finding a linear mapping *locally* in the high dimensional space. This is done by identifying nearest neighbors and then linearizing and projecting the data. However, in the original PC representation, Figure 5.9, it is clear that the virgin microstructures are far

from any of the processed structures. Therefore, the erroneous "closeness" of the virgin and air cooled LLE structure projections is a consequence of the virgin microstructures being vastly different and therefore somewhat isolated from the remaining data in the CLD feature space. A richer, more continuous, data set would likely find a better representation of the virgin microstructure using LLE. For comparing processed microstructures LLE nevertheless is well suited.

Several microstructure features and mechanisms are captured in the principal component bases shown in Figure 5.7. These include large scale isotropic features (ϕ_1), small scale isotropic features (ϕ_2), and small scale structural anisotropy features (ϕ_3). Qualitatively these data-driven quantities agree with the relevant features observed in the microstructure. Namely, there are large isotropic grains and small elongated grains. From the perspective of designing materials, the use of robust microstructure quantifiers is imperative. Consider that the alternative is to a priori define ad-hoc descriptors (mean grain size, grain aspect ratio, volume fraction, etc.), which risk not being sufficiently rich. In this work the mean grain size would have been an ineffective descriptor; there can be up to two populations of grains. In a general sense there may be more than two. Basis ϕ_3 carries *coupled* information that identifies anisotropy at small scales since the annealed structure (large scale) displays no anisotropy. A microstructure descriptor which captures any orientation preference would fail to capture this coupling. In a practical sense the use of CLD statistics generalizes the feature space such that many potential physical features may automatically be captured and identified through the data; ad-hoc descriptors requires a priori definitions. Note however that other statistics, such as two-point statistics, may contain different information [129]. For instance, the CLD statistic contains no information about *spatial* correlations. Are refined grains clustered together or are they randomly distributed among coarser grains? These disparities describe the difference between microstructures produced by continuous and discontinuous DRX [19]. The system considered in this study however is a single phase polycrystalline material and therefore it is difficult to apply two-

point statistics directly using SEM images. Recent works have done so using EBSD data [83, 84].

The proposed inverse strategy is well suited for obtaining posterior *probability densities* of candidate process parameters. Notice that different target property metrics (mean and standard deviation) yield different candidate process conditions. The posterior densities in Figures 5.11 & 5.12 become more diffuse as the target variance is increased. In Figure 5.12 the target is sufficiently diffuse that a multimodal response consisting of both air cooled and quenched process conditions is realized. This offers flexibility in process *selection*. If the design can accommodate a wide range of final properties (Figure 5.12) then a corresponding wide range of process conditions is permitted which include both quenched and air cooled conditions. Agreeing with trends from Figures 5.9 and 5.10, higher cutting speeds under quenched conditions and low cutting speeds under air cooled are preferred for the considered target of $\sigma_o = 350\,MPa$. However, if the designer wishes to have tight constraints on the final properties, the range of permissible process conditions is justifiably more constrained (Figure 5.11).

Identification of a posterior probability density alleviates some issues associated with point-estimate optimization methods often used for design [66]. Minimization of an error function for instance has no statistical interpretation which presents a problem if there are many local minima. How can local minima be compared? Is the numerically global minimum significantly "better" than other local minima or are they practically equivalent? For a manufacturer this is important as perhaps a numerically sub-optimal machining process setting may be preferred over the true global optimum. A statistical framework offers a natural way to answer these questions using the likelihood function (frequentist) or posterior density (Bayesian). Furthermore, the constrained MCMC simulated annealing strategy which we propose for identifying the inverse property $\mapsto$ process is extremely flexible and may account for multimodal solutions, non-convex constraints, etc.. However statistical approaches necessitate the identification of a statistical model (Eqn. (5.7)) which may be

non-trivial for complex systems.

5.6 Conclusions

The large strains imposed via a SPD machining process drives UFG microstructure refinement. Post-machining thermal effects however drive annealing and growth mechanisms, which produce a novel bimodal microstructure. These structures are composed of coarser annealed grains and also some retained fraction of the original UFG structure. In practice, this disparity may occur when machining with and without cutting fluids. The wide span of observed microstructures was efficiently quantified using angularly resolved CLD statistics. A clear trend emerged in the reduced-order PCA space where DRX drove grain refinement relative to the coarse virgin microstructure and post machining annealing/growth provided a return path to the coarse grain microstructure. The structure was further statistically distilled to a single variable using a nonlinear dimensionality reduction technique (LLE) which uncovered a linear structure-property trend. Uniaxial equivalent yield strength estimates for the machined microstructures were estimated using instrumented spherical nanoindentation experiments and a previously established Bayesian inference procedure. This is the first time that the uniaxial equivalent yield strength of machined microstructures has been inferred from nanoindentation experiments. A data-driven multiple output Gaussian process model was built for identifying the process-structure-property forward linkage. A Bayesian inverse strategy was proposed for identifying the inverse property $\mapsto$ process mapping.

CHAPTER 6
STATISTICAL CALIBRATION AND UNCERTAINTY QUANTIFICATION OF COMPLEX MACHINING COMPUTER MODELS

6.1 Introduction

Finite element (FE) models of machining processes have enabled the detailed simulation of complex cutting physics [160]. These numerical models serve as useful tools for the design and optimization of manufacturing processes. The FE models incorporate plasticity, contact mechanics, and heat transfer physics. Therefore, to accurately model a specific machining process, accurate models of these three components are required. A great deal of effort in the machining community has been spent on the plasticity law (flow law) [7, 5, 8, 161, 162, 163, 6] and, to a lesser extent, on the tribological behavior [2, 6]. The difficulty in establishing flow laws appropriate for machining is that the thermomechanical conditions imposed on the material during machining cannot be emulated by standard mechanical tests. During machining, strains between $1 - 10$ can be expected with strain rates on the order of $10^4 - 10^6\, s^{-1}$ and high temperatures due to plastic work. Tension/compression split-Hopkinson bar tests can impose strains typically as high as ~ 0.5 with rates as high as $10^4\, s^{-1}$ [3, 39]. Taylor-impact tests can impose higher rates, $10^5\, s^{-1}$, and larger local strains up to ~ 2. However, it is difficult to directly determine the flow stress from these experiments [164, 165]. Similarly, split-Hopkinson shear tests can impose large shear strains and strain rates [121] but the flow stress cannot be directly observed; instead a model must be invoked to indirectly infer the uniaxial equivalent flow stress. For instance, the von Mises criterion assumes that the stress may be converted via $\sigma = \sqrt{3}\tau$ and strains via $\epsilon = \gamma/\sqrt{3}$. Applying this to Johnson and Cook's original OFHC-Cu data [3] yields reasonable results. However, when comparing with data in [121] the model shows significant disparities. This

discrepancy is most likely material specific, and sensitive to the dependence of the yield surface on stress triaxiality [166], and sensitive to the specimen geometry.

Therefore, identification of material-specific plasticity law directly from machining experiments is an attractive strategy. The difficulty in doing so however is that the machining process is complex and hence, like Taylor impact and shear configuration split-Hopkinson tests, the complexity of the experiment confounds direct assessment of the flow stress relationship. The first work to calibrate a flow law to machining data is that by Özel and Zeren [8]. In this work the authors utilize the Johnson-Cook (JC) [3] model to describe the material flow stress and use Oxley's model [167] to describe the chip formation process. The use of Oxley's analytical model alleviates the need for FE models and allows for efficient iterative error minimization to obtain estimates of the unknown JC parameters. Ulutan and Özel later extended this methodology to incorporate the use of 3D FE based turning simulations to calibrate Ti6Al4V and IN100 plasticity models [161]. The optimization methodology in their work iteratively adjusts the unknown plasticity coefficients until a convergence criterion for the difference between the simulation and experimental forces is satisfied. This process is however extremely costly as acknowledged by the authors who note that each simulation required $50\,hrs$ to complete (utilizing computing resources available in 2013). In comparison, our 2D orthogonal cutting simulations require 1-6 hours per simulation depending on the material settings of each run. Özel, Arisoy, and Guo later extended this methodology to also include a microstructure sensitive plasticity law [162].

There have been a few works in the machining community which employ FE surrogate models for calibration. Kloche, Lung, and Buchkremer employed a step-wise approach for calibrating the JC model parameters where first the strain hardening terms were calibrated to uniaxial quasi-static room temperature data [12]. This was followed by a tabular/interpolation calibration of the rate hardening and thermal softening terms utilizing machining experiments and FE simulations. Tool-chip interface friction was assumed to follow empirical trends reported in the literature. The appeal of this approach is in its sim-

plicity. However, this is also the main limitation since the model decomposition is only possible for simple model forms. As the number of unknown parameters increases, it is unlikely that such a simplified linear interpolation strategy would be suitable, especially if there are strong interactions between the terms in the model. Agmell, Ahadi, and Stahl employed a Kalman filter to identify the JC model parameters [10, 11]. A Coulomb friction coefficient of 0.4 was used in all simulations. To compute the discrepancy between the FE simulations and experiments, a 4^{th} order polynomial surrogate model was built from the FE simulations. The polynomial model modeled the change in machining responses relative to a reference or nominal setting, which is similar to work found in [168, 169]. The influence of each of the model parameters in [10, 11] however was assumed to have no interactions in the surrogate model and therefore can only capture independent effects. In general, polynomials as a basis for developing surrogate models are limited to lower order polynomials and only a few FE model parameters. This is due to the curse of dimensionality i.e. as the dimensionality of the problem increases the number of terms in a polynomial expansion increases exponentially. The authors in [10, 11] circumvent this problem by neglecting interaction terms, which severely limits the utility of the surrogate model. A recent study employed the Response Surface Methodology (RSM) to build a surrogate FE model for calibration [170]. Again, this strategy is fundamentally built on regression of polynomials, which becomes intractable in high dimensions. Furthermore, RSM was developed for physical experiments, which contain observation errors. In contrast, FE model simulations are deterministic and do not have such errors. Therefore, there is a risk that RSM mistakenly fits the FE model responses to an overly smooth manifold and attributes nonlinearities present in the FE model to random error. Furthermore, these surrogate modeling approaches assume some parametric form: linear interpolation [12], 4^{th} order polynomial with no interactions [10, 11], and quadratic functions [170]. If the true response is not well described by the assumed model forms then the surrogates are inadequate. For these reasons, statisticians favor non-parametric Gaussian process models

for calibration [15, 108]. From a model calibration perspective, a limitation shared by the foregoing machining calibration studies is that they only produce point estimates and cannot yield confidence intervals for the obtained quantities. This is perhaps one reason why there exists a large range of reported JC model parameter values in the literature for the same material systems [6]. Additionally, the calibration methodologies employed in these studies seldom consider the interaction with the assumed friction model.

The advantage in utilizing a FE based machining model for identification of the constitutive model parameters is that much more complex physics can be modeled. Analytical models require the use of assumptions and simplifications to produce an easy-to-evaluate algebraic result. The trade-off is that FE simulations are computationally expensive and so the choice of model is dependent on the goals, objectives, and computational budget of the user. A nonlinear regression of a model to experimental data requires iterative (nonlinear) optimization, which renders the direct use of an FE model to be extremely costly. Therefore, traditional calibration of plasticity laws from machining experiments cannot be performed efficiently through direct use of FE models.

The seminal work of Kennedy and O'Hagan addresses this difficulty associated with calibration of computationally expensive computer codes [15]. The inefficiency of an iterative procedure, each step with multiple complex code evaluations, is alleviated instead by only evaluating the code prior to optimization. The user can decide on a reasonable number of model evaluations, which are performed over a suitable *experimental design*. From these evaluations, a Gaussian Process (GP) model of the computer code can be built. The statistical GP model can be interpreted as a surrogate model of the expensive code. The model calibration step is performed by jointly considering both experimental data and model outputs over the experimental design. GP models have good generalizing properties for emulating complex functions. Furthermore, because they are statistical in nature, GP models can also provide confidence bounds associated with function estimates. Among the large class of surrogate models, this attribute makes GPs distinctly unique. This statisti-

cal feature enables practitioners to also consider the uncertainty associated with surrogate model predictions. Just one example where this is useful is for risk-based decision making. In the context of deterministic computer codes, GP models are particularly attractive because they can be shown to be *interpolators* [14]. This is critical since the output of a deterministic simulation has no observation error and thus this information should be preserved exactly. This is distinctly different from regression methods. GP models have been utilized throughout engineering to model many complex systems. A few examples include: cardiac cells [108], large eddy combustion processes [171], knee prosthesis [172], spherical indentation [77], and machined surface roughness [173].

In this work we seek to establish an efficient method for calibrating orthogonal cutting FE models and quantifying the uncertainties of the material flow law used in the FE models. First we establish an appropriate GP model for emulating the simulated cutting and thrust forces. Then we employ a Bayesian inference framework to solve the inverse problem and establish the posterior probability distribution of the material flow law parameters. The approach is validated by performing additional FE simulations at the obtained flow law solution and comparing the simulated deformed cut-chip thicknesses to experimental observations.

6.2 Experimental methods

Tube turning experiments were performed to measure the cutting and thrust forces under idealized orthogonal cutting conditions. All experiments were performed in a CNC lathe (Okuma Spaceturn LB2000EX). Bars of Al6061-T6 (BHN 95) were machined to an outer diameter of 30.48 mm and a wall thickness of 2 mm. In order to obtain the forces over a wide range of strains, strain rates, and temperatures, cutting speeds of 12, 20, 30 and $60\,m \cdot min^{-1}$ were used. Cutting tools were custom manufactured from high speed steel (HSS) blanks with nominal rake angles of 5°, 15°, 25°. Cutting angles were confirmed via an optical comparator to be 3.39°, 14.17°, 24.56° after 10 independent measurements.

These precise values are utilized in all analyses although for the remainder of this work we will refer to the nominal values for simplicity. Each tool was manufactured to have a 8° relief angle. Both rake and relief tool surfaces were finely ground to $R_q \sim 2.5\,\mu m$ and a cutting edge radius $< 20\mu m$ was measured using a Zygo white light interferometer. A feed of 0.3 mm was used for all experiments. Physical experiments were performed over a full-factorial experiment design over the speeds and rake angles listed above. This corresponds to 12 (4×3) unique process settings.

The cutting and thrust forces were measured with a Kistler dynamometer (Model 9257B). Chips were collected after each test and the cut chip thicknesses were measured at 10 locations along these chips. Each cutting tool was utilized for four experiments at the four prescribed speeds. As the tube thickness is $2\,mm$ this necessitated at least $8\,mm$ of cutting edge length to avoid reusing potentially degraded edges. The length of the cutting edge of each tool was therefore chosen to be 20 mm. For each experiment performed, an unused part of the cutting edge was utilized to minimize the effects of tool wear or material adhesion. The tool was inspected after each experiment and there was no significant wear or material adhesion observed for any of the process settings investigated.

The experimental cutting and thrust forces were simultaneously used to calibrate the finite element model. The finite element model and calibration details are elucidated in subsequent sections. The measured chip thickness measurements were not utilized for calibration but rather for validation. We argue that this is a much more demanding validation criteria as the model is calibrated only using cutting forces. Therefore, prediction of a totally different response gives confidence that the calibration methodology and the resulting solution are accurate.

6.3 Finite element model

Orthogonal cutting experiments were simulated using ThirdWave Systems' AdvantEdge V7.0 finite element software [174]. The phenomenological Johnson-Cook (JC) material

flow model was chosen to describe the evolution of flow stress [3]. This model empirically captures rate/strain hardening and thermal softening via a multiplicative flow rule. In the machining setting, the JC model has been observed to provide insufficient softening, particularly in materials likely to form adiabatic shear bands [4, 7, 5, 175]. In response, several authors have devised phenomenological modifications to the JC flow law to simulate segmentation in machined chips [4, 175]. In our previous works, we have developed physics-based models to accommodate additional softening mechanisms [7, 5]. To mitigate against superfluous strain hardening AdvantEdge allows users to specify a hardening cut-off strain value after which no strain hardening is utilized in the computation of the flow stress [174, 160].

Although there is ample evidence suggesting that the original JC model is inadequate for machining conditions, we chose to utilize it because it is ubiquitously used throughout engineering and yet there appear to be many different reported sets of calibration parameters for identical material systems [6]. We wish to address this apparent model non-uniqueness concern through a probabilistic framework where the unknown constitutive parameters are treated as random variables that must be inferred from experimental observations (e.g. forces). Additionally, since many researchers in the machining community continue to utilize the original JC model despite its deficiencies, we believe there is practical merit in utilizing Johnson-Cook.

Finally, as a matter of simplicity for illustrating the utility of the proceeding methods, we wish to utilize a constitutive law that has practical utility and yet a minimal number of constitutive parameters. The JC model contains 5 unknown parameters, the Calamaz et al. model contains 9 [4], and physics based models may have 10 or more [5, 7, 162]. The methods employed here however are general and can accommodate many constitutive parameters but this increases the total computational burden. Furthermore, these methods may be employed towards calibration of tribological parameters in machining and even other complex process models; one example is friction stir welding where tribological cal-

ibration is difficult [176].

A simple Coulomb friction model was utilized to describe the tool-chip interaction. Note that AdvantEdge employs stick-slip criteria which limits the nodal forces exerted on the slave surface (chip) by the master surface (tool); see [160] for details. Therefore, the Coulomb friction coefficient input to the simulation may not necessarily match the apparent friction coefficient evaluated from the simulated forces. Hence, even with a simple Coulomb friction law, there is uncertainty associated with choice of the appropriate friction coefficient. We justify the use of the simple Coulomb friction law since our purpose is to illustrate the efficacy of the proposed model calibration methods in an efficient manner. In general, more complex tool-chip interface friction laws may be utilized and the statistical inference methods presented in this paper can still be used to calibrate the corresponding unknown friction law parameters.

The inputs to each FE simulation are the unknown JC constitutive model parameters $\boldsymbol{\theta} = (A,\, B,\, n,\, c,\, m)$, the Coulomb friction coefficient (μ_c), and the specified cutting speed and rake angle $\boldsymbol{s} = (V,\, \alpha)$. Together these simulation input variables will be denoted as $\boldsymbol{x}$. The simulation output parameters are the cutting and thrust forces (F_c, F_t) and the deformed or cut chip thickness (t_c). Note that only forces will be utilized for calibration and the cut chip thickness will be used for validation. Simulations were run 4 mm beyond the simulation length required to reach steady state in the cutting and thrust forces. This is to ensure that forces and chip thicknesses are unaffected by the transient response.

6.4 Statistical framework

Direct calibration of the constitutive and friction law using the FE model is prohibitively costly. Point estimates of the unknown parameters require many iterations which correspond to many FE model evaluations. Quantifying the uncertainty of constitutive parameters when using point estimate solutions requires strict normality assumptions, which are only asymptotically valid [159]. A Bayesian approach, which is more flexible in describing

complex probability distributions, requires Markov Chain Monte Carlo (MCMC) sampling [59], which is costlier than obtaining point estimate solutions. Therefore, it is clear that direct use of the FE machining model for calibration is not practical. The calibration of computationally expensive models can be performed using a Bayesian calibration strategy [15]. This approach can be interpreted as a two step approach: (1) build a computationally efficient statistical model of the FE machining model, and (2) calibrate the computationally inexpensive statistical model to experimental data. In order to build an efficient surrogate model, the FE model must be evaluated over a suitable experimental design. This experimental design is built over constitutive parameters $\boldsymbol{\theta}$, the friction coefficient μ_c, and the cutting process parameters $\boldsymbol{s}$.

A common approach in other works is to adopt a "step-wise" calibration strategy where the parameters or subsets of the parameters are calibrated sequentially. For instance, in [12] the authors first calibrate A, B, and n to room temperature quasi-static tensile test data and then use a interpolation strategy to identify the remaining c and m parameters using an FE model and machining experiments. This strategy implicitly assumes that quasi-static room temperature hardening is representative of the hardening behavior at high rates and elevated temperatures. This is however untrue at the crystal lattice scale – hardening mechanisms are strongly dependent on the strain rate and especially on thermal activation mechanisms [177]. Alternatively, A, B, and n could be chosen such that they yield accurate results at high strain rates and temperatures (typical of machining) at the expense of obtaining less accurate results at quasi-static room temperature deformation conditions. Therefore, we argue that simultaneous calibration of all parameters is better suited when the goal is to identify the best JC model *for machining*. Historically, step-wise model calibration strategies have been used in part as a matter of numerical convenience. However, this is no longer necessary due to improvements in computing. Furthermore, while a step-wise approach may be suitable for some models, e.g. a standalone JC model, it is not appropriate for models with many interacting terms.

6.4.1 Experimental design of FE simulations

In this work we employ a GP surrogate model in step (1) of the proposed Bayesian calibration procedure. To build this model we evaluate the complex FE model at a suitable number of points (DoE) and observe the outputs of interest (cutting and thrust forces). The DoE for FE model simulation experiments is distinctly different than that of physical experiments since in computer experiments there are no observation (random) errors. Therefore, *space filling* designs are favorable where the goal is to "spread" points favorably in space such that the outputs of the computer simulation experiments are optimally observed subject to some design criteria [14]. The rationale is that two close points $\boldsymbol{x}_1$ and $\boldsymbol{x}_2$ are likely to have a similar response and therefore designs containing close points are inefficient since model evaluations are costly. In this work we employ a Maximum Projection (MaxPro) design [116]. The MaxPro design spreads points in the parameter space while considering the *effect sparsity* principle. This principle suggests that for some $\boldsymbol{x} \in \mathscr{R}^p$ some of the factors (dimensions) of $\boldsymbol{x}$ may not have any influence on the response. Therefore, the spread of points must be space-filling in $\mathscr{R}^p$ but also in all projections to subspaces $\mathscr{R}^{p'}$ where $p' < p$. Latin hypercube and sliced Latin hypercube designs share this property for projections into each single factor but not for all possible subspace projections. Qualitative factors, which have a finite set of levels, can also be accounted for in the MaxPro criteria [168].

Designs are often built over unit hypercubes $\mathcal{D} \in [0, 1]^p$. In our work we have restricted the unknown quantitative variables to the values shown in Table 6.1 based on literature survey and domain expertise. The cutting process settings were treated as qualitative variables and fixed at the following levels: four cutting speeds (12, 20, 30, 60 $m \cdot min^{-1}$) and three rake angles (nominally 5°, 15°, 25°). The rake angle-cutting speed pair, $\boldsymbol{s} = (\alpha, V)$, contains a total of $S = 12$ unique pairs (full-factorial).

The machining problem however requires further care in describing the simulation input parameter space. Consider the two simulations for OFHC copper shown in Figure 6.1. The left image is a direct application of the constitutive model parameter values from the

	lower limit	upper limit
μ_c	0.1	1.0
A (MPa)	10.0	250.0
B (MPa)	0.0	500.0
n	0.0	0.5
c	0.0	0.2
m	1.3	1.5

Table 6.1: Quantitative parameter bounds.

original Johnson-Cook publication [3]; the right image is from a work that calibrated the JC model to Taylor impact data [165]. The left chip does not achieve a steady state chip thickness because the model parameters impose an unrealistic degree of strain hardening at the high strains imposed in machining. Model parameters calibrated using data from Taylor impact experiments, which impose larger strains than split-Hopkinson bar experiments, produce a much more realistic chip. Therefore, it is clear that not all combinations of A, B, and n are physically realistic in the context of machining simulation. An alternative interpretation is that there is not sufficient strain *softening* available in the JC model. As mentioned earlier, researchers have sought to use modified JC models to alleviate these concerns [4, 175]. The approach we utilize here is to estimate a suitable region in parameter space where we can avoid excessive hardening without modifying the JC flow law. This can be done using constraints obtained from machining theory, as explained below.

The shear stress acting on the shear plane, τ_s, can be calculated from the measured chip thickness and the cutting and thrust forces as

$$\begin{aligned} \tau_s &= \frac{F_s}{A_s} \\ F_s &= F_c cos\phi - F_t sin\phi \\ A_s &= \frac{w_o t}{sin\phi}, \end{aligned} \tag{6.1}$$

where ϕ is the shear angle, which can be computed from the prescribed rake angle and the chip thickness ratio. The maximum uniaxial equivalent stress is therefore $\sigma = \sqrt{3}\tau_s$. The

maximum value over all experimental observations made in the current work on machining of Al6061-T6 was found to be 401 MPa. The imposed uniaxial strain at this condition was $\epsilon^* = \gamma/\sqrt{3} = 2.88$. Therefore, we impose the constraint $(A + B\epsilon^*)^n < 500\ MPa$ with $\epsilon^* = 3$, which is slightly more conservative than our observation. However, we observed that this constraint is still insufficient for avoiding excessive material hardening behavior. Consider that A is low while B is moderate/large (relative to A) and n is moderate/large. Then, it is possible that although the constraint on flow stress is satisfied, the hardening rate may still be too high. The consequent effect is that the FE model will continue to "plough" rather than shear the material, as shown in Figure 6.1a. Mechanistically, we believe this is because it is more more energetically favorable to plastically deform fresh material (with low flow stress A) than it is to deform hardened material with high flow stress ($A + B\epsilon^n$). This disparity is more severe for parameters displaying a high rate of hardening relative to the initial stress. In these cases, deformation is accommodated by material deformation increasingly further away from the tool tip. Therefore, an additional constraint on the hardening rate is required. We heuristically chose $(\epsilon_i/\epsilon^*)^{n-1} < 10$, which describes that the hardening rate ($Bn\epsilon_i^{n-1}$) at some incipient value of strain ϵ_i must be $10\times$ higher than the corresponding hardening rate at ϵ^* ($Bn\left[\epsilon^*\right]^{n-1}$). In this work we use $\epsilon_i = 0.01$. Although this is a heuristic, some kind of constraint is needed over the experimental design $\mathcal{D}$ otherwise we risk wasting many model evaluations to produce non-informative responses like that shown in Figure 6.1a. As we will show later in the results, both of these constraints are reasonable.All simulations were run utilizing a modulus of elasticity of 70 GPa and a melting point of 582 $^\circ C$. The remaining parameter settings we prescribed according to a MaxPro design subject to constraints in the parameter space [155, 156]. In the computer experiments community, a popular heuristic for deciding the total number of runs is that $10d$ runs is sufficient where d is the dimensionality of the model input ($\boldsymbol{x}$) [14]. In this work $\boldsymbol{x} \in \mathscr{R}^9$ and so a 100-run design was generated. All paired combinations are shown in Figure 6.2. The design contains empty spaces in the

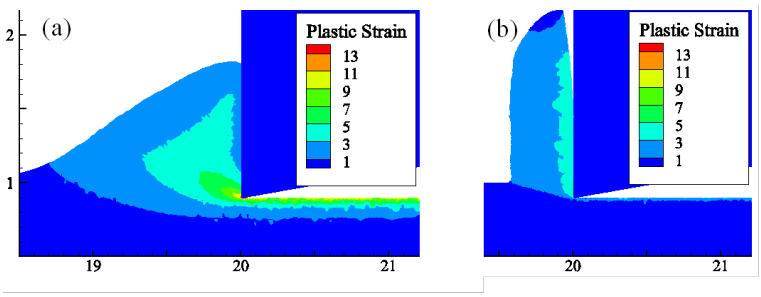

Figure 6.1: OFHC copper simulations at $\alpha = 0°$, $V = 12\,m \cdot min^{-1}$ and feed $f = 0.1\,mm \cdot rev^{-1}$ (a) application of constitutive parameters from original JC work with $n = 0.31$ [3] (b) constitutive parameters derived from Taylor impact experiments $n = 0.03$ [165]

hypercube which illustrates the constraints imposed on A,B, and n. These empty regions correspond to model realizations that exhibit (1) unrealistically high flow stresses, and (2) unrealistically high strain hardening rates.

6.4.2 Surrogate gaussian process model

The surrogate multiple output nonstationary surrogate model built from evaluations of the complex FE code was developed using the methods outlined in Section 2.4.4. Here a few additional details will be included.

The weight function used in equations 2.4.2 and 2.4.4 controls the nonstationary behavior of the composite GP. In this work we use a weight function which includes dependence on the rake angle, α, and the Coulomb friction coefficient, μ_c, as well as interactions between these two,

$$\begin{aligned} w_k(\boldsymbol{x}) &= w_k(\alpha, \mu_c) \\ &\propto exp\left(-\gamma_w I(\alpha \neq \alpha_k) - \phi_w(\mu_c - \mu_k)^2\right). \end{aligned} \tag{6.2}$$

Where $k = 1, \ldots, 9$ and α_k and μ_k take on three distinct values each (α_k=5,15,25 and μ_k=1/6,1/2,5/6) but are coded in a particular fashion, e.g. $(\alpha_1, \mu_1) = (5, 1/6)$, $(\alpha_2, \mu_2) = (5, 1/2)$, $(\alpha_3, \mu_3) = (5, 5/6)$, $(\alpha_4, \mu_4) = (15, 1/6)$, etc.. $I(\alpha \neq \alpha_k)$ is an indicator function that is 1 when $\alpha \neq \alpha_k$ and 0 otherwise. Note that an additional constraint is that $\sum_k w_k =$

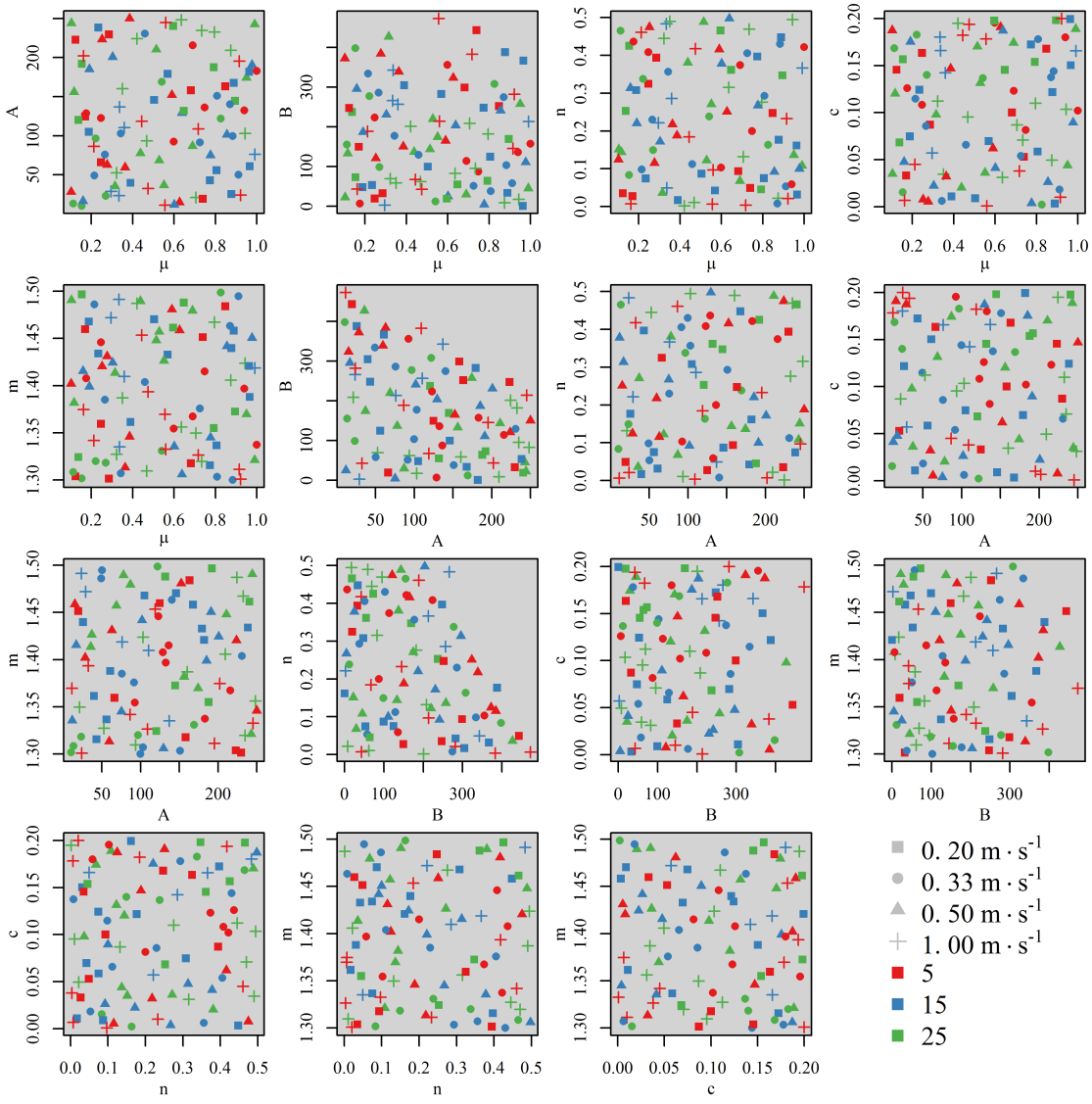

Figure 6.2: Two-dimensional projections of the generated 100-run MaxPro experimental design.

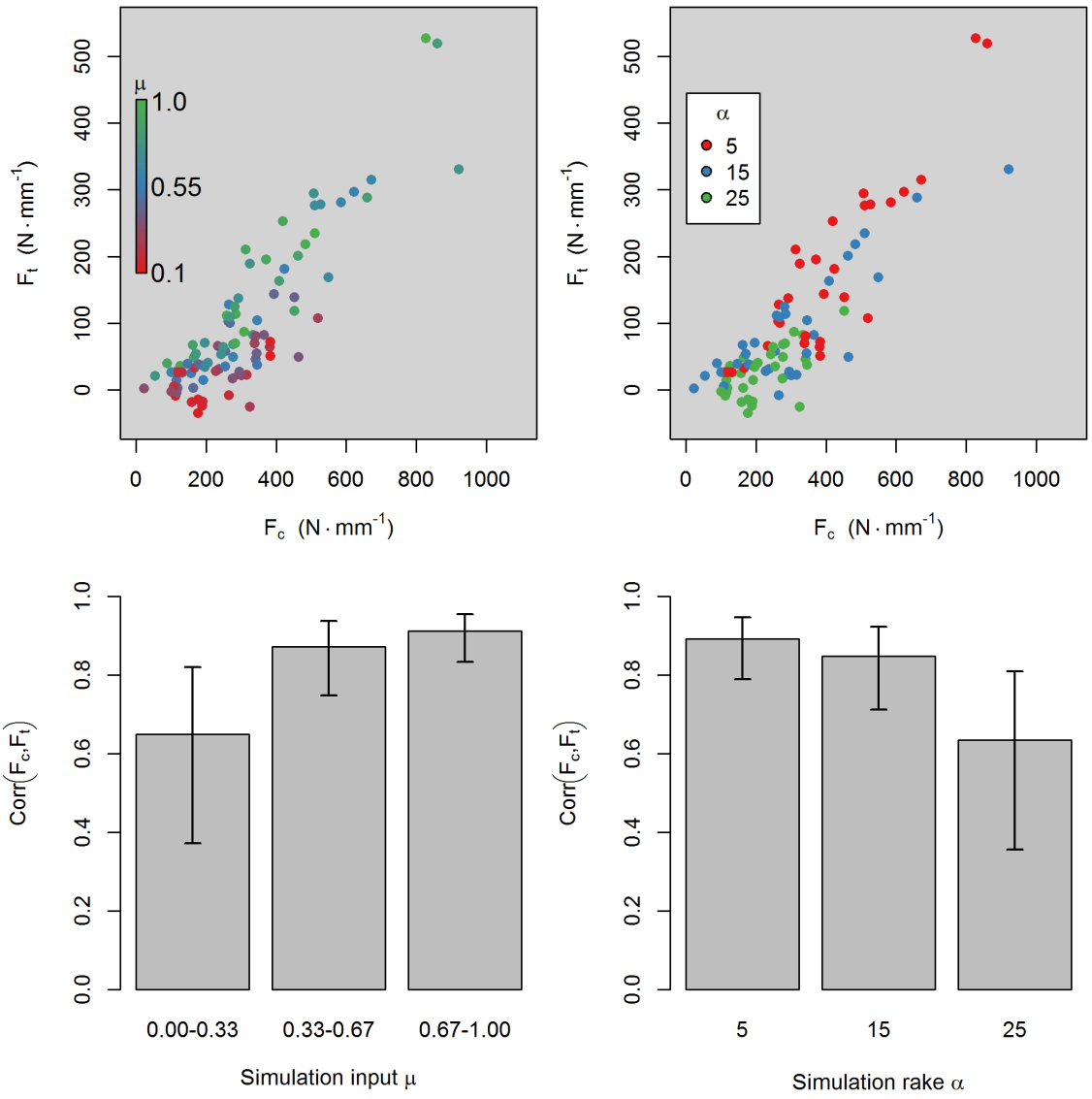

Figure 6.3: Thrust and cutting force correlation trends against Column friction coefficient and rake angle.

1 and thus the expression in equation 6.2, which only defines proportionality, must be normalized by $\sum_k w_k$.

Consider that N simulations have been run over a suitable design, $\mathcal{D}$, and a GP model is to be built from the data. Each simulation produces both cutting and thrust forces and therefore we have $\boldsymbol{F}_c = (F_{c,1}, \ldots, F_{c,N})^T$ and similarly $\boldsymbol{F}_t$. Then the data can be simultaneously modeled as a jointly distributed multivariate normal random variable with a corresponding mean function and covariance matrix,

$$\boldsymbol{y} = \begin{pmatrix} \boldsymbol{F}_c \\ \boldsymbol{F}_t \end{pmatrix} \sim \mathcal{N}(\boldsymbol{\mu}, \boldsymbol{C}) \tag{6.3}$$

$$\boldsymbol{\mu} = \begin{bmatrix} \boldsymbol{F} & \boldsymbol{0} \\ \boldsymbol{0} & \boldsymbol{F} \end{bmatrix} \begin{pmatrix} \boldsymbol{\beta}_c \\ \boldsymbol{\beta}_t \end{pmatrix} \tag{6.4}$$

$$\boldsymbol{C} = \sum_k^K \boldsymbol{S}_k \otimes \left(\boldsymbol{w}_k^T \boldsymbol{w}_k \circ \boldsymbol{R} \right) .. \tag{6.5}$$

The weight vectors consist of weights corresponding to each point in the design e.g. $\boldsymbol{w}_k = \left(w_k(\boldsymbol{x}_1), w_k(\boldsymbol{x}_2), \ldots, w_k(\boldsymbol{x}_N) \right)^T$.

The GP surrogate FE model is built from the observed FE model simulation outputs $\boldsymbol{y}$ evaluated over the design $\mathcal{D}$. This is done through estimation of the unknown hyperparameters $\boldsymbol{\Phi} = (\boldsymbol{\phi}, \phi_w, \boldsymbol{\beta}_c, \boldsymbol{\beta}_t, \boldsymbol{\gamma}, \gamma_w, \boldsymbol{S}_1, \ldots, \boldsymbol{S}_K)$. In general, these hyperparameters can be considered to be random variables and therefore a posterior sampling of $\boldsymbol{\Phi}$ can be obtained via Markov Chain Monte Carlo (MCMC) sampling. However, MCMC sampling of many parameters corresponding to a complex model can be slow and therefore practitioners often approximate the hyperparameters with a single point estimate $\hat{\boldsymbol{\Phi}}$ [15, 14]. The data is interpreted as coming from a random GP and therefore is distributed according to a multivariate normal distribution as shown in equation 6.3. Hence, a reasonable point estimate $\hat{\boldsymbol{\Phi}}$ would correspond to the maximum likelihood estimate (MLE). A Bayesian approach considers

prior beliefs on the hyperparameters and is referred to as the maximum a posteriori (MAP) estimate. No priors were imposed on $\boldsymbol{\beta}_c$ and $\boldsymbol{\beta}_t$. Weakly informative priors were used on the variance and correlation hyperparameters, which improve the stability of the statistical model and reduce the size of the hyperparameter search space. Point estimates of the hyperparameters can thus be obtained via

$$\begin{aligned}\hat{\boldsymbol{\Phi}} &= \arg\max_{\boldsymbol{\Phi}} \; p\left(\boldsymbol{\Phi}|\boldsymbol{F}_c, \boldsymbol{F}_t\right) \\ &= \arg\max_{\boldsymbol{\Phi}} \; p\left(\boldsymbol{F}_c, \boldsymbol{F}_t|\boldsymbol{\Phi}\right)\pi\left(\boldsymbol{\Phi}\right),\end{aligned} \tag{6.6}$$

where $p\left(\boldsymbol{F}_c, \boldsymbol{F}_t|\hat{\boldsymbol{\Phi}}\right)$ is the likelihood function for the multivariate normal in equation 6.3. $\pi\left(\hat{\boldsymbol{\Phi}}\right)$ are priors on the hyperparameters, which are assumed to be independent of one another e.g. $\pi\left(\hat{\boldsymbol{\Phi}}\right) = \pi\left(\boldsymbol{\phi}\right)\cdot\pi\left(\phi_w\right)\cdots\pi\left(\boldsymbol{S}_K\right)$.

Consider now that an estimate of the response at a new point $\boldsymbol{x}$ is desired. The conditional multivariate normal formula may be used to derive an expression for the conditional expectation,

$$\begin{aligned}\begin{pmatrix} F_c\left(\boldsymbol{x}\right) \\ F_t\left(\boldsymbol{x}\right)\end{pmatrix} &= \mu\left(\boldsymbol{x}\right) + \widetilde{\boldsymbol{r}}\left(\boldsymbol{x}\right)^T \boldsymbol{C}^{-1}\left(\boldsymbol{y}-\boldsymbol{\mu}\right) \\ \widetilde{\boldsymbol{r}}\left(\boldsymbol{x}\right) &= \sum_k^K \boldsymbol{S}_k \otimes \left(\boldsymbol{w}_k^T w_k\left(\boldsymbol{x}\right)\circ \boldsymbol{r}\left(\boldsymbol{x}\right)\right),\end{aligned} \tag{6.7}$$

where the spatial correlations between the desired point $\boldsymbol{x}$ and the points in the design $\boldsymbol{x}_i$ for $i = 1, 2, \ldots, N$ are captured through the correlation vector $r_i\left(\boldsymbol{x}\right) = R\left(\boldsymbol{x}, \boldsymbol{x}_i\right)$. An estimate of the variance associated with the conditional expectation can also computed from,

$$\begin{aligned}Var\left(F_c\left(\boldsymbol{x}\right), F_t\left(\boldsymbol{x}\right)\right) &= \hat{\boldsymbol{S}} \\ &= \sum_k^K w_k^2\left(\boldsymbol{x}\right)\boldsymbol{S}_k - \widetilde{\boldsymbol{r}}\left(\boldsymbol{x}\right)^T \boldsymbol{C}^{-1}\widetilde{\boldsymbol{r}}\left(\boldsymbol{x}\right).\end{aligned} \tag{6.8}$$

The statistical model was built in *Stan* [64], a statistical programming language, and evaluated using *RStan* [157] the *R*-language interface for *Stan*. The *Stan* optimizer was

used to identify the MAP estimates of the hyperparameters $\hat{\mathbf{\Phi}}$.

The leave-one-out cross validation results are shown in Figure 6.4. Surrogates were also built using models previously discussed in the literature review [12, 170, 10, 11] as well as a kernel regression model using a radial basis function (RBF) [178]. Leave-one-out cross validation statistics of all the models considered are shown in Table 6.2. The 4^{th} order polynomial strategy [10, 11] was particularly inferior because our design is not suitable for their model. Our design considers interactions while their model neglects interactions. Therefore, fitting a interaction-free model to data containing interactions produces a model that performs poorly. Including interactions requires 5^8 terms (multiplicative model with 4^{th} order polynomials for each of the 8 model variables) and is therefore impractical. These results show that the nonstationary GP model reasonably emulates the FE model and is therefore preferred over all other models considered here. From the root mean squared predicted error (RMSPE), on average, the surrogate model can be expected to produce estimates that are accurate to within 23.4 $N \cdot mm^{-1}$ and 10.2 $N \cdot mm^{-1}$ for the cutting and thrust forces, respectively. The cutting-thrust correlation coefficient ($\rho_{c,t}$) from FE simulations as well as the correlation predictions from the nonstationary surrogate model are shown in Figure 6.5. These results illustrate the surrogate model's ability to model nonstationary behavior present in the FE model output. For comparison, a stationary GP model was built and the leave-one-out cross validation RMSPE for the cutting and thrust forces were found to be 56.9 $N \cdot mm^{-1}$ and 29.3 $N \cdot mm^{-1}$. The nonstationary model's cutting and thrust force predictions yield improvements of 58% and 65%, respectively, over the stationary model. Clearly, a stationary model is insufficient since it cannot capture the nonstationary relationships produced by the FE model.

6.4.3 Bayesian inference

This work seeks to infer the unknown material constitutive model parameters directly from machining experiments while simultaneously capturing parameter uncertainty. This un-

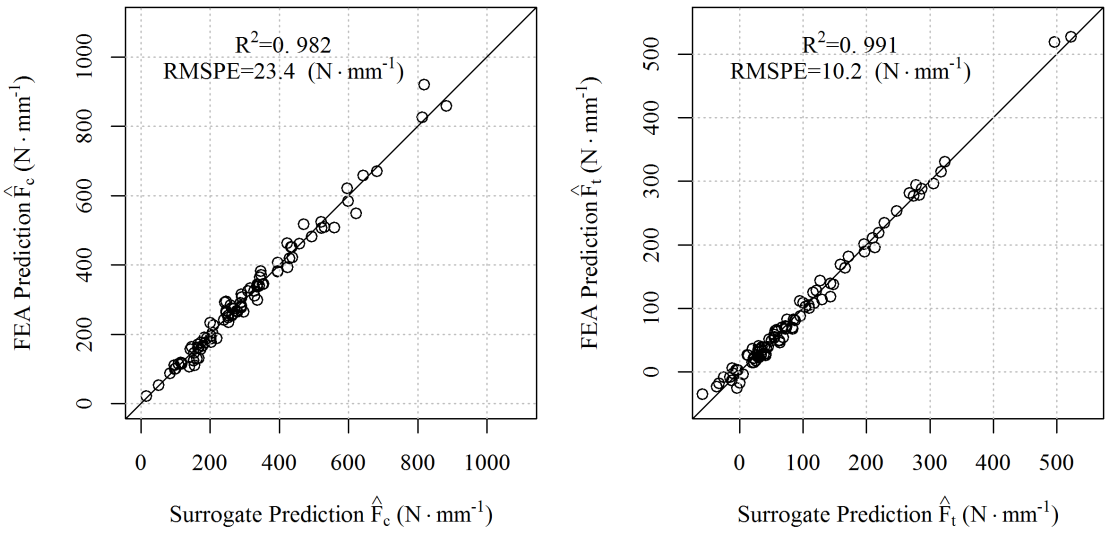

Figure 6.4: Leave-one-out cross validation parity plot for the trained GP model.

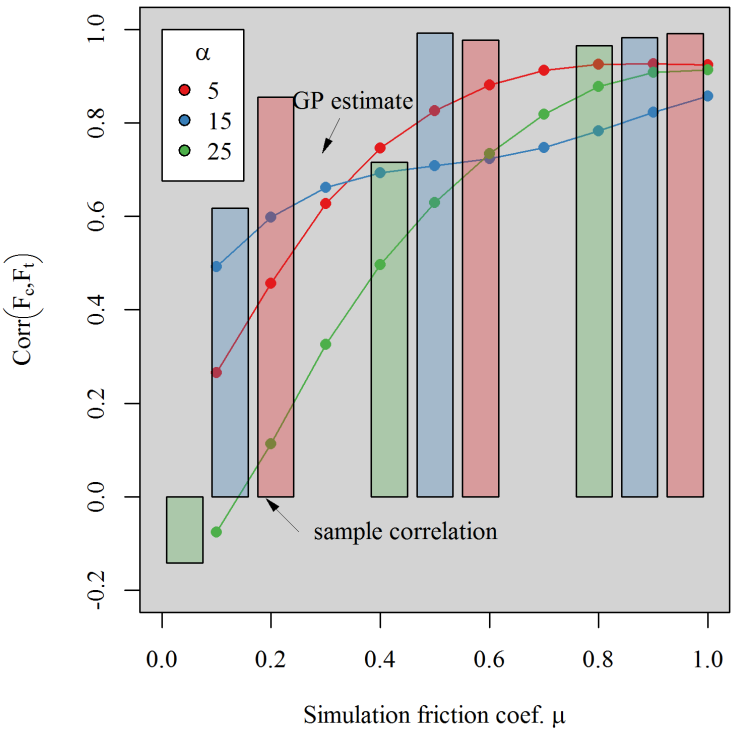

Figure 6.5: Experimental (sample) correlations and predictions from the trained nonstationary GP model.

	RMSPE ($N \cdot mm^{-1}$)	
	F_x	F_y
nonstationary GP	23.4	10.20
stationary GP	56.9	29.3
RBF kernel regression	96.19	58.27
RSM [170]	63.42	39.45
4^{th} order polynomial interaction-free [10, 11]	453.4	653.3

Table 6.2: Leave-one-out cross validation results for several surrogate models.

certainty can be inherited from various sources including observation uncertainty, model inadequacy, model non-uniqueness, etc.. The quantified material model uncertainties may be used to determine the uncertainty in the predicted process responses such as cutting forces, cutting temperatures, etc. [169]. To infer the constitutive behavior we adopt a parametric approach where we assume the constitutive behavior can be modeled as a parametric function (the JC model). The inference is performed via model calibration where values for the unknown model parameters are estimated from physical experiments. Note that recent works relax this assumption and consider nonparametric calibration of *functions* rather than scalar-valued parameters [108]. However, these methods require considerable complexity and are therefore not employed here.

Physical experiments are performed at various process settings and the cutting and thrust forces are measured, which include repeated experiments. Physically, we expect the friction coefficient to vary for different combinations of the process settings and therefore it is inappropriate to assume one μ_c for all experiments. Hence, we adopt an interpretation where each unique process setting is paired with an unknown friction coefficient. In this work there are $S = 12$ unique $\boldsymbol{s} = (\alpha, V)$ pairs of process settings, thus there are 12 unknown friction coefficients that need to be estimated statistically ($\boldsymbol{\mu}_c$). In the statistics community this type of variable, one which exists but cannot be directly observed, is referred to as a *latent* or *lurking* variable. The unknown constitutive parameters may also be considered latent variables since they cannot be directly observed. Experimental obser-

vations consist of pairs of process-force values e.g. $\left\{\boldsymbol{s}_i, (\boldsymbol{F}_{c,exp}, \boldsymbol{F}_{t,exp})_i\right\}$. Now consider the following statistical model which relates the experimental observations to the Gaussian Process model in equations 6.3-6.5,

$$\begin{bmatrix} F_{c,exp}\left(\boldsymbol{s};\mu_c\right) \\ F_{t,exp}\left(\boldsymbol{s};\mu_c\right) \end{bmatrix} = \begin{bmatrix} F_c\left(\boldsymbol{s},\mu_c,\boldsymbol{\theta}^*\right) \\ F_t\left(\boldsymbol{s},\mu_c,\boldsymbol{\theta}^*\right) \end{bmatrix} + \boldsymbol{\epsilon}\left(\boldsymbol{s}\right). \tag{6.9}$$

Here $\boldsymbol{\theta}^*$ are the unknown *true* constitutive model parameters. The finite element model accepts as inputs the process settings, $\boldsymbol{s}$, Coulomb friction coefficient μ_c, and the constitutive model parameters $\boldsymbol{\theta}$. Together these variables constitute the previously utilized $\boldsymbol{x}$. A distinction is made in the experimental observations; $\boldsymbol{s}$ is prescribed and μ_c is present but unobservable. The interpretation of this statistical model is that experimental observations are physical realizations of the model subject to some corruption through observation error $\boldsymbol{\epsilon}\left(\boldsymbol{s}\right)$. The observation errors are assumed to be independent but only identically distributed within a particular process setting $\boldsymbol{s}$; the observation error variance may change for different process settings. The noise is assumed to follow $\boldsymbol{\epsilon}(\boldsymbol{s}) \sim \mathcal{N}\left(\boldsymbol{0}, diag\left[\sigma_c^2(\boldsymbol{s}), \sigma_t^2(\boldsymbol{s})\right]\right)$. For $S = 12$ unique process settings there are 24 unknown variance terms.

Now consider that n physical experiments are performed. Once again we invoke the use of a multivariate normal random variable to model physical and numerical experiments jointly,

$$\begin{pmatrix} \boldsymbol{F}_c \\ \boldsymbol{F}_t \\ \boldsymbol{F}_{c,exp} \\ \boldsymbol{F}_{t,exp} \end{pmatrix} \sim \mathcal{N}\left(\begin{pmatrix} \mu \\ \mu_{exp} \end{pmatrix}, \begin{bmatrix} \boldsymbol{C} & \boldsymbol{C}_{12} \\ \boldsymbol{C}_{12}^T & \boldsymbol{C}_{22} \end{bmatrix}\right), \tag{6.10}$$

where $\boldsymbol{C}$ is the $2N \times 2N$ covariance matrix from equation 6.5, which describes the covariance between simulations, $\boldsymbol{C}_{22}$ is a $2n \times 2n$ matrix that describes the covariance between experiments, and $\boldsymbol{C}_{12}$ is a $2N \times 2n$ matrix which describes the cross-correlations between

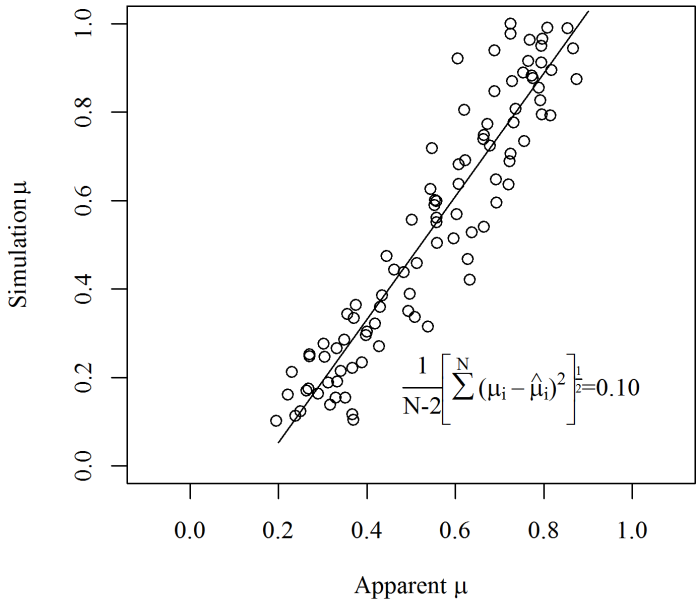

Figure 6.6: Apparent friction coefficient versus simulation input Coulomb friction.

experiments and simulations. These matrices follow the form of equation 6.5,

$$\begin{aligned} \boldsymbol{C}_{12} &= \sum_{k}^{K} \boldsymbol{S}_k \otimes \left(\boldsymbol{w}_{k,N}^T \boldsymbol{w}_{k,n} \circ \boldsymbol{R}_{N\times n} \right) \\ \boldsymbol{C}_{22} &= \sum_{k}^{K} \boldsymbol{S}_k \otimes \left(\boldsymbol{w}_{k,n}^T \boldsymbol{w}_{k,n} \circ \boldsymbol{R}_{n\times n} \right) \end{aligned} \tag{6.11}$$

where indices's are introduced to clarify the dimensions of all relevant quantities. For instance $\boldsymbol{w}_{k,n}$ is the length-n weight vector evaluated at each of the n experimental settings. $\boldsymbol{R}_{N\times n}$ is an $N \times n$ matrix where R_{ij} corresponds to the correlation function evaluated at the i^{th} simulation and j^{th} experimental settings. Note that $\boldsymbol{w}_{k,n}$, $\boldsymbol{C}_{12}$, and $\boldsymbol{C}_{22}$ are functions of the latent variables $\boldsymbol{\mu}_c$ and $\boldsymbol{\theta}^*$.

For inference of the unknown parameters $\boldsymbol{\mu}_c$ and $\boldsymbol{\theta}^*$ we adopt a Bayesian framework. Bayesian methods enable the inclusion of *prior* beliefs into the statistical machinery. In the case of machining, this is relevant as the apparent friction coefficient computed from the

measured forces is a good estimate of the Coulomb friction coefficient. Shown in Figure 6.6 is the relationship between the prescribed Coulomb friction coefficient input to the simulations and the corresponding apparent friction coefficient computed from the simulated forces. The relationship suggests that the apparent friction coefficient is *close* to the true underlying Coulomb friction coefficient and therefore may be used as an informative prior during inference. Bayes formula allows for the inference of the posterior density of $\boldsymbol{\theta}^*$ and $\boldsymbol{\mu}_c$ conditional on the experimental observations to be stated as,

$$\begin{aligned} p\left(\boldsymbol{\theta}^*, \boldsymbol{\mu}_c, \boldsymbol{\sigma}, \boldsymbol{\Phi} | \boldsymbol{F}_{c,exp}, \boldsymbol{F}_{t,exp}, \boldsymbol{F}_c, \boldsymbol{F}_t\right) = \\ \frac{p\left(\boldsymbol{F}_{c,exp}, \boldsymbol{F}_{t,exp}, \boldsymbol{F}_c, \boldsymbol{F}_t | \boldsymbol{\theta}^*, \boldsymbol{\mu}_c, \boldsymbol{\sigma}, \boldsymbol{\Phi}\right) \pi\left(\boldsymbol{\theta}^*, \boldsymbol{\mu}_c, \boldsymbol{\sigma}, \boldsymbol{\Phi}\right)}{p\left(\boldsymbol{F}_{c,exp}, \boldsymbol{F}_{t,exp}, \boldsymbol{F}_c, \boldsymbol{F}_t\right)} \\ \propto p\left(\boldsymbol{F}_{c,exp}, \boldsymbol{F}_{t,exp}, \boldsymbol{F}_c, \boldsymbol{F}_t | \boldsymbol{\theta}^*, \boldsymbol{\mu}_c, \boldsymbol{\sigma}, \boldsymbol{\Phi}\right) \pi\left(\boldsymbol{\theta}^*, \boldsymbol{\mu}_c, \boldsymbol{\sigma}, \boldsymbol{\Phi}\right), \quad (6.12) \end{aligned}$$

where $\pi\left(\boldsymbol{\theta}^*, \boldsymbol{\mu}_c, \boldsymbol{\sigma}, \boldsymbol{\Phi}\right)$ is the joint prior density placed on $\boldsymbol{\theta}^*$, $\boldsymbol{\mu}_c$, $\boldsymbol{\sigma}$, and $\boldsymbol{\Phi}$.
$p\left(\boldsymbol{F}_{c,exp}, \boldsymbol{F}_{t,exp}, \boldsymbol{F}_c, \boldsymbol{F}_t | \boldsymbol{\theta}^*, \boldsymbol{\mu}_c, \boldsymbol{\sigma}, \boldsymbol{\Phi}\right)$ is the likelihood function for the normally distributed random vector in equation 6.10. Note that the denominator, referred to as the model *evidence*, is not a function of any of the unknown parameters and is simply needed for normalizing the posterior density. Since sampling strategies do not require it for obtaining posterior samples, it may be neglected.

Direct inference of the quantities on the left-hand size of equation 6.12 is computationally intractable and therefore a few additional simplifications are required to make the calibration efficient [15]. Experimental data, simulation results, and all necessary calibration codes are available online [158].

6.4.4 Numerical implementation of calibration method

The expression in equation 6.12 is *fully* Bayesian in the sense that it describes the conditional probability of *all* unknown parameters, including surrogate hyperparameters, as a

function of both physical and simulated machining forces; this accounts for all of the uncertainty in all unknown parameters. A sample from the joint-posterior can be obtained by MCMC sampling. However, for complex models with many parameters MCMC sampling can become prohibitively slow. Therefore, inference of *all* parameters is computationally burdensome and renders this problem intractable. Furthermore, only uncertainty in the frictional and constitutive parameters is desired. Therefore, a few assumptions are necessary to improve computational efficiency: (1) hyperparameters corresponding to the surrogate model will be fixed according to $\hat{\boldsymbol{\Phi}} = \arg\max_{\boldsymbol{\Phi}} \; p\left(\boldsymbol{\Phi}|\boldsymbol{F}_c, \boldsymbol{F}_t\right)$, (2) experimental error variances will be fixed at the corresponding MAP values e.g. $\hat{\boldsymbol{\sigma}} = \arg\max_{\boldsymbol{\sigma}} \; p\left(\boldsymbol{\theta}^*, \boldsymbol{\mu}_c, \boldsymbol{\sigma}|\boldsymbol{F}_{c,exp}, \boldsymbol{F}_{t,exp}, \boldsymbol{F}_c, \boldsymbol{F}_t, \hat{\boldsymbol{\Phi}}\right)$, (3) the posterior distribution will be derived using the *mean* machining forces for each unique value of the process parameters (cutting speed and rake angle) $\boldsymbol{s}$. The cost of these assumptions is that some uncertainty is neglected e.g. uncertainty in the surrogate model (via its hyperparameters). The exclusion of these uncertainties propagates into other parameters resulting in optimistic uncertainty estimates corresponding to $\boldsymbol{\theta}^*$ and $\boldsymbol{\mu}_c$. However, there are benefits of these simplifications. Assumption (1) allows the surrogate model to be separately built using a point-estimate for $\hat{\boldsymbol{\Phi}}$, which is much more efficient than MCMC sampling of a large joint model. Assumption (2) again reduces the number of parameters involved in the MCMC sampling by setting experimental variances to appropriate point estimates. Noise parameter point estimates in (2) are obtained from information present in experimental repetitions at each unique process setting, therefore with $\hat{\boldsymbol{\sigma}}$ fixed information from the mean response at each unique process condition is sufficient for MCMC sampling from the poisterior of $\boldsymbol{\theta}^*, \boldsymbol{\mu}_c$. Hence, the variance corresponding to the mean cutting force responses $\bar{F}_{c,exp,i}$ at process setting $\boldsymbol{s}_i$ is $\sigma^2_{c,i}/n_i$ for $i = 1, \ldots, S$ where n_i is the total number of repetitions at setting $\boldsymbol{s}_i$. The analogue is true for the thrust forces as well. The advantage of this simplification is associated with distilling the total number of experimental data points from $n = \sum_i^S n_i$ to S. This decreases the size of the covariance matrix in equation 6.11, which needs to be inverted at

each MCMC step thus improving inference efficiency. The updated posterior is therefore

$$p\left(\boldsymbol{\theta}^*, \boldsymbol{\mu}_c | \bar{\boldsymbol{F}}_{c,exp}, \bar{\boldsymbol{F}}_{t,exp}, \boldsymbol{F}_c, \boldsymbol{F}_t, \hat{\boldsymbol{\sigma}}, \hat{\boldsymbol{\Phi}}\right) \propto$$
$$p\left(\bar{\boldsymbol{F}}_{c,exp}, \bar{\boldsymbol{F}}_{t,exp}, \boldsymbol{F}_c, \boldsymbol{F}_t | \boldsymbol{\theta}^*, \boldsymbol{\mu}_c, \hat{\boldsymbol{\sigma}}, \hat{\boldsymbol{\Phi}}\right) \pi\left(\boldsymbol{\theta}^*, \boldsymbol{\mu}_c | \hat{\boldsymbol{\sigma}}, \hat{\boldsymbol{\Phi}}\right), \quad (6.13)$$

where the bar refers to the computed mean responses over all repetitions at each unique process setting. Note that assumption (1) fixes $\boldsymbol{C}$ in equation 6.10 since $\boldsymbol{C}$ is only a function of $\boldsymbol{\Phi}$. Therefore, the joint covariance inverse, required to compute the likelihood function corresponding to equations 6.12 and 6.13, can be obtained more efficiently by using the 2×2 block matrix identity and applying the Sherman-Morrison-Woodbury formula,

$$\begin{bmatrix} \boldsymbol{C} & \boldsymbol{C}_{12} \\ \boldsymbol{C}_{12}^T & \boldsymbol{C}_{22} \end{bmatrix}^{-1} =$$
$$\begin{bmatrix} \boldsymbol{C}^{-1} + \boldsymbol{B}\left(\boldsymbol{C}_{22} - \boldsymbol{C}_{12}^T\boldsymbol{B}\right)^{-1}\boldsymbol{B}^T & -\boldsymbol{B}\left(\boldsymbol{C}_{22} - \boldsymbol{C}_{12}^T\boldsymbol{B}\right)^{-1} \\ -\left(\boldsymbol{C}_{22} - \boldsymbol{C}_{12}^T\boldsymbol{B}\right)^{-1}\boldsymbol{B}^T & \left(\boldsymbol{C}_{22} - \boldsymbol{C}_{12}^T\boldsymbol{B}\right)^{-1} \end{bmatrix}. \quad (6.14)$$

Here $\boldsymbol{B} = \boldsymbol{C}^{-1}\boldsymbol{C}_{12}$ is introduced to avoid repetition. Note that $\boldsymbol{C}^{-1}$ need only be computed once and can be stored in memory. This manipulation avoids inverting a $2(N+n) \times 2(N+n)$ matrix and instead only a $2n \times 2n$ inversion is needed; clearly, assumption (1) is beneficial. Assumption (3) reduces complexity further to $2S \times 2S$. Note that matrices consisting of Kronecker products enjoy a favorable structure, which makes the inverse and determinant computations much more efficient e.g. $(\boldsymbol{A} \otimes \boldsymbol{B})^{-1} = \boldsymbol{A}^{-1} \otimes \boldsymbol{B}^{-1}$. However, in our case we destroy this structure by introduction of the nonstationary covariance structure in equation 6.5 for which $(\sum_k \boldsymbol{A}_k \otimes \boldsymbol{B}_k)^{-1}$ has no known shortcut computation for $k > 2$ [78]. In this specific case the trade-off is acceptable as we only consider two model

outputs and the total number of unique process settings is small ($S = 12$). Therefore, the inability to exploit the Kronecker structure in this problem is acceptable given that the additional complexity enables the building of a more accurate model.

All point estimates ($\hat{\boldsymbol{\Phi}}$, $\hat{\boldsymbol{\sigma}}$) and MCMC samples were obtained using the *R*-package *RStan* [157]. The Bayesian statistical model was built in *Stan* [64]. The posterior density in equation 6.13 was obtained by generating 100,000 points, which were then thinned to 1,000 points to alleviate any autocorrelation.

6.5 Results

6.5.1 Calibration results

The posterior two-dimensional marginal densities for the constitutive model parameters, $\boldsymbol{\theta}^*$, are shown in Figure 6.7. These densities are computed using a kernel density estimate using the *R*-package *ks* [179]. For reference, the 1,000 MCMC sample points are also displayed. From these marginal distributions, the posterior appears to be *multimodal*. Also shown are the means of the two modes which were computed using using the Gaussian-mixture modeling *R*-package *MClust* [180]. One-dimensional marginal histograms of $\boldsymbol{\theta}^*$ are shown in 6.8. The JC parameter MCMC mean, mode 1 and 2 means, and parameters from the literature are shown in 6.3. To better interpret these results, the 0.2% offset yield strength is also displayed. The posterior Coulomb friction coefficients, $\boldsymbol{\mu}_c$, as well as the experimentally observed apparent friction coefficients, are shown in Figure 6.9. Results of the calibration indicate that models with low strain hardening exponent, n, are favored. This agrees with the discussion from Section 6.3 which suggests that, in machining, JC models with large values of n over-estimate strain hardening. The posterior distribution does contain a small second mode, which contains slightly higher values of n. Higher values of the strain hardening exponent however are balanced by lower values of B, the strain hardening constant. The posterior values of the Coulomb friction coefficient show that the apparent friction coefficient falls within the 95% confidence bounds of the Bayesian

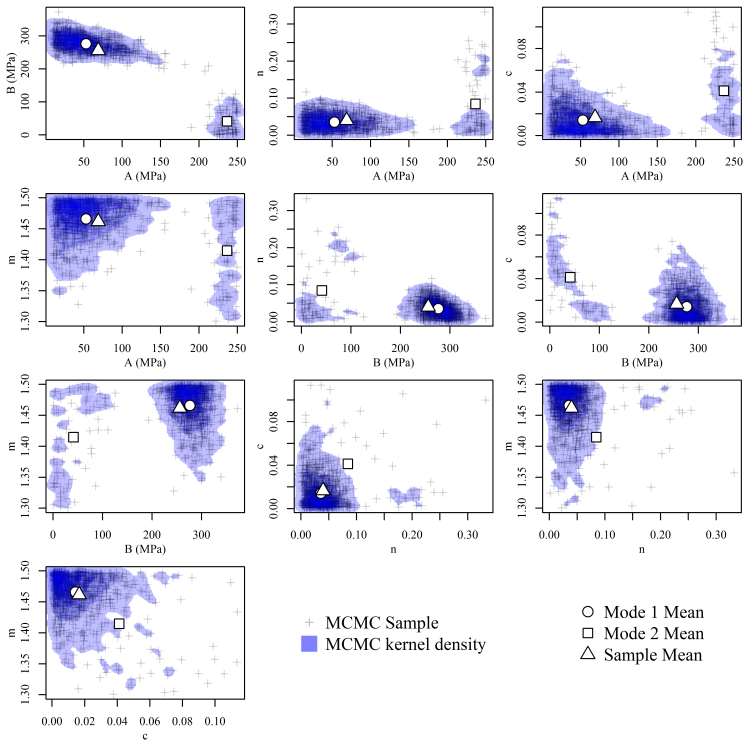

Figure 6.7: Posterior two-dimensional marginal distributions for the Johnson-Cook constitutive model parameters.

solution. This suggests that the apparent friction coefficients obtained from experiments are *close* to the "true" friction coefficients and may be reasonable approximations for use in simulation. The anomalous frictional behavior, which indicates a decrease in friction coefficient at the lowest speed for $\alpha = 15°, 25°$, we believe is due to complex stick-slip behavior present at low cutting speeds.

Experimental and simulated force predictions, as well as the corresponding percentage errors, are shown in Figure 6.10. The force predictions displayed correspond to (1) posterior prediction mean and 95% confidence bounds using the surrogate model, (2) FE evaluations made using the posterior mean values of the JC parameters and the friction coefficient ($\bar{\boldsymbol{\theta}}^*, \bar{\boldsymbol{\mu}}_c$), and (3) FE evaluations made with parameters from a machining study using Oxley's analytical model [38] and the experimental apparent friction coefficients. Note that the strain hardening exponent from [38] is relatively large, $n = 0.23$. Further-

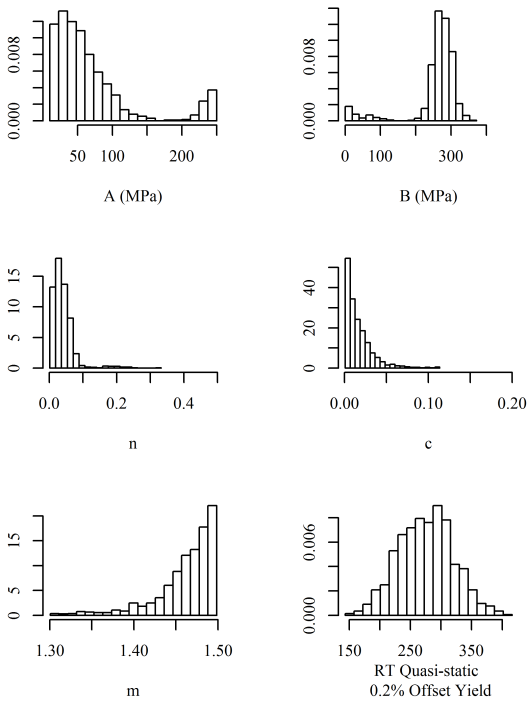

Figure 6.8: One-dimensional marginal histograms. Also shown is the computed 0.2% offset yield evaluated for room temperature (RT) quasi-static conditions.

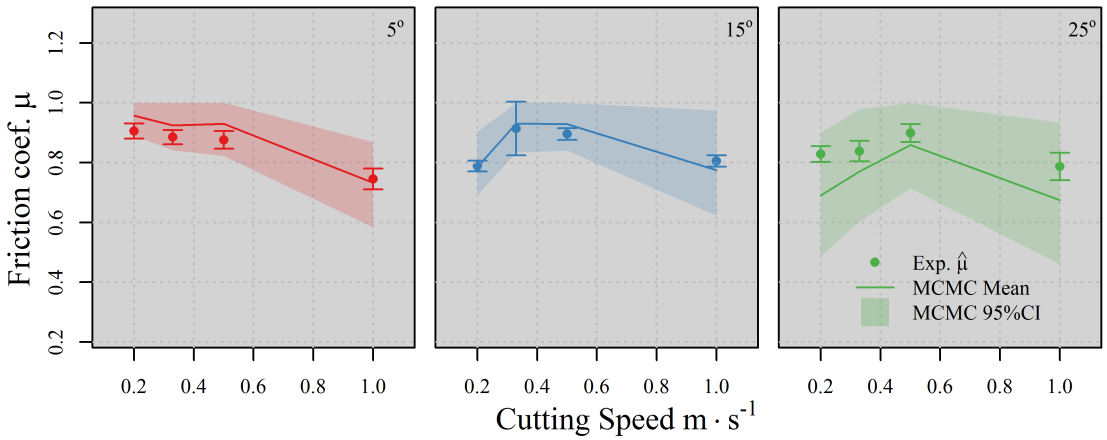

Figure 6.9: Posterior Coulomb friction coefficient mean and 95% confidence interval as well as experimental apparent friction coefficient with corresponding 95% error bars.

mean/Ref	A (MPa)	B (MPa)	n	c	m
MCMC	68.9	256.0	0.040	$1.66 \cdot 10^{-2}$	1.46
Mode 1	52.9	276.4	0.035	$1.42 \cdot 10^{-2}$	1.47
Mode 2	236.7	41.2	0.084	$4.11 \cdot 10^{-2}$	1.41
Ref [38]	293.4	121.26	0.23	$2.00 \cdot 10^{-3}$	1.34
Ref [39]	324	114	0.42	$2.00 \cdot 10^{-3}$	1.34

Table 6.3: JC Parameters.

more, in their work, the cutting speeds are high, specifically between $60\,m \cdot min^{-1}$ and $240\,m \cdot min^{-1}$.

First, it is worth noting that the surrogate model prediction and the full FE predictions are very close. Second, the model "fit" is excellent, particularly at low rake angles. Interestingly, the parameters from [38] are similarly good at $\alpha = 15°, 25°$, however at low rake angle those parameters over-predict the forces. This is a consequence of over-estimating the hardening behavior, which is most pronounced at low rake angles. Furthermore, the discrepancy at the lowest rake angle is most severe at low cutting speeds since there is insufficient thermal softening to counteract the excessive strain hardening.

6.5.2 Validation

For model validation we decided to test our results against a totally different response, namely the deformed or cut chip thickness t_c. Experimental values and simulated results are shown in 6.11. Two simulated results are shown (1) FE model simulation results evaluated at the posterior mean values of the JC parameters and Coulomb friction coefficients, and (2) FE model evaluations using constitutive model parameters from [38] and the experimental apparent friction coefficients. It can be seen that the model results obtained using parameters from the statistical calibration yield more accurate predictions. Interestingly, parameters from [38] again are poorest for the lowest rake angle. As before, we suspect this is because there is too much strain hardening in their model.

In Figure 6.12 three chip geometries derived from the FE simulations are shown: (A) a

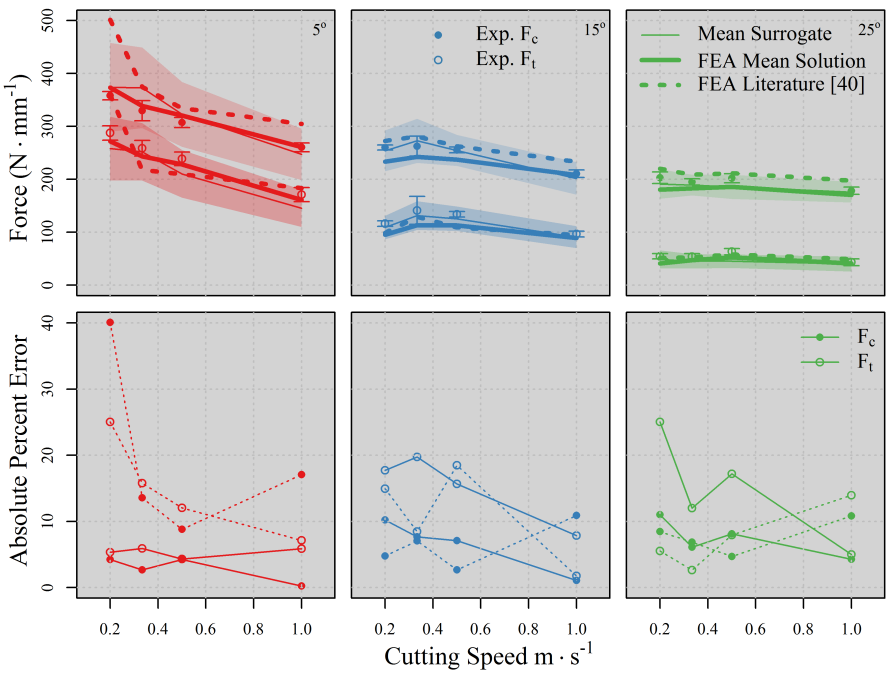

Figure 6.10: Calibrated cutting and thrust force curves.

result evaluated at the posterior mean values of the JC parameters and Coulomb friction coefficients, (B) an FE evaluation made with constitutive model parameters from [38] and the experimental apparent friction coefficients, and (C) an FE evaluation made with constitutive parameters derived from split-Hopkinson tests [39] and the experimental apparent friction coefficients. From the chip morphologies it is clear that application of model parameters calibrated to split-Hopkinson data ($n = 0.42$) is not appropriate for machining simulations where the imposed strains are much larger. We neglected to include the corresponding cutting forces from these simulations since steady state forces could not be achieved at low rake angles and low speeds. The chip corresponding to constitutive parameters ($n = 0.23$) from [38] is more realistic but still over predicts the cut chip thickness. The most accurate chip geometry, based on the chip thickness, corresponds to the model parameters calibrated in this work ($n = 0.04$).

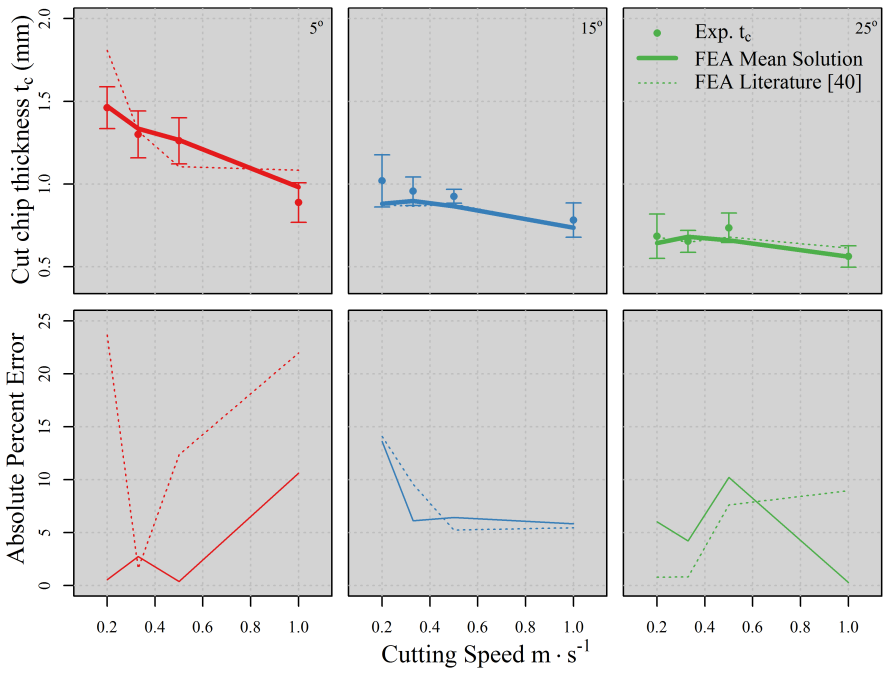

Figure 6.11: Cut chip thickness validation.

6.6 Discussion

Results of the Bayesian calibration illustrate that there is considerable uncertainty associated with identifying model calibration parameters in machining. This includes both constitutive model (JC) calibration constants as well as the frictional parameter (tool-chip interface friction coefficient). Through a Bayesian framework the most likely model parameters can be identified and their uncertainties quantified.

For performing FE simulations following the calibration, we found that utilizing the posterior mean values of the constitutive model parameters provides more accurate FE responses (Figures 6.10 and 6.11). Identifying the mean parameters from simple orthogonal cutting experiments and FE simulations enables the simulation of more complex machining processes (drilling, milling, grinding, hobbing, etc.) using the calibrated JC parameters. The uncertainty in material behavior can be utilized to further quantify the uncertainty in the

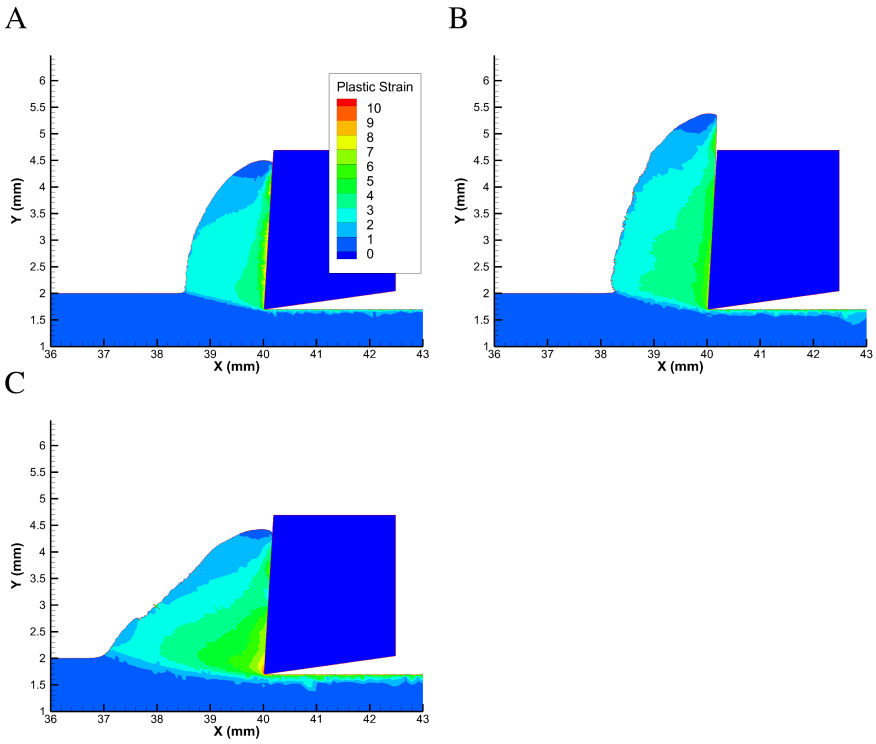

Figure 6.12: Al6061-T6 machining simulations at $\alpha = 5°$ and $V = 12\,m \cdot min^{-1}$. (A) friction and constitutive parameters corresponding to the posterior distribution mean, (B) constitutive parameters from study using JC and Oxley's model cutting model [38] and the experimental apparent friction coefficient, and (C) constitutive parameters obtained via split-Hopkinson bar testing[39] and the experimental apparent friction coefficient

.

predicted process responses such as forces and tool wear [169]. Since machining processes exhibit extreme thermo-mechanical deformation conditions (high strain, strain rate, and temperature), orthogonal cutting experiments are the *best* representative process to emulate material deformation in more complex cutting processes. The supporting evidence for this claim is presented in Figure 6.12; the simulation using constitutive parameters obtained from split-Hopkinson bar experiments are unable to predict the machining response. The split-Hopkinson experiments from [39] utilize tension and compression configurations to achieve uniaxial strains as high as 0.5. In our machining experiments we observed uniaxial equivalent strains as high as 3.0 for $\alpha = 5^{\circ}$. This comparison illustrates the dangers of extrapolating to larger strain regimes present in machining and therefore justifies the use of orthogonal cutting tests for calibrating constitutive models for use in machining.

The obtained results can be further interpreted by studying the resulting uniaxial stress-strain curves shown in 6.13. The mean response values are obtained from

$$E\left[\sigma\left(\epsilon\right)\right] = \sum_{i}^{N_m} \left(A_i + B_i \epsilon^{n_i}\right)\left(1 + c_i log\dot{\epsilon}\right)\left(1 - T_h^{m_i}\right), \tag{6.15}$$

where T_h is the homologous temperature and the sum is over all N_m points in the MCMC sample. The variance, and therefore 95% CI, can be obtained similarly. The mean curves for mode 1 and mode 2 can be computed similarly but only considering points classified as belonging to each mode. These results illustrate that the two modes produce nearly identical results, which suggests that the model choice is plagued by non-uniqueness. The 0.2% offset yield stress in Figure 6.8 further explains this observation. Despite the posterior being bimodal, the yield stress is unimodal. This is because the strain hardening portion is described using a power-law expression. As $n \to 0$ the the yield approaches $A + B$ and the model behavior approaches the perfectly plastic regime (low strain hardening). However, for $n \neq 0$ the yield is $A + B\hat{\epsilon}^n$ where ϵ is the appropriate yield offset (0.2% is used in our work). A,B, and n therefore can be manipulated to produce similar initial yield results. A similar argument can be made for the flow stress at any strain value. The model constants

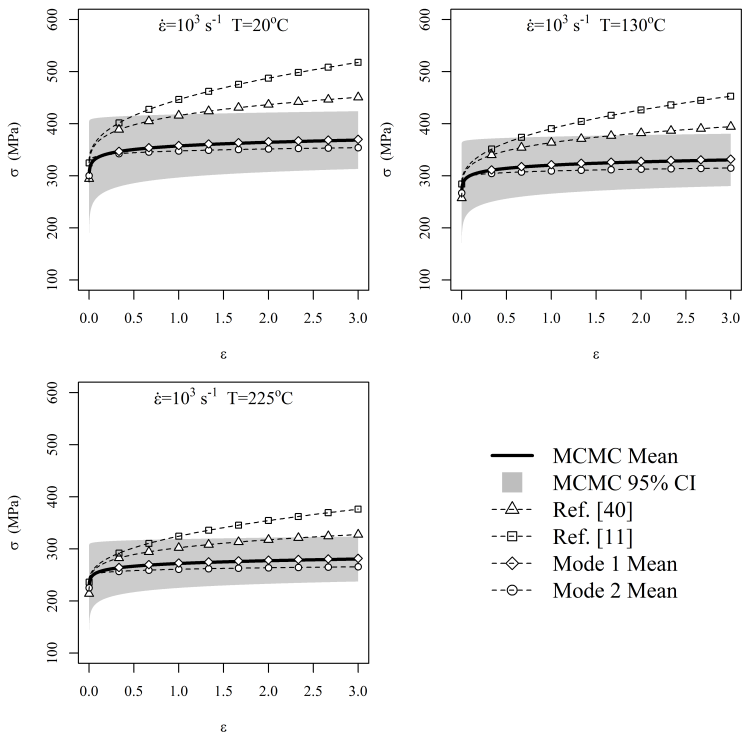

Figure 6.13: Stress-strain curves evaluated at high rate conditions and temperatures corresponding to RT, $130°C$, and $225°C$. Elevated temperatures are estimates from FE MCMC mean estimates corresponding to $\alpha = 5°$ and $V = 12,\ 60\, m \cdot min^{-1}$. Curves shown are (1) the grand MCMC mean, (2) grand MCMC 95% CI, (3) prediction with parameters from [38], (4) prediction with parameters from [39], (5) Mode 1 mean, and (6) Mode 2 mean.

obtained from split-Hopkinson bar tests [39] produce flow stresses much higher than the MCMC results. Flow stresses corresponding to a model fit to compression tests and utilized in a machining study with Oxley's model [38] are also higher than the MCMC results but the discrepancy is less. The temperature dependence shows that the discrepancy decreases with increasing temperature, particularly the [38] curve. This suggests that perhaps at high cutting speeds the latter model would perform adequately because the excessive strain hardening is balanced by increased thermal softening.

Calibration results show that the apparent friction coefficient observed experimentally is close to the "true" underlying friction coefficient under an assumed Coulomb friction law. This justifies the use of the apparent friction coefficient for simulations in the absence

of any other information. In general, however, our choice of friction modeling strategy has little predictive power - What friction coefficient should be used at unobserved values of α and V? This was done purposefully since the scope of this work is to identify the unknown constitutive parameters. In this way, we were not constrained to use the apparent friction coefficient and yet we did not have to commit to developing complex tool-chip interface friction models. The methods utilized in this work are general and could be applied to calibrate more complex friction models. A simple strategy could be to adopt a regression model for the friction coefficient as a function of the process conditions or tool material; $\mu_c = f(\alpha, V, \text{tool})$. The same approach employed in this work could be used to identify the frictional regression coefficients and quantify their uncertainty.

We speculate that the calibrated constitutive parameters are likely to be influenced by the choice of friction law. However, this would still hold even if a more complex friction law was employed. This confounding across the model parameters is not limited to the friction coefficient only. It should be noted that our calibrated values of c and m are sensitive to our choice of the strain-hardening model form. If a material damage evolution model (e.g. JC damage model) were also introduced, the constitutive model parameters would likely change as well. This effect is fundamental and perhaps best understood in a regression setting. In regression, if a new regressor is added the previously established regression coefficients may vary. In other words, the regression coefficients are conditionally dependent on the choice of regressors. In the same way, our results are conditionally dependent on our choice of the JC and Coulomb friction models. These parameters are valid for machining of Al6061-T6 when the Coulomb law is an appropriate descriptor of the underlying tribological interaction.

Model parameters from the literature [38] yielded simulations which failed to capture the force/chip responses at the lowest rake angle and lowest speeds. In their work, the authors used Oxley's analytical model and identified model parameters from quasi-static compression tests. Their model however is evaluated over higher cutting speeds

$60 - 240\, m \cdot min^{-1}$. This suggests that parameters that describe high cutting speed experiments accurately may not necessarily perform well in the low cutting speed regime. At lower cutting speeds, cutting temperatures are lower and therefore thermal softening is less pronounced and is unable to balance the corresponding high degree of strain hardening. Therefore, practitioners and researchers should be careful in calibrating models and should ideally use a rich set of experiments that adequately sample data from the process parameter space.

6.7 Conclusions and summary

In this work we utilized a statistical framework to calibrate the constitutive model (Johnson-Cook) parameters used in a complex finite element based orthogonal cutting model and quantify the uncertainty associated with the calibrated parameters. To do so efficiently requires that first a computationally inexpensive surrogate model be built to emulate the complex finite element model response. A constrained maximum projection design was utilized to evaluate the orthogonal cutting finite element model over model input parameters which consist of the Johnson-Cook constitutive model parameters, friction parameters, and the machining process parameters. These model evaluations produced cutting and thrust force outputs which displayed a nonstationary dependence on the rake angle and the friction coefficient. A nonstationary Gaussian Process model was built to emulate the response and was found to be superior, in terms of cross validation error, over an analogous stationary Gaussian Process model. A Bayesian inference framework was used, together with the computationally efficient surrogate model, to infer the posterior distribution of the constitutive model and friction parameters given experimentally observed cutting and thrust force values over a wide range of cutting speeds and rake angles. Validation of the calibration against the measured deformed chip thickness illustrated the superiority of the proposed method against constitutive parameters obtained from high rate compression tests and from the literature. The methods used here are general and can be used to calibrate

more complex constitutive and frictional laws or used for studying other manufacturing processes.

CHAPTER 7
CONCLUSIONS

This chapter summarizes the main conclusions established in this work.

7.1 Key conclusions

7.1.1 Bayesian estimation of uniaxial constitutive properties

This chapter established a framework for inferring post-elastic uniaxial mechanical constitutive properties from spherical indentation experiments. The following conclusions were obtained:

1. A computationally inexpensive Gaussian process surrogate model was effective in emulating the response of a computationally expensive indentation finite element model. This model considers as inputs parametric values that describe the constitutive response of metallic systems (modulus, yield, hardening coefficient, hardening exponent, etc..).

2. The inexpensive surrogate indentation model was used in a Bayesian regression formulation to "fit" the model to experimental observations and thereby identify the unknown constitutive parameters.

3. The proposed methodology was tested on Al6061 subject to different heat treatments (experimental data obtained from the literature [92]). The inferred uniaxial behavior matched the tensile curves well.

4. The Bayesian methodology also captures uncertainty in the unknown inferred constitutive parameters. This represents an improvement in the state-of-the-art which previously only considered point estimates [103, 82].

7.1.2 PSP linkages using EBSD data

In this work we studied a severe plastic deformation machining process, which drives microstructure evolution via continuous dynamic recrystallization (CDRX). Various stages of microstructure evolution were captured by considering a wide range of rake angles, which induce shear strains varying from $\sim 1 - 6$. Rate and temperature effects were considered by varying the cutting speed. The following conclusions were obtained:

1. Large strain conditions produced sub-micron crystal structures whereas low strain experiments yielded highly deformed structures, which still resembled the coarse parent material. Distinctive deformation substructures, indicative of early stage CDRX, can be observed even in relatively low strain ($\gamma \sim 1$) machined structures.

2. At the largest strains a dependence on the cutting speed was observed with higher cutting speeds producing structures with lower crystallographic misorientations.

3. A novel statistical microstructure descriptor was derived using generalized spherical harmonics to efficiently quantify local orientation state and the autocorrelation spatial statistic to quantify the orientation "spread" or misorientation. The novel descriptor is physically intuitive and targets morphological information present in the orientation imagining data.

4. The reduced dimension principal component (PC) bases capture intuitive physical observations. The first basis captures highly localized crystallographic autocorrelations. The spatial region considered in this basis is $< 500\,nm$, which corresponds to the finest crystallites observed in this work. The second basis captures competing behaviors; correlations at large length scales $> 3\,\mu m$ and medium length scales $0.5 - 2\,\mu m$. The PC weights evolve appropriately with cutting speed and rake angle in such a way that agrees with the physics of the process.

5. A data driven model using a multiple output Gaussian process regression framework

was established for quantifying process-structure-property linkages in additional to capturing the corresponding uncertainties. The model is flexible, enables inclusion of various kinds of structure and property data, does not necessitate fully paired input data, captures the full process-structure-property pipeline, and produces uncertainty estimates associated with future predictions.

7.1.3 PSP linkages using chord length statistics

This chapter considered the evolution of microstructure and properties subject to a high-strain machining process. Furthermore, thermal effects were considered by allowing the chips to be quenched in water or be air cooled. The following conclusions were obtained:

1. Large strains imposed via machining drives microstructure refinement into the ultra fine grain size range. Post-machining thermal effects drive annealing and fast kinetic growth mechanisms, which produces novel bimodal microstructure. In practice, this disparity may occur when machining with and without cutting fluids.

2. At low cutting speeds the quenched chips consisted entirely of extremely refined elongated structures. At high cutting speeds the quenched structures were slightly more coarse. At low cutting speeds the air cooled samples were mostly fine grained with a small fraction of annealed grains. At high cutting speeds the air cooled samples were entirely annealed. A mix of microstructures were produced at intermediate cutting speeds.

3. The wide span of observed microstructures was efficiently quantified using angularly resolved chord length statistics. The reduced dimension principal component bases captured the coupled physical features observed in the microstructure; the asymmetric fine grains in one basis, and the coarse isotropic grains in another.

4. A clear trend emerged in the reduced-order PCA space where DRX drove grain

refinement relative to the coarse virgin microstructure and post machining annealing/growth provided a return path to the coarse grain microstructure.

5. Uniaxial equivalent yield strengths of the machined structures were estimated using the previously established Bayesian inverse methods. This is the first time machined uniaxial properties have been inferred from indentation experiments and the second time they have ever been reported. The estimated yield strengths ($450 - 550\,MPa$ quenched) agree well with the prior machining work [18] and other SPD works on copper [145].

6. A data-driven multiple output Gaussian process model was built for identifying the process-structure-property forward linkage. A Bayesian inverse strategy was proposed for identifying the inverse property-process mapping

7.1.4 Machining FEM constitutive model calibration

In this chapter a statistical methodology was utilized to calibrate the constitutive model (Johnson-Cook) parameters used in a complex nite element based orthogonal cutting model and to quantify the uncertainty associated with the calibrated parameters. The following conclusions were obtained:

1. The FE model evaluations produced cutting and thrust force outputs which displayed a nonstationary dependence on the rake angle and the friction coefficient. Physically, this makes sense as the friction coefficient and rake angle *physically tie* together the cutting and thrust forces.

2. A nonstationary Gaussian Process model was built to emulate the response and was found to be superior, in terms of cross validation error, over an analogous stationary Gaussian Process model (40% improvement in cross validation error).

3. A Bayesian inference framework was used, together with the computationally efficient surrogate model, to infer the posterior distribution of the constitutive model

and friction parameters given experimentally observed cutting and thrust force values over a wide range of cutting speeds and rake angles.

4. Validation of the calibrated model against the measured deformed chip thickness illustrated the superiority of the proposed method against constitutive parameters obtained from high rate compression tests and from the literature.

5. Calibration directly to machining data displayed a preference for material models that display limited hardening at large strains. The validation shows that better machining models are obtained by utilizing machining data for calibration, *not* traditional mechanical testing data. This observation illustrates that the constitutive response during machining cannot be simply obtained by extrapolating from low-strain or low-rate data.

7.2 Recommendations for future work

Related areas for further research include the following:

1. The indentation inverse modeling assumes a parametric form for the constitutive model description. Inference is therefore simply a calibration problem where unknown parameters are estimated from the data. However, the inference is sensitive to the constitutive model choice. Research into nonparametric methods would be extremely powerful, especially when considering exotic material systems (metallic glasses, shape memory alloys, etc.) where the response is complex and not easily described parametrically. There is recent research in the statistics literature on this topic [108].

2. Machined chips are studied in this work as they are relatively easy to characterize. Furthermore, there is a body of work which illustrates that the machined chip and the machined workpiece subsurface are subject to similar deformation histories [20].

Therefore, we justify the study of the chip by citing these works. However, in practice it is the workpiece surface that most practitioners are interested in. Therefore, analogous studies on the workpiece surface would be of practical and academic value.

3. The microstructures produced during machining display anisotropic structures due to the intense shearing imposed by the process. Therefore, it is possible that this anisotropy is manifested in the corresponding properties as well. We circumvented this issue by using spherical (axisymetric) indenters and always indenting perpendicular to the direction of anisotropy. In practice however this structural anistropy may be important - consider tribological response in different directions on a machined surface. Therefore, there may be merit in studying property anisotropy. An easy way to do this is to consider anisotropic indenters (wedge indenter, Knoop indenter) and perform a study measuring the hardness with the indenter oriented in different directions relative to the sample/microstructure.

4. The property differences induced in quenched copper chips are fairly small ($\pm 100\, MPa$ uniaxial yield). This made all analysis fairly difficult as the signal-to-noise ratio was relatively small. In fact, this is the reason we introduced hardness as a multi-fidelity property measure. For future studies it would be better to utilize a material system that displays a larger sensitivity to machining. This may be achieved by considering systems that are unstable or metastable, are sensitive to stress induced phase transformation, etc.. Conversely, the process could be modified to achieve a large range in properties. Several researchers obtained a wider range of hardness values in copper (upto 180 HV) by considering a wider range of strains, cutting speeds, and introducing cryogenic cooling conditions [19, 20, 147, 146].

5. In the GSH study crystallographic considerations are neglected by careful derivation of the mean autocorrelation parameter. This was done because we wanted to avoid the need for prohibitively long scan times. In order to obtain sufficiently good

resolution to resolve small features in the $< 1\,\mu m$ range, a small raster step size is needed ($50\,nm$ in this work). A $15 \times 15 \mu m$ region requires 20 minutes to scan at that resolution. For texture we would perhaps need $100 \times 100 \mu m$ (or more for low strain samples) which would require scans $\sim 40\times$ longer (12 hrs). An alternative is to use multi-fidelity/multi-scale structure measurements to capture morphological information with fine scans at small length scales and to obtain texture information with coarse scans over large length scales. The analysis then requires combining these sources of data.

6. The machining model calibration study only considers the Johnson-Cook constitutive model. An interesting follow up study could consider multiple different models. A model selection study would then follow using statistical methods.

7. The machining model calibration study only utilized cutting forces to estimate the unknown calibration parameters. However, there are a wealth of techniques for in-situ process monitoring of machining processes. This includes deformation fields obtained using particle image velocimetry, temperature measurements using various methods, residual stress measurements in the workpiece surface, and property measurements of the machined chips (for instance using techniques utilized in this work). All these measurements provide "information" which may be used to calibrate models, discriminate between good and bad models, etc..

8. A nonstationary model was used in the machining surrogate model development. However, perhaps some of the nonstationarity could be "captured" by simply using a better mean function. This would be helpful in the study proposed above where more than two descriptors (forces, temperatures, deformation fields, material microstructure/properties) would be considered. One possibility is to simply use a complex machining model (e.g. Oxley's model [167]) to describe the mean behavior of the FE model. Oxley's model is sufficiently complex that it may capture much of the

nonstationary behavior. The portion of the FE response that cannot be captured by Oxley's model would then be captured using a regular stationary Gaussian process model. This kind of strategy is common and one such example where it has been used is a study on the modeling of silicon wafer wire slicing [70]. The mean function in that study corresponds to the solution of a partial differential equation.

Appendices

APPENDIX A
MULTIFIDELITY IMPLEMENTATION

Statistically we can build a simple model that allows for sharing of information between the physically informative quantities (Y_{ind}) and the cheaper less informative quantities (HV)

$$\begin{aligned} Y_{ind} &= Z + \tau \\ HV &= \rho Z + W + \gamma, \end{aligned} \tag{A.1}$$

where Z is the underlying mean function we seek described as a Gaussian process (GP), τ is error associated with Y_{ind}, ρ is a scaling quantity, W is an independent zero-mean GP which allows HV to vary from ρZ systematically (e.g. bias function) and γ is the measurement error in HV. This form is identical to the form introduced in the seminal Kennedy and O'Hagan paper [15]. Note that Z is part of the multivariate GP previously introduced but we simply denote it here as Z for simplicity. The model states that HV scales with Z (and hence the mean of Y_{ind}) except when the simple scaling fails in which case W "captures" or "soaks up" this deviation.

The covariance of HV with the other MOGPR quantities can be easily derived. First assume that $Y_{ind} = Y_{M-1}$ in the model e.g. the indentation yield is ordered as the second to last output, and HV is the last $Y_M = HV$. Therefore,

$$\begin{aligned} \mathrm{Cov}[Y_{ind}\left(\boldsymbol{x}_{M-1,k}\right), \quad HV\left(\boldsymbol{x}_{Ml}\right)] &= \mathrm{Cov}[Z\left(\boldsymbol{x}_{M-1,k}\right) + \tau, \\ &\quad \rho Z\left(\boldsymbol{x}_{Ml}\right) + W\left(\boldsymbol{x}_{Ml}\right) + \gamma] \\ &= \rho S_{M-1,M-1} R\left(\boldsymbol{x}_{M-1,k} - \boldsymbol{x}_{Ml}\right), \end{aligned} \tag{A.2}$$

where σ_b^2 and R_b are the bias variance and correlation function. The bias correlation function contains additional hyperparameters $\boldsymbol{\phi}_b$. Note there is no error term since there are no off-diagonal terms in the error covariance structure. This is because indentation-hardness

experiments are not "paired" experimentally; observations are made independently of one another. All other correlations can be easily obtained simply by following the above "plug-in" strategy. The bias function "kicks in" only for $HV - HV$ covariances,

$$\begin{aligned} \mathrm{Cov}[HV(\boldsymbol{x}_{Mk}), \quad HV(\boldsymbol{x}_{Ml})] &= \rho^2 S_{M-1,M-1} R(\boldsymbol{x}_{Mk} - \boldsymbol{x}_{Ml}) \\ &+ \sigma_b^2 R_b(\boldsymbol{x}_{Mk} - \boldsymbol{x}_{Ml}) + \\ &\gamma \delta_{kl}, \end{aligned} \tag{A.3}$$

REFERENCES

[1] M. C. Shaw, *Metal Cutting Principles*. Oxford university press New York, 2005, vol. 2.

[2] T. H. Childs, P.-J. Arrazola, P Aristimuno, A. Garay, and I. Sacristan, "Ti6al4v metal cutting chip formation experiments and modelling over a wide range of cutting speeds," *Journal of Materials Processing Technology*, vol. 255, pp. 898–913, 2018.

[3] G. R. Johnson and W. H. Cook, "Fracture characteristics of three metals subjected to various strains, strain rates, temperatures and pressures," *Engineering Fracture Mechanics*, vol. 21, no. 1, pp. 31–48, 1985.

[4] M. Calamaz, D. Coupard, and F. Girot, "A new material model for 2d numerical simulation of serrated chip formation when machining titanium alloy ti–6al–4v," *International Journal of Machine Tools and Manufacture*, vol. 48, no. 3-4, pp. 275–288, 2008.

[5] P. Fernandez-Zelaia, S. Melkote, T. Marusich, and S. Usui, "A microstructure sensitive grain boundary sliding and slip based constitutive model for machining of ti-6al-4v," *Mechanics of Materials*, vol. 109, pp. 67–81, 2017.

[6] S. N. Melkote, W. Grzesik, J. Outeiro, J. Rech, V. Schulze, H. Attia, P.-J. Arrazola, R. MSaoubi, and C. Saldana, "Advances in material and friction data for modelling of metal machining," *CIRP Annals*, vol. 66, no. 2, pp. 731–754, 2017.

[7] S. N. Melkote, R. Liu, P. Fernandez-Zelaia, and T. Marusich, "A physically based constitutive model for simulation of segmented chip formation in orthogonal cutting of commercially pure titanium," *CIRP Annals*, vol. 64, no. 1, pp. 65–68, 2015.

[8] T. Özel and E. Zeren, "Determination of work material flow stress and friction for fea of machining using orthogonal cutting tests," *Journal of Materials Processing Technology*, vol. 153, pp. 1019–1025, 2004.

[9] T. Özel and T. Altan, "Determination of workpiece flow stress and friction at the chip–tool contact for high-speed cutting," *International Journal of Machine Tools and Manufacture*, vol. 40, no. 1, pp. 133–152, 2000.

[10] M. Agmell, A. Ahadi, and J.-E. Ståhl, "The link between plasticity parameters and process parameters in orthogonal cutting," *Procedia CIRP*, vol. 8, pp. 224–229, 2013.

[11] M. Agmell, A. Ahadi, and J.-E. Stahl, "Identification of plasticity constants from orthogonal cutting and inverse analysis," *Mechanics of Materials*, vol. 77, pp. 43–51, 2014.

[12] F Klocke, D Lung, and S Buchkremer, "Inverse identification of the constitutive equation of inconel 718 and aisi 1045 from fe machining simulations," *Procedia CIRP*, vol. 8, pp. 212–217, 2013.

[13] J. Sacks, W. J. Welch, T. J. Mitchell, and H. P. Wynn, "Design and analysis of computer experiments," *Statistical Science*, pp. 409–423, 1989.

[14] T. J. Santner, B. J. Williams, and W. I. Notz, *The Design and Analysis of Computer Experiments*. Springer Science & Business Media, 2013.

[15] M. C. Kennedy and A. O'Hagan, "Bayesian calibration of computer models," *Journal of the Royal Statistical Society: Series B (Statistical Methodology)*, vol. 63, no. 3, pp. 425–464, 2001.

[16] M. E. Merchant, "Mechanics of the metal cutting process. i. orthogonal cutting and a type 2 chip," *Journal of Applied Physics*, vol. 16, no. 5, pp. 267–275, 1945.

[17] R Komanduri and B. Von Turkovich, "New observations on the mechanism of chip formation when machining titanium alloys," *Wear*, vol. 69, no. 2, pp. 179–188, 1981.

[18] S Shekhar, J Cai, J Wang, and M. Shankar, "Multimodal ultrafine grain size distributions from severe plastic deformation at high strain rates," *Materials Science and Engineering: A*, vol. 527, no. 1-2, pp. 187–191, 2009.

[19] T. L. Brown, C. Saldana, T. G. Murthy, J. B. Mann, Y. Guo, L. F. Allard, A. H. King, W. D. Compton, K. P. Trumble, and S. Chandrasekar, "A study of the interactive effects of strain, strain rate and temperature in severe plastic deformation of copper," *Acta Materialia*, vol. 57, no. 18, pp. 5491–5500, 2009.

[20] Y. Guo, C. Saldana, W. D. Compton, and S. Chandrasekar, "Controlling deformation and microstructure on machined surfaces," *Acta Materialia*, vol. 59, no. 11, pp. 4538–4547, 2011.

[21] R. M'Saoubi, T. Larsson, J. Outeiro, Y. Guo, S. Suslov, C. Saldana, and S. Chandrasekar, "Surface integrity analysis of machined inconel 718 over multiple length scales," *CIRP Annals-Manufacturing Technology*, vol. 61, no. 1, pp. 99–102, 2012.

[22] A Mahato, Y Guo, N Sundaram, T. Murthy, C Saldana, and S Chandrasekar, "Unconstrained plastic flow at surfaces in sliding and cutting," *International Journal of Precision Technology*, vol. 3, no. 4, pp. 370–387, 2013.

[23] S. Basu and M. R. Shankar, "Crystallographic textures resulting from severe shear deformation in machining," *Metallurgical and Materials Transactions A*, vol. 46, no. 2, pp. 801–812, 2015.

[24] J. D. Thiele and S. N. Melkote, "Effect of cutting edge geometry and workpiece hardness on surface generation in the finish hard turning of aisi 52100 steel," *Journal of Materials Processing Technology*, vol. 94, no. 2-3, pp. 216–226, 1999.

[25] H Ni, M Elmadagli, and A. Alpas, "Mechanical properties and microstructures of 1100 aluminum subjected to dry machining," *Materials Science and Engineering: A*, vol. 385, no. 1-2, pp. 267–278, 2004.

[26] F. Ambrosy, F. Zanger, V. Schulze, and I. Jawahir, "An experimental study of cryogenic machining on nanocrystalline surface layer generation," *Procedia CIRP*, vol. 13, pp. 169–174, 2014.

[27] S. Swaminathan, M. R. Shankar, S. Lee, J. Hwang, A. H. King, R. F. Kezar, B. C. Rao, T. L. Brown, S. Chandrasekar, W. D. Compton, *et al.*, "Large strain deformation and ultra-fine grained materials by machining," *Materials Science and Engineering: A*, vol. 410, pp. 358–363, 2005.

[28] Z. Wang, S. Basu, and C. Saldana, "Low-temperature machining in a fully submerged cryogenic environment," *Machining Science and Technology*, vol. 21, no. 1, pp. 19–36, 2017.

[29] S Shekhar, S Abolghasem, S Basu, J Cai, and M. Shankar, "Effect of severe plastic deformation in machining elucidated via rate-strain-microstructure mappings," *Journal of Manufacturing Science and Engineering*, vol. 134, no. 3, p. 031 008, 2012.

[30] Z. Wang, C. Saldana, and S. Basu, "Subsurface microstructure and crystallographic texture in surface severe plastic deformation processes," in *ASME 2017 12th International Manufacturing Science and Engineering Conference collocated with the JSME/ASME 2017 6th International Conference on Materials and Processing*, American Society of Mechanical Engineers, 2017, V002T03A030–V002T03A030.

[31] Z. Wang, S. Basu, T. G. Murthy, and C. Saldana, "Gradient microstructure and texture in wedge-based severe plastic burnishing of copper," *Journal of Materials Research*, vol. 33, no. 8, pp. 1046–1056, 2018.

[32] S. Basu, Z. Wang, R. Liu, and C. Saldana, "Enhanced subsurface grain refinement during transient shear-based surface generation," *Acta Materialia*, vol. 116, pp. 114–123, 2016.

[33] Z. Wang, M. Rifat, C. Saldana, and S. Basu, "Quantifying the spread in crystallographic textures due to transients in strain path in shot-peening," *Materialia*, vol. 2, pp. 231–249, 2018.

[34] H. J. Frost and M. F. Ashby, *Deformation Mechanism Maps: the Plasticity and Creep of Metals and Ceramics*. Pergamon press, 1982.

[35] S. Basu, Z. Wang, and C. Saldana, "Deformation heterogeneity and texture in surface severe plastic deformation of copper," *Proc. R. Soc. A*, vol. 472, no. 2187, p. 20 150 486, 2016.

[36] S. Torquato, *Random Heterogeneous Materials: Microstructure and Macroscopic Properties*. Springer Science & Business Media, 2013, vol. 16.

[37] S. R. Kalidindi, *Hierarchical Materials Informatics: Novel Analytics for Materials Data*. Elsevier, 2015.

[38] A. H. Adibi-Sedeh, V. Madhavan, and B. Bahr, "Extension of oxleys analysis of machining to use different material models," *Journal of Manufacturing Science and Engineering*, vol. 125, no. 4, pp. 656–666, 2003.

[39] D. R. Lesuer, G. Kay, and M. LeBlanc, "Modeling large-strain, high-rate deformation in metals," Lawrence Livermore National Lab., CA (US), Tech. Rep., 2001.

[40] C. Zener and J. H. Hollomon, "Effect of strain rate upon plastic flow of steel," *Journal of Applied Physics*, vol. 15, no. 1, pp. 22–32, 1944.

[41] D. L. Holt, "Dislocation cell formation in metals," *Journal of Applied Physics*, vol. 41, no. 8, pp. 3197–3201, 1970.

[42] S Gourdet and F Montheillet, "A model of continuous dynamic recrystallization," *Acta Materialia*, vol. 51, no. 9, pp. 2685–2699, 2003.

[43] S Abolghasem, S Basu, S Shekhar, J Cai, and M. Shankar, "Mapping subgrain sizes resulting from severe simple shear deformation," *Acta Materialia*, vol. 60, no. 1, pp. 376–386, 2012.

[44] A Tabei, D. Shih, H Garmestani, and S. Liang, "Dynamic recrystallization of al alloy 7075 in turning," *Journal of Manufacturing Science and Engineering*, vol. 138, no. 7, p. 071 010, 2016.

[45] A Tabei, D. Shih, H Garmestani, and S. Liang, "Derivation of process path functions in machining of al alloy 7075," *Journal of Materials Engineering and Performance*, vol. 24, no. 11, pp. 4503–4509, 2015.

[46] S. R. Kalidindi, A. J. Medford, and D. L. McDowell, "Vision for data and informatics in the future materials innovation ecosystem," *JOM*, vol. 68, no. 8, pp. 2126–2137, 2016.

[47] S. R. Kalidindi, D. B. Brough, S. Li, A. Cecen, A. L. Blekh, F. Y. P. Congo, and C. Campbell, "Role of materials data science and informatics in accelerated materials innovation," *MRS Bulletin*, vol. 41, no. 8, pp. 596–602, 2016.

[48] B. L. Adams, X. C. Gao, and S. R. Kalidindi, "Finite approximations to the second-order properties closure in single phase polycrystals," *Acta Materialia*, vol. 53, no. 13, pp. 3563–3577, 2005.

[49] A. Cecen, H. Dai, Y. C. Yabansu, S. R. Kalidindi, and L. Song, "Material structure-property linkages using three-dimensional convolutional neural networks," *Acta Materialia*, vol. 146, pp. 76–84, 2018.

[50] Z. Yang, Y. C. Yabansu, R. Al-Bahrani, W.-k. Liao, A. N. Choudhary, S. R. Kalidindi, and A. Agrawal, "Deep learning approaches for mining structure-property linkages in high contrast composites from simulation datasets," *Computational Materials Science*, vol. 151, pp. 278–287, 2018.

[51] Y. Jiao, F. Stillinger, and S. Torquato, "A superior descriptor of random textures and its predictive capacity," *Proceedings of the National Academy of Sciences*, vol. 106, no. 42, pp. 17 634–17 639, 2009.

[52] A. Cecen, "Calculation, utilization, and inference of spatial statistics in practical spatio-temporal data," PhD thesis, Georgia Institute of Technology, 2017.

[53] D. M. Turner, S. R. Niezgoda, and S. R. Kalidindi, "Efficient computation of the angularly resolved chord length distributions and lineal path functions in large microstructure datasets," *Modelling and Simulation in Materials Science and Engineering*, vol. 24, no. 7, p. 075 002, 2016.

[54] E. Wargo, A. Hanna, A Cecen, S. Kalidindi, and E. Kumbur, "Selection of representative volume elements for pore-scale analysis of transport in fuel cell materials," *Journal of Power Sources*, vol. 197, pp. 168–179, 2012.

[55] M. I. Latypov, M. Kühbach, I. J. Beyerlein, J.-C. Stinville, L. S. Toth, T. M. Pollock, and S. R. Kalidindi, "Application of chord length distributions and principal component analysis for quantification and representation of diverse polycrystalline microstructures," *Materials Characterization*, vol. 145, pp. 671–685, 2018.

[56] A. Gokhale, "Estimation of bivariate size and orientation distribution of microcracks," *Acta Materialia*, vol. 44, no. 2, pp. 475–485, 1996.

[57] H Singh, A. Gokhale, S. Lieberman, and S Tamirisakandala, "Image based computations of lineal path probability distributions for microstructure representation," *Materials Science and Engineering: A*, vol. 474, no. 1-2, pp. 104–111, 2008.

[58] P. D. Hoff, *A First Course in Bayesian Statistical Methods*. Springer Science & Business Media, 2009.

[59] W. R. Gilks, S. Richardson, and D. Spiegelhalter, *Markov Chain Monte Carlo in Practice*. CRC press, 1995.

[60] N. Metropolis, A. W. Rosenbluth, M. N. Rosenbluth, A. H. Teller, and E. Teller, "Equation of state calculations by fast computing machines," *The Journal of Chemical Physics*, vol. 21, no. 6, pp. 1087–1092, 1953.

[61] W. K. Hastings, "Monte carlo sampling methods using markov chains and their applications," *Biometrika*, vol. 57, no. 1, pp. 97–109, 1970.

[62] S. Brooks, A. Gelman, G. Jones, and X.-L. Meng, *Handbook of Markov Chain Monte Carlo*. CRC press, 2011.

[63] M. D. Hoffman and A. Gelman, "The no-u-turn sampler: Adaptively setting path lengths in hamiltonian monte carlo.," *Journal of Machine Learning Research*, vol. 15, no. 1, pp. 1593–1623, 2014.

[64] B. Carpenter, A. Gelman, M. D. Hoffman, D. Lee, B. Goodrich, M. Betancourt, M. Brubaker, J. Guo, P. Li, and A. Riddell, "Stan: A probabilistic programming language," *Journal of Statistical Software*, vol. 76, no. 1, 2017.

[65] J. Ching and Y.-C. Chen, "Transitional markov chain monte carlo method for bayesian model updating, model class selection, and model averaging," *Journal of Engineering Mechanics*, vol. 133, no. 7, pp. 816–832, 2007.

[66] T. D. Huan, A. Mannodi-Kanakkithodi, and R. Ramprasad, "Accelerated materials property predictions and design using motif-based fingerprints," *Physical Review B*, vol. 92, no. 1, p. 014 106, 2015.

[67] S. Golchi and J. L. Loeppky, "Monte carlo based designs for constrained domains," *arXiv preprint arXiv:1512.07328*, 2015.

[68] S. Golchi and D. A. Campbell, "Sequentially constrained monte carlo," *Computational Statistics & Data Analysis*, vol. 97, pp. 98–113, 2016.

[69] A. Jasra, D. A. Stephens, A. Doucet, and T. Tsagaris, "Inference for lévy-driven stochastic volatility models via adaptive sequential monte carlo," *Scandinavian Journal of Statistics*, vol. 38, no. 1, pp. 1–22, 2011.

[70] H. Zhao, R. Jin, S. Wu, and J. Shi, "Pde-constrained gaussian process model on material removal rate of wire saw slicing process," *Journal of Manufacturing Science and Engineering*, vol. 133, no. 2, p. 021 012, 2011.

[71] S. Ba, V. R. Joseph, *et al.*, "Composite gaussian process models for emulating expensive functions," *The Annals of Applied Statistics*, vol. 6, no. 4, pp. 1838–1860, 2012.

[72] D. Higdon, "A process-convolution approach to modelling temperatures in the north atlantic ocean," *Environmental and Ecological Statistics*, vol. 5, no. 2, pp. 173–190, 1998.

[73] R. B. Gramacy and H. K. H. Lee, "Bayesian treed gaussian process models with an application to computer modeling," *Journal of the American Statistical Association*, vol. 103, no. 483, pp. 1119–1130, 2008.

[74] R. B. Gramacy and D. W. Apley, "Local gaussian process approximation for large computer experiments," *Journal of Computational and Graphical Statistics*, vol. 24, no. 2, pp. 561–578, 2015.

[75] V. R. Joseph, "Limit kriging," *Technometrics*, vol. 48, no. 4, pp. 458–466, 2006.

[76] M. Fuentes, "A high frequency kriging approach for non-stationary environmental processes," *Environmetrics: The official journal of the International Environmetrics Society*, vol. 12, no. 5, pp. 469–483, 2001.

[77] P. Fernandez-Zelaia, V. R. Joseph, S. R. Kalidindi, and S. N. Melkote, "Estimating mechanical properties from spherical indentation using bayesian approaches," *Materials & Design*, vol. 147, pp. 92–105, 2018.

[78] C. F. Van Loan, "The ubiquitous kronecker product," *Journal of Computational and Applied Mathematics*, vol. 123, no. 1-2, pp. 85–100, 2000.

[79] H.-J. Bunge, *Texture Analysis in Materials Science: Mathematical Methods*. Elsevier, 2013.

[80] S. Pathak, D. Stojakovic, and S. R. Kalidindi, "Measurement of the local mechanical properties in polycrystalline samples using spherical nanoindentation and orientation imaging microscopy," *Acta Materialia*, vol. 57, no. 10, pp. 3020–3028, 2009.

[81] D. K. Patel, H. F. Al-Harbi, and S. R. Kalidindi, "Extracting single-crystal elastic constants from polycrystalline samples using spherical nanoindentation and orientation measurements," *Acta Materialia*, vol. 79, pp. 108–116, 2014.

[82] D. K. Patel and S. R. Kalidindi, "Estimating the slip resistance from spherical nanoindentation and orientation measurements in polycrystalline samples of cubic metals," *International Journal of Plasticity*, vol. 92, pp. 19–30, 2017.

[83] N. H. Paulson, M. W. Priddy, D. L. McDowell, and S. R. Kalidindi, "Reduced-order structure-property linkages for polycrystalline microstructures based on 2-point statistics," *Acta Materialia*, vol. 129, pp. 428–438, 2017.

[84] N. H. Paulson, M. W. Priddy, D. L. McDowell, and S. R. Kalidindi, "Data-driven reduced-order models for rank-ordering the high cycle fatigue performance of polycrystalline microstructures," *Materials & Design*, 2018.

[85] A. T. Wu, A. Gusak, K. Tu, and C. Kao, "Electromigration-induced grain rotation in anisotropic conducting beta tin," *Applied Physics Letters*, vol. 86, no. 24, p. 241 902, 2005.

[86] A. T. Wu and Y. Hsieh, "Direct observation and kinetic analysis of grain rotation in anisotropic tin under electromigration," *Applied Physics Letters*, vol. 92, no. 12, p. 121 921, 2008.

[87] Y. C. Yabansu, D. K. Patel, and S. R. Kalidindi, "Calibrated localization relationships for elastic response of polycrystalline aggregates," *Acta Materialia*, vol. 81, pp. 151–160, 2014.

[88] B. Efron and R. J. Tibshirani, *An Introduction to the Bootstrap*. CRC press, 1994.

[89] S. Pathak, J. Shaffer, and S. R. Kalidindi, "Determination of an effective zero-point and extraction of indentation stress–strain curves without the continuous stiffness measurement signal," *Scripta Materialia*, vol. 60, no. 6, pp. 439–442, 2009.

[90] S. R. Kalidindi and S. Pathak, "Determination of the effective zero-point and the extraction of spherical nanoindentation stress–strain curves," *Acta Materialia*, vol. 56, no. 14, pp. 3523–3532, 2008.

[91] A. Khosravani, A. Cecen, and S. R. Kalidindi, "Development of high throughput assays for establishing process-structure-property linkages in multiphase polycrystalline metals: Application to dual-phase steels," *Acta Materialia*, vol. 123, pp. 55–69, 2017.

[92] J. S. Weaver, A. Khosravani, A. Castillo, and S. R. Kalidindi, "High throughput exploration of process-property linkages in al-6061 using instrumented spherical microindentation and microstructurally graded samples," *Integrating Materials and Manufacturing Innovation*, vol. 5, no. 1, p. 10, 2016.

[93] J. S. Weaver and S. R. Kalidindi, "Mechanical characterization of ti-6al-4v titanium alloy at multiple length scales using spherical indentation stress-strain measurements," *Materials & Design*, vol. 111, pp. 463–472, 2016.

[94] W. C. Oliver and G. M. Pharr, "An improved technique for determining hardness and elastic modulus using load and displacement sensing indentation experiments," *Journal of Materials Research*, vol. 7, no. 6, pp. 1564–1583, 1992.

[95] F. Mohs, *Treatise on Mineralogy: Or, The Natural History of the Mineral Kingdom*. A. Constable et al., 1825, vol. 1.

[96] H. R. Hertz, *Miscellaneous Papers: With an Introd. by Philipp Lenard. Authorised English Translation by DE Jones and GA Schott*. Macmillan, 1896.

[97] J. Brinell, "Way of determining the hardness of bodies and some applications of the same," *Teknisk Tidskrift*, vol. 5, p. 69, 1900.

[98] D. Tabor, *The Hardness of Metals*. Oxford university press, 2000.

[99] A. C. Fischer-Cripps, *Factors Affecting Nanoindentation Test Data*. Springer, 2000.

[100] S. Vachhani, R. Doherty, and S. Kalidindi, "Effect of the continuous stiffness measurement on the mechanical properties extracted using spherical nanoindentation," *Acta Materialia*, vol. 61, no. 10, pp. 3744–3751, 2013.

[101] A. Giannakopoulos and S Suresh, "Determination of elastoplastic properties by instrumented sharp indentation," *Scripta Materialia*, vol. 40, no. 10, pp. 1191–1198, 1999.

[102] M Dao, N. v. Chollacoop, K. Van Vliet, T. Venkatesh, and S Suresh, "Computational modeling of the forward and reverse problems in instrumented sharp indentation," *Acta Materialia*, vol. 49, no. 19, pp. 3899–3918, 2001.

[103] D. K. Patel and S. R. Kalidindi, "Correlation of spherical nanoindentation stress-strain curves to simple compression stress-strain curves for elastic-plastic isotropic materials using finite element models," *Acta Materialia*, vol. 112, pp. 295–302, 2016.

[104] M Rodríguez, J. M. Molina-Aldareguía, C González, and J LLorca, "Determination of the mechanical properties of amorphous materials through instrumented nanoindentation," *Acta Materialia*, vol. 60, no. 9, pp. 3953–3964, 2012.

[105] B. R. Donohue, A. Ambrus, and S. R. Kalidindi, "Critical evaluation of the indentation data analyses methods for the extraction of isotropic uniaxial mechanical

properties using finite element models," *Acta Materialia*, vol. 60, no. 9, pp. 3943–3952, 2012.

[106] A. Muliana, R. M. Haj-Ali, R. Steward, and A. Saxena, "Artificial neural network and finite element modeling of nanoindentation tests," *Metallurgical and Materials Transactions A*, vol. 33, no. 7, pp. 1939–1947, 2002.

[107] M. W. Priddy, "Exploration of forward and inverse protocols for property optimization of ti-6al-4v," PhD thesis, Georgia Institute of Technology, 2016.

[108] M. Plumlee, V. R. Joseph, and H. Yang, "Calibrating functional parameters in the ion channel models of cardiac cells," *Journal of the American Statistical Association*, vol. 111, no. 514, pp. 500–509, 2016.

[109] D. S. Simulia, "Abaqus 6.12 documentation," *Providence, Rhode Island, US*, 2012.

[110] D. Gamerman and H. F. Lopes, *Markov Chain Monte Carlo: Stochastic Simulation for Bayesian Inference*. Chapman and Hall/CRC, 2006.

[111] S. Mak, V. R. Joseph, *et al.*, "Support points," *The Annals of Statistics*, vol. 46, no. 6A, pp. 2562–2592, 2018.

[112] G. M. Laslett, "Kriging and splines: An empirical comparison of their predictive performance in some applications," *Journal of the American Statistical Association*, vol. 89, no. 426, pp. 391–400, 1994.

[113] B. Williams, D. Higdon, J. Gattiker, L. Moore, M. McKay, S. Keller-McNulty, *et al.*, "Combining experimental data and computer simulations, with an application to flyer plate experiments," *Bayesian Analysis*, vol. 1, no. 4, pp. 765–792, 2006.

[114] J. Rougier, "Efficient emulators for multivariate deterministic functions," *Journal of Computational and Graphical Statistics*, vol. 17, no. 4, pp. 827–843, 2008.

[115] M. J. Bayarri, J. O. Berger, M. C. Kennedy, A. Kottas, R. Paulo, J. Sacks, J. A. Cafeo, C.-H. Lin, and J. Tu, "Predicting vehicle crashworthiness: Validation of computer models for functional and hierarchical data," *Journal of the American Statistical Association*, vol. 104, no. 487, pp. 929–943, 2009.

[116] V. R. Joseph, E. Gul, and S. Ba, "Maximum projection designs for computer experiments," *Biometrika*, vol. 102, no. 2, pp. 371–380, 2015.

[117] D. Sagapuram, H. Yeung, Y. Guo, A. Mahato, R. M'Saoubi, W. D. Compton, K. P. Trumble, and S. Chandrasekar, "On control of flow instabilities in cutting of metals," *CIRP Annals*, vol. 64, no. 1, pp. 49–52, 2015.

[118] R. Z. Valiev, R. K. Islamgaliev, and I. V. Alexandrov, "Bulk nanostructured materials from severe plastic deformation," *Progress in Materials Science*, vol. 45, no. 2, pp. 103–189, 2000.

[119] A. P. Zhilyaev and T. G. Langdon, "Using high-pressure torsion for metal processing: Fundamentals and applications," *Progress in Materials Science*, vol. 53, no. 6, pp. 893–979, 2008.

[120] L. Murr, A. Ramirez, S. Gaytan, M. Lopez, E. Martinez, D. Hernandez, and E Martinez, "Microstructure evolution associated with adiabatic shear bands and shear band failure in ballistic plug formation in ti–6al–4v targets," *Materials Science and Engineering: A*, vol. 516, no. 1-2, pp. 205–216, 2009.

[121] K Minnaar and M Zhou, "An analysis of the dynamic shear failure resistance of structural metals," *Journal of the Mechanics and Physics of Solids*, vol. 46, no. 10, pp. 2155–2170, 1998.

[122] Y Me-Bar and D Shechtman, "On the adiabatic shear of ti 6al 4v ballistic targets," *Materials Science and Engineering*, vol. 58, no. 2, pp. 181–188, 1983.

[123] S. Fatemi-Varzaneh, A Zarei-Hanzaki, and H. Beladi, "Dynamic recrystallization in az31 magnesium alloy," *Materials Science and Engineering: A*, vol. 456, no. 1-2, pp. 52–57, 2007.

[124] S. Ion, F. Humphreys, and S. White, "Dynamic recrystallisation and the development of microstructure during the high temperature deformation of magnesium," *Acta Metallurgica*, vol. 30, no. 10, pp. 1909–1919, 1982.

[125] L. Tóth, B Beausir, C. Gu, Y Estrin, N Scheerbaum, and C. Davies, "Effect of grain refinement by severe plastic deformation on the next-neighbor misorientation distribution," *Acta Materialia*, vol. 58, no. 20, pp. 6706–6716, 2010.

[126] Z. Yang, X. Li, L. C. Brinson, A. N. Choudhary, W. Chen, and A. Agrawal, "Microstructural materials design via deep adversarial learning methodology," *arXiv preprint arXiv:1805.02791*, 2018.

[127] S. Pathak, D. Stojakovic, R. Doherty, and S. R. Kalidindi, "Importance of surface preparation on the nano-indentation stress-strain curves measured in metals," *Journal of Materials Research*, vol. 24, no. 3, pp. 1142–1155, 2009.

[128] A. Cecen, Y. C. Yabansu, and S. R. Kalidindi, "A new framework for rotationally invariant two-point spatial correlations in microstructure datasets," *Acta Materialia*, vol. 158, pp. 53–64, 2018.

[129] A Çeçen, T Fast, E. Kumbur, and S. Kalidindi, "A data-driven approach to establishing microstructure–property relationships in porous transport layers of polymer electrolyte fuel cells," *Journal of Power Sources*, vol. 245, pp. 144–153, 2014.

[130] A. Iskakov, Y. C. Yabansu, S. Rajagopalan, A. Kapustina, and S. R. Kalidindi, "Application of spherical indentation and the materials knowledge system framework to establishing microstructure-yield strength linkages from carbon steel scoops excised from high-temperature exposed components," *Acta Materialia*, vol. 144, pp. 758–767, 2018.

[131] P. Deshpande, B. Gautham, A Cecen, S Kalidindi, A. Agrawal, and A Choudhary, "Application of statistical and machine learning techniques for correlating properties to composition and manufacturing processes of steels," in *Proceedings of the 2nd World Congress on Integrated Computational Materials Engineering (ICME)*, Springer, 2013, pp. 155–160.

[132] C. E. Rasmussen, "Gaussian processes in machine learning," in *Advanced Lectures on Machine Learning*, Springer, 2004, pp. 63–71.

[133] C. M. Bishop, *Pattern Recognition and Machine Learning (Information Science and Statistics)*. Berlin, Heidelberg: Springer-Verlag, 2006, ISBN: 0387310738.

[134] S. J. Pan, Q. Yang, *et al.*, "A survey on transfer learning," *IEEE Transactions on Knowledge and Data Engineering*, vol. 22, no. 10, pp. 1345–1359, 2010.

[135] B. Haaland and P. Z. Qian, "An approach to constructing nested space-filling designs for multi-fidelity computer experiments," *Statistica Sinica*, vol. 20, no. 3, p. 1063, 2010.

[136] R. Tuo, C. J. Wu, and D. Yu, "Surrogate modeling of computer experiments with different mesh densities," *Technometrics*, vol. 56, no. 3, pp. 372–380, 2014.

[137] A Cecen, E. Wargo, A. Hanna, D. Turner, S. Kalidindi, and E. Kumbur, "3-d microstructure analysis of fuel cell materials: Spatial distributions of tortuosity, void size and diffusivity," *Journal of The Electrochemical Society*, vol. 159, no. 3, B299–B307, 2012.

[138] A. Agrawal, P. D. Deshpande, A. Cecen, G. P. Basavarsu, A. N. Choudhary, and S. R. Kalidindi, "Exploration of data science techniques to predict fatigue strength of steel from composition and processing parameters," *Integrating Materials and Manufacturing Innovation*, vol. 3, no. 1, p. 8, 2014.

[139] G. Pilania, A. Mannodi-Kanakkithodi, B. Uberuaga, R. Ramprasad, J. Gubernatis, and T. Lookman, "Machine learning bandgaps of double perovskites," *Scientific Reports*, vol. 6, p. 19 375, 2016.

[140] M. A. Meyers, A Mishra, and D. J. Benson, "Mechanical properties of nanocrystalline materials," *Progress in Materials Science*, vol. 51, no. 4, pp. 427–556, 2006.

[141] Y. Wang, M. Chen, F. Zhou, and E. Ma, "High tensile ductility in a nanostructured metal," *Nature*, vol. 419, no. 6910, p. 912, 2002.

[142] Z. Lee, D. Witkin, V Radmilovic, E. Lavernia, and S. Nutt, "Bimodal microstructure and deformation of cryomilled bulk nanocrystalline al–7.5 mg alloy," *Materials Science and Engineering: A*, vol. 410, pp. 462–467, 2005.

[143] X Guo, G Yang, and G. Weng, "The saturation state of strength and ductility of bimodal nanostructured metals," *Materials Letters*, vol. 175, pp. 131–134, 2016.

[144] X Guo, G Yang, G. Weng, and J Lu, "Interface effects on the strength and ductility of bimodal nanostructured metals," *Acta Mechanica*, pp. 1–13, 2018.

[145] A Mishra, B. Kad, F Gregori, and M. Meyers, "Microstructural evolution in copper subjected to severe plastic deformation: Experiments and analysis," *Acta Materialia*, vol. 55, no. 1, pp. 13–28, 2007.

[146] C Saldana, A. H. King, and S Chandrasekar, "Thermal stability and strength of deformation microstructures in pure copper," *Acta Materialia*, vol. 60, no. 10, pp. 4107–4116, 2012.

[147] C Saldana, T. Murthy, M. Shankar, E. Stach, and S Chandrasekar, "Stabilizing nanostructured materials by coherent nanotwins and their grain boundary triple junction drag," *Applied Physics Letters*, vol. 94, no. 2, p. 021 910, 2009.

[148] S. Abolghasem, S. Basu, and M. R. Shankar, "Quantifying the progression of dynamic recrystallization in severe shear deformation at high strain rates," *Journal of Materials Research*, vol. 28, no. 15, pp. 2056–2069, 2013.

[149] S. Kirkpatrick, C. D. Gelatt, and M. P. Vecchi, "Optimization by simulated annealing," *Science*, vol. 220, no. 4598, pp. 671–680, 1983.

[150] T. L. Bergman, F. P. Incropera, A. S. Lavine, and D. P. Dewitt, *Introduction to Heat Transfer*. John Wiley & Sons, 2011.

[151] D. Fullwood, B. Adams, and S. Kalidindi, "Generalized pareto front methods applied to second-order material property closures," *Computational Materials Science*, vol. 38, no. 4, pp. 788–799, 2007.

[152] S. T. Roweis and L. K. Saul, "Nonlinear dimensionality reduction by locally linear embedding," *Science*, vol. 290, no. 5500, pp. 2323–2326, 2000.

[153] F. Pedregosa, G. Varoquaux, A. Gramfort, V. Michel, B. Thirion, O. Grisel, M. Blondel, P. Prettenhofer, R. Weiss, V. Dubourg, *et al.*, "Scikit-learn: Machine learning in python," *Journal of Machine Learning Research*, vol. 12, no. Oct, pp. 2825–2830, 2011.

[154] E. S. Pearson and H. O. Hartley, "Biometrika tables for statisticians," 1966.

[155] V. R. Joseph, "Space-filling designs for computer experiments: A review," *Quality Engineering*, vol. 28, no. 1, pp. 28–35, 2016.

[156] V. R. Joseph, "Rejoinder to space-filling designs for computer experiments: A reviewi," *Quality Engineering*, vol. 28, no. 1, 2016.

[157] Stan Development Team, *RStan: The R interface to Stan*, R package version 2.17.3, 2018.

[158] P. Fernandez-Zelaia, *Inverse spherical indentatioon*, `https://github.com/pfz3/Inverse-Spherical-Indentation`, 2018.

[159] G. Casella and R. L. Berger, *Statistical Inference*. Duxbury Pacific Grove, CA, 2002, vol. 2.

[160] T. Marusich and M. Ortiz, "Modelling and simulation of high-speed machining," *International Journal for Numerical Methods in Engineering*, vol. 38, no. 21, pp. 3675–3694, 1995.

[161] D. Ulutan and T. Özel, "Determination of constitutive material model parameters in fe-based machining simulations of ti-6al-4v and in-100 alloys: An inverse methodology," *Proceedings of NAMRI/SME*, vol. 41, 2013.

[162] T Özel, Y. Arısoy, and C Guo, "Identification of microstructural model parameters for 3d finite element simulation of machining inconel 100 alloy," *Procedia CIRP*, vol. 46, pp. 549–554, 2016.

[163] D Umbrello, R Msaoubi, and J. Outeiro, "The influence of johnson–cook material constants on finite element simulation of machining of aisi 316l steel," *International Journal of Machine Tools and Manufacture*, vol. 47, no. 3-4, pp. 462–470, 2007.

[164] G. R. Johnson and T. J. Holmquist, "Evaluation of cylinder-impact test data for constitutive model constants," *Journal of Applied Physics*, vol. 64, no. 8, pp. 3901–3910, 1988.

[165] M Martin, A Mishra, M. Meyers, and N. Thadhani, "Instrumented anvil-on-rod tests for constitutive model validation and determination of strain-rate sensitivity of

ultrafine-grained copper," *Materials Science and Engineering: A*, vol. 464, no. 1-2, pp. 202–209, 2007.

[166] J. R. Rice and D. M. Tracey, "On the ductile enlargement of voids in triaxial stress fields," *Journal of the Mechanics and Physics of Solids*, vol. 17, no. 3, pp. 201–217, 1969.

[167] P. L. B. Oxley and H.-T. Young, "The mechanics of machining: An analytical approach to assessing machinability," Chichester, England: Ellis Horwood Publisher, 1990.

[168] E. Gul, "Designs for computer experiments and uncertainty quantification," PhD thesis, Georgia Institute of Technology, 2016.

[169] E. Gul, V. R. Joseph, H. Yan, and S. N. Melkote, "Uncertainty quantification of machining simulations using an in situ emulator," *Journal of Quality Technology*, vol. 50, no. 3, pp. 253–261, 2018.

[170] A. Malakizadi, S. Cedergren, I. Sadik, and L. Nyborg, "Inverse identification of flow stress in metal cutting process using response surface methodology," *Simulation Modelling Practice and Theory*, vol. 60, pp. 40–53, 2016.

[171] S. Mak, C.-L. Sung, X. Wang, S.-T. Yeh, Y.-H. Chang, V. R. Joseph, V. Yang, and C. J. Wu, "An efficient surrogate model for emulation and physics extraction of large eddy simulations," *Journal of the American Statistical Association*, no. just-accepted, 2017.

[172] G. Han, T. J. Santner, W. I. Notz, and D. L. Bartel, "Prediction for computer experiments having quantitative and qualitative input variables," *Technometrics*, vol. 51, no. 3, pp. 278–288, 2009.

[173] V. R. Joseph and S. N. Melkote, "Statistical adjustments to engineering models," *Journal of Quality Technology*, vol. 41, no. 4, pp. 362–375, 2009.

[174] T. Systems, *Advantedge*, version 7.0, Minneapolis, MN, 2015.

[175] M. Sima and T. Özel, "Modified material constitutive models for serrated chip formation simulations and experimental validation in machining of titanium alloy ti–6al–4v," *International Journal of Machine Tools and Manufacture*, vol. 50, no. 11, pp. 943–960, 2010.

[176] M. Assidi, L. Fourment, S. Guerdoux, and T. Nelson, "Friction model for friction stir welding process simulation: Calibrations from welding experiments," *International Journal of Machine Tools and Manufacture*, vol. 50, no. 2, pp. 143–155, 2010.

[177] U. Kocks and H Mecking, "Physics and phenomenology of strain hardening: The fcc case," *Progress in Materials Science*, vol. 48, no. 3, pp. 171–273, 2003.

[178] T. Hayfield, J. S. Racine, *et al.*, "Nonparametric econometrics: The np package," *Journal of Statistical Software*, vol. 27, no. 5, pp. 1–32, 2008.

[179] T. Duong *et al.*, "Ks: Kernel density estimation and kernel discriminant analysis for multivariate data in r," *Journal of Statistical Software*, vol. 21, no. 7, pp. 1–16, 2007.

[180] C. Fraley and A. E. Raftery, "Mclust version 3: An r package for normal mixture modeling and model-based clustering," Washington Univ. Seattle Dept. of Statistics, Tech. Rep., 2006.